The Initial Conditions and Evolution of Open Clusters

by

Joseph Mitchell Converse

A dissertation submitted in partial satisfaction of the
requirements for the degree of
Doctor of Philosophy

in

Astrophysics

in the

Graduate Division
of the
University of California, Berkeley

Committee in charge:
Doctor Steven Stahler, Co-chair
Professor Chris McKee, Co-chair
Professor James Graham
Professor Michael Manga

Fall 2010

The Initial Conditions and Evolution of Open Clusters

Abstract

The Initial Conditions and Evolution of Open Clusters

by

Joseph Mitchell Converse
Doctor of Philosophy in Astrophysics

University of California, Berkeley

Doctor Steven Stahler, Co-chair
Professor Chris McKee, Co-chair

Despite being some of the most familiar objects observed in the sky, much remains unknown about open clusters. The theory of their formation admits many unanswered questions, and the complex dynamics of their evolution remains an extremely difficult problem to address. In this thesis, I present results that both help to constrain formation theories, as well as to shed new understanding on the many physical processes that drive their evolution.

Starting with a photometric catalog of a cluster, I employ a maximum likelihood technique to determine the mass distribution of its members, including single stars and both components of binary systems. This method allows me to determine not just the fraction of systems which are binary, but also the typical degree of correlation between the masses of their components. I also examine the spatial distribution of the cluster members. The issue of mass segregation is also addressed, introducing a new method for quantifying it.

After quantifying many different properties of the cluster, N-body simulations are used to find the initial state that evolves to most closely match the current cluster. Although a few similar studies have been done in the past, I use a far larger breadth of parameters to compare with the actual data than any previous work. This results in a fairly confident determination of the properties of very young clusters, which any theory of cluster formation will be required to explain. How the cluster evolves from that initial state to the current day and beyond is also examined in detail.

These techniques are used to examine two relatively close and well-known examples of open clusters: the Pleiades and the Alpha Persei cluster. In the case of the former, I find in particular that the overall binary fraction is as high as 76%, significantly higher than the accepted field-star result. The primary and secondary masses within binaries are found to be correlated, in the sense that their ratios are closer to unity than under the hypothesis of random pairing. I also find unambiguous evidence of mass segregation within the cluster.

Building on these results, I find the original cluster, newly stripped of gas, to have already had a virial radius of 4 pc. This configuration was larger than most observed, embedded clusters. Over time, the cluster expanded further and the central surface density fell by about a factor of two. I attribute both effects to the liberation of energy from

tightening binaries of short period. Indeed, the original binary fraction was close to unity. The ancient Pleiades also had significant mass segregation, which persists in the cluster today. In the future, the central density of the Pleiades will continue to fall. For the first few hundred Myr, the cluster as a whole will expand because of dynamical heating by binaries. The expansion process is aided by mass loss through stellar evolution, which weakens the system's gravitational binding. At later times, the Galactic tidal field begins to heavily deplete the cluster mass. Barring destruction by close passage of a giant molecular cloud, the density falloff will continue for as long as 1 Gyr, by which time most of the cluster mass will have been tidally stripped away by the Galactic field.

This same analysis is also applied to Alpha Persei. Here I fist compile the most complete photometric catalog of the system to date. The stellar mass function is found to be weighted more heavily toward higher-mass stars than in the Pleiades. Also in contrast with the Pleiades, I find there to be essentially no mass segregation in the cluster, either today or in its initial state. The binary fraction, however, is found to be quite similar between the two clusters, as high as 70% in Alpha Persei. Once more the initial state is found to be quite large compared to embedded systems. The results of these two clusters together argue strongly the young clusters experience a period of significant expansion associated with the loss of their natal gas. Over time, Alpha Persei will globally expanded as a result of the Galactic tidal field. Dynamical heating by binaries, along with mass loss through stellar evolution, will also inflate the cluster into the future. I predict that Alpha Persei will completely dissolve within the next 300 Myr.

Utilizing a series of N-body simulations, I go on to argue that gravitationally bound stellar clusters of modest population evolve very differently from the picture presented by classical dynamical relaxation theory. The system's most massive stars rapidly sink towards the center and form binary systems. These binaries efficiently heat the cluster, reversing any incipient core contraction and driving a subsequent phase of global expansion. Most previous theoretical studies demonstrating deep and persistent dynamical relaxation have either conflated the process with mass segregation, ignored three-body interactions, or else adopted the artificial assumption that all cluster members are single stars of identical mass. In such a uniform-mass cluster, binary formation is greatly delayed, as we confirm here both numerically and analytically. The relative duration of core contraction and global expansion is effected by stellar evolution, which causes the most massive stars to die out before they form binaries. In clusters of higher N, the epoch of dynamical relaxation lasts for progressively longer periods. By extrapolating our results to much larger populations we can understand, at least qualitatively, why some globular clusters reach the point of true core collapse.

TO MY MOTHER

Contents

List of Figures

List of Tables

Acknowledgments

My mother tells the story of when I was about 4 years old, and asked if you could be a doctor without being a medical doctor. After being told that you could earn a doctorate in any field, I declared then, 25 years ago, that I would become a doctor of science. Like any rational parent would, she smiled and said that was a good dream, but had little serious expectation of a 4-year-old seeing such a thing through. And yet, here I am today.

Now, one does not simply set out and earn a Ph.D. in Astrophysics alone. No matter how much of a personal accomplishment it is, I could never have achieved this goal without the help of many, many people. This has been an epic journey, decades in the making, and a countless number of friends, family, teachers, and mentors have all contributed to shaping who I am and helping me get this far. Too many even to remember the names of everyone who has given a small bit of their lives to me. But even if I cannot list their names, it does not diminish the debt of gratitude I owe to them.

First and foremost among those who have helped me achieve this dream is my thesis advisor, Steve Stahler. For almost four years he has worked with me, guided me, and mentored me through the research process. The result is four, first-author published papers which, when assembled together, constitute this dissertation. Even through the times when methods failed and needed to be re-thought from scratch, or code that was obsessed with seg-faulting no matter how much debugging I did, or through periods of intense personal stress, he has kept me focused on our research. He is by far the single biggest influence in the work presented here, and I could never have accomplished these results without him.

Steve was, of course, not the only person who helped mentor me through the process of this research. I also owe many thanks to the rest of my dissertation committee, Chris McKee, James Graham, and Michael Manga. Whether grilling me with questions during my qualifying exam, or picking apart the details of my research, they have also helped to push me further. This thesis was strengthened significantly through the discussions and revisions following their review. Beyond Berkeley, I also should thank Steve Mcmillan for all the times he helped me get Starlab working and understand its results. John Stauffer was similarly helpful on the observational side, providing the data needed to connect our theoretical ideas to reality. And, of course, I thank the NSF (for grants AST 06-39743 and AST 09-08573 in particular) who provided much of the money that paid for the luxuries of my graduate career, such as rent and food. Finally, a graduate student cannot get by through the help of faculty alone. For the many, MANY hassles of dealing with university bureaucracy and

always knowing how to get anything accomplished, Dexter Stewart has been more helpful than I ever could have imagined. Although it is her job to do such things, Dexter goes well beyond the call of duty in being there for all the graduate students. I am very glad to be leaving Berkeley before she retires, as I cannot imagine going through these years without her help.

Although Berkeley has been the place that provided my graduate education, I could never have gotten here to begin with without the mentors who came before. Colgate University was a beautiful place which I will fondly remember my entire life. My time there in many ways shaped my development into adulthood, much more than just academic development. The friends I made there (and I count my professors among my friends from Colgate) are more people to whom I owe much. Foremost among them are Tom Balonek and Tony Aveni. These two professors were my friends and my guides both academically, and at times personally. They were especially influential in developing my teaching skills. Between them, they trusted me to help them teach others for 7 of my 8 semesters at Colgate, giving me an invaluable depth of experience. But here again, faculty alone cannot get a student through a university's hoops. Like Dexter at Berkeley, Diane Janney was every student's best friend for anything and everything that faculty couldn't help with (which is a lot).

During my time at Colgate, I also benefitted greatly from the summer research internships I did. In particular, the fateful summer of 2002 saw me working at the Space Telescope Science Institute, primarily with a post-doc there at the time named Rupali Chandar. This was probably my first serious exposure to doing real, original research. Rupali quickly proved herself to be a phenomenal advisor in this endeavor. So much so that she later became the de facto advisor on my senior project for Colgate, which itself was spun off from that original summer work. I'm sure the experience and recommendation from her did much to help me get into Berkeley. Perhaps more importantly, I know that summer did much to help me get the postdoctoral position I am now preparing to start; working at the University of Toledo under the mentoring of Professor Rupali Chandar.

Stepping back further, my successes in college were already built upon what I had learned from still earlier mentors through high school. Chief among them, Neil Shade is a physics teacher who has been acknowledged by countless students for having been their inspiration to love science, and is often remembered by many as their favorite teacher in school. I am among this crowd. Had I known then how great of a teach he was, I might have considered intentionally failing his classes just so that I could take them twice. And somehow my small town of Piqua had not just one, but many great teachers (Greg Stewart, David Williams, Larry Hamilton, and Jana Krogman as just a few examples). Peggy Thoma was a guidance counselor who fulfilled that title in many more ways than the job actually expected of her. She was another key player in both my intellectual development during high school, as well as helping to guide me into the future that followed.

There were more teachers who had a still-earlier influence on me, of course. Charlie Tamplin taught me BASIC on a Commodore 64 and got me into HAM radio at an early age, thus beginning a still-continuing affection for technology and computing. My 8th grade English teacher, Gary Yates, many times graded my work a B not because it was not of A

quality, but because he knew I had done the minimal amount needed. Instead, he refused to give me an A until he could see that I put effort into doing my best with my work instead. Even as young as the 4th grade, another teacher could see that I was coasting by without actually trying. After earning a detention for not doing homework (simply due to not wanting to do it), Lysbeth Klosterman left a comment on my report card that quarter telling me, "Don't ever be content with mediocrity." I hope today she can see that I did not do so. Finally, from elementary school through college I also pursued an interest in playing the baritone horn. This endeavor was guided by Jarrel Morgan, who continued to teach me with private lessons even after he retired as the school's band director. Here again he continued to push me to push my limits, culminating in my earing a superior rating at state competition for my rendition of the Carnival of Venice, a traditional trumpet solo, on my much-larger instrument.

Of course, life is about much more than just education. Although the teachers and professors of my past have shaped my academic development, there are still many friends who I could never have made it here without. Here at Berkeley, the quasi-weekely games nights that I have enjoyed with other grad students have been my primary means of enjoying their friendship. Dan Perley, Charles Hansen, Onsi Fakhouri, and Eric Huff stand chief among those I have felt closest to. They have been there for everything from discussions of science and research that fueled new progress in my work, to the victories and defeats of Smash Brothers, Mario Kart, and Dominion; even to the lengths of hearing Dan sing karaoke. "Fun times" is an understatement to be sure.

Before moving to California, it was my friends at Colgate who shared with me four of the best years of my life. Certainly Jeyhan Kartaltepe and Emily Miller must be called out as the two who shared both the classes of the astronomy curriculum and the time in the Astro Lab with me. Brian Mooney deserves many thanks for being willing to live with me for three of those years. (Or maybe for not making it too hard for me to live with him?) Johny Chaklader, despite being the world's dorkiest dork, was certainly my single closest friend in Hamilton, and to this day I would happily "squeeze the rabbit" with him anytime. (And I'd let him explain why that's a euphemism for playing ping-pong.) There were also other good friends, such as Michael Tringali and Kenda Post, who, although I didn't get to enjoy the full four years with them, were nonetheless also good friends who helped enrich this period of my life.

Growing up in my hometown, I was a more introverted person who kept a smaller, but tighter circle of friends. In junior high and high school, Chris Broyles and Dan Grise were the two most dear friends to me. Though the years have separated us to our different lives, and I do not keep up with them as much as I wish I did, I still have too many fond memories of times spent with them to not list them among the people who have influenced me. Though my youngest days in elementary school, it was Ryan Gantt who filled this same role. To have recently reconnected with him after growing quite far apart over the years was a welcomed surprise.

In today's modern world, friends need not always be located physically near you. The internet has provided a world of communication that has let me meet many new people,

and developed some close friendships. Though I met him online, Alex Osaki has grown to become my closest, dearest, and most real friend. In several ways he has profoundly changed my life, and all for the better. To say I cannot imagine having gotten through these past few years without him is a gross understatement. I owe him many thanks for having been there for me throughout, not just for helping me through the bad times, but just as much for every game of Civilization and every run for fast food. Alongside Alex, Mike Quintana also should be singled out for generally being an awesome guy to know. I wish everyone could know someone as genuinely kind-hearted and giving as he is.

And there are many other friends I have met online, even just as screennames. Baikal, Kaiser57, SlavicBalto, OSDCC, Klisoura, Mazekais, Margaret, Sofia, Keshet, and even Samantha, just to name a few of those whom I am glad to have met. Each of them have their stories in how they have touched my life. There are also the many patrons of my favorite tavern. Even when they have thought me crazy for what I do, they have never doubted that I was actually crazy like a fox. Though the faces seen there have changed over the past 6 years, I look forward to spending many more with whatever lot of people stumble into it.

To all of those teachers, mentors, and friends, I must give some credit for my accomplishment to you. They are the people who have defined the experiences and development through my life. But there are others, still closer to me, without whom my life would not have occurred. And despite the myriad of other influences, these few are the ones who have most fundamentally shaped who I am. I count among these people not just the parents who gave me their genes, but also the step-mother who has never shown me anything but a deep love and hearty meals. Though for many years I thought of her only as my father's wife, the truth is that Bonnie Converse has always been, and always will be, my mother in every sense of the word.

To this day, I still remember the nights when my father (Dan Converse) would visit me and wake me up at 2am to view the rings of Saturn through his telescope. He always harbored a deep love for the cosmos, and it would be disingenuous for me to try to claim that he wasn't the principle reason for my own passion for astronomy. Though I only saw him a scant few times a year, whether it was through his genes or those fleeting times, my father left a deep impression on me. He was the one who originally gave me my love of science. He was the one who introduced me to the wonder of the sky. For better and worse, for the good and the bad, I love my father for who he is, and I owe him an endless thanks for what he has given me.

Finally, we come to the one singular individual to whom I owe more than all the others mentioned here combined. The one woman who has sacrificed herself in countless ways over the years in order to better provide for me. Even while working full time in a job that carried no end of stress for her, she was always there for me. She filled the roles of mother, father, sibling, and friend. After all the times with everyone else in my life, it has always been to her that I have returned home in the end. To try and enumerate the ways in which she has shaped and helped me would require more pages than are found in an encyclopedia. And even then, I would still lack the words to describe just how wonderful and special she is. All that I am today, all that I have accomplished, all that I will do in my future; all of it

is because of her. She is the one who has always been the wind beneath my wings. Others have said that if they have seen farther, it was because they have stood on the shoulders of giants. In my case, hers are the shoulders I have stood on (at least metaphorically; doing so literally wouldn't gain me much extra height).

I dedicate this dissertation first and foremost to my mother, Janet Converse, because without her, nothing I have done could ever have been possible. To all the others mentioned here, and the countless others I have neglected to mention by name, I also give my deepest thanks for all that you have given me.

Chapter 1

Introduction and Outline

1.1 Clusters of Stars

It has been recognized since ancient times that stars are not distributed uniformly throughout the sky. Not only do they aggregate along the band today identified as the plane of our Milky Way Galaxy, but they also are seem to appear in various discrete clumps. Today it is understood that these overdensities of stars are physically coherent groups. These star clusters are observed to range from a few dozens to millions of members. The larger of these groups, the globular clusters, are several Gyr old and populate the halo of our Galaxy and most other large galaxies.

The smaller groups, containing typically $\sim 10^2$ to 10^4 members live within the Galactic disk, and are much younger, some as young as only a few Myr (e.g. Hillenbrand 1997), and with very few older than 1 Gyr (Friel 1995). Many of the youngest groups, the so-called T- and OB-associations, are bound together only by the mass of the gas and dust around them. Those whose stellar mass alone is able to bind the group together are known as open clusters.[1] It is these systems on which this thesis focuses.

Although not as dense as globular clusters, the central concentrations of open clusters are nonetheless greatly enhanced over the background of field stars. They are thus relatively easy to identify. Over a thousand systems are known, and the census is thought to be complete out to 2 kpc (Brown 2001; Dias et al. 2002). Because the clusters are no longer buried within interstellar gas and dust, their internal structure and dynamics is also more accessible than for younger groups.

Despite these favorable circumstances, many basic questions remain unanswered. Most fundamentally, how do open clusters form? All observed systems have undergone some degree of dynamical relaxation. Thus, the present-day distribution of stellar mass differs from the one just after disruption of the parent cloud. Recovering this initial configuration will clearly be of value in addressing the formation issue. But such reconstruction presupposes, and

[1]The term "open" here comes from the fact that their central densities are much lower than those of globular clusters. Hence their cores appear more open to investigation.

indeed requires, that the stellar content of *present-day* clusters is first accurately known.

These are the issues which will be examined in this thesis. The goal will be, first, to accurately quantify the observable properties of open clusters as they are today. As will be shown, even this first step is no easy task. Once this knowledge is in hand, however, it will be used to determine the sought-after initial state. But beyond simply describing the clusters as they appear today and in their infancy, I will also explore their full evolution to the present time. And I will further ask where this same evolution will carry them into the future.

While much insight has been gained from studies by numerous other researchers, a clear advance would be made if the original state of one or more observed clusters could be established empirically. I will take two clusters in particular, the Pleaides and the Alpha Persei cluster, as examples to be studied in detail. By combining the established theory of stellar dynamics with the tools of numerical simulations, as well as new methods for the analysis of the current state of the clusters, this thesis will present a significantly more complete description of the initial configuration and evolution of open clusters than any previous work.

1.2 Present Understanding

1.2.1 The Formation of Open Clusters

Despite recent advances in the field of star formation (for a comprehensive review, see McKee & Ostriker 2007), the origin of open clusters remains a mystery. It is now generally accepted that all stars are born within groups. These groups are at first heavily embedded within molecular clouds, their members obscured optically by copious interstellar dust. By the time the stars are revealed, only about 10% are in open clusters (Miller & Scalo 1978; Adams & Myers 2001). The remainder are in either T- or OB associations, both destined to disperse within a few Myr. In contrast, the stars within open clusters are gravitationally bound to each other, and the group can survive intact for several Gyr (Friel 1995). How do molecular clouds spawn these relatively rare but stable configurations?

One intriguing aspect of the mystery is that open clusters are intermediate in their properties between T- and OB associations. The former are relatively sparse in projected stellar density, and contain up to about 100 members (e.g., Kenyon & Hartmann 1995; Luhman 2007). The latter, as exemplified by the nearby Orion Nebula Cluster, begin with extraordinarily high density (McCaughrean & Stauffer 1994) and contain well over a thousand members (Hillenbrand 1997), far more than the eponymous O and B stars. A published compilation of Galactic open clusters (Mermilliod 1995) shows them to have from a few hundred to roughly a thousand stars, i.e., just in the middle range. Apparently, systems born with either too low or too high a population and density are fragile, while the relative minority falling in between can survive over long periods.

There is already an extensive literature on young, bound clusters, both observational

and theoretical (for reviews, see Clarke et al. 2000; Elmegreen et al. 2000). Models for the origin of open clusters, dating back at least to Lada et al. (1984), have focused on the need for a high star formation efficiency (the fraction of the mass of the initial cloud eventually turned into stars) in the parent cloud (see, however, Huff & Stahler 2006, for a different perspective). A standard computational technique, using N-body simulations, is to create stars in a background potential well, remove that potential through various prescriptions, and then assess the result (e.g., Kroupa & Boily 2002; Goodwin & Bastian 2006; Baumgardt & Kroupa 2007; Goodwin 2009). Some researchers using this approach, implemented either analytically or numerically, have hypothesized that open clusters are the bound remnants of expanding OB associations (Adams 2000; Kroupa et al. 2001). Observations of young clusters have confirmed that the early stage of gas loss causes the cluster to expand, if not disrupt completely (Elson 1991; Fall et al. 2005; Bastian & Goodwin 2006; Bastian et al. 2008). In recent years, most theoretical ideas have been motivated by fluid dynamical simulations of turbulent, collapsing clouds (Klessen et al. 2000; Vázquez-Semadeni et al. 2003; Li et al. 2003).

One of the most widely quoted hypotheses for the origin of the open clusters is based on the model of Kroupa et al. (2001), which began with a group of 10,000 stars embedded in its parent cloud. But this is far larger than the observed sizes of embedded clusters (Lada & Lada 2003). More recently, observations of the Antennae galaxies (Fall et al. 2009) and the Magellanic Clouds (Chandar et al. 2010) have begun to suggest that clusters may form from a simple power-law distribution of masses, and that their rate of disruption is independent of mass. This is in stark contrast with the more commonly accepted theory put forth by Kroupa & Boily (2002), who predict that clusters with masses on the order of 10^3 to 10^5 $M_\odot$ should disperse quickly due to the rapid loss of gas which has been ionized by O- and B-stars. Smaller systems lack a source of ionizing radiation, while larger ones are massive enough to retain even this heated gas. The observational data from extragalactic clusters is still too uncertain to say definitively whether or not there is an evolutionary difference between cluster that do or do not produce O- and B-stars. The data does suggest, however, that clusters on both sides of 10^5 $M_\odot$ are equally likely to survive to older age. These results have resulted in a re-evaluation of our understanding of the physical processes by which star clusters lose their natal gas (Fall et al. 2010). Clearly there is still much to be learned about the origin and evolution of star clusters.

In this thesis, I will present results establishing the earlier, post-gas loss state of the two clusters examined. Such initial states will serve to constrain and inform models that seek to explain how these particular systems were produced by star formation activity in their parent clouds, and how they evolved through the loss of their natal gas. These systems are not as massive as the larger ones considered by extragalactic studies, and thus serve to compliment those results by extending our knowledge to smaller clusters.

1.2.2 Stellar Dynamical Evolution

The dynamical evolution of gravitationally bound stellar clusters has been extensively studied for decades, and the basic theory is thought to be secure. Populous systems evolve, over many crossing times, through the processes known collectively as dynamical relaxation (Binney & Tremaine 2008, Chapter 7). The inner core of the cluster contracts, effectively transferring energy to the outer halo, which expands as a result. Concurrently, stars of relatively high mass sink toward the cluster center. Theory predicts further that the interior contraction leads eventually to core collapse, a catastrophic rise in central density (Lynden-Bell & Wood 1968). As first suggested by Hills (1975), the runaway is halted when hard binaries form near the center and release energy through three-body encounters. Observations of globular clusters, which can be significantly older than their relaxation times, have confirmed these expectations beautifully. The surface brightness profiles of Milky Way globular clusters indicate that some 20% harbor collapsed cores (Djorgovski & King 1986; Chernoff & Djorgovski 1989; Trager et al. 1995). Near the centers of many systems are X-ray binaries and blue stragglers (Bailyn 1995), both created at high stellar density, perhaps during the collapse phase.

Globular clusters have impressive populations ($N \sim 10^5$ - 10^6), but are relatively rare and distant groups. Open clusters are sparser ($N \sim 10^2$ - 10^3), but much more common and closer at hand. Ironically, their evolutionary status is much less clear. Half of open clusters disintegrate within 2×10^8 yr after birth (Wielen 1974), a span corresponding to at most a few initial relaxation times. Not surprisingly, there is little observational signature that relaxation has occurred, aside possibly from mass segregation, first found by van den Bergh & Sher (1960). A small fraction of open clusters, located at the outskirts of the Galaxy, have survived for over 1 Gyr (Friel 1995). Even these ancient systems show no sign of core collapse. A prototypical example, M67, has a smooth surface density profile that, unlike post-collapse systems, is well fit by a King model (Bonatto & Bica 2003); the system appears to be in the last stages of tidal disruption (Davenport & Sandquist 2010).

Hurley et al. (2005) performed N-body simulations to follow the evolution of M67 from infancy to its inferred age of 4 Gyr. Their preferred model began with 12,000 single stars and an equal number of binaries; only about 10% of these stars survived to the end. Even over the protracted time of the simulation, the cluster never exhibited classical dynamical relaxation. Instead, the central mass density rose slightly and then declined. Hurley et al. (2005) attributed this behavior to the binary-rich initial population. Hard binaries undergo superelastic encounters with other stars and effectively heat the cluster (Heggie 1975), counteracting the outward energy transfer driving dynamical relaxation. Indeed, it has long been appreciated that the presence of even a few binaries can radically alter the evolution of the sparsest groups (Terlevich 1987). These findings prompt us to ask a more general question: Under what conditions does binary heating prevent significant core collapse?

In this thesis, I will begin to address this larger issue, utilizing my own suite of N-body simulations. The basic answer is that *the presence of massive stars* is essential. These massive stars couple with others to form pairs that, through three-body interactions, frustrate core

contraction relatively early, so that there is little or no rise of the central density. The system thereafter undergoes *global expansion*. Here, the stellar density falls everywhere. However, there a mitigating factor in this scenerio - stellar evolution. In more populous clusters with longer relaxation times, the most massive stars die out. Binary heating is tamed, and does not effectively oppose core contraction until later in the cluster's evolution. As a result, this contraction proceeds to yield a higher density contrast. Such is the case in the globular clusters that have undergone true core collapse.

1.2.3 Open Cluster Examples

Although there are no shortage of theoretical studies about the evolution of open clusters, few make direct connections to observations of actual clusters. Portegies Zwart et al. (2007) studied the evolution of the stellar mass function in a cluster near the Galactic center in order to explain peculiarities observed in the Arches cluster. Bastian & Goodwin (2006) examined the effects of early gas loss on clusters, comparing their results directly with three young massive clusters. Most notably, Kroupa et al. (2001) attempted to match their simulations to both the Orion Nebula Cluster and the Pleiades, suggesting that the latter's ancestor was similar to the former. Spanning far longer evolutionary timespans than other studies, Hurley et al. (2005) simulated the 4 Gyr evolution of M67. However, these studies have generally focused on only a small few aspects of the clusters they target. More definite answers require comparrisons with data over a much broader parameter space. It is in this spirit that I examine the two systems below.

The Pleiades

I first consider one of the most intensively studied open clusters, the Pleiades. The group of stars has been known since ancient times, and has been known for centuries to be more than just a coincidental overdensity of stars (Michell 1767). Modern studies looking to confirm which stars are members of the cluster began with Trumpler (1921). More recent surveys have continued to push the sensitivity limits of such membership catlogs to include ever fainter stars (e.g. Adams et al. 2001; Pinfield et al. 2003; Deacon & Hambly 2004). The work of nearly a century of determining the cluster's population was recently summarized and compiled into a single catalog by Stauffer et al. (2007).

My ultimate goal is to trace its evolution from the earliest, post-embedded phase to the present epoch and beyond. Focusing first on the current state of the cluster, I ask the following questions: What are the actual masses of the member stars? Do they follow the field-star initial mass function? How many of the members are single, and how many are in binary pairs? Are the primary and secondary masses of binaries correlated? What is the overall density distribution in the cluster? What is the evidence for mass segregation, and how can this phenomenon be quantified?

All of these questions have been addressed previously by others. Deacon & Hambly (2004) constructed a global mass function for the Pleiades. Their method was to assign

masses based on the observed distribution of R-magnitudes. A more accurate assessment should account for the photometric influence of binaries. Several studies directed specifically at binaries have probed selected regions for spectroscopic pairs (Raboud & Mermilliod 1998; Bouvier et al. 1997). However, the overall binary fraction has not been carefully assessed, despite some preliminary attempts (Steele & Jameson 1995; Bouvier et al. 1997; Pinfield et al. 2003; Moraux et al. 2004). Structural properties such as the density profile, total mass, and detections of mass segregation have also been pursued (Pinfield et al. 1998; Adams et al. 2001), but more work is needed, especially on finding a quantitative measure of the latter aspect.

The current state of the cluster provides the point of comparison for my simulations to real data. The age of the Pleiades has been determined, from observations of lithium depletion, to be 125 Myr (Stauffer et al. 1998). I have run a suite of N-body calculations over just this time period, to find that initial state which evolved to the current cluster, as gauged by the first stage of the investigation. This established the detailed history of the group over that epoch, and into the future.

A key assumption here is that the Pleiades divested itself of cloud gas relatively soon after its birth. There is currently no direct means to assess the duration of the initial, embedded phase, either in the Pleiades or any other open cluster. We may take a clue from T associations, which are still surrounded (but not completely obscured) by molecular gas. No systems are observed with ages exceeding about 5 Myr, a striking fact first noted by Herbig (1978). Presumably, older groups consisting of post-T Tauri stars have already driven away their clouds and are merged observationally into the field population. If a similar embedded period held for the Pleiades, it indeed represents a small fraction of the total age. Hence, we can establish, with some confidence, the cluster's structure just after cloud dispersal.

Alpha Persei

In comparing our simulations to real star clusters, the intention is not simply to be able to say how that specific cluster evolved, but to draw conclusions about the evolution of open clusters in general. One could reasonably ask, for example, if the Pleiades is really representative of all open clusters. In order to address this concern, I also repeat the same analyses on the Alpha Persei cluster, and compare the results to those found for the Pleiades. As will be shown, the two clusters share much in common, bolstering the idea that those aspects are similarly shared with most other open clusters. Differences will also be seen, and it will be important for any complete theory of open cluster formation and evolution to address those differences.

Like the Pleiades, Alpha Persei has been the subject of intense investigations in the past. It has been known to be a comoving group of stars for a century now (Eddington 1910). Heckmann et al. (1956) undertook the first systematic search to identify which stars where bona fide members of the cluster. This catalog was refined and expanded upon for many years, the results at the time compiled together by Prosser (1992). Since then, many

more studies have continued to push the list of known members towards fainter and fainter stars (e.g. Barrado y Navascués et al. 2002; Deacon & Hambly 2004). Unlike the Pleaides, however, there is no recent single compilation of this body of work. Thus, in the spirit of the work of Stauffer et al. (2007) on the Pleiades, I have taken it upon myself to assemble the most complete photometric catalog of known members of Alpha Persei.

Much work has also been undertaken to study more than simply the membership of stars in Alpha Persei, though the body of work is not nearly as extensive or complete as for the Pleiades. The cluster is known to be fairly large in extent, with members extending out more than 20 pc from the cluster center (Artyukhina 1972; Terlevich 1983; Makarov 2006). It is also seen to be significantly tidally stretched (Prosser 1992). Its mass function has been found by some authors to be fairly similar to that of the Pleiades (Barrado y Navascués et al. 2002), while others have noted differences (Deacon & Hambly 2004; Makarov 2006). This study will attempt to shed light on this apparent controversy. Similarly, its binary fraction has also been found by previous authors to be abnormally low, (Patience et al. 2002; Mermilliod et al. 2008), though these studies were only sensitive to finding systems in a fairly limited range of orbital separations.

Thus there remains much to be learned about the Alpha Persei cluster just in terms of its present state. Its evolutionary history and future have been even less studied. As with the Pleiades, simulations over the cluster's age of 90 Myr (Stauffer et al. 1999) will give insight into both its initial structure and what forces drive its dynamical evolution. Combined with the results for the Pleiades, this pair of star clusters will be used here to shed light on many unsolved questions of open cluster evolution, and provide new constraints on theories for their formation.

1.3 Outline of Thesis

A full investigation of the properties of a cluster's current state requires statistical methods; these should prove generally useful in characterizing stellar populations. Chapter 2 will begin by describing my approach, which employs a regularized maximum likelihood technique (e.g. Cowan 1998). A similar method has been applied to other astronomical problems, including the reconstruction of cloud shapes (Tassis 2007) and the investigation of binarity within globular clusters (Romani & Weinberg 1991). This study is the first to apply this versatile tool to young stellar groups.

I will then describe in more detail my approach to the problem of determining a cluster's initial state. The parameters characterizing the initial configuration of the cluster will be defined, and the various distribution functions used to set up our simulations will be presented. The results of the simulations must be "observed" to obtain the same parameters as found for the real system before they can be compared. This process is described, with detailed descriptions of how these quantities are computed. Finally, I will outline my strategy for finding the optimal initial state, i.e., the one whose descendent matches most closely the present-day cluster.

Chapter 3 will then delve into the specific results for the Pleiades. After reviewing the observational data used, I will present the derived mass function for the cluster, along with the results for binarity. The density distribution, as well as a new quantification of mass segregation will also be presented. These findings for the present state will then be summarized, critically reexamines the binarity issue. The numerical results of my simulations will follow. Here, I will give the detailed properties of the inferred initial state. I will also describe how the cluster changed up to the present, and how it will develop in the future. One of my key findings is that the cluster's evolution did *not* proceed in the classic manner associated with dynamical relaxation (Binney & Tremaine 2008, Chapter 7). The origin of this discrepancy will be explored. Finally, I will discuss the implications of my findings on the earlier, embedded evolution of this, and other, open clusters.

The results for Alpha Persei are then present in Chapter 4. This will start first with a description of the photometric catalog of members I compiled to use as our primary data for the cluster. The statistical analysis is then repeated for this system. Results for the mass function, binary fraction, density profile, and mass segregation will be discussed. N-body simulations are then applied to determine the initial state of the cluster, and describe its evolution. All of these results will be compared and contrasted to those of the Pleaides. In doing so, a clearer picture will develop of what initial and evolutionary features are common to most open clusters.

Many physical processes are at work in the dynamical evolution of star clusters. Two-body relaxation, dynamical friction, heating by binary systems, mass loss due to stellar evolution, and tidal gravitational fields all act simultaneously upon the cluster. Chapter 5 elucidate these processes in a step-by-step fashion, beginning with very simple, highly idealized systems, and progressively adding more realistic features. An energy analysis will be introduced that quantitatively distinguishes classical dynamical relaxation from global expansion. This analysis will be applied to both single-mass systems and those with a more realistic stellar mass distribution; only in the latter does binary heating come into play. I will then describe in more detail the discontinuous manner in which binary heating actually operates. The role of stellar evolution in lessening this effect will then be addressed. Finally, I discuss the implications of these results for both open clusters, which I have simulated more or less accurately, and globular clusters, which I cannot model directly.

Chapter 2

Methodology

2.1 Characterizing the Current State of a Cluster

As a first step in understanding how clusters evolve, we must first understand their present-day properties. Once given a catalog of probably members (based on proper motions, for example), we wish to determine such things as its current mass function, density profile, and other characteristics. We developed a method to find the mass function from the photometric distribution, taking into account such things as the photometric error and unresolved binary companions. The properties of the radial distribution are then easily found once this first task is accomplished.

2.1.1 Stellar Mass Probability Function

The basic problem is how to assign stellar masses to all the point-like sources believed to be cluster members. In many cases, the source is actually a spatially unresolved binary pair. More rarely, it is a triple or higher-order system; for simplicity, we ignore this possibility. The available observational data consists of photometry in several wavebands. Given the inevitable, random error associated with each photometric measurement, it is not possible to identify a unique primary and secondary mass for each source. Instead we adopt a statistical approach that finds the relative probability for each source to contain specific combinations of primary and secondary masses.

Two Dimensional Mass Function

We introduce a stellar mass probability density, to be denoted $\Phi(m_p, m_s)$. This two-dimensional function is defined so that $\Phi(m_p, m_s)\Delta m_p \Delta m_s$ is the probability that a binary system exists with primary mass (hereafter expressed in solar units) in the interval m_p to $m_p + \Delta m_p$ and secondary mass from m_s to $m_s + \Delta m_s$. Single stars are viewed here as binaries

with $m_s = 0$. We normalize the function over the full mass range:

$$\int_{m_{\min}}^{m_{\max}} dm_p \int_0^{m_p} dm_s \Phi(m_p, m_s) = 1. \tag{2.1}$$

Note that we integrate the secondary mass m_s only to m_p, its maximum value. Furthermore, we set the lower limit of m_s to 0, in order to account for single stars. It is assumed that $\Phi = 0$ for $0 < m_s < m_{\min}$. Here, the global minimum mass $m_{\min}$ is taken to be 0.08, the brown dwarf limit (see Section 3.2.5 for a discussion of the effect of ignoring substellar objects). We consider $m_{\max}$ to be the highest mass still on the main sequence, based on the age of the cluster being studied.

We examine separately the handful of stars that are ostensibly more massive than $m_{\max}$, and hence on post-main-sequence tracks. For these sources, we assign approximate masses from the observed spectral types and obtained data on their known unresolved binary companions; this information was taken from the Bright Star Catalogue (Hoffleit & Jaschek 1991). These systems are then added by hand to our mass functions. Finally, we ignore the brown dwarf population, thought to comprise from 10 to 16% of the total system mass of a cluster (e.g. Pinfield et al. 1998; Schwartz & Becklin 2005).

The most direct method for evaluating $\Phi(m_p, m_s)$ would be to guess its values over a discrete grid of m_p- and m_s-values. Each (m_p, m_s) pair makes a certain contribution to the received flux in various wavebands. Thus, any guessed $\Phi(m_p, m_s)$ yields a predicted distribution of fluxes, which will generally differ from that observed. One changes the guessed function until the observed flux distribution is most likely to be a statistical realization of the predicted one.

Unfortunately, this straightforward approach is impractical. The basic difficulty is the mass-sensitivity of stellar luminosities. For secondary masses m_s only modestly less than m_p, the binary is indistinguishable photometrically from a single star having the primary mass. A 0.6 $M_\odot$ main-sequence star, for example, has an absolute K-band flux of 5.19 mag. Pairing this star with a 0.2 $M_\odot$ secondary (which is not yet on the main sequence) only changes the flux to 5.06 mag. In summary, the function $\Phi(m_p, m_s)$ evaluated in this way is unconstrained throughout much of the m_p-m_s plane.

Correlation within Binaries

Since binaries of even modestly large primary to secondary mass ratio are difficult to recognize observationally, we need to infer their contribution indirectly, within the context of a larger theoretical framework. The physical origin of binaries is far from settled (Zinnecker & Mathieu 2001). There is a growing consensus, however, that most pairs form together, perhaps within a single dense core. The accumulating observations of protobinaries, i.e., tight pairs of Class 0 or Class I infrared sources, have bolstered this view (e.g., Haisch et al. 2004).

If binaries indeed form simultaneously, but independently, within a single dense core, there is no reason to expect a strong correlation between the component masses. (Such a

correlation would be expected if the secondaries formed within the primaries' circumstellar disks, for example.) A credible starting hypothesis, then, is that each component mass is selected randomly from its own probability distribution. If the formation mechanism of each star is identical, then these distributions are also the same. That is, we postulate that the true binary contribution to $\Phi(m_p, m_s)$ is $\phi(m_p)\phi(m_s)$, where the single-star probability density ϕ is properly normalized:

$$\int_{m_{\min}}^{m_{\max}} \phi(m)dm = 1. \tag{2.2}$$

Of course, not all sources are unresolved binaries. Let b represent the fraction of sources that are. We suppose that the chance of a star being in a binary system is independent of its mass, provided the mass in question can represent either the primary or secondary of a pair. While this hypothesis is reasonable for low-mass stars, it surely fails for O- and early B-type stars, which have an especially high multiplicity (e.g., Mason et al. 1998; García & Mermilliod 2001). Such massive objects, however, are not present in clusters of the Pleiades age.

It should be emphasized that this assumption does not mean that a sample of low-mass systems will have the same binary fraction as a sample of high-mass systems. Smaller stars will most often be secondaries in their systems. Thus only a small fraction of systems with low-mass primaries will be binary systems. Figure 2.1 emphasizes this point by plotting the binary fraction b_m which would be observed for a sample of stars chosen to have primary mass m_p (see equation (2.149) in Section 2.3.2). The particular mass function and value for b chosen have been taken to match our results for the Pleiades (see Section 3.2), but the qualitative picture would hold for any mass function or binary fraction. Here the overall binary fraction is $b = 0.68$. The odds for a star to be in a binary system can be shown to then be $2b/(1 + b)$, which is independent of mass. Since high-mass stars are nearly always primaries, it is this value which the curve approaches for larger stars.

Accepting the assumption of a global binary fraction, we have a tentative expression for the full stellar mass probability:

$$\Phi(m_p, m_s) = 2b\phi(m_p)\phi(m_s) + (1 - b)\phi(m_p)\delta(m_s). \tag{2.3}$$

Here, the first term represents true binaries, and the second single stars of mass m_p. The factor of 2 multiplying the first term is necessary because of the restricted range of integration for m_s in equation (2.1). That is, this integration effectively covers only half of the m_p-m_s plane. On the other hand, the normalization condition of equation (2.2) applies to both the primary and secondary star, and covers the full range of mass, from $m_{\min}$ to $m_{\max}$, for each component.

We shall see below that the strict random pairing hypothesis, as expressed in equation (2.3), does not yield the optimal match between the predicted and observed distribution of magnitudes. The match can be improved, in the statistical sense outlined previously, if one allows for a limited degree of correlation between the primary and secondary masses

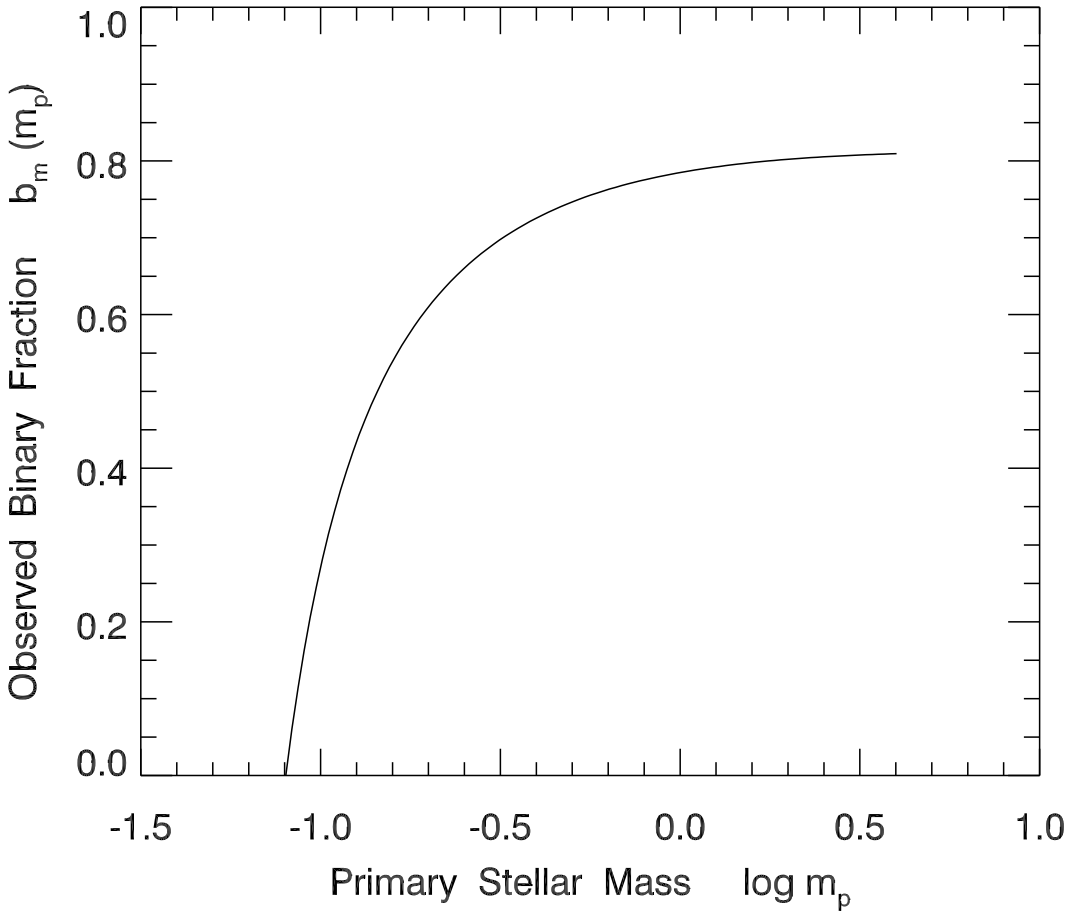

Figure 2.1: Fraction of systems observed with primary mass m_p which are binary. Here it is assumed that the odds of a star being in a binary system (regardless of whether primary or secondary) is independent of its mass. A sample of low-mass primaries is nonetheless seen to have a lower binary fraction than a sample of high-mass primaries. The specific mass function and overall binary fraction used for this curve are those found to best match the Pleiades (see Section 3.2).

within binaries. In other words, there is an apparent tendency for more massive primaries to be accompanied by secondaries that have a greater mass than would result from random selection.

A simple way to quantify this effect is to consider the extreme cases. If there were *perfect* correlation between primary and secondary masses, then the contribution to $\Phi(m_p, m_s)$ from binaries would be $b\phi(m_p)\delta(m_p - m_s)$. With no correlation at all, $\Phi(m_p, m_s)$ is given by equation (2.3). We accordingly define a correlation coefficient c, whose value lies between 0 and 1. Our final expression for $\Phi(m_p, m_s)$ uses c to define a weighted average of the two extreme cases:

$$\Phi(m_p, m_s) = 2b(1-c)\phi(m_p)\phi(m_s) + bc\phi(m_p)\delta(m_p - m_s) + (1-b)\phi(m_p)\delta(m_s). \quad (2.4)$$

Note that the last righthand term, representing the probability of the source being a single star, is unaffected by the degree of mass correlation within binaries.

2.1.2 Maximum Likelihood Analysis

From Masses to Magnitudes

Reconstructing the stellar mass probability $\Phi(m_p, m_s)$ requires that we evaluate the constants b and c, as well as the single-star probability $\phi(m)$. To deal with this continuous function, we divide the full mass range into discrete bins of width Δm_i. Integrating over each bin, we find y_i, the probability of a star's mass being in that narrow interval:

$$y_i \equiv \int_{m_i}^{m_i + \Delta m_i} \phi(m) dm. \quad (2.5)$$

We symbolize the full array of y_i-values by the vector $\boldsymbol{y}$, and similarly denote other arrays below. Our task, then, is to find optimal values not only for b and c, but also for all but one element of $\boldsymbol{y}$. The normalization of ϕ is now expressed by the constraint

$$\sum_i y_i = 1. \quad (2.6)$$

which sets the last $\boldsymbol{y}$-value.

For each choice of b, c, and $\boldsymbol{y}$, equation (2.4) tells us the relative probability of binaries being at any location in the m_p-m_s plane. After dividing the plane into discrete bins, each labeled by an index α, we define μ_α as the predicted number of systems associated with a small bin centered on an (m_p, m_s) pair. If $\mu_{\rm tot}$ is the total number of systems, i.e., of unresolved sources in all magnitude bins, then our chosen b, c, and y_i-values yield the relative fractions $\boldsymbol{\mu}/\mu_{\rm tot}$.

As an example, consider a bin α in which m_p and m_s have different values lying between $m_{\rm min}$ and $m_{\rm max}$. Then the system is an unequal-mass binary, for which equation (2.4) gives

$$\frac{\mu_\alpha}{\mu_{\rm tot}} = 2b(1-c)y_p y_s. \quad (2.7)$$

Here, y_p is the element of $\boldsymbol{y}$ corresponding to the selected m_p, while y_s is similarly associated with m_s. For a bin where $m_p = m_s$, the corresponding relation is

$$\frac{\mu_\alpha}{\mu_{\rm tot}} = b(1-c)y_p^2 + bcy_p. \tag{2.8}$$

Note the additional term accounting for correlated binaries. Note also that a factor of 2 has been dropped from equation (2.4), since we are integrating only over that portion of the mass bin with $m_s < m_p$. Finally, if the system is a single star, so that $m_s = 0$, we have

$$\frac{\mu_\alpha}{\mu_{\rm tot}} = (1-b)y_p. \tag{2.9}$$

Our observational data consists of a catalog of $n_{\rm tot}$ sources, each of which has an apparent magnitude in at least two broadband filters. (In practice, these will be the I- and K-bands; see Sections 3.1 and 4.1.2.) As before, we divide this two-dimensional magnitude space into small bins. Our choice of b, c, and $\boldsymbol{y}$ leads not only to a predicted distribution in mass space, but also in magnitude space.

Let ν_β be the predicted number of sources in each magnitude bin, now labeled by the index β. Then we may write the transformation from the mass to the magnitude distribution as

$$\nu_\beta = \sum_\alpha \mathcal{R}_{\beta\alpha}\mu_\alpha. \tag{2.10}$$

which may be recast in the abbreviated form

$$\boldsymbol{\nu} = \mathcal{R}\boldsymbol{\mu}. \tag{2.11}$$

Here, $\mathcal{R}$ is the *response matrix*, whose elements $\mathcal{R}_{\alpha\beta}$ give the probability that a source in a mass bin α is observed in a magnitude bin β. In detail, this probability utilizes a theoretical isochrone in the color-magnitude diagram (see Section 2.1.2 below). We must also account for random errors in the measured photometry. In other words, a given magnitude pair can have contributions from a range of mass pairs. It is for this reason that each element of $\boldsymbol{\nu}$ involves a *sum* over all α-values.

We previously showed how to obtain the relative mass distribution $\boldsymbol{\mu}/\mu_{\rm tot}$, not the actual $\boldsymbol{\mu}$ itself. However, it is the latter that we need for equation (2.11). To find $\mu_{\rm tot}$, we sum equation (2.10) over all β-values, and demand that this sum be $n_{\rm tot}$, the total number of observed sources:

$$n_{\rm tot} = \sum_\beta \nu_\beta = \sum_\beta \sum_\alpha \mathcal{R}_{\beta\alpha}\mu_\alpha, \tag{2.12}$$

so that

$$n_{\rm tot} = \mu_{\rm tot} \sum_\beta \sum_\alpha \mathcal{R}_{\beta\alpha} \left(\frac{\mu_\alpha}{\mu_{\rm tot}} \right). \tag{2.13}$$

In summary, choosing b, c, and $\boldsymbol{y}$ gives us $\boldsymbol{\mu}/\mu_{\rm tot}$ through equations (2.7), (2.8) and (2.9). We then solve equation (2.13) for $\mu_{\rm tot}$. This gives us the normalization needed to compute $\boldsymbol{\mu}$ itself, and supplied with this knowledge, we finally use equation (2.11) to compute $\boldsymbol{\nu}$.

The Response Matrix

In order to find the predicted photometry distribution produced by a given mass distribution, we must first establish a mass-luminosity relation for the stars. We do this by combining a theoretical zero-age main sequence for $m > 1$ from the models of Siess et al. (2000) and, for lower-mass stars, a pre-main-sequence isochrone from Baraffe et al. (1998). The isochrone is that for the measured cluster age. Our basic assumption is that the observed scatter about this curve stems from two effects - binarity and intrinsic errors in the photometric measurements. We do not consider, for now, possible uncertainty in the cluster's age. (See Section 3.2.5 and Section 4.5.2 for discussion of the effect of this uncertainty.) We also ignore the finite duration of star formation. This duration is roughly 10^7 yr (Palla & Stahler 2000).

We then do a polynomial fit to the mass-magnitude relations found by Siess et al. (2000) and Baraffe et al. (1998) in order to smooth out any jumps where they join. We then have analytic expressions for $M_I^*(m_p, m_s)$ and $M_K^*(m_p, m_s)$, the absolute I- and K-magnitudes for a binary consisting of a primary mass m_p and secondary m_s. Here, the superscripts indicate that the magnitudes are theoretically derived. Both M_I^* and M_K^* are calculated by appropriately combining the individual absolute magnitudes for m_p and m_s. It should be noted that although I and K bands proved to give the best results with the most stars for which data was available in the clusters we analyzed, the method described here could be used with any combination of wavebands.

We do not, however, actually observe M_I^* or M_K^* for any source. What we have are dereddened, apparent magnitudes in these wavebands. Given the distance to the cluster of interest, these apparent magnitudes are readily converted to absolute ones, M_I and M_K. The salient question is: Given a source with intrinsic magnitudes M_I^* and M_K^* (or, equivalently, with masses m_p and m_s), what is the probability that it is observed to have magnitudes M_I and M_K?

Here we confront the issue of photometric errors. We assume the errors in the two wavebands to be normally distributed. Then the relevant probability density is

$$T\left(M_I, M_K; m_p, m_s\right) = \frac{1}{2\pi\sigma_I\sigma_K} \exp\left[\frac{\left(M_I - M_I^*\right)^2}{2\sigma_I^2} - \frac{\left(M_K - M_K^*\right)^2}{2\sigma_K^2}\right]. \tag{2.14}$$

Here, $T\Delta M_I \Delta M_K$ is the probability of observing a source from mass bin α in magnitude bin β, centered on (M_I, M_K), and having widths ΔM_I and ΔM_K.

Suppose now that m_p and m_s are centered within a mass bin α, which has widths Δm_p and Δm_s. Then the response matrix $\mathcal{R}_{\alpha\beta}$ is obtained by integrating $T(M_I, M_K; m_p, m_s)$ over the magnitude bin, then averaging over the mass bin:

$$\mathcal{R}_{\alpha\beta} = \frac{1}{\Delta m_p \Delta m_s} \int_{m_p}^{m_p+\Delta m_p} dm_p \int_{m_s}^{m_s+\Delta m_s} dm_s \int_{M_I}^{M_I+\Delta M_I} dM_I \int_{M_K}^{M_K+\Delta M_K} dM_K T. \tag{2.15}$$

The magnitude integrals can be expressed in terms of error functions if we reinterpret σ_K as being a function of M_K^* rather than M_K. The remaining numerical integrals over m_p

and m_s are performed by finding, for each (m_p, m_s) pair, the M_I^*- and M_K^*-values from our polynomial fits to the mass-magnitude relations.

Likelihood and Regularization

Having chosen b, c, and $\boldsymbol{y}$, how do we adjust these so that the predicted and observed magnitude distributions best match? Our technical treatment here closely follows that in Cowan (1998, Chapter 11), but specialized to our particular application. Let n_β be the number of sources actually observed in each two-dimensional magnitude bin. We first seek the probability that the full array $\boldsymbol{n}$ is a statistical realization of the predicted $\boldsymbol{\nu}$. The supposition is that each element ν_β represents the *average* number of sources in the appropriate bin. This average would be attained after a large number of random realizations of the underlying distribution. If individual observed values follow a Poisson distribution about the mean, then the probability of observing n_β sources is

$$P\left(n_\beta\right) = \frac{{\nu_\beta}^{n_\beta} \mathrm{e}^{-\nu_\beta}}{n_\beta!}. \tag{2.16}$$

This probability is highest when n_β is close to ν_β.

The likelihood function L is the total probability of observing the full set of n_β-values:

$$L \equiv \prod_\beta P(n_\beta). \tag{2.17}$$

We will find it more convenient to deal with a sum rather than a product. Thus, we use

$$\ln L = \sum_\beta n_\beta \ln \nu_\beta - \nu_\beta - \ln\left(n_\beta!\right). \tag{2.18}$$

The strategy is then to find, for a given $\boldsymbol{n}$, that $\boldsymbol{\nu}$ which maximizes $\ln L$. For this purpose, we may neglect the third term in the sum, which does not depend on $\boldsymbol{\nu}$. We thus maximize a slightly modified function:

$$\ln L' \equiv \sum_\beta n_\beta \ln \nu_\beta - \nu_\beta. \tag{2.19}$$

Since, for a given $\boldsymbol{n}$, each $P\left(n_\beta\right)$ peaks at $\nu_\beta = n_\beta$, maximizing $\ln L'$ is equivalent to setting $\boldsymbol{\nu}$ equal to $\boldsymbol{n}$ in equation (2.11), and then inverting the response matrix to obtain $\boldsymbol{\mu}$. Such a direct inversion procedure typically yields a very noisy $\boldsymbol{\mu}$, including unphysical (negative) elements. The solution is to *regularize* our result by employing an entropy term S:

$$S \equiv -\sum_i y_i \ln\left(y_i\right). \tag{2.20}$$

The function S is largest when the elements of $\boldsymbol{y}$ are evenly spread out. Adding S to $\ln L'$ and maximizing the total guarantees that the $\boldsymbol{y}$-values are smoothly distributed, i.e., that $\phi(m)$ is also a smooth function.

In practice, we also want to vary the relative weighting of S and $\ln L'$. We do this by defining a *regularization parameter* λ, and then maximizing the function Γ, where

$$\Gamma \equiv \lambda \ln L' + \mathcal{S}. \tag{2.21}$$

For any given value of λ, maximizing Γ yields an acceptably smooth $\boldsymbol{y}$ that reproduces well the observed data. For the optimal solution, we find that value of λ which gives the best balance between smoothness of the derived $\phi(m)$ and accuracy of fit. We do this by considering another statistical measure, the bias.

Minimizing the Bias

Our observational dataset, $\boldsymbol{n}$, is an imperfect representation of the unknown probability density $\phi(m)$ in two senses. As already noted, $\boldsymbol{n}$ may be regarded as only one particular realization of the underlying distribution. Even this single realization would directly reveal $\phi(m)$ (or, equivalently, $\boldsymbol{y}$) if the sample size were infinite, which of course it is not.

Imagine that there were other realizations of $\phi(m)$. For each, we employ our maximum likelihood technique to obtain $\boldsymbol{y}$. Averaging each y_i over many trials yields its expectation value, $E(y_i)$. However, because of the finite sample size, $E(y_i)$ does not necessarily converge to the true value, $y_i^{\rm true}$. Their difference is the bias, b_i:

$$b_i \equiv E(y_i) - y_i^{\rm true}. \tag{2.22}$$

The values of the biases, collectively denoted $\boldsymbol{b}$, reflect the sensitivity of the estimated $\boldsymbol{y}$ to changes in $\boldsymbol{n}$. Following Cowan (1998, Section 11.6), we define a matrix $\mathcal{C}$ with elements

$$\mathcal{C}_{i\beta} \equiv \frac{\partial y_i}{\partial n_\beta}. \tag{2.23}$$

The bias is then given by

$$\boldsymbol{b} = \mathcal{C}(\boldsymbol{\nu} - \boldsymbol{n}). \tag{2.24}$$

To evaluate the derivatives in $\mathcal{C}$, we consider variations of the function Γ about its maximum. In matrix notation,

$$\mathcal{C} = -\mathcal{A}^{-1}\mathcal{B}. \tag{2.25}$$

where the matrix $\mathcal{A}$ has elements

$$\mathcal{A}_{ij} \equiv \frac{\partial^2 \Gamma}{\partial y_i \partial y_j}. \tag{2.26}$$

and $\mathcal{B}$ is given by

$$\mathcal{B}_{i\beta} \equiv \frac{\partial^2 \Gamma}{\partial y_i \partial n_\beta}. \tag{2.27}$$

Since Γ is a known function of both the $\boldsymbol{y}$ and $\boldsymbol{n}$, the derivatives appearing in both $\mathcal{A}$ and $\mathcal{B}$ may be evaluated analytically. Another matrix that will be useful shortly is $\mathcal{D}$, whose elements

$$\mathcal{D}_{\alpha i} \equiv \frac{\partial \mu_\alpha}{\partial y_i} \tag{2.28}$$

are also known analytically from equations (2.7)-(2.9).

To determine the regularization parameter λ appearing in Γ, we seek to minimize the biases. In practice, we consider the weighted sum of their squared values:

$$\chi_b^2 \equiv \sum_i \frac{b_i^2}{\mathcal{W}_{ii}}. \tag{2.29}$$

and vary λ to reduce this quantity.[1] Here, the $\mathcal{W}_{ii}$ are diagonal elements of $\mathcal{W}$, the covariance of the biases. Recall that the elements of $\boldsymbol{b}$ are here considered to be random variables that change with different realizations.

We find the covariance matrix $\mathcal{W}$ by repeated application of the rule for error propagation (Cowan 1998, Section 1.6). We begin with $\mathcal{V}$, the covariance of $\boldsymbol{n}$. Since these values are assumed to be independently, Poisson-distributed variables, $\mathcal{V}$ has elements

$$\mathcal{V}_{\alpha\beta} = \nu_\beta \delta_{\alpha\beta}. \tag{2.30}$$

Here we have used the fact that the variance of the Poisson distribution equals its mean, ν_β. In this equation only, both α and β range over the ν-values, i.e., $\mathcal{V}$ is a square matrix.

We next consider $\mathcal{Y}$, the covariance of $\boldsymbol{y}$. This is given by

$$\mathcal{Y} = \mathcal{C}\mathcal{V}\mathcal{C}^{\mathrm{T}}. \tag{2.31}$$

Finally, we obtain the desired $\mathcal{W}$ by

$$\mathcal{W} = \mathcal{F}\mathcal{Y}\mathcal{F}^{\mathrm{T}}. \tag{2.32}$$

The matrix $\mathcal{F}$ in this last equation has elements

$$\mathcal{F}_{ij} \equiv \frac{\partial b_i}{\partial y_j}. \tag{2.33}$$

Differentiating equation (2.24) and applying the chain rule, we find $\mathcal{F}$ to be

$$\mathcal{F} = \mathcal{C}\mathcal{R}\mathcal{D} - \mathcal{I}, \tag{2.34}$$

where $\mathcal{I}$ is the identity matrix.

Calculation of Radial Structure

Thus far, we have focused on determining global properties of the cluster, especially the mass function $\phi(m)$. We also want to investigate the spatial distribution of stellar masses.

[1] In practice, we require that χ_b^2 be reduced to N, the number of free parameters in our fit. As noted by Cowan (1998, Section 11.7), the average b_i-value at this point is about equal to its standard deviation, and so is statistically indistinguishable from zero.

For this purpose, we need not perform another maximum likelihood analysis. The reason is that we can treat the mass distribution at each radius as a modification of the global result.

We divide the (projected) cluster into circular annuli, each centered on a radius r. What is μ_α^r, the number of sources in an annulus that are within mass bin α? (As before, each bin is labeled by the masses of both binary components.) The quantity we seek is

$$\mu_\alpha^r = \sum_\beta \mathcal{Q}_{\alpha\beta}\nu_\beta^r. \tag{2.35}$$

Here, $\mathcal{Q}_{\alpha\beta}$ is the probability that a source observed within magnitude bin β has component masses within bin α. In principle, this probability depends on radius. For example, the source could have a high probability of having a certain mass if there exist many such stars in that annulus, even stars whose real magnitude is far from the observed one. If we discount such extreme variations in the underlying stellar population, then we may approximate $\mathcal{Q}$ by its global average.

The factor ν_β^r in equation (2.35) is the estimated number of sources at radius r in magnitude bin β. We only compute, via the maximum likelihood analysis, ν_β, the estimated number of sources in the entire cluster. But we also know n_β^r, the *observed* number of sources in the annulus. If the total number of observed sources, n_β, is non-zero, then we take

$$\nu_\beta^r \equiv \frac{n_\beta^r}{n_\beta}\nu_\beta. \tag{2.36}$$

In case $n_\beta = 0$, then n_β^r vanishes at all radii. We then assume

$$\nu_\beta^r \equiv \frac{n_{\rm tot}^r}{n_{\rm tot}}\nu_\beta, \tag{2.37}$$

where $n_{\rm tot}^r$ is the observed source number of all magnitudes in the annulus. This latter assumption for these cases does inherently assume there is no mass segregation. However, the maximum likelihood fit guarantees that for those bins in which $n_\beta = 0$, ν_β will also be very small. Thus the contribution of bins that use this assumption will similarly be very small. In the end, equation (2.35) attributes the radial mass variation to changes in the local magnitude distribution, rather than to improbable observations of special objects.

It is clear that the global $\mathcal{Q}$ must be closely related to the response matrix $\mathcal{R}$, which is the probability that a source with a given mass has a certain magnitude. The precise relation between the two follows from Bayes Theorem:

$$\mathcal{Q}_{\alpha\beta} = \mathcal{R}_{\beta\alpha}\frac{\mu_\alpha/\mu_{\rm tot}}{\nu_\beta/\nu_{\rm tot}}. \tag{2.38}$$

The numerator of the fraction is the probability that a source at any radius lies within the mass bin α, while the denominator is the probability of it lying within magnitude bin β. Note that $\mu_{\rm tot}$ and $\nu_{\rm tot}$ need not be identical. The first quantity is the estimated number of

sources covering all possible masses. The second is the observed number in the magnitude range under consideration. In practice, this range is extensive enough that the two are nearly the same. We thus write

$$\mathcal{Q}_{\alpha\beta} = \mathcal{R}_{\beta\alpha}\frac{\mu_\alpha}{\nu_\beta}. \tag{2.39}$$

Using this last equation, along with equation (2.36), equation (2.35) now becomes

$$\mu^r_\alpha = \mu_\alpha \sum_\beta \mathcal{R}_{\beta\alpha}\frac{n^r_\beta}{n_\beta}. \tag{2.40}$$

For those terms where $n_\beta = 0$, equation (2.37) tells us to replace the ratio n^r_β/n_β by $n^r_{\rm tot}/n_{\rm tot}$.

Summing μ^r_α over all α and dividing by the area of the annulus gives the projected surface number density of sources as a function of radius. The total mass in each annulus is

$$\Delta m^r = \sum_\alpha \mu^r_\alpha m_\alpha. \tag{2.41}$$

where m_α is the sum of the masses of both binary components in the appropriate bin. Division of Δm^r by the annulus area gives the projected surface mass density. Under the assumption of spherical symmetry, the corresponding volume densities are then found by the standard transformation of the Abel integral (Binney & Merrifield 1998, Section 4.2.3).

2.1.3 Mass Segregation: The Gini Coefficient

As a cluster evolves through many two-body interactions, one natural consequence is for the most massive systems to naturally sink to the center. We thus wish to find a way to measure the degree to which a given cluster demonstrates this effect. Consider f_N, the number of sources enclosed in a given projected radius, divided by the total number of sources in the cluster.

More precisely, if $n(r)$ is the system number density such that the number of systems between r and $r + dr$ is $n(r)dr$, then

$$f_N(r) = \frac{1}{N_{\rm tot}}\int_0^r n(r')dr'. \tag{2.42}$$

Similarly, if $\bar{m}_r(r)$ is the average system mass (primary plus secondary) in a shell with outer radius r, then the analogous fractional mass inside any projected radius is

$$f_M(r) = \frac{1}{M_{\rm tot}}\int_0^r \bar{m}_r(r')n(r')dr'. \tag{2.43}$$

Here $N_{\rm tot}$ is the total number of systems at all radii,

$$N_{\rm tot} = \int_0^\infty n(r)dr, \tag{2.44}$$

and $M_{\rm tot}$ is the total mass of systems at all radii,

$$M_{\rm tot} = \int_0^\infty \bar{m}_r(r) n(r) dr. \tag{2.45}$$

Both f_N and f_M range from 0 at the center to 1 at the edge of the cluster. In the absence of mass segregation, f_M would equal f_N at each annulus since the mass and radial position of a star would be uncorrelated. Plotting f_M versus f_N for this hypothetical situation would thus yield a straight 45° line.

In a cluster with mass segregation, f_M would rise above f_N, before they both reach unity at the cluster boundary. This rise indicates that the innermost portion of the cluster has an anomalously large average mass, i.e., that mass segregation is present (see Figures 3.9 and 3.10 in Section 3.2.4 and Figure 4.8 in Section 4.3.3 for examples of this applied to real clusters). Moreover, the *area* between the actual curve and theoretical line of no segregation is a direct measure of the effect. In the case of "perfect" mass segregation, a few stars near the center would contain virtually all the cluster mass. The solid curve would trace the upper rectangular boundary of the plot, and the enclosed area would be 0.5.

We thus define the *Gini coefficient*, G, as *twice* the area between the actual $f_M - f_N$ curve and the central diagonal,[2]

$$G = 2 \int_0^1 (f_M - f_N)\, df_N. \tag{2.46}$$

If the mass is centrally concentrated, as expected in a real stellar cluster, then $f_M \geq f_N$ at all radii, and $G \geq 0$. Hypothetical clusters in which larger masses are preferentially located farther from the center would have $G \leq 0$.

Alternatively, G may be defined in terms of the mean mass difference between radial shells in the cluster. Here we describe more precisely, and prove the equivalence of, this second interpretation. The average system mass throughout the entire cluster is

$$\bar{m} = \frac{1}{N_{\rm tot}} \int_0^\infty \bar{m}_r(r) n(r) dr, \tag{2.47}$$

and thus $M_{\rm tot} = \bar{m} N_{\rm tot}$. We will be concerned with the *relative mean difference* in the mass of shells. This is

$$\bar{\Delta} = \frac{1}{\bar{m} N_{\rm tot}^2} \int_0^\infty dr \int_0^\infty dr' \, |\bar{m}_r(r) - \bar{m}_r(r')| \, n(r) n(r'). \tag{2.48}$$

We will prove that the Gini coefficient, as defined above, is also $\bar{\Delta}/2$.

A central assumption we will make is that $\bar{m}_r(r)$ declines monotonically with r. We may then expand the righthand side of equation (2.48). We split the integral over r' into two

[2]The name derives from economics, where the coefficient is used to measure inequality in the distribution of wealth (Sen 1997).

parts, one for $r' \leq r$ and the other for $r' > r$. Under our assumption, $\bar{m}_r(r') \geq \bar{m}_r(r)$ in the first integral, and $\bar{m}_r(r') < \bar{m}_r(r)$ in the second. After pulling $n(r)$ from the r'-integration, we further split the integrands to find

$$\bar{\Delta} = \frac{1}{\bar{m}N_{\rm tot}} \int_0^\infty \left(-\mathcal{I}_1 + \mathcal{I}_2 + \mathcal{I}_3 - \mathcal{I}_4\right) n(r) dr. \tag{2.49}$$

The first two terms of the integrand are

$$\mathcal{I}_1 \equiv \frac{\bar{m}_r(r)}{N_{\rm tot}} \int_0^r n(r')dr' = \bar{m}_r(r) f_N(r), \tag{2.50}$$

$$\mathcal{I}_2 \equiv \frac{1}{N_{\rm tot}} \int_0^r \bar{m}_r(r') n(r') dr' = \bar{m} f_M(r). \tag{2.51}$$

The third term is

$$\begin{aligned}
\mathcal{I}_3 &\equiv \frac{\bar{m}_r(r)}{N_{\rm tot}} \int_r^\infty n(r')dr' && (2.52)\\
&= \frac{\bar{m}_r(r)}{N_{\rm tot}} \int_0^\infty n(r')dr' - \frac{\bar{m}_r(r)}{N_{\rm tot}} \int_0^r n(r')dr' && (2.53)\\
&= \bar{m}_r(r) - \bar{m}_r(r) f_N(r), && (2.54)
\end{aligned}$$

while the fourth is

$$\begin{aligned}
\mathcal{I}_4 &\equiv \frac{1}{N_{\rm tot}} \int_r^\infty \bar{m}_r(r') n(r') dr' && (2.55)\\
&= \frac{1}{N_{\rm tot}} \int_0^\infty \bar{m}_r(r') n(r') dr' - \frac{1}{N_{\rm tot}} \int_0^r \bar{m}_r(r') n(r') dr' && (2.56)\\
&= \bar{m} - \bar{m} f_M(r). && (2.57)
\end{aligned}$$

Putting equations (2.50), (2.51), (2.54), and (2.57) back into equation (2.49) yields

$$\begin{aligned}
\bar{\Delta} &= \frac{1}{\bar{m}N_{\rm tot}} \int_0^\infty \left[2\bar{m} f_M(r) - 2\bar{m}_r(r) f_N(r) + \bar{m}_r(r) - \bar{m}\right] n(r) dr && (2.58)\\
&= 2\left(\int_0^\infty f_M(r) \frac{n(r)}{N_{\rm tot}} dr - \int_0^\infty f_N(r) \frac{\bar{m}_r(r) n(r)}{\bar{m}N_{\rm tot}} dr\right), && (2.59)
\end{aligned}$$

where we have used both equations (2.44) and (2.47) to cancel the last two terms on the right side of equation (2.59). Taking the differentials of f_N and f_M finds

$$df_N = \frac{n(r)}{N_{\rm tot}} dr, \tag{2.60}$$

and

$$df_M = \frac{\bar{m}_r(r) n(r)}{\bar{m}N_{\rm tot}} dr. \tag{2.61}$$

Using equations (2.60) and (2.61), we can transform equation (2.59) into

$$\bar{\Delta} = 2\left(\int_0^1 f_M df_N - \int_0^1 f_N df_M\right). \tag{2.62}$$

The second integral in this equation is

$$\int_0^1 f_N df_M = \int_{f_N f_M=0}^{f_N f_M=1} d(f_N f_M) - \int_0^1 f_M df_N \tag{2.63}$$

$$= 1 - \int_0^1 f_M df_N, \tag{2.64}$$

since f_M and f_N attain their upper and lower bounds simultaneously. Using this result, equation (2.62) becomes

$$\bar{\Delta} = 2\left(2\int_0^1 f_M df_N - 1\right). \tag{2.65}$$

Finally, we note that

$$2\int_0^1 f_N df_N = 1. \tag{2.66}$$

Thus, equation (2.65) becomes

$$\bar{\Delta} = 4\left(\int_0^1 f_M df_N - \int_0^1 f_N df_N\right) \tag{2.67}$$

$$= 4\int_0^1 (f_M - f_N)\, df_N \tag{2.68}$$

$$= 2G, \tag{2.69}$$

as claimed.

2.1.4 Procedure and Synthetic Data Tests

Before turning to a real cluster, we first employed a number of synthetic datasets, in order to test various aspects of the code and the validity of the methodology. We shall describe these tests shortly. First, however, we summarize the standard procedure we adopted for the analysis of any cluster, real or synthetic.

Summary of Procedure

The basic problem, we recall, is to guess the optimal values of b, c, and $\boldsymbol{y}$ that maximize the function Γ, as given in equation (2.21). The entropy part of Γ, labeled S, is directly a function of $\boldsymbol{y}$ (equation (2.20)), while the modified likelihood function L' depends on the observed magnitude distribution $\boldsymbol{n}$ and the guessed one $\boldsymbol{\nu}$ (see equation (2.19).) The guessed

$\boldsymbol{y}$ does not yield $\boldsymbol{\nu}$ itself, but the guessed mass distribution $\boldsymbol{\mu}$, through equations (2.7)-(2.9). It is in this transformation that the binary fraction b and correlation coefficient c appear. Finally, $\boldsymbol{\nu}$ is obtained from $\boldsymbol{\mu}$ via the response matrix (equation (2.11)).

We begin the maximization procedure by first setting the regularization parameter λ to zero. Since $\Gamma = S$ in this case, the optimal set of $\boldsymbol{y}$-values will be uniformly distributed, while subject to the normalization constraint of equation (2.6). We guess b, c, and $\boldsymbol{y}$, and vary them to maximize Γ. For the actual maximization, we employ a standard downhill simplex algorithm (Press et al. 2002, Chapter 10). The resulting best-fit parameters are then perturbed and the maximization rerun. This check, which may be redone several times, is done both to confirm convergence and to avoid becoming trapped in small, local maxima of the function Γ. We record the relevant covariances and biases, to be used in estimating errors in predicted quantities and to set the optimal λ-value.

The next step is to increase λ slightly. We maximize Γ in the same way as before, again recording covariances and biases. We again increase λ, repeating the entire procedure until χ_b^2, the weighted sum of the biases, starts to become acceptably small. At this point, the best-fit b, c, and $\boldsymbol{y}$ have been established. The radial structure and Gini coefficient are then computed from these results.

Synthetic Data Tests

As a first test of the procedure, we introduced an artificial cluster whose single-star probability, $\phi(m)$, we selected beforehand. Sources were chosen randomly to have masses according to this distribution. In a certain fraction of the sources, our preset binary fraction b, a second star was added to the source. The mass of this object was also randomly chosen from $\phi(m)$. Thus, the correlation coefficient c was initially zero. Given both masses in a source, its intrinsic M_I^* and M_K^* are readily obtained. These magnitudes are smeared out into neighboring bins according to Gaussian errors with the appropriate standard deviations σ_I and σ_K. Thus, the "observed" magnitude distribution, $\boldsymbol{n}$, is established.

Figure 2.2 shows two representative examples. In the left panel, the chosen $\phi(m)$, is a power law: $\phi(m) \propto m^{-2.8}$. On the right, we used a lognormal distribution:

$$\phi(m) = \frac{C}{m} \exp\left[-\frac{(\log m - \log m_0)^2}{2\sigma_m^2}\right], \tag{2.70}$$

where C is the normalization constant. The central mass was chosen as $m_0 = 0.2$ and the logarithmic width σ_m was 0.4. The binary fraction b was chosen to be 0.30 in the power law example, and 0.68 for the lognormal distribution. The total source number $n_{\rm tot}$ was 10,000 in both cases.

The smooth curve in both panels is $\phi(m)$, while the data points are the best-fit values of $y_i/\Delta m_i$, where Δm_i is the bin width. Shown also is the estimated error for each value. This was derived from the covariance matrix $\mathcal{Y}$, introduced in Section 2.1.2. Specifically, the plotted error is $\sqrt{\mathcal{Y}_{ii}}/\Delta m_i$. We divide each y_i and its associated error by Δm_i because y_i is integrated over the bin (equation (2.5)).

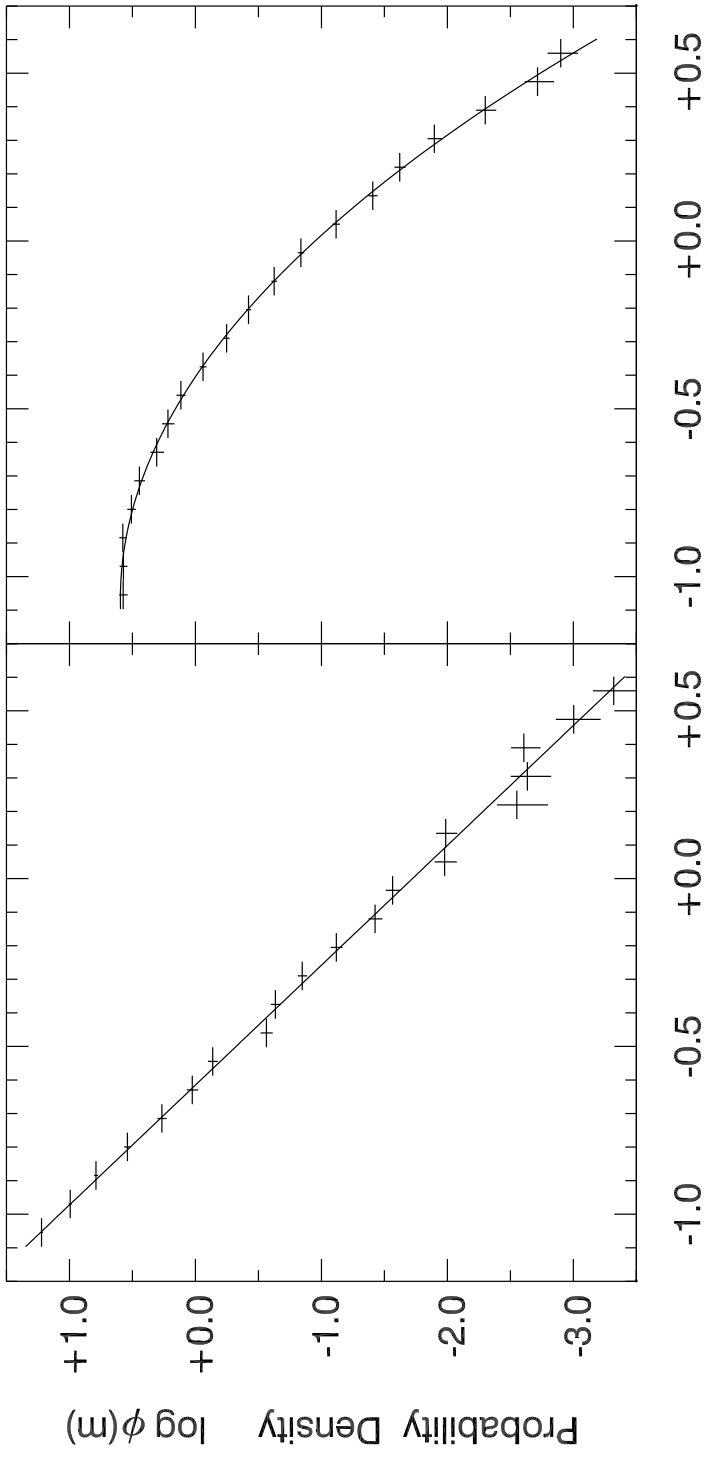

Figure 2.2: Sample synthetic data results for the single star mass function $\phi(m)$. In both panels, the smooth curve is the input function from which the synthetic data were drawn. Shown also are the best-fit values, along with errors, for our discrete representation of the function. In the left panel, the input $\phi(m)$ is a power law with slope -2.8; in the right panel, it is a lognormal function with peak $m_0 = 0.2$ and width $\sigma_m = 0.4$.

It is evident that the code reproduces well the assumed $\phi(m)$ in these two examples. Note that most of the scatter seen in both plots, especially in the left panel, was already present in the input data, which were finite realizations of the analytic distributions. The derived (i.e., predicted) binary fractions, $b = 0.293 \pm 0.008$ and $b = 0.672 \pm 0.011$, respectively, are also in good agreement. We had similar success when we reduced $n_{\rm tot}$ to 1245, the actual number in our Pleiades source catalog (see Section 3.1). In this smaller sample, the errors in our predicted mass function and binary fraction increased, roughly as $n_{\rm tot}^{-1/2}$.

Figure 2.3, taken from a dataset with $n_{\rm tot} = 1245$, shows in more detail how the regularization parameter λ was chosen. The figure also illustrates some of the subtlety involved in this procedure. Plotted here, as a function of λ, is χ_b^2, defined in equation (2.29). As λ is gradually increased, χ_b^2 takes a sudden, sharp dip. After climbing back, χ_b^2 then more slowly declines, eventually falling below $N = 21$, the number of tunable parameters in this maximization (b, c, and 19 $\boldsymbol{y}$-values).

It is the second threshold ($\lambda = 0.027$ in this case) that marks the true stopping point. The earlier dip in χ_b^2 is due, not to a decrease in the biases, but to a sharp *increase* in the covariances $\mathcal{W}$. This increase commonly occurs when the likelihood term $\ln L'$ starts to become comparable to the entropy S in the full function Γ. At that point, $\boldsymbol{y}$ makes an abrupt shift away from its earlier, nearly uniform, distribution. With further increase in λ, $\boldsymbol{y}$ settles down gradually to its optimal form.

Binary Correlation Tests

Continuing our synthetic data tests, we next introduced a correlation between the primary and secondary masses. First, we generated uncorrelated pairs, as above. Generalizing the prescription of de La Fuente Marcos (1996b), we then altered the secondary mass in each source according to

$$m_s \rightarrow m_s \left(\frac{m_p}{m_s} \right)^{\gamma} . \tag{2.71}$$

Here, γ, a preset number between 0 and 1, represents our imposed degree of correlation. Thus, setting $\gamma = 0$ yields the previous, uncorrelated case, while, for $\gamma = 1$, every binary has equal-mass components. Note that although this model for corerelation depletes the number of very low-mass secondary stars, this has minimal effect on our results. The reason is that the light from the smallest secondaries is completely dominated by their brighter primaries, and so they have little effect on the photometric distribution, which is what we are fundamentally comparing to. We ran our routine with a variety of input single-star mass functions, binary fractions, and degrees of correlation.

Our general result was that the predicted $\boldsymbol{y}$ still reproduced well the synthetic $\phi(m)$. The binary fraction b was similarly accurate. Most significantly, the predicted c-value tracked the input quantity γ. Figure 2.4 shows this relation. We conclude that our statistical model, while crudely accounting for correlation by inserting a fraction of equal-mass pairs, nevertheless mimics a smoother correlation, such as would be found naturally. The shaded

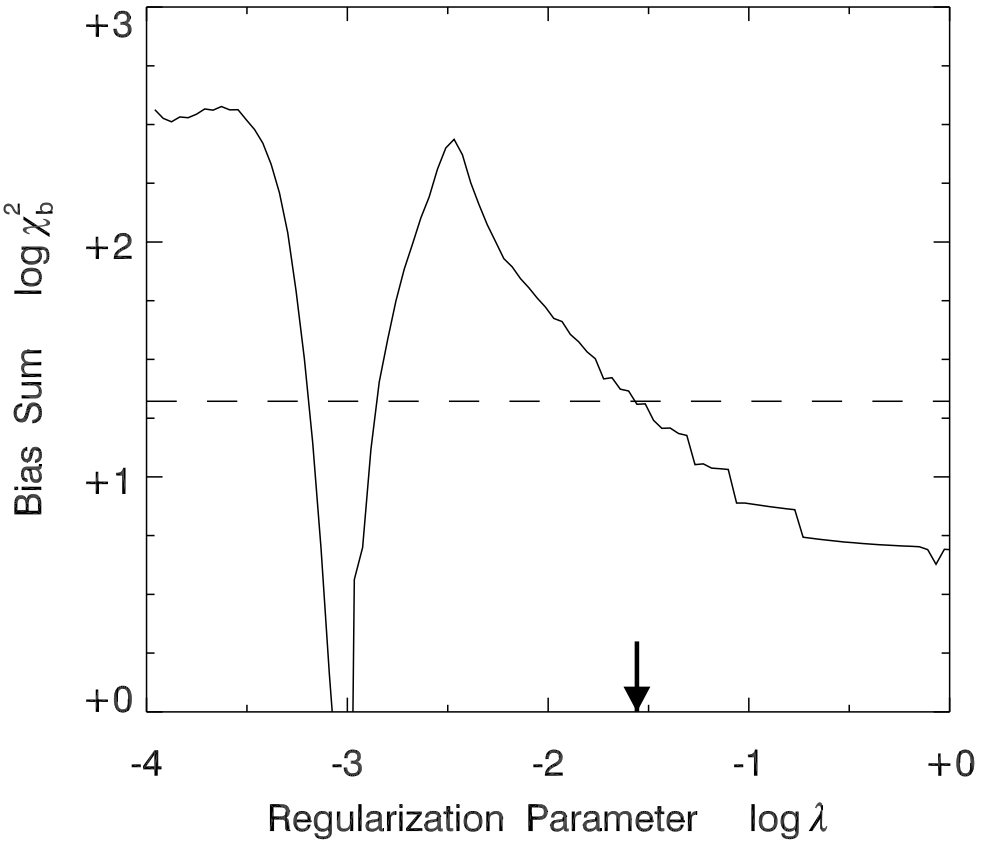

Figure 2.3: Weighted sum of the biases as a function of the regularization parameter λ. The synthetic input here was a lognormal function with 1245 sources. The dashed, horizontal line is drawn at $\chi_b^2 = N$, where $N = 21$ is the number of free parameters in our fitting. The short, vertical arrow indicates the final value of λ used for this synthetic dataset.

patch in the figure is the probable region occupied by the real Pleiades; see Section 3.2.2 for justification of this assessment.[3]

One price we paid for our simplified account of correlation was that our matching of $\phi(m)$ was less accurate than for randomly paired input binaries. Consider, for example, the lognormal function of equation (2.70). While our best-fit $\boldsymbol{y}$ still reproduced $\phi(m)$ reasonably well, the output function peaked at too high a mass compared to m_0. The filled circles in Figure 2.5 shows that this shift, Δm_0, increased with the input γ-value. Concurrently, our output function was too narrow compared to the input σ_m. The (negative) difference, $\Delta\sigma_m$, displayed as open circles in Figure 2.5, was also more pronounced at higher γ. These systematic errors need to be considered when analyzing a real cluster. The two patched areas in the figure again represent the likely regime of the Pleiades, as we explain in Section 3.2.2.

2.2 Initial Cluster Parameters

Once the present-day cluster has been characterized, we wish to determine the cluster's properties when it was first formed. This is useful for placing constraints on the which young stellar groups are most likely to evolve into a long-lived, gravitationally bound cluster. We also wish to understand the physical processes that govern its evolution from that initial configuration to its current state, and how it will continue to evolve into the future. This is done using N-body simulations (described in Section 2.3 below). Before we can simulate the cluster, however, we must first parameterize its initial configuration.

2.2.1 Density and Velocity Distribution

We model the cluster as a perfectly spherical system, even if the cluster is observed to be slightly elongated (e.g. Raboud & Mermilliod 1998; Prosser 1992). Such an elongation would likely be created by the tidal gravity of the Galaxy (Wielen 1974), which would have exerted influence throughout the cluster's dynamical history. We assume that this modest tidal stretching had negligible effect on the internal evolution, and that relatively few stars were lost by tidal stripping over the cluster's age. Thus we can safely ignore the associated Galactic potential. For the moment, we also ignore mass loss through stellar evolution, which is negligible for the mass function we adopt below, for clusters which are only $\sim$100 Myr old. In Sections 3.3.2, 3.3.3, and 4.4 we will discuss simulations that include these effects.

Returning to our standard runs, we further assume that the cluster was in virial equilibrium following expulsion of the gas. Any significant departure from equilibrium would be erased on a dynamical time scale, about 10 Myr for typical input parameters and therefore much shorter than the evolutionary span of interest. Two popular choices for spherical

[3]The prescription for mass correlation given in equation (2.71) is more realistic than introducing a subpopulation of identical-mass binaries (equation (2.4)). We employed the latter device only for convenience. If we had parameterized the correlation through γ, equations (2.7) and (2.8) would have been numerical integrals, and the derivative matrix $\mathcal{D}$ in equation (2.28) would also have required numerical evaluation.

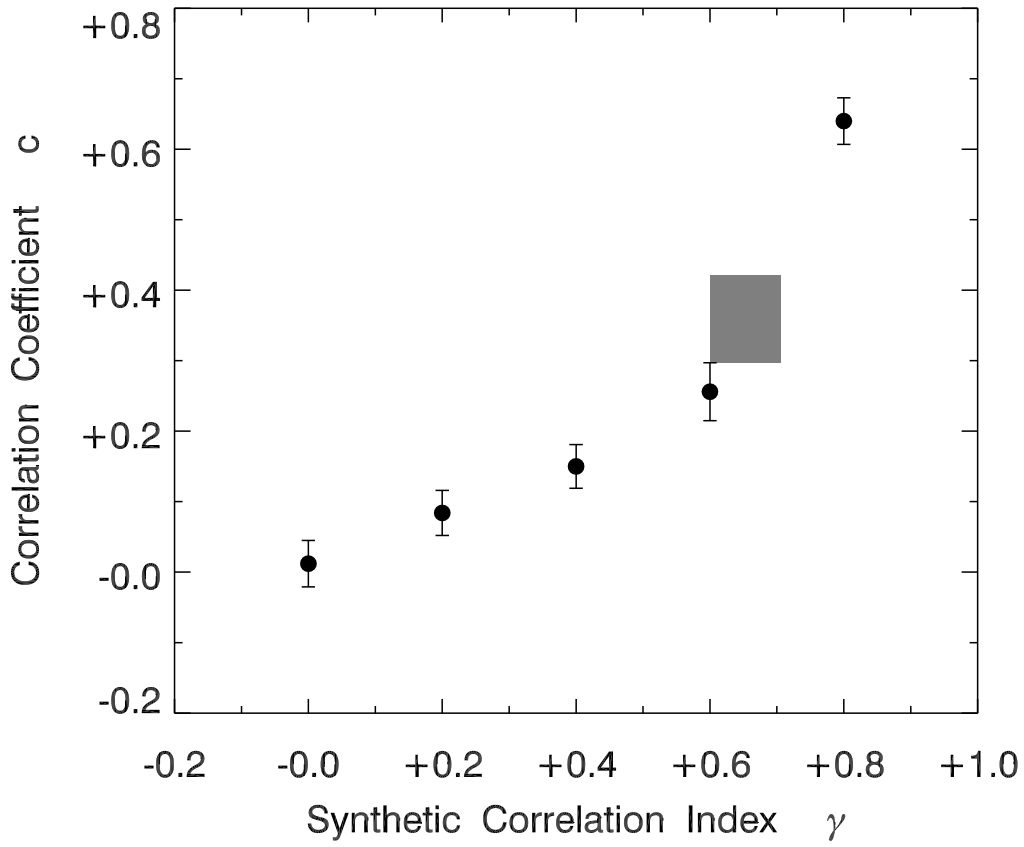

Figure 2.4: Comparison of our fitted correlation coefficient c with γ, the imposed degree of correlation in the synthetic dataset. The gray area indicates the region in which the Pleiades most likely falls.

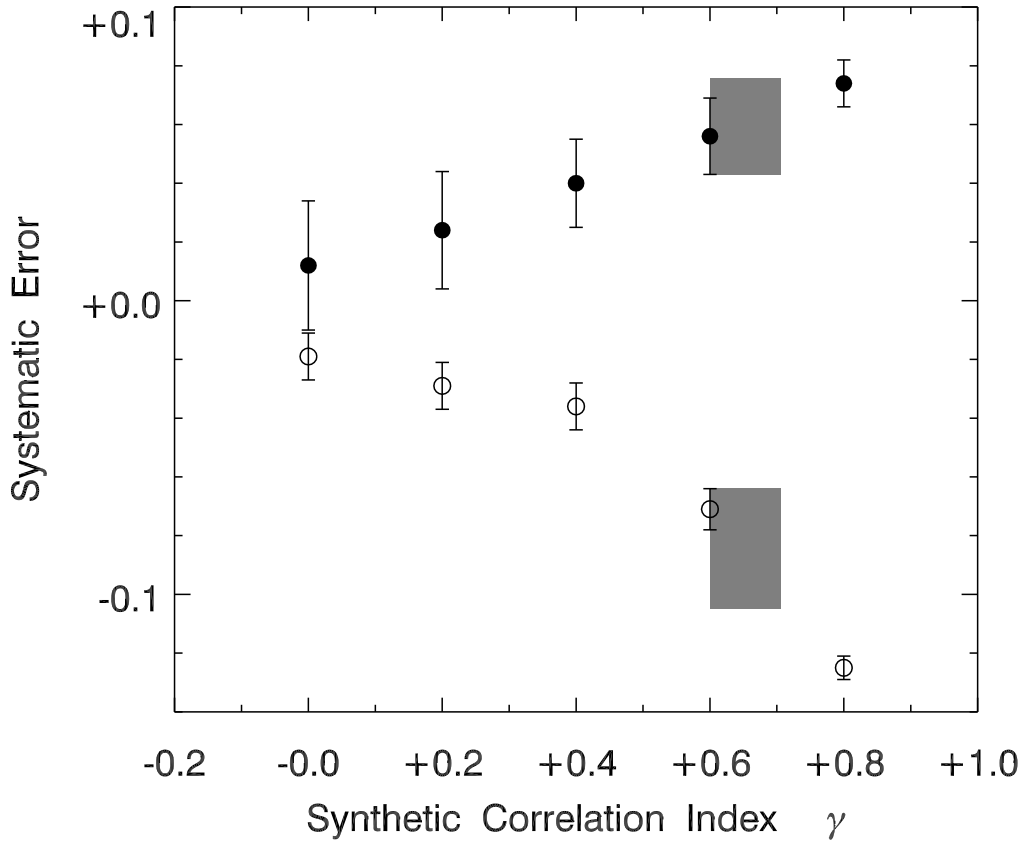

Figure 2.5: Systematic errors in parameters of the lognormal fit to $\phi(m)$, plotted as a function of the synthetic binary correlation γ. Filled circles show Δm_0, the error in m_0. Open circles show $\Delta\sigma_m$, the error in σ_m. The gray areas indicate the regions in which the Pleiades most likely falls.

equilibria are King (1966) models and polytropes. King models do not include low enough density contrasts for a full exploration of initial states. We therefore used polytropes, which are more versatile in this regard. We start, however by first showing that King models reduce to polytropes in the limit of low concentration.

King models are a spherically symmetric self-gravitating stellar distribution function whose velocity dispersion is isotropic. The system is always finite in extent, meaning there is a well-defined maximum radius for stars within it, and with finite total mass. Stars are assumed to all have the same mass m. There are N stars in the system, thus making the total mass $M = Nm$.

Defining the Distribution Function

The energy per unit mass of a star in the system is simply $E/m = \Phi(r) + v^2/2$, where $\Phi(r) = -GM_r(r)/r$ is the conventional gravitational potential and $M_r(r)$ is the mass enclosed within the radius r. It is more convenient to use a different zero-point for the potential and define a new relative potential $\Psi(r)$ such that it is zero at the boundary of the cluster. Further, we will take it to be positive for bound systems, thus

$$\Psi(r) \equiv -(\Phi(r) - \Phi(r_t)), \tag{2.72}$$

where r_t is the outer ("tidal") radius of the system, and thus $\Phi(r_t) = -GM/r_t$ using the total mass M. We will similarly define the relative energy per unit mass with this new zero point and reversed sign,

$$\mathcal{E} \equiv -(\Phi(r) + v^2/2 - \Phi(r_t)) = \Psi(r) - v^2/2. \tag{2.73}$$

Any star which is part of the system must be bounded, which means that $\mathcal{E} \geq 0$.

The King distribution function is then a truncated isothermal sphere,

$$f(\mathcal{E}) = \begin{cases} A_K \left(e^{W_0 \mathcal{E}/\Psi_0} - 1\right) & \mathcal{E} \geq 0 \\ 0 & \mathcal{E} < 0 \end{cases} \tag{2.74}$$

where $f d^3r d^3v$ is the number of systems occupying a differential volume of phase space, A_K is a normalization constant, Ψ_0 is the central value of the relative potential and sets the energy scale, and W_0 is a dimensionless parameter that varies over the family of models. There exists a one-to-one, monotonic (though non-analytic) relationship between W_0 and the more common King concentration parameter $c_K \equiv \log(r_t/r_c)$, where r_c is the core radius (see Section 2.3.1). See Figure 4.9 in Binney & Tremaine (2008) for this relation, where their $\Phi(0)/\sigma^2 = W_0$.

Any physically plausible cluster must have a finite central potential, therefore as $W_0 \to 0$, it must always be true that in this limit the exponential quantity in the distribution function becomes very small for all positions in phase space. Taking the Taylor series, the distribution becomes (for the $\mathcal{E} \geq 0$ case)

$$f(\mathcal{E}) = A_K W_0 \mathcal{E}/\Psi_0 = A'_K \mathcal{E}. \tag{2.75}$$

Here A'_K is a new normalization constant, which must be finite and non-zero for the cluster to exist at all.

Stellar polytropes are defined by the distribution function

$$f(\mathcal{E}) = \begin{cases} A\mathcal{E}^{n-3/2} & \mathcal{E} \geq 0 \\ 0 & \mathcal{E} < 0, \end{cases} \tag{2.76}$$

with some different normalization constant, A. Thus we see that in the limit of $W_0 \to 0$, King models approach an $n = 5/2$ polytrope. Polytropic models with $n < 5/2$ are then less centrally concentrated than any King model.

The number of stars per unit volume is found by integrating the distribution function over velocity space. The manipulations here are standard (Binney & Tremaine 2008, Chapter 4), so we give only the essential results. We let m denote the stellar mass, assumed provisionally to be identical for all cluster members. Then ρ, the mass density of stars, is

$$\rho(r) = 4\pi m A \int_0^{v_{\max}} \mathcal{E}^{n-3/2} v^2 dv. \tag{2.77}$$

Here, $v_{\max}(r) \equiv \sqrt{2\Psi(r)}$ is the maximum speed for a star at radius r. For such a star, $\mathcal{E} = 0$. The total physical energy per unit mass, $\Phi(r) + v^2/2$, is $\Phi(r_t)$, so the star can just reach r_t. Using equation (2.73), equation (2.77) becomes

$$\rho(r) = 4\pi m A \Psi^{n-3/2} \int_0^{\sqrt{2\Psi}} \left(1 - \frac{v^2}{2\Psi}\right)^{n-3/2} v^2 dv. \tag{2.78}$$

We define a new variable $\theta \equiv \arcsin\left(v/\sqrt{2\Psi}\right)$, so that

$$\rho(r) = 2^{5/2}\pi m A \frac{\Psi^n}{n} \int_0^{\pi/2} \cos^{2n-2}\theta d\theta \tag{2.79}$$

$$= (2\pi)^{3/2} m A \frac{\Gamma(n-1/2)}{\Gamma(n+1)} \Psi^n(r). \tag{2.80}$$

To calculate the relative potential $\Psi(r)$, we use Poisson's equation. For our spherical system, this is

$$\frac{1}{r^2}\frac{d}{dr}\left(r^2 \frac{d\Psi}{dr}\right) = -4\pi G\rho_0 \left(\frac{\Psi}{\Psi_0}\right)^n, \tag{2.81}$$

where ρ_0 and Ψ_0 are the central values of $\rho(r)$ and $\Psi(r)$, respectively. We define a dimensionless potential as $\psi \equiv \Psi/\Psi_0$, and a dimensionless radius as $\xi \equiv r/r_0$, where the scale radius r_0 is

$$r_0 \equiv \sqrt{\frac{\Psi_0}{4\pi G\rho_0}}. \tag{2.82}$$

Since $\rho = \rho_0 \psi^n$, the new potential obeys the Lane-Emden equation:

$$\frac{1}{\xi^2}\frac{d}{d\xi}\left(\xi^2 \frac{d\psi}{d\xi}\right) = -\psi^n, \tag{2.83}$$

with boundary conditions $\psi(0) = 1$ and $\psi'(0) = 0$. The nondimensional tidal radius $\xi_t \equiv r_t/r_0$ is the point where ψ falls to zero. [4]

For any chosen polytropic index n, equation (2.83) can readily be solved numerically. Our task is to translate this nondimensional solution into a physical model of the initial cluster. Given n, the basic quantities characterizing the cluster are: $N_{\rm tot}$, the total number of stars; r_v, the virial radius; and m, the mean stellar mass.[5] The virial radius is defined by

$$r_v \equiv -\frac{GM^2}{2W}. \tag{2.84}$$

Here, $M \equiv N_{\rm tot} m$ is the total cluster mass, while W is the gravitational potential energy:

$$W = \frac{1}{2}\int_0^{r_t} 4\pi r^2 \rho \Phi dr. \tag{2.85}$$

Below, we show how to obtain the dimensional quantities r_0, ρ_0, and Ψ_0 from our three input parameters and the solution $\psi(\xi)$.

Physical Scale of the Polytropic Cluster

We first define a relative potential energy:

$$W' \equiv \frac{1}{2}\int_0^{r_t} 4\pi r^2 \rho \Psi dr. \tag{2.86}$$

This has the same form as the true potential energy W, but uses the relative potential Ψ instead of the physical one Φ. Indeed, solving equation (2.72) for Φ in terms of Ψ and subsituting into equation (2.85) for W yields

$$W = \frac{1}{2}\Phi(r_t)M - W' \tag{2.87}$$

$$= -\frac{GM^2}{2r_t} - W'. \tag{2.88}$$

Since W is related to r_v, we should next establish a relationship between W' and other dimensional quantities.

[4] The value of ξ_t is derived within each polytropic model. We stress that, despite the nomenclature, this "tidal" radius bears no relation to the truncation created by the Galactic potential. In Sections 3.3.3 and 4.4, we describe simulations that include the external field.

[5] Unlike $N_{\rm tot}$ and r_v, the mean mass m is not an independent parameter, but follows from our specified mass function and prescription for binaries; see Section 2.2.2 below.

Following King (1966), we define a nondimensional potential as

$$\beta \equiv \int_0^{\xi_t} 4\pi\xi^2\psi^{n+1}d\xi \tag{2.89}$$

$$= \frac{1}{r_0^3}\int_0^{r_t} 4\pi r^2 \frac{\rho}{\rho_0}\frac{\Psi}{\Psi_0}dr \tag{2.90}$$

$$= \frac{2W'}{\rho_0 r_0^3 \Psi_0}. \tag{2.91}$$

We also define a nondimensional cluster mass:

$$\mu \equiv \int_0^{\xi_t} 4\pi\xi^2\psi^{n}d\xi \tag{2.92}$$

$$= \frac{1}{r_0^3}\int_0^{r_t} 4\pi r^2 \frac{\rho}{\rho_0}dr \tag{2.93}$$

$$= \frac{M}{\rho_0 r_0^3}. \tag{2.94}$$

Both β and μ can be calculated using the solution $\psi(\xi)$ and ξ_t (the value of ξ for which $\psi(\xi) = 0$). Their ratio is

$$\frac{\beta}{\mu} = \frac{2W'}{M\Psi_0} \tag{2.95}$$

$$= \frac{2W' r_0 \mu}{4\pi G M^2}, \tag{2.96}$$

where we have used equations (2.94) and (2.82) to make the last transformation. Solving this equation for W' and substituting into equation (2.88), we find

$$W = -\frac{GM^2}{2}\left(\frac{1}{r_t} + \frac{4\pi\beta}{r_0\mu^2}\right). \tag{2.97}$$

This last relation gives us more information about the virial radius. We now see that the nondimensional version, $\xi_v \equiv r_v/r_0$, obeys

$$\frac{1}{\xi_v} = \frac{1}{\xi_t} + \frac{4\pi\beta}{\mu^2}. \tag{2.98}$$

Thus, ξ_v can be obtained at once from the nondimensional solution. Since r_v itself is an input, the dimensional scale radius, r_0, can be obtained from

$$r_0 = \frac{r_v}{\xi_v}. \tag{2.99}$$

Similarly, the central density ρ_0 is

$$\rho_0 = \frac{M}{\mu r_0^3} \tag{2.100}$$

$$= \left(\frac{\xi_v^3}{\mu}\right) \frac{N_{\rm tot} m}{r_v^3}, \tag{2.101}$$

while Ψ_0 is found from

$$\Psi_0 = 4\pi G \rho_0 r_0^2 \tag{2.102}$$

$$= \left(\frac{4\pi\xi_v}{\mu}\right) \frac{G N_{\rm tot} m}{r_v}. \tag{2.103}$$

Sampling the Distribution Function

Given the scale factors r_0 and ρ_0, we know the dimensional mass density $\rho(r)$. We then populate space with stars according to a normalized distribution $p_1(r)$ such that $p_1(r)dr$ is the probability a star is located between r and $r + dr$. This probability is simply

$$p_1(r) = \frac{4\pi r^2 \rho}{N_{\rm tot} m}. \tag{2.104}$$

The actual position vector of each star is then distributed isotropically within each radial shell.

Finally, we require an analogous distribution for stellar speeds. At a given radius, the speed must be consistent with the prescribed energy distribution. Let $p_2(v|r)dv$ be the probability that the speed lies between v and $v + dv$ *given* that its radius is r. Clearly,

$$p_2(v|r)dv \times p_1(r)dr = \frac{f d^3v d^3r}{N_{\rm tot}}. \tag{2.105}$$

Replacing d^3r by $4\pi r^2 dr$ and d^3v by $4\pi v^2 dv$, we have, after using equation (2.104),

$$p_2(v|r) = \frac{4\pi v^2 m f}{\rho}. \tag{2.106}$$

We take $f = f(\mathcal{E})$ from equation (2.76) and use the definition of $\mathcal{E}$ from equation (2.73), finding

$$p_2(v|r) = \frac{2}{\pi} \frac{\Gamma(n+1)}{\Gamma(n-1/2)} \Psi^{-3/2} \left(1 - \frac{v^2}{2\Psi}\right)^{n-3/2} v^2. \tag{2.107}$$

Here, the relative potential is calculated at each r from $\Psi = \Psi_0 \psi(\xi)$, where we recall that ξ is the nondimensional radius. Given the stellar speed, i.e., the magnitude of the velocity vector, the direction of that vector is again distributed isotropically in space.

2.2.2 Stellar Masses: Single and Binary

Thus far, we have described a cluster that is composed of members with identical mass. In actual practice, we assign masses to the stars according to a realistic distribution. The parameters of this mass function for the initial cluster are among those we vary to obtain an optimal match between the evolved system and the present-day Pleiades. In the course of evolution, some stars will be given enough energy, through three-body interactions, to escape the cluster. The most massive ones die out as the cluster ages. It is therefore not obvious that the initial mass function is identical to that found today.

Lognormal-Power Law Mass Function

We suppose that the distribution of stellar masses in the young cluster is similar in form to the initial mass function for the field population. In recent years, large-scale surveys of low-luminosity objects, combined with spectroscopy, have established an accurate initial mass function down to the brown dwarf limit (e.g., Covey et al. 2008). The consensus is that the original power law of Salpeter (1955) for masses above solar is joined at the lower end by a lognormal function. This basic form appears to hold in diverse environments, including young clusters (Chabrier 2005).

Let $\phi(m)dm$ be the probability that a star's mass (in solar units) is between m and $m + dm$. We posit that this probability is

$$\phi(m) = \begin{cases} \frac{B}{m} e^{-y^2} & m_{\rm min} \leq m \leq \mu \\ C m^{\alpha} & \mu \leq m \leq m_{\rm max}. \end{cases} \tag{2.108}$$

where B, C, α, and the joining mass μ are all constants. We set $m_{\rm min} = 0.08$ and $m_{\rm max} = 10$ (although we also tested a higher mass limit; see Section 3.3.2). The variable y is given by

$$y(m) \equiv \frac{\log m - \log m_0}{\sqrt{2}\sigma_m}. \tag{2.109}$$

Here, m_0 is the centroid of the lognormal function, and σ_m its width. For input parameters α, m_0, and σ_m, the constants B, C, and μ are determined by the normalization condition

$$\int_{m_{\rm min}}^{m_{\rm max}} \phi(m) dm = 1, \tag{2.110}$$

and by requiring that $\phi(m)$ and its first derivative be continuous at $m = \mu$. Analytic expressions may be found for the three constants.

We first define $y_0 = y(\mu)$. The continuity requirement then gives us

$$\frac{C}{B} = e^{-y_0^2} \mu^{-(\alpha+1)}. \tag{2.111}$$

The derivative of this mass function is given by

$$\frac{d\phi}{dm} = \begin{cases} -\frac{B}{m^2}e^{-y^2}\left(1+\frac{\sqrt{2}y}{\ln(10)\sigma_m}\right) & m_{min} \le m \le \mu \\ C\alpha m^{\alpha-1} & \mu \le m \le m_{max} \end{cases} \tag{2.112}$$

Continuity of this derivative at $m = \mu$ combined with equation (2.111) then gives

$$-C\mu^{\alpha-1}\left(1+\frac{\sqrt{2}y_0}{\ln(10)\sigma_m}\right) = \alpha C\mu^{\alpha-1}. \tag{2.113}$$

This is then solved for y_0 to yield

$$y_0 = -\frac{\ln(10)}{\sqrt{2}}\sigma_m(\alpha+1). \tag{2.114}$$

We can then use equation (2.109) to express y_0 in terms of μ and solve the resulting equation for this joining mass. This gives

$$\log\mu = \log m_0 - \ln(10)\sigma_m^2(\alpha+1). \tag{2.115}$$

Finally, we return to the normalization condition.

$$\int_{m_{\min}}^{m_{\max}} \phi(m)dm = \int_{m_{\min}}^{\mu} \frac{B}{m}e^{-y^2}dm + \int_{\mu}^{m_{\max}} Cm^{\alpha}dm. \tag{2.116}$$

The first integral can be solve by transforming it to an integration over y and recognizing the result as the error function. Requiring that this sum must total to 1 and using equation (2.111) to eliminate C, this can then be solved for B in terms of the given parameters and μ (which is computed from the input parameters via equation (2.115)). The result is

$$B = \left[\sqrt{\frac{\pi}{2}}\ln(10)\sigma_m\left(\mathrm{erf}(y_0) - \mathrm{erf}(y_{\min})\right) + \frac{1}{\alpha+1}e^{-y_0^2}\left(\left(\frac{m_{\max}}{\mu}\right)^{\alpha+1} - 1\right)\right]^{-1}, \tag{2.117}$$

where $y_{\min}$ is $y(m_{\min})$. Once B is known, C is then compute from equation (2.111),

$$C = Be^{-y_0^2}\mu^{-(\alpha+1)}. \tag{2.118}$$

The average mass of this mass function has an analytic form found by integrating

$$\int_{m_{\min}}^{m_{\max}} m\phi(m)dm = \int_{m_{\min}}^{\mu} Be^{-y^2}dm + \int_{\mu}^{m_{\max}} Cm^{\alpha+1}dm. \tag{2.119}$$

The first integral on the right hand side can be solved by transforming it into an integration over y to get

$$\int_{m_{\min}}^{\mu} Be^{-y^2}dm = 2Dm_0\int_{y_{\min}}^{y_0} Be^{-y^2+2Dy}dy, \tag{2.120}$$

where $D = \ln(10)\sigma_m/\sqrt{2}$. This integral can then be solved by completing the square in the exponent. The full result for the average mass is then

$$\langle m\rangle = \sqrt{\pi}BDe^{D^2}m_0\left(\mathrm{erf}(y_0 - D) - \mathrm{erf}(y_{\min} - D)\right) + \frac{C}{\alpha+2}\left(m_{\max}^{\alpha+2} - \mu^{\alpha+2}\right). \tag{2.121}$$

Binary Systems

Most stars are not single objects, but have binary companions. (See Sections 3.2.2 and 4.3.2 for our results for the Pleiades and Alpha Persei clusters.) Such pairing must have been present in the initial cluster. We therefore view the positions and velocities established in Section 2.2.1 as pertaining to $N_{\rm tot}$ *stellar systems*, rather than individual stars. Similarly, the symbol m used, e.g., in equation (2.104), actually denotes the *average system mass*, after accounting for binaries. We specify the global binary fraction as a parameter b, which gives the probability that a system actually consists of two stars. Conversely, a fraction $1 - b$ of the systems are indeed single stars. Their mass is distributed according to the probability $\phi(m)$.

We wish to also allow for a varying degree of correlation between the masses of stars within a binary. Such a correlation must also have been present at early times. Accordingly, we include the effect in our initial state. Within the fraction b of systems that are binaries, we first independently assign masses to each component, using the probability distribution $\phi(m)$. After identifying the primary mass m_p and the secondary mass m_s (the former being the larger of the two), we then alter the latter to m_s', where

$$m_s' = m_s \left(\frac{m_p}{m_s} \right)^{\gamma}. \tag{2.122}$$

Here, γ is an input parameter that measures the degree of mass correlation within binaries (see equation (2.71)). If $\gamma = 0$, the component masses are uncorrelated, while $\gamma = 1$ corresponds to perfect matching. As already noted in Section 2.1.4, although this model artificially depletes the number of very low-mass secondaries it has only a negligible effect on the photometric distributions. It also turns out that low-mass binaries have a negligible influence ont he cluster's dynamical evolution as well (see Section 5.2.2).

We give our binaries randomly inclined orbital planes with the orbit's major axis randomly oriented within that plane. The period and eccentricity distribution used is characteristic of present, solar-type binaries both in the field (Duquennoy & Mayor 1991) and in clusters such as the Pleiades (Bouvier et al. 1997). If $p_3(\mathcal{P})d\mathcal{P}$ is the fraction of systems with periods between $\mathcal{P}$ and $\mathcal{P} + d\mathcal{P}$, then $p_3(\mathcal{P})$ is lognormal:

$$p_3(\mathcal{P}) = \frac{1}{\sqrt{2\pi}\sigma_{\mathcal{P}}} e^{-z^2}, \tag{2.123}$$

where

$$z \equiv \frac{\log \mathcal{P} - \log \mathcal{P}_0}{\sqrt{2}\sigma_{\mathcal{P}}}. \tag{2.124}$$

We set the centroid period to $\log \mathcal{P}_0 = 4.8$ and the width to $\sigma_{\mathcal{P}} = 2.3$, where the period is measured in days. The eccentricity distribution has a thermal distribution:

$$p_4(e) = 2e, \tag{2.125}$$

as motivated both by observations (Duquennoy & Mayor 1991) and theory (Heggie 1975).

Finally, we start the binary pair at a random phase angle within its orbit. We wish for the true anomaly to be distributed such that the probability of finding the system at that position in its orbit is proportional to the relative amount of time spent there, $p_5(\theta)d\theta = p(t)dt$. Since we desire a uniform probability distribution for the time (all times equally likely), $p_5(t) = 1/\mathcal{P}$. Kepler's Second Law tells us that $\frac{dA}{dt}$ is a constant. Integrating over a full period gives that this constant must be $\frac{dA}{dt} = \frac{A}{\mathcal{P}}$, where A is the area of the ellipse. Thus

$$p_5(\theta)d\theta = p(t)dt = \frac{dt}{\mathcal{P}} = \frac{dA}{A}. \tag{2.126}$$

The area of an ellipse is given by

$$A = \pi a^2\sqrt{1-e^2}, \tag{2.127}$$

where a is the semimajor axis and e the eccentricity. We find the semimajor axis from Kepler's Third Law,

$$a = \left(\frac{Gm\mathcal{P}^2}{4\pi^2}\right)^{1/3}, \tag{2.128}$$

where m is the total mass of the system. A small sliver of area dA swept out by the line connecting the ellipse's circumference to one of its foci while rotated through a small angle $d\theta$ is

$$dA = \frac{1}{2}r^2 d\theta, \tag{2.129}$$

where r is the current distance from the focus, and is given by

$$r = \frac{a(1-e^2)}{1+e\cos\theta}. \tag{2.130}$$

Combining equations (2.126)-(2.130) gives an expression for $p_5(\theta)$ in terms of the mass, period, and eccentricity of the binary. Once these parameters are determined, the phase angle is picked from the distribution

$$p_5(\theta) = \frac{(1-e^2)^{3/2}}{2\pi(1+e\cos\theta)^2}. \tag{2.131}$$

Primordial Mass Segregation

The initial cluster described thus far is homogenous, in the sense that any volume containing an appreciable number of systems has the same average system mass. However, there have long been claims of observed *mass segregation* in young clusters, i.e., an increase of average stellar mass toward the center (Sagar et al. 1988; Jones & Stauffer 1991; Moitinho et al. 1997; Stolte et al. 2006). Our own examination of the Pleiades finds it to also exhibit this phenomenon to a striking degree (see Section 3.2.4). We want to see if this property

developed on its own or was inherited from an earlier epoch. We accordingly include a quantitative prescription for mass segregation in our initial state.

One system has a higher probability of being near the cluster center than another, in a time-averaged sense, if its relative energy $\mathcal{E}$ is greater. Mass segregation therefore manifests itself as a correlation between the system mass m and $\mathcal{E}$. This fact was noted by Baumgardt et al. (2008), who used it to implement a specific procedure for mass segregation. Here we have adopted a variant of their method that allows us to include the effect to a variable degree. We first assign $\mathcal{E}$- and m-values to all member systems according to equation (2.76) and our prescription for binary masses. We then place the systems in two lists - the first ordered by increasing m, and the second by increasing $\mathcal{E}$. When we first construct these lists, the ranking of the system in the first is unrelated to its ranking in the second. This is the case of zero mass segregation. There would be perfect mass segregation if the two rankings were identical.

Let us quantify the intermediate case. For a star of given mass, we find its index in the mass-ordered list. To assign an energy to that star, we choose the second (energy-ordered) index from a Gaussian distribution centered on the mass index. The width of this distribution, denoted $\sigma_{\mathcal{E}}$, can be infinite (no mass segregation) or zero (perfect segregation). More generally, we define a parameter β, the degree of mass segregation, which varies between 0 and 1. After some trial and error, we adopted the following prescription relating the width $\sigma_{\mathcal{E}}$ to β:

$$\sigma_{\mathcal{E}} = -\frac{1}{2} N_{\rm tot} \ln \beta. \tag{2.132}$$

The logarithmic dependence on β ensures that $\sigma_{\mathcal{E}}$ has the desired behavior in the extreme limits. The proportionality with $N_{\rm tot}$ ensures that our algorithm gives the same degree of biasing in clusters of any population.

In summary, β becomes another input parameter that we vary within the initial configuration. As we will see, having a non-zero β will be critical to obtaining a proper match between an evolved cluster and the Pleiades today. Mass segregation was therefore present at a relatively early epoch.

Since relatively massive stars preferentially reside near the center, our imposition of mass segregation alters the shape of the gravitational potential from that of a single-mass polytrope. Relative to the total gravitational energy, the total kinetic energy has a value slightly below that for virial equilibrium. We rescaled all stellar velocities by a uniform factor to restore exact equilibrium. In practice, this factor was typically about 1.05.

To summarize, there are nine input parameters into our simulations. $N_{\rm tot}$ is the total number of stellar systems. The density profile shape is defined by n, the polytropic index. The size of the cluster is set by the virial radius, r_v. The lognormal portion of the mass function is set by the peak, m_0, and width, σ_m. The power law slope is α. The fraction of systems which are binary is set by b, and the degree of correlation in the masses of their component stars is determined by γ. Finally, the degree of initial mass segregation is set by the parameter β. It is these nine characteristics which we will be determining when matching our simulations to actual clusters.

2.3 N-Body Simulations

Using the publicly available code Starlab (Portegies Zwart et al. 2001, Appendix B), we ran suites of N-body calculations over over the current age of the cluster. The goal was to find that initial state which evolved to the current cluster, as gauged by using the characteristics discussed above. In doing so, we also establish the detailed history of the group over that epoch, and even into the future.

A key assumption here is that the cluster divested itself of cloud gas relatively soon after its birth. There is currently no direct means to assess the duration of the initial, embedded phase in any other open cluster. We may take a clue from T associations, which are still surrounded (but not completely obscured) by molecular gas. No systems are observed with ages exceeding about 5 Myr, a striking fact first noted by Herbig (1978). Presumably, older groups consisting of post-T Tauri stars have already driven away their clouds and are merged observationally into the field population. If a similar embedded period held for our clusters of interest, it indeed represented a small fraction of the total age. Hence, we can establish, with some confidence, the cluster's structure just after cloud dispersal.

2.3.1 Characterizing the Evolved Cluster

After evolving a particular initial state for the age of the cluster in question, we compare the outcome with the actual cluster. In making this comparison, it is important to "observe" the simulated cluster under the same conditions as the real one. Thus, we project the three-dimensional distribution of stars onto a two-dimensional plane, assumed to lie at the mean same distance as the cluster. The angular separation $\Delta\theta$ between each pair of stars is then determined. If $\Delta\theta_{\rm res}$ denotes the telescope resolution, then any pair with $\Delta\theta < \Delta\theta_{\rm res}$ is taken to be an unresolved point source. Note that our unresolved sources include a small fraction (typically less than 0.5%) of triples and high-order systems, as well as a few unrelated pairs observed to be close in projection. We denote as N_s the total number of point sources out to a radius from the cluster center equal to the largest radius observed for the real cluster. For each simulated evolution, we compare the final N_s-value with the observed population of the cluster.

The vast majority of stars in the young clusters we consider are on the main sequence or pre-main sequence isochrone (see Figure 3.1 in Section 3.1). The number of post-main-sequence objects, while relatively small, is sensitive to the shape of the stellar mass function. Hence, it is important that we reproduce, as closely as possible, the number inferred for the present-day cluster. For the ages of the cluster we will be considering, the main-sequence turnoff is around 4-5 $M_\odot$. We thus denote the number of stars (singles or primary stars in binaries) whose mass exceeds this turnoff mass as N_4 or N_5, depending on the age of that particular cluster. This may then also be compared directly with the actual number in the cluster.

Similarly, we compare $M_{\rm tot}$, the total mass of all stars in the evolved cluster, with the total mass obtained through the statistical analysis of Section 2.1. For our assumed

resolution limit $\Delta\theta_{\rm res}$, we can also assess $b_{\rm unres}$ computationally for each evolutionary run. This is the fraction of point sources representing two or more unresolved stars. Note that $b_{\rm unres}$ is less than the *initially* imposed binary fraction b, both because some pairs are wide enough to be resolved, and because others are torn apart in the course of evolution.

We next consider the projected density profile. We divide the cluster into radial bins that match those used in the analysis of the Pleiades. The resulting surface density of stellar systems is then fit to the empirical prescription of King (1962):

$$\Sigma(R) = k\left(\frac{1}{\sqrt{1+(R/R_c)^2}} - \frac{1}{\sqrt{1+(R_t/R_c)^2}}\right)^2. \tag{2.133}$$

Here, R is the projected radius, k is a constant with the dimensions of a surface density, and R_c and R_t are the core and tidal radii, respectively. We determine the values of k, R_c and R_t which give the best match the simulated cluster's density profile. However, only R_c is used directly in the final comparison to the actual cluster. Instead we use two different parameters derived from these. First is the King concentration parameter,

$$c_K \equiv \log(R_t/R_c), \tag{2.134}$$

computed both for each evolved simulation and in the real cluster. Second, from equation (2.133), the central surface density Σ_0 is

$$\Sigma_0 = k\left(1 - \frac{1}{\sqrt{1+(R_t/R_c)^2}}\right)^2. \tag{2.135}$$

This is also compared to the value for the real cluster.

We also measure the degree of mass segregation. For the evolved cluster, we compute the cumulative fraction of systems contained within a projected radius R, both by number ($f_N(R)$) and mass ($f_M(R)$). As in Section 2.1.3, the Gini coefficient is computed from equation (2.46) and then compared to that found in the actual cluster.

The distribution of stellar masses is, of course, another property that should be compared with the actual cluster. As just described, we set the form of the distribution within the initial configuration as a lognormal function with a power law tail. The apportionment of masses within the evolved state could in principle differ, due to the escape of some stars from the cluster and the death of others with sufficiently high mass. Our procedure is first to find, within the output state, the normalized distribution of single stars. Included in this distribution are both isolated stars and the components of *resolved* binaries. We then peer within *unresolved* binaries and find the analogous distributions of primary mass m_p and secondary mass m_s. Finally, we record the distribution of the binary mass ratio, $q \equiv m_s/m_p$.

When examining the real cluster, the data for the single-star mass distribution was fit to a pure lognormal with centroid m_0 and width σ_m. For consistency, we characterize the evolved cluster in our simulations in a similar fashion. Now for a given single-star

function and binary correlation parameter γ, the primary, secondary, and q-distributions are all uniquely determined. Section 2.3.2 below gives the mathematical derivation. The task is to vary γ, as well as m_0 and σ_m, for the presumed lognormal single-star distribution until this function, as well as the primary, secondary, and q-distributions, best fit those we find directly in the numerical output. We then compare γ, m_0, and σ_m to these same quantities derived in a similar way for the observed cluster. Notice that m_0 and σ_m found here will not match those in the initial state. This discrepancy arises partly from real changes of the stellar masses, but even more from our adoption of a simple lognormal when fitting the evolved cluster.

Since we populated the cluster stochastically, according to probability distributions (e.g., $\phi(m)$ in equation (2.108)), initial states differed from one another in detail. In order to prevent this stochastic sampling from having too large an influence on our measured output parameters, we ran 25 simulations, all with identical input parameters. We then use the average result from each of these parameters, and compute the standard deviations for each quantity in the evolved cluster, due solely to differing realizations of the initial state.

2.3.2 Distribution of Binary Component Masses

Even if both components of a binary system are drawn from this same mass function, the distribution of each will be different. This is because the primary is defined as the more massive of the pair, and the secondary the smaller. Thus the distribution of all primary stars is biased towards higher masses, because lower mass stars are more likely to be the secondary in their system. Similarly, secondary stars are far less likely to have a higher mass. Correlating the two masses as in equation (2.122) further changes the secondary mass and mass ratio distributions. Here we show how to find, for a given γ, the distribution of primary and secondary masses, as well as the distribution of the secondary-to-primary mass ratio q.

Results for a General Mass Function

We first let the primary and secondary masses have provisional masses m_p^* and m_s^*, respectively. Assume that both components within binaries are drawn independently from the same distribution ϕ. This function is assumed to hold from a minimum mass $m_{\min}$ to maximum mass $m_{\max}$ with the normalization such that

$$\int_{m_{\min}}^{m_{\max}} \phi(m) dm = 1. \tag{2.136}$$

The two-dimensional mass function of the binaries is then

$$\Phi_b\left(m_p^*, m_s^*\right) = 2\phi(m_p^*)\phi(m_s^*). \tag{2.137}$$

Here, $\Phi_b\left(m_p^*, m_s^*\right) \Delta m_p^* \Delta m_s^*$ is the probability of finding a system with primary mass between m_p^* and $m_p^* + \Delta m_p^*$, and secondary mass between m_s^* and $m_s^* + \Delta m_s^*$. The initial factor of 2

on the righthand side of equation (2.137) normalizes the function so that

$$\int_{m_{\min}}^{m_{\max}} dm_p^* \int_{m_{\min}}^{m_p^*} dm_s^* \Phi_b(m_p^*, m_s^*) = 1. \tag{2.138}$$

To implement binary mass correlation, we consider new primary and secondary masses, m_p and m_s, related to the previous ones by

$$m_p = m_p^* \tag{2.139}$$

$$m_s = m_s^* \left(\frac{m_p^*}{m_s^*}\right)^{\gamma}. \tag{2.140}$$

We are interested in the distribution function $\Phi_b(m_p, m_s)$, which is

$$\Phi_b(m_p, m_s) = \Phi_b(m_p^*, m_s^*) \left|\frac{\partial(m_p^*, m_s^*)}{\partial(m_p, m_s)}\right|. \tag{2.141}$$

After evaluating the Jacobian, we find

$$\Phi_b(m_p, m_s) = \frac{2}{1-\gamma} \left(\frac{m_s}{m_p}\right)^{\gamma/(1-\gamma)} \phi(m_p)\phi\left[m_s \left(\frac{m_s}{m_p}\right)^{\gamma/(1-\gamma)}\right]. \tag{2.142}$$

Let us first consider $\phi_p(m_p)$, the distribution of primary masses. This function is the integral of $\Phi_b(m_p, m_s)$ over all appropriate values of m_s:

$$\phi_p(m_p) = \int_{m_{\mathrm{s,min}}(m_p)}^{m_{\mathrm{s,max}}(m_p)} \Phi_b(m_p, m_s) dm_s. \tag{2.143}$$

The largest mass a secondary can have, given the primary mass, is m_p itself:

$$m_{\mathrm{s,max}}(m_p) = m_p. \tag{2.144}$$

However, the smallest mass is *not* $m_{\min}$. This is indeed the smallest mass for m_s^*. The correlation of primary and secondary masses implies that the minimum for m_s is

$$m_{\mathrm{s,min}}(m_p) = m_{\min} \left(\frac{m_p}{m_{\min}}\right)^{\gamma}. \tag{2.145}$$

Thus, the two integration limits in equation (2.143) are themselves functions of m_p. For any arbitrary mass function, the substitution of

$$m_s' = m_s \left(\frac{m_s}{m_p}\right)^{\gamma/(1-\gamma)} \tag{2.146}$$

can be used to find that

$$\phi_p(m_p) = 2\phi(m_p) \int_{m_{\min}}^{m_p} \phi(m'_s) dm'_s. \tag{2.147}$$

This is simply doing the inverse of the original transformation. This result shows that although $\phi_p(m_p) \neq \phi(m_p)$, the primary mass distribution is unaffected by the correlation. This is because this formulation for the correlation only changes the mass of the secondary stars and leaves the primaries unchanged.

It can be asked what fraction of systems with primary mass m_p would be seen to be binary (here singles are viewed as systems with $m_s = 0$). For a cluster with N stars and overall binary fraction b, then the number of binaries with primary stars of mass near m_p is $bN\phi_p(m_p)dm_p$. Similarly, the number of singles with mass near m_p is $(1-b)N\phi(m_p)dm_p$. Thus we can compute the fraction of systems, $b_m(m_p)$ with primary masses near m_p which are binary.

$$b_m(m_p) = \frac{bN\phi_p(m_p)dm_p}{bN\phi_p(m_p)dm_p + (1-b)N\phi(m_p)dm_p} \tag{2.148}$$

$$= \frac{1}{1 + \frac{1-b}{b}\frac{\phi(m_p)}{\phi_p(m_p)}}. \tag{2.149}$$

An example of this result is seen in Figure 2.1 for the mass function and overall binary fraction found for the Pleiades in Section 3.2. As with the primary mass function, this result is independent of the degree of correlation between binary component masses.

The secondary mass function, $\phi_s(m_s)$, is similarly found by integrating $\Phi_b(m_p, m_s)$ over all possible primary masses:

$$\phi_s(m_s) = \int_{m_{\mathrm{p,min}}(m_s)}^{m_{\mathrm{p,max}}(m_s)} \Phi_b(m_p, m_s) dm_p. \tag{2.150}$$

The smallest value a primary mass can be, for a given secondary, is m_s:

$$m_{\mathrm{p,min}}(m_s) = m_s. \tag{2.151}$$

Somewhat surprisingly, the largest value is not necessarily $m_{\max}$, again because of the imposed correlation. To find the correct maximum, we solve equation (2.140) for m_p^*:

$$m_p^* = m_p = m_s^{1/\gamma} \left(m_s^*\right)^{(\gamma-1)/\gamma}. \tag{2.152}$$

Since γ lies between 0 and 1, the exponent of m_s^* is negative. Thus, for a given m_s, m_p is greatest when m_s^* is smallest. Since the lowest value of m_s^* is $m_{\min}$, we have

$$m_{\mathrm{p,max}}(m_s) = m_s^{1/\gamma} \left(m_{\min}\right)^{(\gamma-1)/\gamma} = m_{\min} \left(\frac{m_s}{m_{\min}}\right)^{1/\gamma}. \tag{2.153}$$

However, for $m_s > m_{\min}(m_{\max}/m_{\min})^\gamma$, this would give $m_{\rm p,max} > m_{\max}$, which is impossible. In summary, $m_{\rm p,max}(m_s)$ is given by

$$m_{\rm p,max}(m_s) = \begin{cases} m_{\min}\left(\frac{m_s}{m_{\min}}\right)^{1/\gamma} & m_s \le m_{\min}\left(\frac{m_{\max}}{m_{\min}}\right)^\gamma \\ m_{\max} & m_s \ge m_{\min}\left(\frac{m_{\max}}{m_{\min}}\right)^\gamma . \end{cases} \tag{2.154}$$

Finally, we need $\phi_q(q)$, the distribution of the binary mass ratio $q \equiv m_s/m_p$. As a first step, we find the two-dimensional mass function $\Phi_b(m_p, q)$. Proceeding as before, we have

$$\Phi_b(m_p, q) = \Phi_b(m_p^*, m_s^*)\left|\frac{\partial(m_p, m_s)}{\partial(m_p, q)}\right| \tag{2.155}$$

$$= m_p \Phi_b(m_p, m_s) \tag{2.156}$$

$$= \frac{2m_p}{1-\gamma} q^{\gamma/(1-\gamma)} \phi(m_p)\phi\left[m_p q^{1/(1-\gamma)}\right]. \tag{2.157}$$

The desired distribution is the integral of $\Phi_b(m_p, q)$ over suitable m_p-values:

$$\phi_q(q) = \int_{m_{\rm p,min}(q)}^{m_{\rm p,max}(q)} \Phi_b(m_p, q) dm_p. \tag{2.158}$$

As the notation indicates, the limits of m_p are subject to the restriction of a fixed q. Using equation (2.140), q itself is given in terms of $m_p^*(= m_p)$ and m_s^* by

$$q = \frac{m_s^*}{m_p}\left(\frac{m_p}{m_s^*}\right)^\gamma = \left(\frac{m_p}{m_s^*}\right)^{\gamma-1}. \tag{2.159}$$

Solving the last equation for m_p gives

$$m_p = m_s^* q^{-1/(1-\gamma)}. \tag{2.160}$$

Since the exponent of q is negative, and since q itself lies between 0 and 1, we see that $m_p > m_s^*$. Thus, for any q-value, there is always some m_s^* for which $m_p = m_{\max}$. We therefore set

$$m_{\rm p,max}(q) = m_{\max}. \tag{2.161}$$

The smallest value of m_p corresponds to $m_s^* = m_{\min}$. It follows that

$$m_{\rm p,min}(q) = m_{\min} q^{-1/(1-\gamma)}. \tag{2.162}$$

There is, however, one more caveat to the mass ratio distribution. Because of the limited range of possible masses between $m_{\min}$ and $m_{\max}$, there is a minimum possible q. This occurs when $m_p^* = m_{\max}$ and $m_s^* = m_{\min}$. Thus the minimum possible q is

$$q_{\min} = \left(\frac{m_{\min}}{m_{\max}}\right)^{1-\gamma}. \tag{2.163}$$

Below this, $\phi_q(q) = 0$. Thus q never achieves the full theoretical range of 0 to 1, but instead is always limited to $q_{\min} \le q \le 1$.

Results for Limiting Cases

A note should be made here about the limiting cases of $\gamma = 0$ and $\gamma = 1$. In the former case, it's clear that the two-dimensional mass function (equations (2.142) and (2.157)) reduces to it's non-correlated form (equation (2.137)), as it should. However, it should be noted that even in this case $\phi_p(m_p) \neq \phi_s(m_s) \neq \phi(m)$. That is, the primary and secondary mass functions are still different from that for single stars, and from each other. As mentioned before, although both stars are drawn from the single star mass function, the primary star is always chosen to be the more massive of the pair, and is thus biased towards higher masses. Similarly, secondary stars are biased towards lower masses.

At first thought, a non-correlated mass function might be expected to produce a flat q-distribution. This is not the case, however. Even when there is not correlation, the different probabilities of finding stars with different masses results in some mass ratios being more likely than others, and thus q is non-flat. Figure 3.15 in Section 3.3.1 demonstrates this alongside the q-distribution predicted for the Pleiades based on our best-fit parameters.

In the case of $\gamma = 1$, many terms in the equations above become singular the integration ranges shrink to 0. Although it is not readily obvious from the equations above, this case can be handled easily. As shown above, the primary mass function is not changed, even in this case. The secondary mass function and q-distribution, however, cannot be used in the forms presented above.

We next consider the secondary mass function, found by using equation (2.142) in equation (2.150). Applying the substitution

$$m'_p = m_s \left(\frac{m_s}{m_p}\right)^{\gamma/(1-\gamma)} \tag{2.164}$$

we have

$$\phi_s(m_s) = \frac{2}{\gamma} \int_{m'_{\mathrm{p,min}}}^{m_s} \left(\frac{m_s}{m'_p}\right)^{(1-\gamma)/\gamma} \phi\left[m_s \left(\frac{m_s}{m'_p}\right)^{(1-\gamma)/\gamma}\right] \phi(m'_p) dm'_p. \tag{2.165}$$

Here $m'_{\mathrm{p,min}}$ is found from $m_{\mathrm{p,max}}$ (it has become a minimum since m'_p gets smaller as m_p increases at fixed m_s),

$$m'_{\mathrm{p,min}} = \begin{cases} m_{\mathrm{min}} & m_s \leq m_{\mathrm{min}} \left(\frac{m_{\mathrm{max}}}{m_{\mathrm{min}}}\right)^{\gamma} \\ m_s \left(\frac{m_s}{m_{\mathrm{max}}}\right)^{\gamma/(1-\gamma)} & m_s \leq m_{\mathrm{min}} \left(\frac{m_{\mathrm{max}}}{m_{\mathrm{min}}}\right)^{\gamma}. \end{cases} \tag{2.166}$$

At first glance this does not appear to achieve any simplification, and indeed, for an arbitrary value of γ, it is not. Whereas direct substitution of equation (2.142) into equation (2.150) results in an expression that is good for lower γ, but singular at $\gamma = 1$, equation (2.165) is not singular at $\gamma = 0$, but is much easier to work with for larger values of γ. Simply plugging in $\gamma = 1$ results in

$$\phi_s(m_s) = 2\phi(m_s) \int_{m_{\mathrm{min}}}^{m_s} \phi(m'_p) dm'_p. \tag{2.167}$$

It can be seen by inspection that this is the same as equation (2.147) with a simple renaming of the variables. Thus $\phi_s = \phi_p$ in the limit of perfect correlation ($\gamma = 1$) for all single star mass functions $\phi(m)$.

In considering the q-distribution, we first note that when $\gamma = 1$, $q_{\min} = 1$. Thus $\phi_q(q) = 0$ for all $q \neq 1$. But we know that ϕ_q is a probability distribution function, and thus must be integrable. Furthermore, integrating it over all possible values must yield 1. A general property of any probability distribution function is that the average value of a quantity X that is a function of q is found by

$$\langle X \rangle = \int_{-\infty}^{\infty} X(q)\phi_q(q)dq. \tag{2.168}$$

But since q can only take on the value $q = 1$, then $X = X(1)$ is the only possible value. Thus $\langle X \rangle = X(1)$. So we have that

$$\int_{-\infty}^{\infty} X(q)\phi_q(q)dq = X(1), \tag{2.169}$$

for any arbitrary function $X(q)$. This is precisely the definitive property of the δ function. Thus as intuition would have suspected, in the limit of perfection correlation, the q-distribution is simply a delta function at $q = 1$,

$$\phi_q(q) = \delta(1 - q). \tag{2.170}$$

Results for a Lognormal Mass Function

We may, in principle, perform the integrals in equations (2.143), (2.150), and (2.158) for any specified single-star function $\phi(m)$. In practice, we choose a lognormal. With this form of $\phi(m)$, the integrations may all be done analytically. A pure lognormal mass function is given by

$$\phi(m) = \frac{A}{m}e^{-y^2}, \tag{2.171}$$

where as in equation (2.109),

$$y(m) \equiv \frac{\log m - \log m_0}{\sqrt{2}\sigma_m}. \tag{2.172}$$

We further define that $y_{\min} = y(m_{\min})$, $y_{\max} = y(m_{\max})$, $y_p = y(m_p)$, and $y_s = y(m_s)$. As before, m_0 and σ_m are the two parameters which define the function. The normalization constant A is found by requiring the function to satisfy equation (2.136). The integral is readily solvable in terms of the error function by transforming the integration to be over y. The result gives that

$$A = \sqrt{\frac{2}{\pi}}\frac{1}{\ln(10)\sigma_m}\left[\mathrm{erf}(y_{\max}) - \mathrm{erf}(y_{\max})\right]^{-1}. \tag{2.173}$$

We can now use this in the integrals above for the primary mass function, secondary mass function, and mass ratio distribution. We look first to the primary. Substituting equation (2.142) into equation (2.143) gives

$$\phi_p(m_p) = \frac{2}{1-\gamma}\int_{m_{\rm s,min}(m_p)}^{m_p}\left(\frac{m_s}{m_p}\right)^{\gamma/(1-\gamma)}\phi(m_p)\phi\left(m_s\left(\frac{m_s}{m_p}\right)^{\gamma/(1-\gamma)}\right)dm_s, \tag{2.174}$$

with $m_{\rm s,min}(m_p)$ given by equation (2.145). We now make the substitution given in equation (2.146). Using this and equation (2.171) along with a bit algebra, the integral becomes

$$\phi_p(m_p) = \frac{2A^2}{m_p}e^{-y^2(m_p)}\int_{m_{\rm min}}^{m_p}\frac{1}{m_s'}e^{-y^2(m_s')}dm_s'. \tag{2.175}$$

Transforming this into an integration over y leads to the result

$$\phi_p(m_p) = \sqrt{2\pi}\ln(10)A^2\sigma_m\frac{1}{m_p}e^{-y^2(m_p)}\left(\mathrm{erf}[y(m_p)] - \mathrm{erf}(y_{\rm min})\right). \tag{2.176}$$

Next we turn to the secondary mass function. Substituting equation (2.142) into equation (2.150) gives

$$\phi_s(m_s) = \frac{2}{1-\gamma}\int_{m_s}^{m_{\rm p,max}}\left(\frac{m_s}{m_p}\right)^{\gamma/(1-\gamma)}\phi(m_p)\phi\left(m_s\left(\frac{m_s}{m_p}\right)^{\gamma/(1-\gamma)}\right)dm_p, \tag{2.177}$$

where $m_{\rm p,max}$ is given by equation (2.154). The evaluation of ϕ for the modified secondary mass will include a term e^{-Y^2} in the exponential that will be of the form

$$Y = \frac{1}{\sqrt{2}\sigma_m}\left[\log\left(m_s\left(\frac{m_s}{m_p}\right)^{\gamma/(1-\gamma)}\right) - \log(m_0)\right] \tag{2.178}$$

$$= \frac{1}{1-\gamma}y_s - \frac{\gamma}{1-\gamma}y_p. \tag{2.179}$$

Using this and equation (2.171) we have for the secondary mass function

$$\phi_s(m_s) = \frac{2A^2}{(1-\gamma)m_s}\int_{m_s}^{m_{\rm p,max}(ms)}\exp\left[-\frac{1}{(1-\gamma)^2}\left((1-2\gamma+2\gamma^2)y_p^2 - 2\gamma y_s y_p + y_s^2\right)\right]\frac{dm_p}{m_p}. \tag{2.180}$$

In order to solve this integral we must complete the square inside the exponential. To simply the notation, define $\Gamma^2 = 1-2\gamma+2\gamma^2$. With this, the terms inside the exponential can be re-written as

$$-\frac{1}{(1-\gamma)^2}\left((1-2\gamma+2\gamma^2)y_p^2 - 2\gamma y_s y_p + y_s^2\right) = -\left(\frac{\Gamma}{1-\gamma}y_p - \frac{\gamma}{\Gamma(1-\gamma)}y_s\right)^2 - \frac{1}{\Gamma^2}y_s^2. \tag{2.181}$$

This can be plugged back into the mass function along with changing the variable of integration to y_p,

$$\phi_s(m_s) = \frac{\sqrt{8}\ln(10)A^2\sigma_m}{(1-\gamma)m_s}e^{-y_s^2/\Gamma^2}\int_{y_s}^{y_{\mathrm{p,max}}}\exp\left[-\left(\frac{\Gamma}{1-\gamma}y_p - \frac{\gamma}{\Gamma(1-\gamma)}y_s\right)^2\right]dy_p, \quad (2.182)$$

where $y_{\mathrm{p,max}} = y(m_{\mathrm{p,max}})$. The substitution

$$t(y_p) = \frac{\Gamma}{1-\gamma}y_p - \frac{\gamma}{\Gamma(1-\gamma)}y_s \quad (2.183)$$

now allows the integral to be solved, giving us

$$\phi_s(m_s) = \frac{\sqrt{2\pi}\ln(10)A^2\sigma_m}{\Gamma m_s}e^{-y^2(m_s)/\Gamma^2}\left[\mathrm{erf}(t(y_{\mathrm{p,max}})) - \mathrm{erf}(t(y_s))\right]. \quad (2.184)$$

Evaluating $t(y_s)$ finds

$$t(y_s) = \frac{1-2\gamma}{\Gamma}y(m_s). \quad (2.185)$$

Evaluating $t(y_{\mathrm{p,max}})$ requires returning to our expression for $m_{\mathrm{p,max}}$, equation (2.154). For the first find that

$$y(m_{\mathrm{p,max}}) = \frac{1}{\gamma}y_s - \frac{1-\gamma}{\gamma}y_{\mathrm{min}}, \quad (2.186)$$

and thus

$$t(y_{\mathrm{p,max}}) = \frac{1-\gamma}{\gamma\Gamma}y_s - \frac{\Gamma}{\gamma}y_{\mathrm{min}}. \quad (2.187)$$

For the second case we have more simply that $y_{\mathrm{p,max}} = y_{\mathrm{max}}$. Overall, therefore, we have

$$t(y_{\mathrm{p,max}}) = \begin{cases} \frac{1-\gamma}{\gamma\Gamma}y(m_s) - \frac{\Gamma}{\gamma}y(m_{\mathrm{min}}) & m_s \leq m_{\mathrm{min}}\left(\frac{m_{\mathrm{max}}}{m_{\mathrm{min}}}\right)^{\gamma} \\ \frac{\Gamma}{1-\gamma}y(m_{\mathrm{max}}) - \frac{\gamma}{\Gamma(1-\gamma)}y(m_s) & m_s \geq m_{\mathrm{min}}\left(\frac{m_{\mathrm{max}}}{m_{\mathrm{min}}}\right)^{\gamma} \end{cases}. \quad (2.188)$$

Finally we come to the mass ratio distribution. Similar to before, we use equation (2.157) in equation (2.158) to give

$$\phi_q(q) = \frac{2}{1-\gamma}q^{\gamma/(1-\gamma)}\int_{m_{\mathrm{p,min}}(q)}^{m_{\mathrm{max}}} m_p\phi(m_p)\phi\left(m_p q^{1/(1-\gamma)}\right)dm_p, \quad (2.189)$$

with $m_{\mathrm{p,min}}(q)$ found in equation (2.162). Plugging in the mass function, we will use the notation of $y_p = y(m_p)$ again, and define a similar quantity for the mass ratio,

$$y_q = \frac{\log(q)}{2\sigma_m(1-\gamma)}. \quad (2.190)$$

The modified secondary mass will again contain a term of the form e^{-Y^2} where this time

$$Y = \frac{1}{\sqrt{2}\sigma}\left[\log\left(m_p q^{1/(1-\gamma)}\right) - \log(m_0)\right]^2 \tag{2.191}$$

$$= y_p + \sqrt{2}y_q. \tag{2.192}$$

With these the mass ratio distribution can be found to be given by

$$\phi_q(q) = \frac{2A^2}{(1-\gamma)q}\int_{m_{\mathrm{p,min}}(q)}^{m_{\max}} \exp\left[-\left(y_p^2 + y_p^2 + 2\sqrt{2}y_p y_q + 2y_q^2\right)\right]\frac{dm_p}{m_p}. \tag{2.193}$$

Once more we transform the integral to be over y_p and complete the square in the exponential, resulting in

$$\phi_q(q) = \frac{2\sqrt{2}\ln(10)A^2\sigma_m}{(1-\gamma)q}e^{-y_q^2}\int_{y_{\mathrm{p,min}}}^{y_{\max}} e^{-(\sqrt{2}y_p + y_q)^2}dy_p. \tag{2.194}$$

Finally, we let $t(y_p) = \sqrt{2}y_p + y_q$ and solve the integral to find

$$\phi_q(q) = \frac{\sqrt{\pi}\ln(10)A^2\sigma_m}{(1-\gamma)q}e^{-y_q^2}\left[\mathrm{erf}(t(y_{\max}) - \mathrm{erf}(t(y_{\mathrm{p,min}}))\right]. \tag{2.195}$$

Evaluating $t(y_{\max}$ gives

$$t(y_{\max} = \sqrt{2}y(m_{\max}) + y_q, \tag{2.196}$$

and $t(y_{\mathrm{p,min}})$ is found to be

$$t(y_{\mathrm{p,min}}) = \sqrt{2}y(m_{min}) - y_q. \tag{2.197}$$

2.3.3 Optimization Procedure

With our simulation input parameters and methods for "observing" the results defined, we are now ready to begin evaluating which input parameters generate a cluster that evolves to best match the real one under consideration. Initially we set input parameters to be close to the present day values of their equivalent observed properties, though the results were usually not a good match. Changes to the inputs were initially guessed and their resemblance to the real cluster evaluated by eye.

Gradient Search

Once our computed cluster began to roughly resemble the real one, we changed to a more systematic gradient method for refining the initial state. Let $\boldsymbol{x}$ be the vector whose elements are the 9 input parameters defined in Section 2.2. Similarly, let $\boldsymbol{y}$ represent the 11 evolved cluster properties described in Section 2.3.1. This latter vector is, of course, a function of $\boldsymbol{x}$. To move $\boldsymbol{y}$ toward the values characterizing the real cluster today, we need to evaluate, in some sense, the gradient of this function.

A practical complication is one to which we alluded earlier. Even among evolutionary runs assuming an identical input vector $\boldsymbol{x}$, the resulting $\boldsymbol{y}$ differs because of the stochastic sampling of the various assumed distribution functions. In computing the gradient, we need to take a step size $\boldsymbol{h}$ large enough that the resulting change in $\boldsymbol{y}$ exceeds that due to this realization variance. We found that the prescription $\boldsymbol{h} = 0.5\boldsymbol{x}$ sufficed for this purpose (see Section 5.7 of Press et al. 2002, for a more rigorous justification).

For each $\boldsymbol{x}$, we first do 9 runs and average the result to obtain $\boldsymbol{y}(\boldsymbol{x})$. We then decrease, in turn, each element x_j to $x_j - h_j$, and find the average output of two runs at each decreased x_j-value. Similarly, we find the average result of two runs at each $x_j + h_j$. We thus establish the 11×9 matrix of derivatives $\mathcal{D}$, whose elements are

$$\mathcal{D}_{ij} \equiv \frac{y_i(x_j + h_j) - y_i(x_j - h_j)}{2h_j}. \tag{2.198}$$

The change in outputs for any subsequent input change $\Delta\boldsymbol{x}$ may then be approximated by

$$\Delta\boldsymbol{y} = \mathcal{D}\Delta\boldsymbol{x}. \tag{2.199}$$

Here, the vector $\Delta\boldsymbol{y}$ is taken to be the difference between the current $\boldsymbol{y}$-vector and that for the real cluster. We may evaluate the 9 elements Δx_j by solving the 11 linear equations summarized in (2.198). Since the system is overdetermined, we did a least-squares fit to find that set of Δx_j which best satisfied the equations.

Evaluating the Goodness of Fit

As we took a step in $\boldsymbol{x}$, we evaluated how close the resulting $\boldsymbol{y}$ was to $\boldsymbol{y}_c$, the aggregate properties of the actual cluster. We did a χ^2-test, where

$$\chi^2 = \sum_{i=1}^{11} \frac{(\langle y_i \rangle - y_{c,i})^2}{\sigma_i^2}. \tag{2.200}$$

Here, each $\langle y_i \rangle$ is the average y_i value, established by doing 9 runs with identical input values. The standard deviation σ_i includes errors in both the inferred real cluster properties and those generated by different statistical realizations of the input state:

$$\sigma_i^2 \equiv \sigma_{c,i}^2 + \sigma_{\langle y_i \rangle}^2. \tag{2.201}$$

The first righthand term is the real cluster variance from the uncertainties in the observations. The quantity $\sigma_{\langle y_i \rangle}^2$ is the error in the *mean* y_i. This error in the mean is related to $\sigma_{y,i}$, the variance in each individual y_i, by

$$\sigma_{\langle y_i \rangle}^2 \equiv \frac{1}{9}\sigma_{y,i}^2. \tag{2.202}$$

For the first few $\boldsymbol{x}$-steps, χ^2 declined, but then stalled. Beyond this point, the gradient method itself was clearly failing, as it indicated initial states which evolved to configurations

less resembling the real cluster. The difficulty was that the numerical derivatives of equation (2.198) were too crude to refine the initial state further. Refinements are possible in principle, but prohibitive computationally. After pushing the method to its limit, we were forced to stop the search before χ^2 reached a true minimum. We took the last state in the sequence where χ^2 declined to be the best-fit initial configuration.

Our final task was to assess the errors in all input parameters for this state. These should reflect uncertainties in properties of the actual cluster, as well as the variation in output parameters among different runs using identical inputs. This latter effect is quantified by the covariance matrix $\mathcal{Y}$, whose elements are

$$\mathcal{Y}_{ij} \equiv \langle (y_i - \langle y_i \rangle)\,(y_j - \langle y_j \rangle) \rangle\,. \tag{2.203}$$

The averaging here refers to different realizations using identical input parameters. Standard error propagation (Cowan 1998, Section 1.6) dictates that the known $\mathcal{Y}$ is related to $\mathcal{X}$, the desired covariance matrix of input parameters, through the derivative matrix and its transpose:

$$\mathcal{Y} = \mathcal{D}\mathcal{X}\mathcal{D}^{\mathrm{T}}. \tag{2.204}$$

We need to invert this equation to obtain $\mathcal{X}$. As noted, the input errors should also reflect the observational uncertainties in the real cluster. We do not know the correlation of these observational uncertainties. Thus, we use on the lefthand side of equation (2.204) a matrix $\mathcal{Y}'$, formed by adding $\sigma_{c,i}^2$ to each diagonal element $\mathcal{Y}_{ii}$.

Since $\mathcal{D}$ is not a square matrix, a standard inverse cannot be defined. However, the product $\mathcal{D}^{\mathrm{T}}\mathcal{D}$ *is* square, and so has an inverse, provided it is not singular. As discussed in Graybill (1983), this fact allows us to define the pseudo-inverse of $\mathcal{D}$:

$$\mathcal{D}^{+} \equiv \left(\mathcal{D}^{\mathrm{T}}\mathcal{D}\right)^{-1}\mathcal{D}^{\mathrm{T}}. \tag{2.205}$$

The term "pseudo-inverse" is appropriate since

$$\mathcal{D}^{+}\mathcal{D} = \left(\mathcal{D}^{\mathrm{T}}\mathcal{D}\right)^{-1}\mathcal{D}^{\mathrm{T}}\mathcal{D} = \mathcal{I}, \tag{2.206}$$

where $\mathcal{I}$ is the identity matrix. Taking the transpose of this last equation, we also find

$$\left(\mathcal{D}^{+}\mathcal{D}\right)^{\mathrm{T}} = \mathcal{D}^{\mathrm{T}}\left(\mathcal{D}^{+}\right)^{\mathrm{T}} = \mathcal{I}^{\mathrm{T}} = \mathcal{I}. \tag{2.207}$$

By employing equations (2.206) and (2.207), inversion of the modified equation (2.204) is straightforward:

$$\mathcal{D}^{+}\mathcal{Y}'\left(\mathcal{D}^{+}\right)^{\mathrm{T}} = \mathcal{D}^{+}\mathcal{D}\mathcal{X}\mathcal{D}^{\mathrm{T}}\left(\mathcal{D}^{+}\right)^{\mathrm{T}} = \mathcal{X}. \tag{2.208}$$

The uncertainties in the initial cluster parameters are then the standard deviations obtained from the diagonal elements of $\mathcal{X}$.

Chapter 3

The Pleiades

3.1 Observational Data

With the tools in hand to thoroughly study and model an open cluster, we now turn to applying these methods to actual data. We take as our first example one of the best-known and most well-studied clusters, the Pleiades. At a distance of 133 pc (the distance to the Pleiades has been an issue of some debate in recent years, see Soderblom et al. 2005, for a full discussion), it near enough to be able to observe the stars down to the stellar limit. The age of the Pleiades has been established from lithium dating as 125 Myr (Stauffer et al. 1998). This figure represents the main-sequence lifetime for a star of 4 $M_\odot$ (Siess et al. 2000), which we adopt as $m_{\max}$ for the mass function in our maximum likelihood analysis (see Section 2.1.1).

We take as our fundamental dataset the catalog of Stauffer et al. (2007); itself a compilation of many previous studies which determine high probability memberships, as gauged by colors, radial velocities, and proper motions (see, e.g., Deacon & Hambly (2004) for one such proper motion study.) Figure 3.1 is a dereddened $(I, I-K)$ color-magnitude diagram for this catalog. The lower open circles correspond to probable brown dwarfs; we exclude such objects from our study. Most brown dwarfs are too faint to be observed, and the population, in any case,is more sparsely sampled. (The magnitude cutoffs corresponding to a 0.08 $M_\odot$ object are $M_I = 12$ mag and $M_K = 9$ mag.) After also excluding the 11 bright, post-main-sequence stars, shown here as large, filled circles, we have a total sample size of $n_{\rm tot} = 1245$.

The solid curve near the lower boundary of the stellar distribution is a combination of the theoretical zero-age main sequence for $m_* > 1$ (Siess et al. 2000) and, for lower-mass stars, a pre-main-sequence isochrone (Baraffe et al. 1998). Both theoretical results are presented in magnitudes. We have applied corrections to the theoretical K-band magnitudes to make them consistent with the 2MASS K_s-band used in Stauffer's catalog. See Cohen et al. (2003) for this transformation. We further ignore the effect of differential reddening across the cluster. Stauffer et al. (2007) adjusted individually the fluxes from sources in

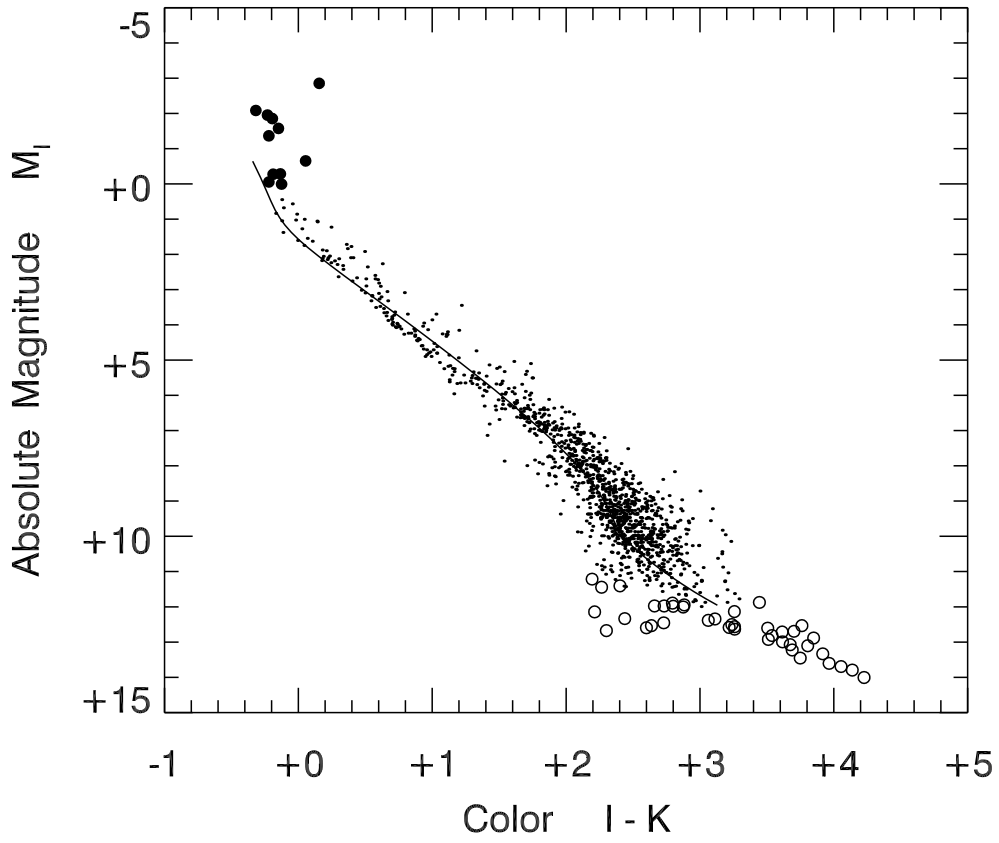

Figure 3.1: Near-infrared color-magnitude diagram for the Pleiades. Small dots represent the 1245 stars in our sample. Open circles are the 41 likely sub-stellar objects which have been removed from the sample. Filled circles are the 11 brightest stars, which are likely post-main-sequence objects. The 125 Myr isochrone for stars with masses between 0.08 and 4.0 $M_\odot$ is shown as the smooth, solid curve.

especially obscured regions, bringing their effective extinction to the observed average A_V of 0.12 mag. We therefore constructed Figure 1 by applying uniformly the corresponding A_I- and A_K-values of 0.06 mag and 0.01 mag, respectively. These values were computed using the reddening law of Rieke & Lebofsky (1985).

The quantities σ_I and σ_K used to compute the response matrix in equation (2.14) are the standard deviations of the photometric measurements. According to Stauffer et al. (2007), the average standard deviation in the I-band is about 0.15 mag. Figure 3.2, constructed from Table 2 of Stauffer et al. (2007), shows that σ_K is generally lower, and rises steeply with M_K for the dimmest sources.[1] The two branches of the curve presumably represent the results from two different observations. We do a polynomial fit to the upper, majority, branch, and thus have an explicit expression for $\sigma_K(M_K)$.

3.2 The Pleiades Today

3.2.1 Empirical Mass Distributions

We now present the results of applying our maximum likelihood analysis to the Pleiades itself, i.e., to the I- and K-magnitudes of 1245 sources from our catalog. Our best-fit binary fraction was $b = 0.68 \pm 0.02$, while the correlation coefficient was $c = 0.36 \pm 0.06$. (These and other uncertainties represent only random statistical error, and do not include systematic effects; see Section 3.2.5.) We will discuss the implications of these findings in the following section. First, we examine the global distribution of stellar mass.

The data points in Figure 3.3 are the best-fit values of each $y_i/\Delta m_i$ (see equation (2.5)). As in Figure 2.2, these points are a discrete representation of the single-star mass function $\phi(m)$. The large error bars on the two points at highest mass are due to the small number of sources gauged to be in the respective bins. The smooth, solid curve in Figure 3.3 is a lognormal mass function that best matches the empirical $\boldsymbol{y}$. Referring again to equation (2.70), we find that $m_0 = 0.20 \pm 0.04$ and $\sigma_m = 0.38 \pm 0.02$. The presence of a finite binary correlation affects both estimates. Judging from Figure 2.5, our m_0 is overestimated by about 0.06, while σ_m should be raised by 0.08.

Each of our mass bins has contributions from both the primary and secondary components of binary pairs, as quantified by equation (2.4). Integrating the full stellar mass probability $\Phi(m_p, m_s)$ over all secondary masses, we obtain $\phi_p(m_p)$, the probability distribution of primary masses:

$$\phi_p(m_p) = \int_0^{m_p} dm_s \Phi(m_p, m_s). \tag{3.1}$$

[1] This rise in σ_K occurs because the observed K-magnitudes are approaching the sensitivity limit of the observations. Many of the I-band measurements come from POSS II plates, for which the limit is 18.5 mag (Hambly et al. 1993). Another large source of data was the observations of Pinfield et al. (2000), whose limiting magnitude was 19.7 mag. Our lower cutoff for brown dwarfs corresponds to an apparent I-magnitude of 17.7 mag, so the rise in our σ_I should be modest.

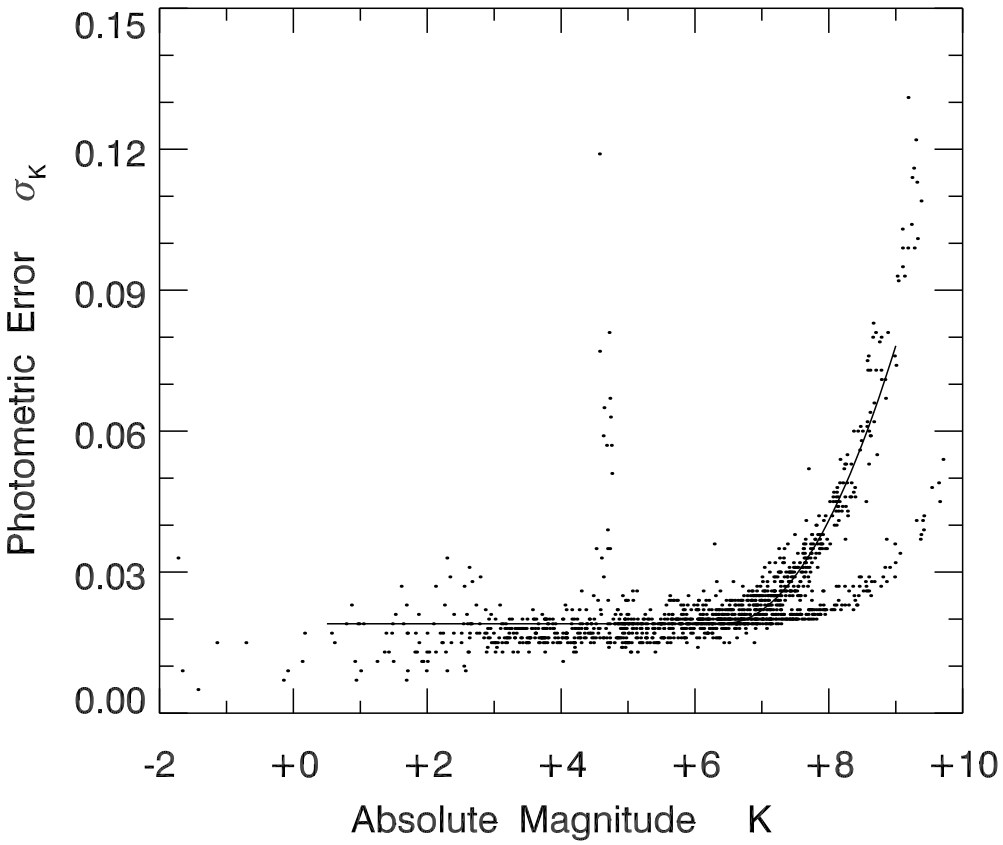

Figure 3.2: Observational error in the K-band measurements as a function of absolute magnitude for all 1417 stars in the catalog of Stauffer et al. (2007). The smooth curve is the approximate fit used in our maximum likelihood analysis.

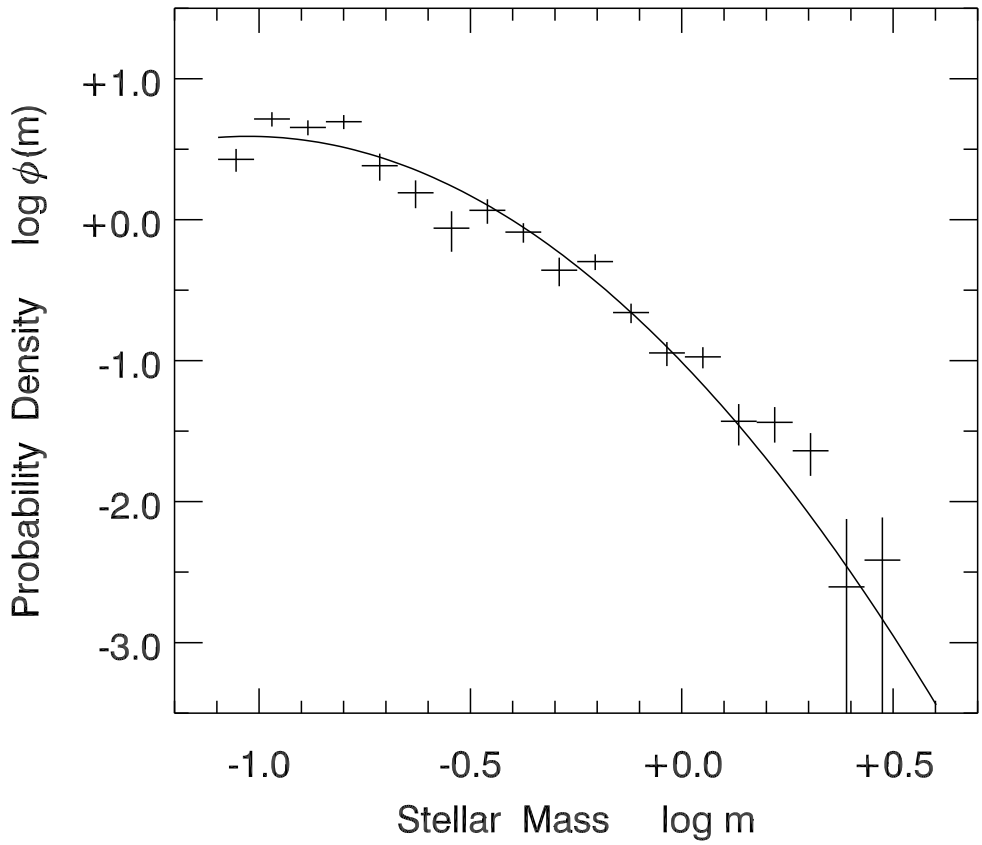

Figure 3.3: Best-fit single star probability density $\phi(m)$ for the Pleiades. Actual bin values $y_i/\Delta m_i$ are shown with associated errors. The smooth curve is a lognormal approximation to the results.

Note that this distribution includes the possibility that the star is single ($m_s = 0$).

The solid curve in Figure 3.4 is a lognormal fit to the empirical $\phi_p(m_p)$. Shown for comparison as a dashed curve is the fit for $\phi(m)$ from Figure 3.3. Relative to the latter function, the primary distribution falls off at lower masses. This falloff simply reflects the fact that less massive objects are more likely to be part of a binary containing a higher-mass star, and thus to be labeled as "secondaries."[2] In any event, we now see why the peak of $\phi_p(m_p)$, $m_0 = 0.27 \pm 0.02$, is elevated with respect to the peak of $\phi(m)$. Similarly, the primary distribution is also slightly narrower than the single-star mass function, with $\sigma_m = 0.35 \pm 0.01$.

The parameters of our lognormal approximation to $\phi_p(m_p)$ may be compared to those of Moraux et al. (2004). These authors fit the entire mass function. Since, however, they did not account for binarity, their results are more closely analogous to our primary distribution. Their best-fit m_0 of 0.25 is close to ours, while their σ_m of 0.52 is higher, mostly because of their inclusion of the highest-mass members. These parameters are also close to those given by Chabrier (2003) in his lognormal fit to the field-star initial mass function ($m_0 = 0.22$, $\sigma_m = 0.57$).

In Figure 3.5, we compare our single-star distribution $\phi(m)$ to the field-star initial mass function (dashed curve). The latter, which has been raised in the figure for clarity, is taken from Kroupa (2001), who did correct for binarity. It is apparent that $\phi(m)$ itself veers away from the IMF for both low- and high-mass objects. When these are added in, the resemblance improves. The open circles in Figure 3.5 are Pleiades low-mass stars and brown dwarfs found by Bihain et al. (2006). We have normalized their data, taken from a limited area of the cluster, so that their total number of stars matches ours within the overlapping mass range. No such normalization was necessary for the 11 B-type stars (filled circles), which are from the catalog of Stauffer et al. (2007) but not included in our maximum likelihood analysis. Adding both these groups not only improves the match to the IMF, but also reveals a gap in the stellar distribution between about 2 and 5 $M_\odot$. A similar gap is seen in the Pleiades mass function of Moraux et al. (2004, see their Figure 1).

Our estimate for the total cluster mass, based solely on the 1245 catalog sources, is 738 $M_\odot$, with a 4% uncertainty. Adding in the brightest stars brings this total to 820 $M_\odot$, with the same relative error. Tests with synthetic data indicate that the systematic bias due to binary correlation raises this figure by roughly 50 $M_\odot$, to 870 $M_\odot$. Addition of the brown dwarfs would cause a further, relatively small, increase. For comparison, Pinfield et al. (1998) found 735 $M_\odot$ in stars, and an upper limit of 131 $M_\odot$ for the brown dwarf contribution. Raboud & Mermilliod (1998) used the virial theorem to estimate a total mass of 720 $M_\odot$, with a 28% uncertainty. Direct integration of their mass function gave 950 $M_\odot$, with an 18% fractional error.

[2]We may similarly calculate a secondary mass distribution $\phi_s(m_s)$ by integrating $\Phi(m_p, m_s)$ over m_p, from m_s to $m_{\max}$. The function ϕ_s has an excess of low-mass stars and drops very steeply at high masses, as most such objects are primaries.

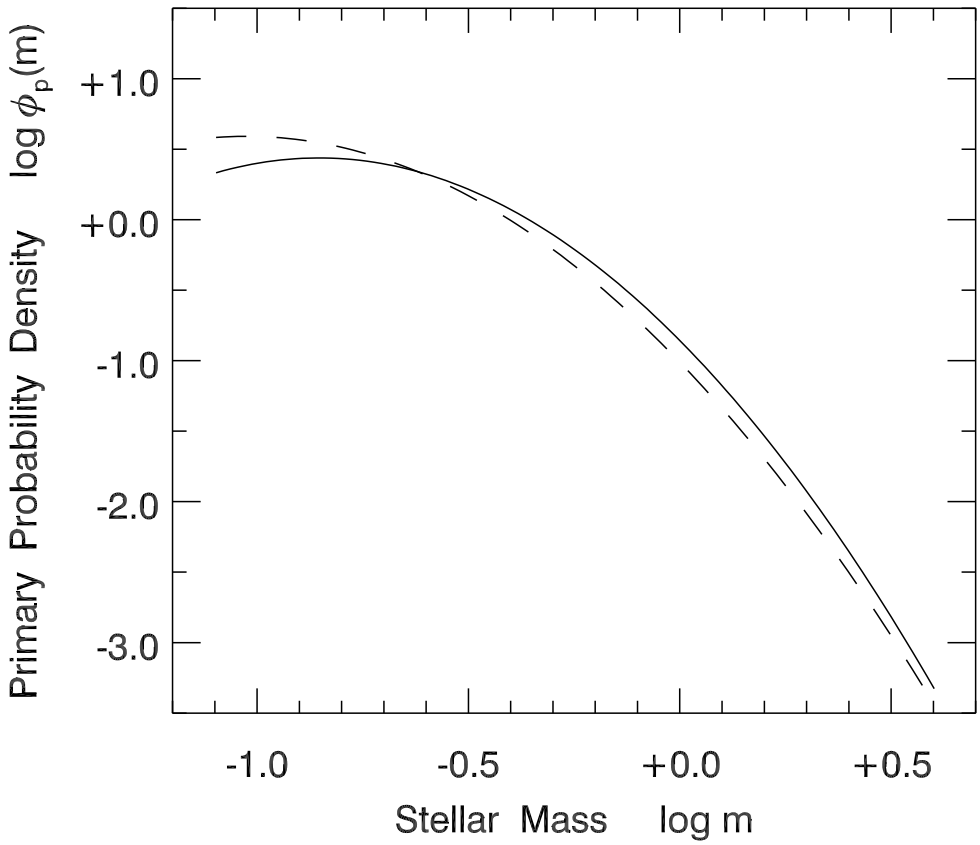

Figure 3.4: Comparison of lognormal fits to the primary probability density $\log \phi_p(m_p)$ (solid curve) and the single star probability density $\log \phi(m)$ (dashed curve). The primary function peaks at larger mass and has a smaller width. Note that $\phi_p(m)$ includes single stars.

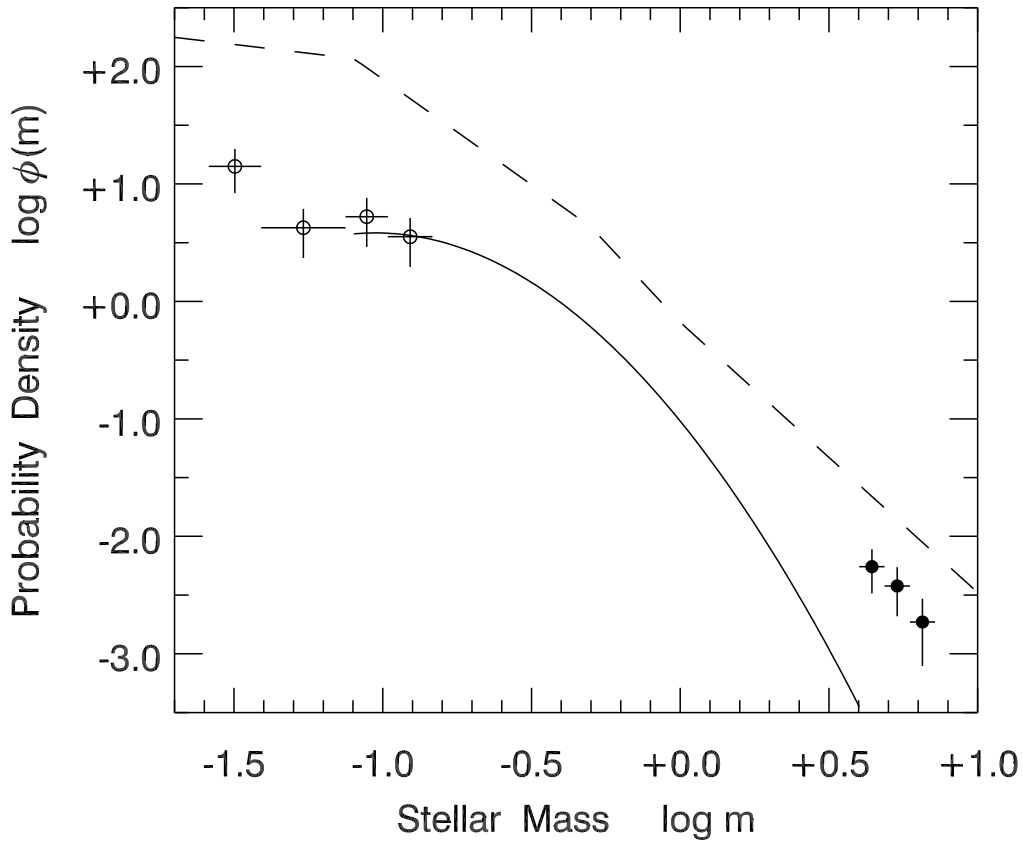

Figure 3.5: Comparison of the Pleiades single star probability density to the field-star initial mass function of Kroupa (2001), where the latter has been shifted upward for clarity. Shown here is the lognormal approximation to $\log \phi(m)$ (solid curve), augmented with the data of Bihain et al. (2006) for low-mass members and brown dwarfs (open circles) and our 11 brightest, post-main-sequence stars (filled circles).

3.2.2 Binarity

The global binary fraction, $b = 0.68$, obtained in our analysis represents most, but not all, of the full binary population. Omitted here are spatially resolved systems. For these, the primary and secondary appear as separate sources in the catalog of Stauffer et al. (2007). Counting resolved pairs raises the total fraction to about 76%, as we now show.

The smallest angular separation between stars in the catalog is $10''$. At the Pleiades distance of 133 pc, the corresponding physical separation is 1400 AU. An edge-on circular binary of exactly this orbital diameter will still be unresolved, since the components spend most of their time closer together. The true minimum separation in this case is 2200 AU. Here, we have divided 1400 AU by $2/\pi$, which is the average of $|\sin\theta|$, for θ randomly distributed between 0 and 2π.

Of course, only a relatively small fraction of binaries have separations that exceed 2200 AU. The average total mass of our unresolved systems is 0.71 $M_\odot$. A binary of that total mass and a 2200 AU diameter has a period of 1.2×10^5 yr. What fraction of binaries have even longer periods? Our average *primary* mass is 0.46 $M_\odot$, corresponding to a spectral type of M1. Fischer & Marcy (1992) studied the period distribution of binaries containing M-type primaries. They claimed that this distribution was indistinguishable from that found by Duquennoy & Mayor (1991) for G-type primaries. In this latter sample, 11% of the systems had periods greater than our limiting value. If the Pleiades periods are similarly distributed, then the total fraction of binaries - both resolved and unresolved - becomes $0.66/(1 - 0.11) = 0.76$.

Even without this augmentation, our total binary fraction appears to be inconsistent with the available direct observations of the Pleiades. Thus, Bouvier et al. (1997) found visual pairs with periods between 40 and 3.4×10^4 yr. Using the period distribution of Duquennoy & Mayor (1991) to extrapolate their observed binary fraction of 28% yields a total fraction of 60%. Mermilliod et al. (1992) observed spectroscopic pairs with periods under 3 yr. A similar exercise again yields 60%. We note, however, that this ostensible concurrence of results is based on very broad extrapolations from limited data. (See Figure 4 of Bouvier et al. (1997).)

Our derived binary fraction also exceeds that found in the field-star population. Duquennoy & Mayor (1991) found that 57% of G stars are the primaries of binary or higher-order systems. Note that our b represents the total probability that a star is in a binary, whether as the primary or secondary component. Since G stars are rarely secondaries, the comparison with Duquennoy & Mayor (1991) is appropriate. On the other hand, M stars *are* frequently secondaries, so we would expect the fraction of binaries with M-type primaries to be reduced. Lada (2006) has found that only 25% of M-stars are the primary components of binaries. Our own analysis yields a binary fraction of 45% for M-star primaries, still in excess of the field-star result.

If our finding of a relatively high binary fraction proves robust, it may provide a clue to the progenitor state of the Pleiades and other open clusters. A similar statement applies to the correlation between component masses within binaries. Our adopted method of gauging

this correlation - inserting a fraction of equal-mass pairs in the mass function - is admittedly crude. Nevertheless, the strong result ($c = 0.36 \pm 0.06$) is significant. Referring back to Figure 2.4, we find that the Pleiades correlation is equivalent to setting γ equal to about 0.65 in the alternative description of equation (2.71). Whatever the origin of the Pleiades binaries, the primaries and secondaries were not formed by completely independent processes.

3.2.3 Number and Mass Profiles

We now employ the procedure outlined in Section 2.1.2 to investigate both the surface and volumetric density as a function of the projected distance from the cluster center. The filled circles in Figure 3.6, along with the associated error bars, represent the surface number density of sources, measured in pc^{-2}. The solid curve is a density profile using the empirical prescription of King (1962). Here, the core radius is 2.1 pc, while the tidal radius is 19 pc. For comparison, Adams et al. (2001) also fit the surface number density profile of their low-mass stars to a King model, with a core radius of 2.3-3.0 pc. Our profile is also at least roughly consistent with the cumulative number distribution displayed by Raboud & Mermilliod (1998). Our best-fit tidal radius is slightly larger than the 17 pc cited by these authors.

The surface mass density is plotted in an analogous fashion, again as a function of the projected radius. We show both the data points (small open circles) and, as the dashed curve, the best-fit King model. Here, the core radius is 1.3 pc, and the tidal radius is 18 pc. Note that the mass density profile falls off more steeply than the number density. Thus, stars near the center are abnormally massive, a trend we shall explore more extensively below.

Figure 3.7 displays the corresponding volumetric densities. As we indicated, the deconvolution from surface profiles assumes spherical symmetry (see Section 2.1.2). In fact, the Pleiades is slightly asymmetric, with a projected axis ratio of 1.2:1 (Raboud & Mermilliod 1998). This ellipticity is thought to stem from the tidal component of the Galactic gravitational field (Wielen 1974). Under the spherical assumption, the filled circles and solid, smooth curve show the number density. Here, the King model is the same used for the surface number density in Figure 3.6, but deprojected into three-dimensional space.

Figure 3.7 also shows, as the small open circles and dashed curve, the mass density as a function of spherical radius. Again, the King model here is the deprojected version of that from Figure 3.6. The relatively rapid falloff in the mass, as opposed to the number, density is another sign of the tendency for more massive stars to crowd toward the center.

The information we used in obtaining these profiles also gives us the spatial variation of the binary fraction b. That is, we first used equation (2.40) to obtain $\boldsymbol{\mu}^r$, the predicted mass distribution in each radial annulus. Recall that the distribution refers to both primaries and secondaries, as well as single stars. The binary fraction can thus be computed locally. To within our uncertainty, about ± 0.05 at each radial bin, we find no variation of b across the cluster.

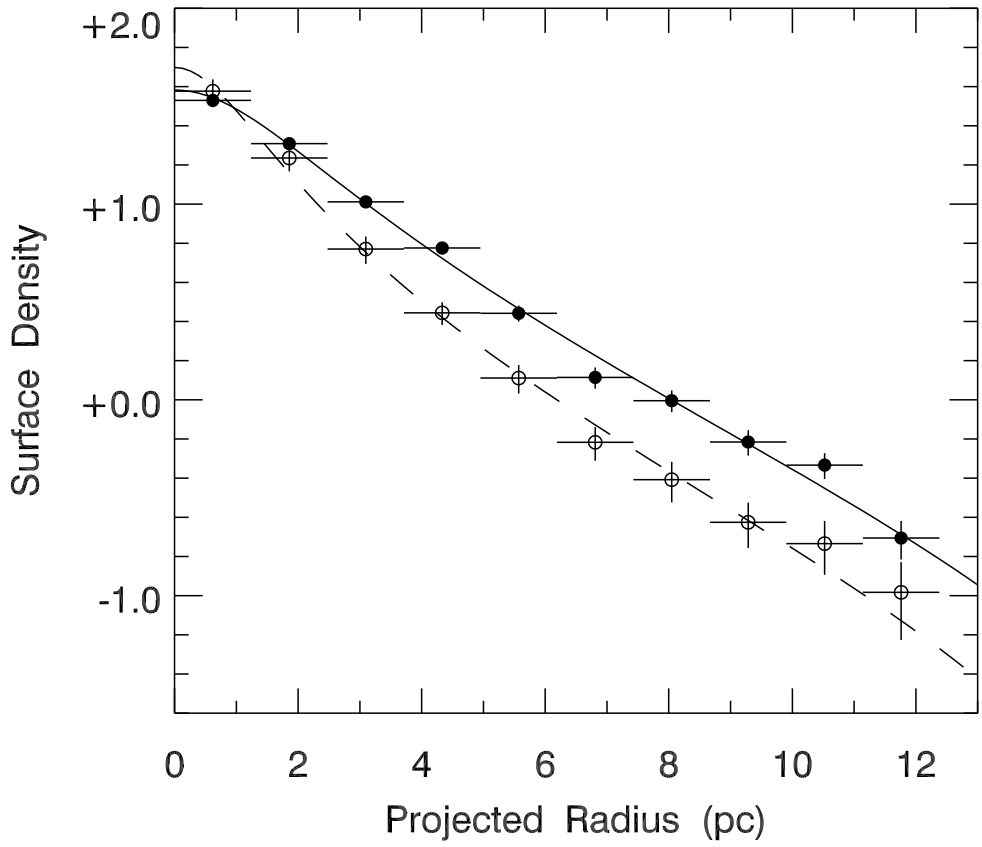

Figure 3.6: Surface density distribution in the Pleiades. The filled circles represent the surface number density (pc^{-2}), displayed on a logarithmic scale. Open circles are the mass density, in $M_\odot$ pc^{-2}. The solid and dashed smooth curves are King model fits.

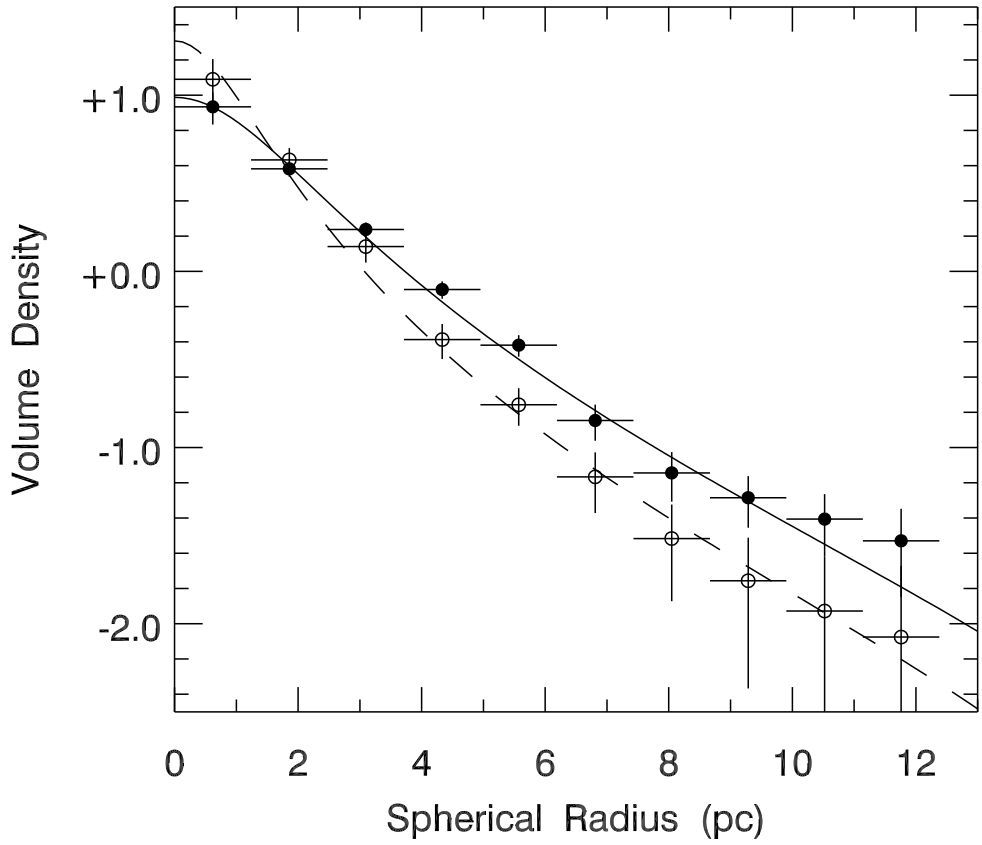

Figure 3.7: Volume density profiles. The filled circles represent the number density (pc^{-3}), again displayed logarithmically. Open circles are the mass density, in $M_\odot$ pc^{-3}. The solid and dashed smooth curves are the same King model fits as in Figure 3.6, but now deprojected into three-dimensional space.

3.2.4 Mass Segregation

We have mentioned, in a qualitative manner, that more massive cluster members tend to reside nearer the center. In Figure 3.8, we explicitly show this trend. Here, we plot $\langle m_p + m_s \rangle$, the average system mass (primary plus secondary) as a function of the projected cluster radius. It is apparent that $\langle m_p + m_s \rangle$ monotonically falls out to about 4 pc. Beyond that point, the average mass is roughly constant.

The pattern here is consistent with mass segregation, but is not a clear demonstration of that effect. The problem is that Figure 3.8 gives no indication of the relative populations at different annuli. If the outer ones are occupied by only a small fraction of the cluster, is mass segregation present? To gauge any variation in the mass distribution of stars, that distribution must be calculated over an adequate sample size.

Previous authors have also claimed evidence of mass segregation, using various criteria. Adams et al. (2001) looked at the distribution of surface and volumetric number densities for a number of different mass bins. Raboud & Mermilliod (1998) divided the population by magnitude into relatively bright and faint stars. They calculated the cumulative number as a function of radius for both groups, and found the bright stars to be more centrally concentrated. Finally, Pinfield et al. (1998) fit King profiles to the surface density of various mass bins. As the average mass increases, the core radius shrinks.

Figure 3.9 gives a simpler and more clear-cut demonstration of the effect. Here, we consider f_N, the number of sources enclosed in a given projected radius, divided by the total number of sources in the cluster. We also consider f_M, the analogous fractional mass inside any projected radius. The figure then plots f_M versus f_N. In the absence of mass segregation, f_M would equal f_N at each annulus. This hypothetical situation is illustrated by the dotted diagonal line. From this we can compute the Gini coefficient (see Section 2.1.3). For the Pleiades, we find that $G = 0.20 \pm 0.02$.

It is possible, at least in principle, that this effect is due entirely to a few exceptionally massive stars located near the center. In fact, this is *not* the case. We have artificially removed the 11 brightest sources (all late-B stars) and recalculated f_M versus f_N. The result is shown by the dashed curve in Figure 3.9. While the rise above the diagonal is diminished, it is still present. That is, the intermediate-mass population exhibits segregation, as well.

An interesting contrast is presented by another populous group, the Orion Nebula Cluster (ONC). The distribution of stellar masses in this far younger system was recently studied by Huff & Stahler (2006). Figure 2 in that paper compares the stellar populations in the inner and outer halves of the cluster.[3] Apart from a few high-mass objects, the two populations are essential identical.

We may also construct an $f_M - f_N$ curve for the ONC, as shown here in Figure 3.10. The solid curve again lies well above the fiducial diagonal, ostensibly indicating mass segregation. However, removal of just the four Trapezium stars gives a dramatically different result (dashed curve) that is virtually indistinguishable from the diagonal. All stars except this tiny subset are similarly distributed. The cluster is too young to have undergone true

[3]Note that the axis labels in Figure 2 of Huff & Stahler (2006) were inadvertently switched.

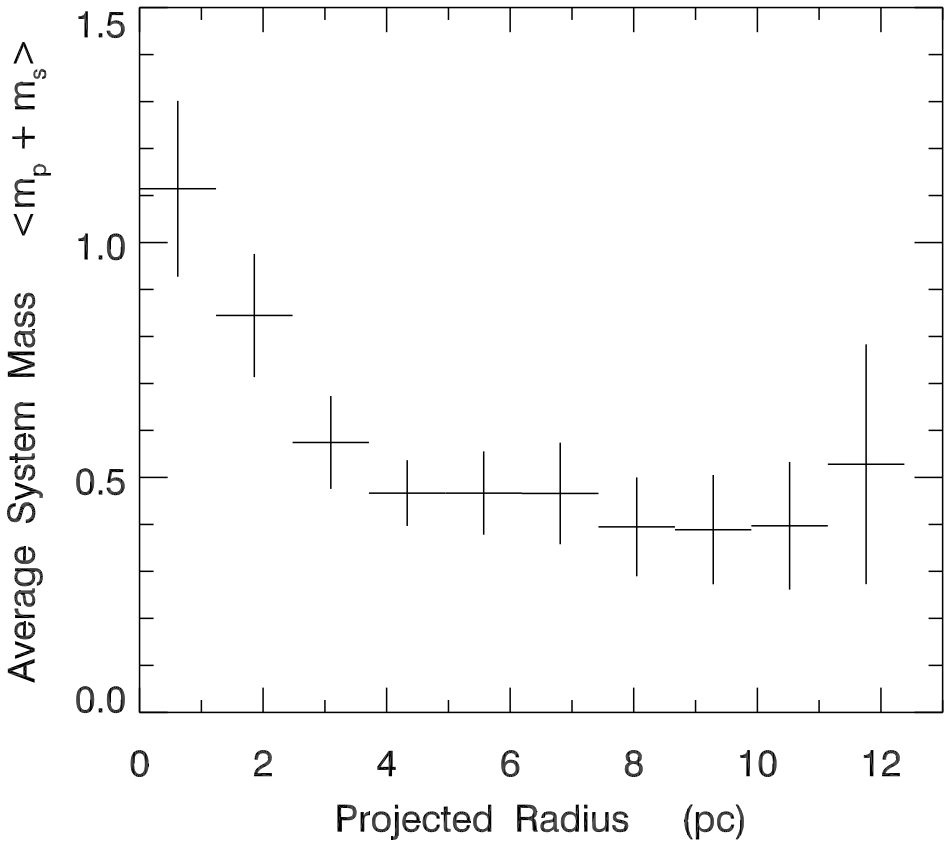

Figure 3.8: Average system mass (primaries plus secondaries) as a function of projected cluster radius. The bins here have constant radial width.

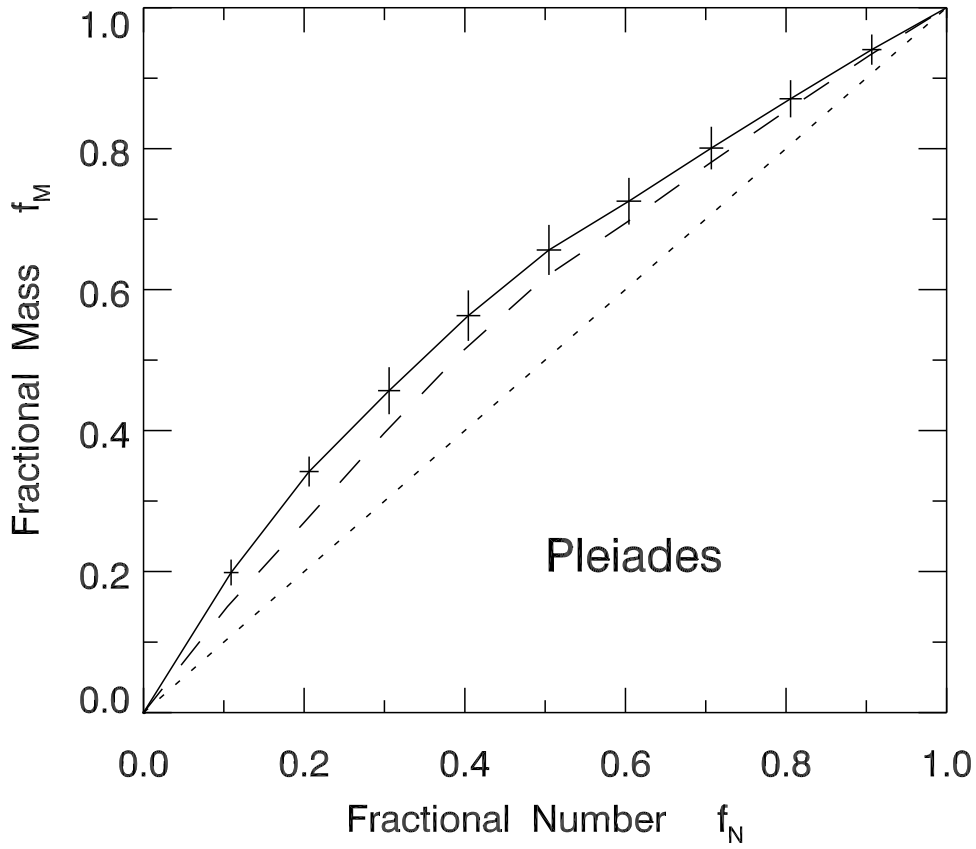

Figure 3.9: Fractional mass versus fractional number for the Pleiades. The data points and error bars, along with the solid curve, utilize all sources in the catalog of Stauffer et al. (2007). The dashed curve shows the result when the 11 brightest stars are removed. In both cases, the radial bins contain roughly equal numbers of stars. Finally, the dotted diagonal is the hypothetical result for no mass segregation.

mass segregation, a conclusion drawn previously from N-body simulations (Bonnell & Davies 1998). The Trapezium represents a special population, one that probably formed just prior to cloud dispersal (Huff & Stahler 2007).

3.2.5 Potential Systematic Uncertainties

We have applied a versatile statistical tool, the maximum likelihood technique, to assess the distribution of stellar mass and the incidence of binaries in the Pleiades. We began with a near-infrared catalog of cluster members. Our basic assumption was that all cluster members share the same evolutionary age, and that any dispersion in the color-magnitude plane stems from binarity and random photometric errors. We were then able to infer the most probable distribution of masses, both for the cluster as a whole, and as a function of distance from its center. Finally, we introduced a simple method for gauging the degree of mass segregation in the cluster.

One possible source of error is that we have ignored the population of substellar objects that surely does exist in the cluster. In particular, the lowest mass stars in our system are preferentially single due to not allowing yet-lower mass objects to exist which could be their secondaries. Our measured binary fraction, however, will not be significantly affected by this. The reason is that our method will model a combination of single and nearly-equal mass binaries for these faint systems in order to best fit the observed photometric distribution. It will thus find that low-mass binaries are required, even if it does not properly model the component masses. However, there will still be some under-estimation of low mass-binary systems.

Figure 3.11 shows that this effect is quite small, however. The histogram in the plot gives the K-band luminosity function for the observed Pleaides. The data points are the results predicted by our $\phi(m)$ (the data points in figure 3.3), b, and c. Although our results are indeed somewhat low at the faint end, the effect is small, and our results reproduce the observed luminosity function quite well. Since none of our results are dependent on the few smallest mass bins alone, we conclude that this produces no significant systematic error.

One of our surprising results is the relatively high fraction of binaries. We estimate that 68% of all systems in the cluster are unresolved binaries; this figure climbs to about 76% if resolved pairs are included. These fractions are significantly higher than the accepted field-star result, so we should scrutinize them carefully. Could they stem from an underestimate of the photometric error at faint magnitudes? Since the error in I is greater than K, we artificially increased the dispersion σ_I. We kept σ_I at 0.15 mag until $M_I = 9.5$ mag, below which we increased it linearly, reaching $\sigma_I = 0.20$ mag at $M_I = 12$ mag. After redoing the maximum likelihood analysis, the global binary fraction b for unresolved pairs is unchanged.

Another potential difficulty is our neglect of the physical thickness of the cluster. We have assigned all members a distance of 133 pc, although there will naturally be some variation. However, this effect is also relatively small. From Section 3.2.3, the volumetric number density falls off with radius approximately as a King model with core and tidal radii of 2.1 and 19 pc, respectively. Consider the front half of a spherical cluster with such a

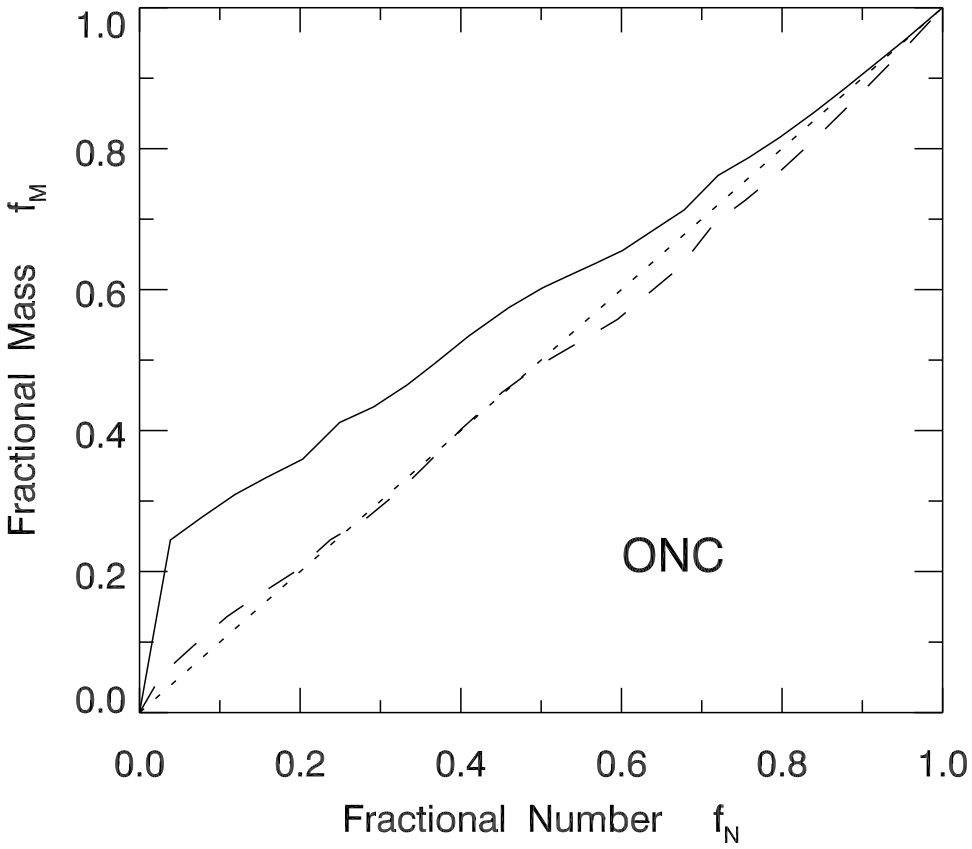

Figure 3.10: Fractional mass versus fractional number for the ONC. The solid curve was computed using all the ONC sources analyzed by Huff & Stahler (2006). The dashed curve shows the result if only the four Trapezium stars are removed. As in Figure 3.9, the radial bins contain roughly equal numbers of stars. The dotted diagonal again shows the hypothetical condition of no mass segregation.

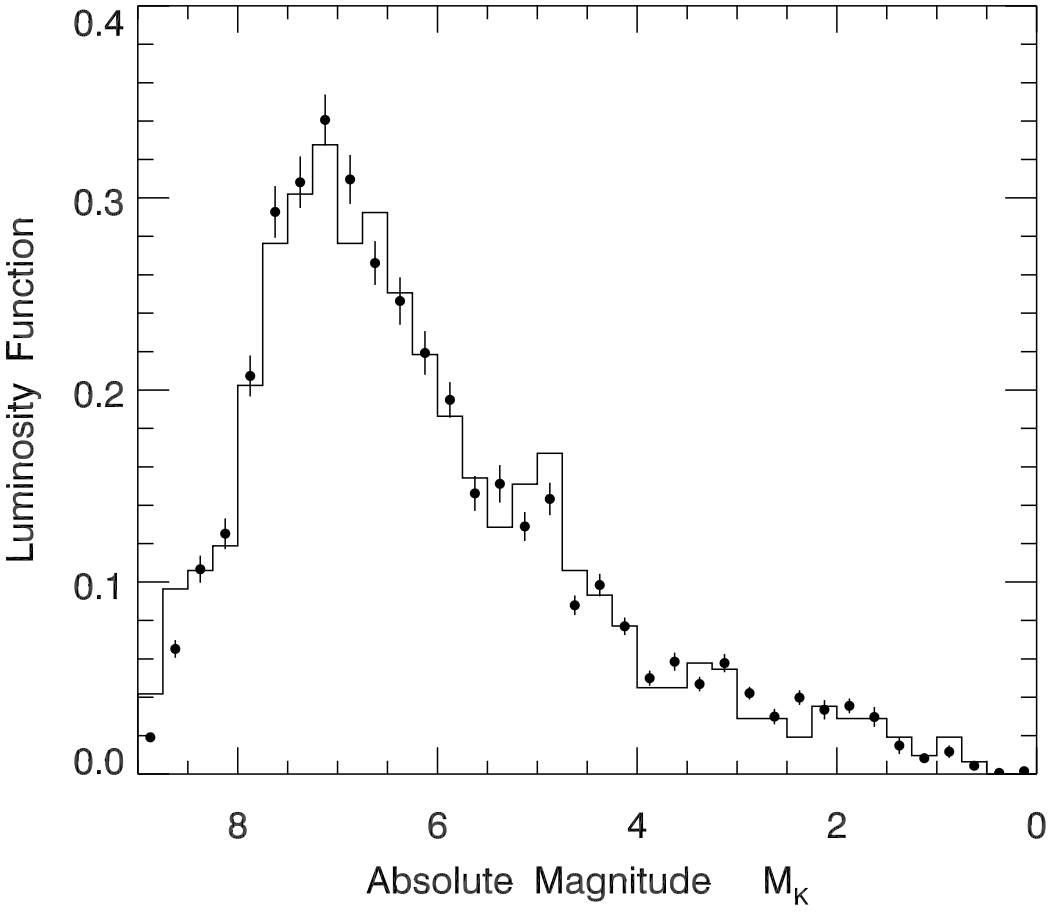

Figure 3.11: Observed and predicted K-band luminosity function. The histogram shows the observed M_K distribution for our Pleiades sources. The data points are the predicted results from the mass function found by our maximum likelihood analysis. Note the number of sources in the very faintest bins is underestimated due to our neglect of brown dwarves.

density distribution. It may readily be shown that the mean distance from the plane of the sky of any cluster member is $d = 2.6$ pc. For a cluster at mean distance D, the induced magnitude spread is $5\log[(D+d)/D]$, which is 0.04 mag in our case. Although the actual spread in magnitudes is not Gaussian, we have added this figure in quadrature to both σ_I and σ_K, and rerun the analysis. Again, the binarity is unaffected.

The errors due to both photometry and finite cluster thickness induce a symmetric spread in stellar magnitudes. That is, they scatter as many sources below the fiducial isochrone as above it. Thus, they cannot reduce the estimated binarity, which stems from an excess of stars above the isochrone. One systematic error that *would* affect b is an overestimation of the cluster distance. If D were lowered, the absolute magnitudes of all sources would decrease equally, as would the inferred b-value. Quantitatively, the distance would have to decrease by about 15 pc to bring the binary fraction down to the field-star result for G-dwarf primaries. An error of this size for the average distance is excluded by current observations, for which the estimated uncertainty is only 1 pc (Soderblom et al. 2005).

Since our method relies solely on photometry to assess binarity, we cannot distinguish between physically linked pairs and chance alignments. As mentioned in Section 3.2.2, the resolution limit of our data is $10''$, or $\Delta r_0 = 1400$ AU at the distance of the Pleiades. Consider a star at a radius r from the cluster center. Its average number of neighbors within Δr_0 is $\pi \Delta r_0^2 n_s(r)$, where $n_s(r)$ is the projected surface number density of the cluster. Since each ring of width dr contains $2\pi n_s r dr$ stars, integration over all members yields the total number of chance alignments:

$$N_{\rm chance} = 2\pi^2 \Delta r_0^2 \int_0^R n_s^2(r) r dr, \tag{3.2}$$

where R is the cluster's outer radius, Using $n_s(r)$ from Figure 3.6, we find $N_{\rm chance} = 2.4$. Thus, chance alignments have no quantitative impact.

Yet another source of systematic error is the cluster age. We have adopted the lithium-based figure of 125 Myr from Stauffer et al. (1998). Earlier estimates, using the main-sequence turnoff, yielded a range of answers. For example, Meynet et al. (1993) found 100 Myr. Even this minor reduction affects our results, since it lifts the low-mass end of the isochrone toward higher luminosity. For an age of 100 Myr, our analysis gives $b = 0.57 \pm 0.02$ and $c = 0.28 \pm 0.06$. The binary fraction is augmented to 0.64 when we include resolved pairs. From Figure 3 of Stauffer et al. (1998), a 100 Myr age corresponds to a lithium edge at $M_I = 11.7$ mag, or $I = 17.3$ mag at the Pleiades distance. Such a result seems incompatible with the lithium data shown in their Figure 2, but the total number of observations is relatively small.

We conclude that the enhanced binarity is a real effect. What this fact tells us about the origin of open clusters remains to be seen. Our next step in addressing this basic issue is to try and account theoretically for the empirical properties just obtained through our statistical analysis. We will ascertain, using direct numerical simulations, the range of initial states that can relax dynamically to the present-day Pleiades.

Table 3.1: Initial Pleiades Parameters

Symbol	Definition	Reference	Optimal Value
n	Polytropic index	Section 2.2.1	3.0 ± 1.3
$N_{\rm tot}$	Number of stellar systems	Section 2.2.1	1215 ± 59
r_v	Virial radius	Section 2.2.1	4.0 ± 0.9 pc
m_0	Centroid of mass function	Section 2.2.2	0.12 ± 0.04 $M_\odot$
σ_m	Width of mass function	Section 2.2.2	0.33 ± 0.06
α	Exponent in mass function	Section 2.2.2	-2.20 ± 0.04
b	Fraction of binaries	Section 2.2.2	0.95 ± 0.08
γ	Mass correlation in binaries	Section 2.2.2	0.73 ± 0.09
β	Degree of mass segregation	Section 2.2.2	0.5 ± 0.3

3.3 Simulating the Seven Sisters

We are now ready to take the second step and begin to model the evolution of the Pleiades. Following the proceedure outlines in Section 2.3, we find the initial state that evolves to best match the present-day cluster. This initial state is defined by the nine parameters in Table 3.1 (which gives references to the sections in which the parameters were originally discussed). Anticipating the results detailed below, the last column gives the numerical value of each parameter in the optimal configuration. We also list the associated uncertainties, computed as in Section 2.3.3.

Table 3.2 displays the quantities evaluated for the evolved cluster (see Section 2.3.1), as well as the corresponding figures in the actual Pleiades. Notice that m_0 and σ_m for the mass function do not match those in the initial state, as given in Table 3.1. This discrepancy arises partly from real changes of the stellar masses, but even more from our adoption of a simple lognormal when fitting the evolved cluster. The tabulated errors for the calculated quantities were obtained by running 25 simulations, all with identical input parameters. The errors represent the standard deviations for each quantity in the evolved cluster, due solely to differing realizations of the initial state. N_s and N_4 are assumed to be Poisson-distributed, so that the errors are $\sqrt{N_s}$ and $\sqrt{N_4}$, respectively, for the Pleiades values.

3.3.1 The Initial State

Global and Radial Properties

The polytropic index n is about 3, corresponding to a volumetric, center-to-average, number density contrast of 54.[4] This particular polytrope closely resembles a King (1966) model with $W_0 \approx 1.4$. Note the relatively large uncertainty in the optimal n, reflecting the

[4]Because of mass segregation, the center-to-average contrast in the volumetric mass density is higher, about 100.

Table 3.2: Evolved Pleiades Properties

Symbol	Definition	Calculated Value	Pleiades Value
$N_{\rm s}$	Number of point sources	1244 ± 32	1256 ± 35
N_4	Number of systems with $m > 4$	13 ± 4	11 ± 3
$M_{\rm tot}$	Cluster mass	939 ± 30 $M_\odot$	870 ± 35 $M_\odot$
$b_{\rm unres}$	Unresolved binary fraction	0.68 ± 0.02	0.68 ± 0.02
m_0	Centroid of mass function	0.12 ± 0.03 $M_\odot$	0.14 ± 0.05 $M_\odot$
σ_m	Width of mass function	0.49 ± 0.05	0.46 ± 0.04
γ	Binary correlation index	0.66 ± 0.01	0.65 ± 0.05
R_c	Core radius	2.2 ± 0.4 pc	2.0 ± 0.1 pc
c_K	King concentration parameter	0.98 ± 0.09	0.99 ± 0.04
Σ_0	Central surface density	36 ± 8 $\rm pc^{-2}$	40 ± 3 $\rm pc^{-2}$
G	Gini coefficient	0.18 ± 0.02	0.20 ± 0.02

fact that a range in initial density contrasts relaxes to a similar state after 125 Myr. There is much less uncertainty in the virial radius r_v, which is surprisingly large compared to observed embedded clusters (see Section 3.3.4 below). Smaller assumed r_v-values, however, evolved to systems with too high a density contrast.

Figure 3.12 shows, as the dashed curve, the initial surface density as a function of projected radius. Also plotted (*solid curve*) is the evolved surface density, along with observed data from the Pleiades. Notice how the surface density *decreases* with time, a result of the inflation experienced by the entire cluster. This behavior contrasts with expectations from the standard account of dynamical relaxation (e.g. Binney & Tremaine 2008, Chapter 7). The swelling of the central region that we find is consistent, however, with previous simulations of *binary-rich* clusters with relatively low populations (Portegies Zwart et al. 2001). We explore further the underlying physical mechanism in Section 3.3.3 below.

Note from Table 3.1 that $N_{\rm tot}$, the initial number of stellar systems, is determined to within about 5% uncertainty. The main constraint here is the need to match N_s, the final, observed number of point sources. Note also that $N_{\rm tot} < N_s$ throughout the evolution. Almost all the stellar systems are binaries. Some of these are wide enough that they could be resolved observationally. Thus, the total number of point-like (i.e., unresolved) sources is always higher than $N_{\rm tot}$, the number of stellar systems (resolved or unresolved). By the same token, the unresolved binary fraction, $b_{\rm unres} = 0.68$, is significantly less than the full initial binary fraction, $b = 0.95$. Indeed, we were forced to choose a b-value close to unity in order to make $b_{\rm unres}$ close to the observationally inferred figure (see Table 3.2).

Figure 3.13 quantifies the degree of mass segregation in the evolved cluster. As before, we plot f_M, the fractional cumulative mass at any projected radius, against f_N, the fractional cumulative number. The fact that this curve rises above the dashed diagonal ($f_M = f_N$) indicates the existence of mass segregation. The empirical $f_M - f_N$ relation for the Pleiades, shown by the points with error bars, is well matched by the simulation. We were able

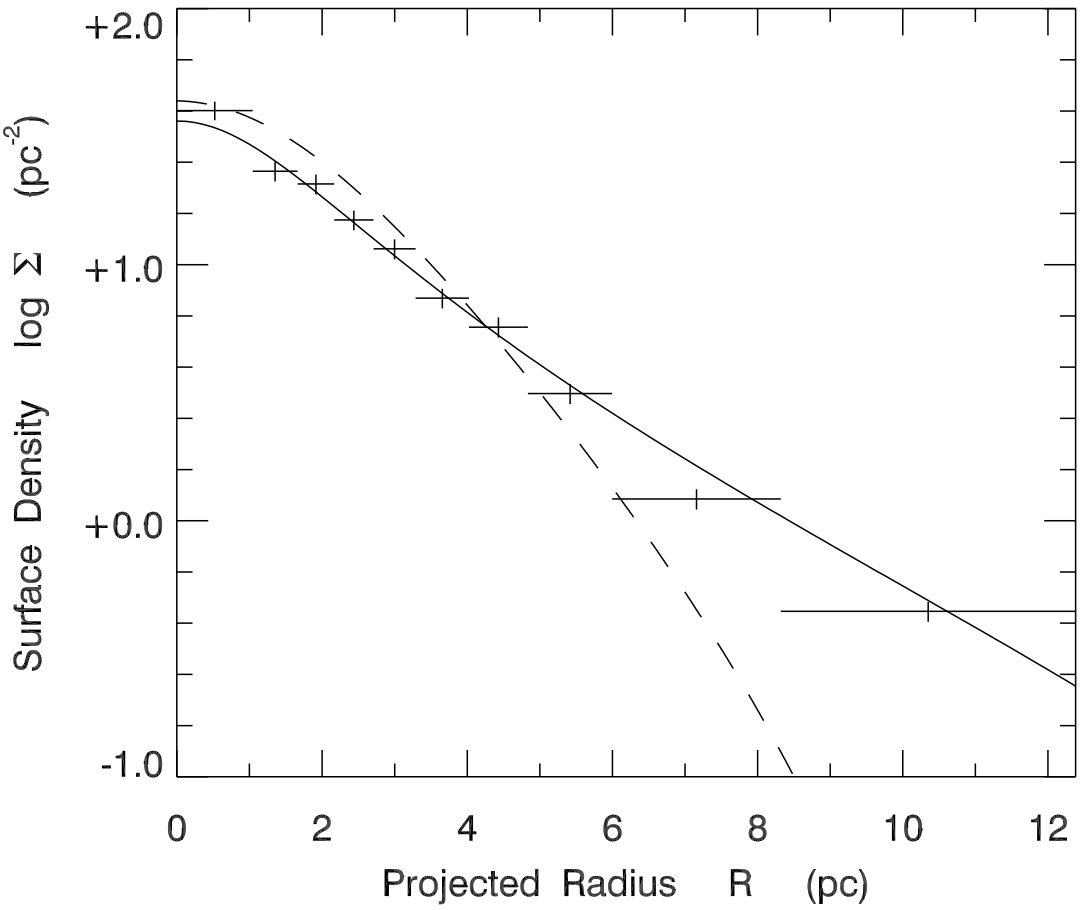

Figure 3.12: Surface number density as a function of projected radius. The dashed curve represents our initial configuration, an $n = 3$ polytrope. The solid curve is a King (1962) model fit to our simulation results for the evolved cluster. Table 3.2 lists the parameters for this optimal model. The numerical results displayed are an average of 25 simulation runs. Also shown are Pleiades data with error bars, taken from Figure 3.6.

to obtain this match only by adopting a non-zero value of β, the *initial* degree of mass segregation defined in equation (2.132).[5]

Mass Function Parameters

Four quantities in Table 3.1, m_0, σ_m, α, and γ, concern the mass function. The number of stars escaping the cluster during its evolution is relatively small (on average, 280 of the 2400 stars present initially). Because of this small loss, and because few members evolve off the main sequence, the initial and final mass functions are essentially identical, and all four parameters are highly constrained by the observations. Note, in particular, that the exponent α of the power law tail directly influences N_4, the observed number of massive stars. The binary correlation parameter γ is independent of the single-star mass function, but influences the primary, secondary, and q-distributions, as described in Section 2.3.1. Any substantial variation in γ would alter the corresponding parameter obtained statistically for the observed cluster.

Figure 3.14 compares our *evolved* single-star mass function with the Pleiades. The solid curve is a lognormal fit to the simulation result, which is fully characterized by m_0 and σ_m in Table 3.2. The data points, along with error bars, represent the inferred single-star mass function for the Pleiades, obtained through the maximum likelihood analysis of Section 3.2.1. The agreement with the simulation is naturally poorest at the highest masses, since we modeled the output as a pure lognormal, in order to be consistent with the procedure adopted in Section 3.2.1.

Finally, Figure 3.15 shows the initial distribution of the binary mass ratio q. We see how nearly equal-mass systems are strongly favored for our best-fit γ of 0.73. In the simulations, this distribution evolves almost unchanged, and closely matches the one inferred for the Pleiades today. The figure also displays the q-distribution for the hypothetical case of $\gamma = 0$. Such random pairing of stellar masses does not result in a flat curve, as one might expect. Instead, it reflects the character of the single-star mass function, which here is lognormal. As seen in Figure 3.15, the q-distribution for $\gamma = 0$ peaks at $q = 0.34$ and still vanishes as q approaches 0.

Two-Point Correlations

We have already established photometrically the existence of a substantial population of unresolved binaries in the Pleiades. In Section 3.2.2, we further estimated that another 8% of the stars in the cluster are part of binary systems wide enough to be been resolved in the catalog of Stauffer et al. (2007). These systems would present themselves as an over-abundance of stellar pairs observed at close separations, relative to what would be expected from pure random sampling of the density profile. We know that our simulations do contain

[5]Table 3.1 lists, for convenience, a symmetrical error on the best-fit β. Although the lower bound is accurate, even higher values give acceptable results, due to the saturation of mass segregation described in Section 3.3.2 below.

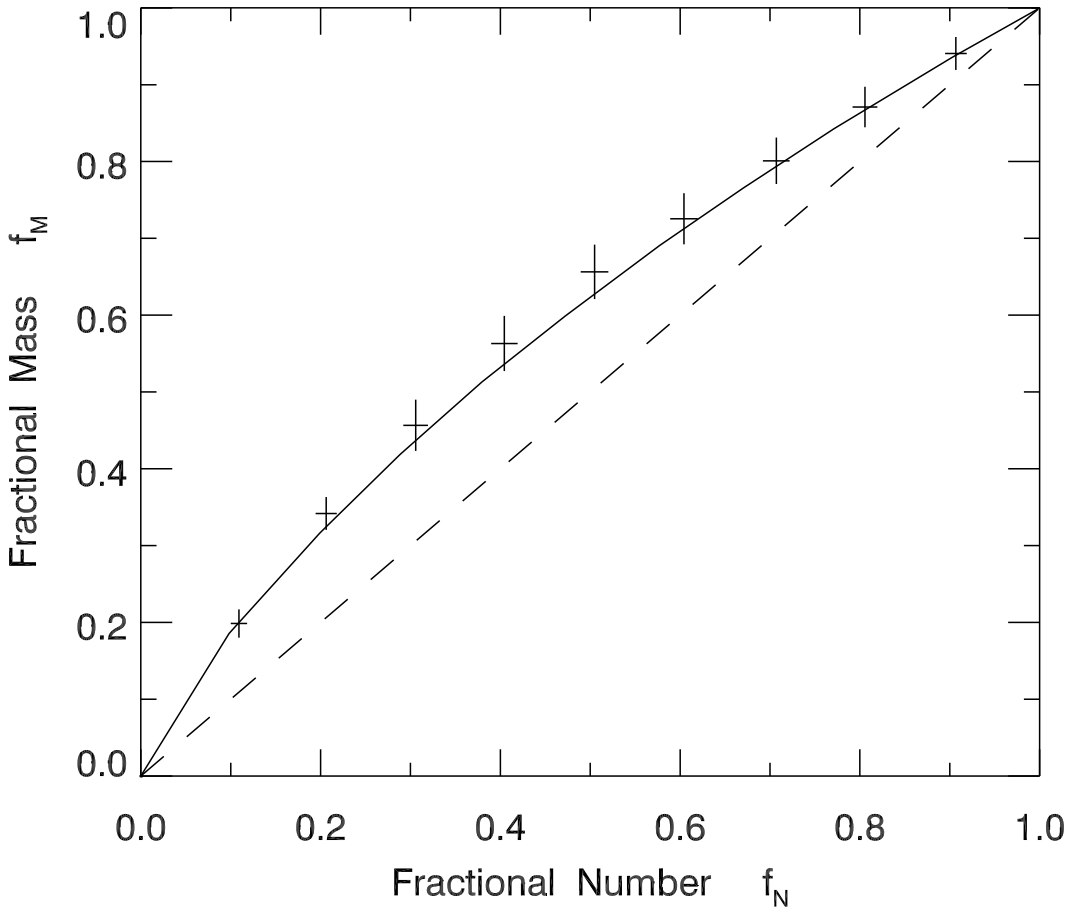

Figure 3.13: Fractional mass versus fractional number for the Pleiades. The solid curve shows the average results of our simulations. The crosses represent Pleiades data with error bars, taken from Figure 3.9. The dashed diagonal line is the hypothetical result for zero mass segregation.

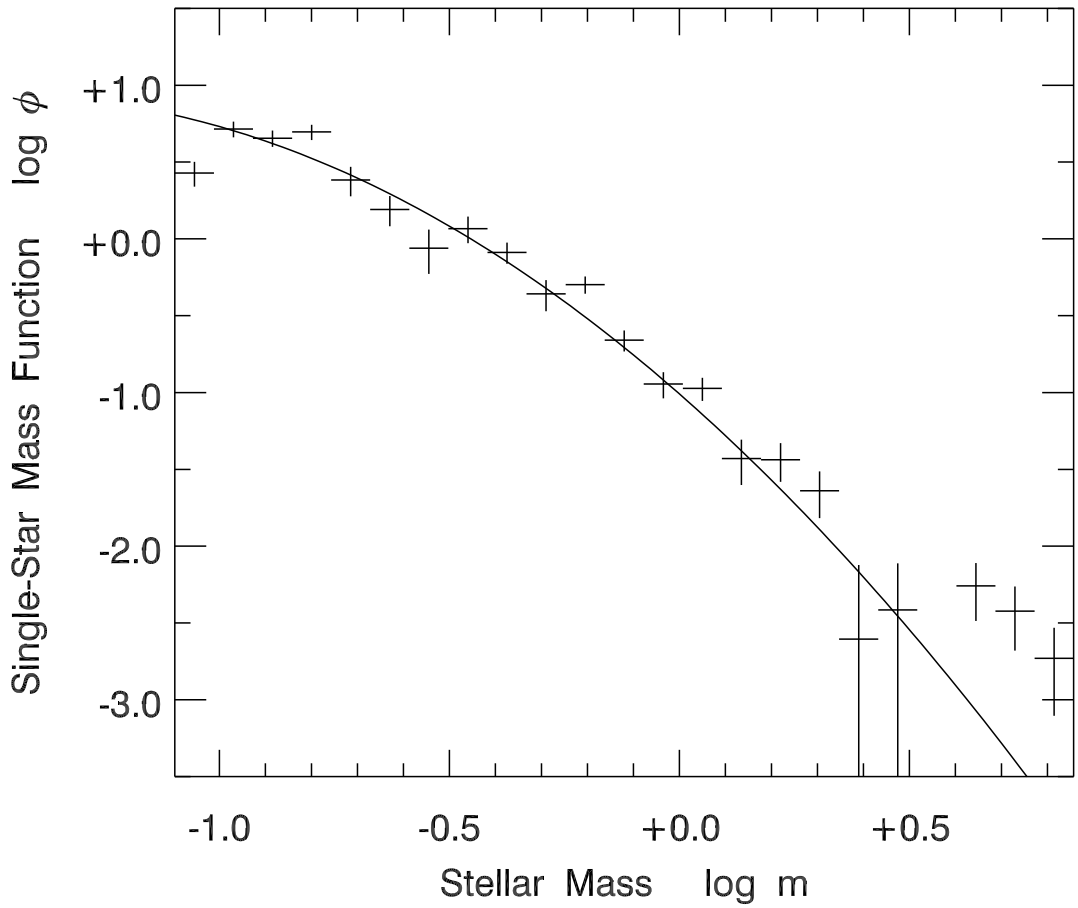

Figure 3.14: Single-star mass function for the evolved cluster. The solid curve is a lognormal fit to simulation data. Also shown are Pleiades data, with error bars, from Figure 3.3.

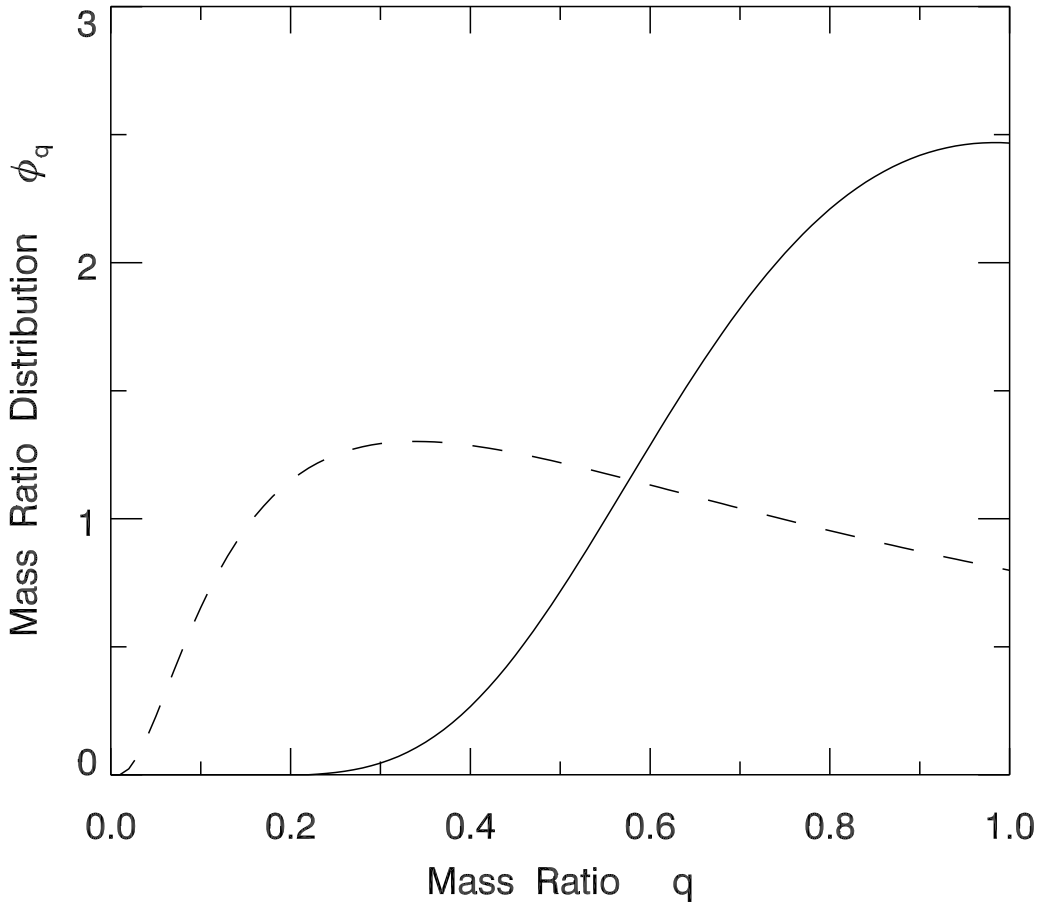

Figure 3.15: Initial distribution of the mass ratio within binaries, $q \equiv m_s/m_p$. The solid curve was obtained using a lognormal fit to the calculated single-star mass function, including the proper binary mass correlation parameter γ. The dashed curve is the hypothetical distribution obtained with the same single-star mass function, but with no mass correlation ($\gamma = 0$).

just such a population by design. In principle this could provide another means of comparing our simulations with the actual cluster.

Quantitatively, the two-point angular correlation $w(\theta)$ measures the excess probability of finding two sources separated by an angle θ on the sky over that expected from a purely random distribution (Peebles 1980). More explicitly, we compute the spacing between all pairs of particles. Then we take $N_{DD}(\theta)$ to be the number of pairs with separations within $\Delta\theta$ of θ, and then normalize this to the total number of possible pairs,

$$DD = \frac{N_{DD}}{n(n-1)/2}, \tag{3.3}$$

where n is the total number of sources.

We then need a random sample to compare this to. Stars in a cluster are, of course, not spread uniformly through the cluster area. They are more closely spaced at the center. Comparing a cluster to a uniformly random set of sources would give results that mostly represented the density profile, and not resolved binary systems. We need to compare to a random set of single stars distributed to give the same average density profile. Thus we generated random data sets according to a King (1966) model which had the same core radius and concentration parameter as we found for the Pleiades. We then computed $N_{RR}(\theta)$ on the random data analogous to N_{DD} above, and normalized it to get

$$RR = \frac{N_{RR}}{n(n-1)/2}. \tag{3.4}$$

We wish for sampling statistics to play as little role as possible. In order to accomplish this, we generate 100 such random data sets, and compute the average result, $\langle RR \rangle$. For each random set, we also compute the cross-correlation between the actual data and the random one. For each source in the real data, we find the distance to all sources in the random data from that same coordinate. We then count the number of such cross-system pairs are in a given separation bin as $N_{DR}(\theta)$. We then have,

$$DR = \frac{N_{DR}}{n^2}. \tag{3.5}$$

Note that the normalization is different here because there are more pairs between the two data sets than within just one of them. As with RR, DR is computed using each of the 100 random data sets, and the results averaged together to give $\langle DR \rangle$.

A nearly optimal estimator for the two-point correlation function is given by (Landy & Szalay 1993)

$$w(\theta) = \frac{DD - 2\langle DR \rangle + \langle RR \rangle}{\langle RR \rangle}. \tag{3.6}$$

We also compute error estimates for each w over each bin of angular separation as given by Landy & Szalay (equation 48 of 1993). In this way we find $w(\theta)$ for both the real Pleiades data and the simulation data.

The results, however, were disappointing. Largely this was because with only 1215 data points, the error bars on our data are far too large to draw any conclusions. However, it is also largely possible that there actually are very few if any such wide binaries to be seen. Very wide binaries are suseptible to being disrupted by encounters with other stars. The dividing line between which binaries get disrupted and which do not is based on how their internal binding energy compares with the average kinetic energy of a star within the cluster. Wide binaries with low binding energies get disrupted, while tight ones become tighter (Heggie 1975).

The parameters of our best-fit mass function give an average stellar mass of 0.3 $M_\odot$, and an average binary system mass of 0.7 $M_\odot$. The velocity dispersion in the Pleiades ranges from about 0.3 to 0.8 km s^{-1}, with the less massive stars moving more quickly (Pinfield et al. 1998). Taking $\sigma = 0.8$ km s^{-1} and $m = 0.3$ $M_\odot$, then a system with a separation of $a = 2000$ AU would have

$$\frac{|U|}{K} = \frac{2Gm^2}{am\sigma^2} \approx 0.4. \tag{3.7}$$

The majority of binaries wide enough to be resolved would also be soft. Although the two-point correlation function is a useful comparison in principle, this unfortunate coincidence of our resolution limit with the hard-soft boundary for the cluster makes it of little use for our analysis of the Pleiades.

3.3.2 Past Evolution

Global Expansion

We can now describe, based on our suite of simulations, the evolution of the cluster from its initial state to the present epoch. The main trend is an overall expansion of the system. This tendency is clear in Figure 3.16, which shows the variation in time of the virial radius, r_v. After an initial drop, lasting about two crossing times ($t_{\rm cross} = 10$ Myr) the radius steadily swells, increasing by about 40% to the present. From the definition of r_v in equation (2.84), we infer that the gravitational potential energy W is decreasing in absolute magnitude, i.e., the cluster is gradually becoming less bound. Note that we do not obtain r_v by calculating W directly, but through fitting the cluster at each time to a King model, and then finding the appropriate r_v for the best-fit model parameters.

Figure 3.16 shows that R_c, the projected core radius, displays similar behavior to r_v. After the transient phase which again lasts about two crossing times, R_c also swells, albeit more slowly. Analogous early adjustments are evident in other global quantities (see Figures 3.17 - 3.19). This transient results from our implementation of mass segregation, which alters slightly the gravitational potential (recall Section 2.2.2). Although the initial cluster is in virial equilibrium, the stellar distribution function is no longer a steady-state solution to the collsionless Boltzmann equation. Within the first two crossing times, the distribution readjusts to become such a solution. The core radius bounces, before settling to a value that subsequently evolves more gradually.

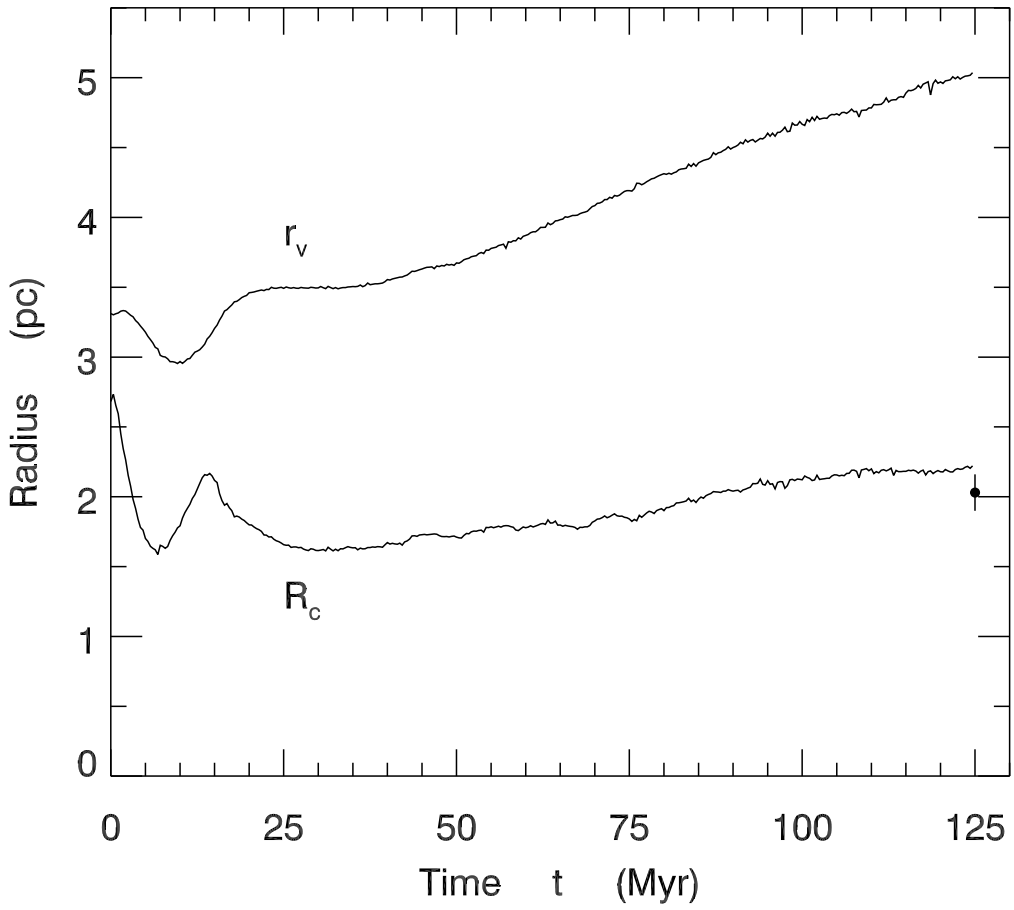

Figure 3.16: Evolution of characteristic radii. The upper curve shows the three-dimensional virial radius r_v, and is an average over simulation runs. The lower curve shows the projected core radius R_c, and is also an average. The data point in the lower right is the observed Pleiades value for R_c, along with error bars.

Expansion of a cluster's outer halo is one manifestation of dynamical relaxation. However, application of equation (1.37) of Binney & Tremaine (2008), with $\ln \Lambda = \ln(0.4N)$, reveals that the relaxation time is 250 Myr, or about twice the Pleiades age. In addition, the inner cores of relaxing systems shrink, giving energy to the halo. The secular expansion of R_c further indicates that we are *not* witnessing the usual effects of dynamical relaxation. Figure 3.17 provides yet another illustration of this point. Here, we see that the King concentration parameter c_K remains virtually constant, again following an initial adjustment. Recall that $c_K \equiv \log(R_t/R_c)$, where R_t is the projected tidal radius. Thus, R_t and R_c swell at about the same pace.

The projected surface number density, $\Sigma(R)$, currently peaks strongly at $R = 0$ (Figure 3.12). The actually central value, however, previously declined from an even higher level. Figure 3.18 shows this gradual decline, which is consistent with the previously noted rise in R_c. Thus, R_c increases from 1.6 to 2.2 pc over the period from $t = 30$ Myr to $t = 125$ Myr. Over the same interval, Σ_0 falls by a factor of 0.50, which is close to $(1.6/2.2)^2$. The number of systems in the core therefore remains virtually constant as the core itself expands. The volumetric number density similarly falls in the central region.

In Section 3.2.4, we documented a strong degree of mass segregation in the current Pleiades, quantifying this property through the Gini coefficient. Another result of the current study is that G did *not* attain its current value through purely stellar dynamical evolution. As seen in the top curve of Figure 3.19, $G(t)$ rose only slightly at first, and then remained nearly constant, even declining somewhat in the recent past. Initial states in which the parameter β was too low never attained the requisite degree of mass segregation. As an illustration, Figure 3.19 shows also the result from a single simulation using $\beta = 0$ initially. The Gini coefficient does grow, but not by enough to match observations. We note, parenthetically, that $G(t)$ exhibits oscillatory behavior over the a period that roughly matches the crossing time. These oscillations (unlike the initial readjustment) were washed out in the averaging procedure that produced the top curve in the figure. Finally, we remark that $G(t)$ appears to saturate in time. We will return to this interesting phenomenon shortly.

Effects of Stellar Evolution

All the simulations we have described thus far ignored any effects of stellar evolution. We could afford this simplification because of the relatively small number of cluster members that would have evolved significantly over 125 Myr. However, the code Starlab does have the capability of tracking stellar evolution, including mass loss, through fitting formulae. As a check, we retained our usual maximum mass of 10 $M_\odot$ and ran 25 simulations using the best-fit initial cluster parameters, but with stellar evolution included. The mass loss from relatively massive cluster members did not have a significant dynamical effect, and the endstate of the cluster was essentially identical. With reference to Table 3.2, the only parameter that changed appreciably was N_4, which fell.

In more detail, the few stars above 7 $M_\odot$ usually evolved to white dwarfs of approximately solar mass. On average, about 10 white dwarfs formed, of which 7 were the sec-

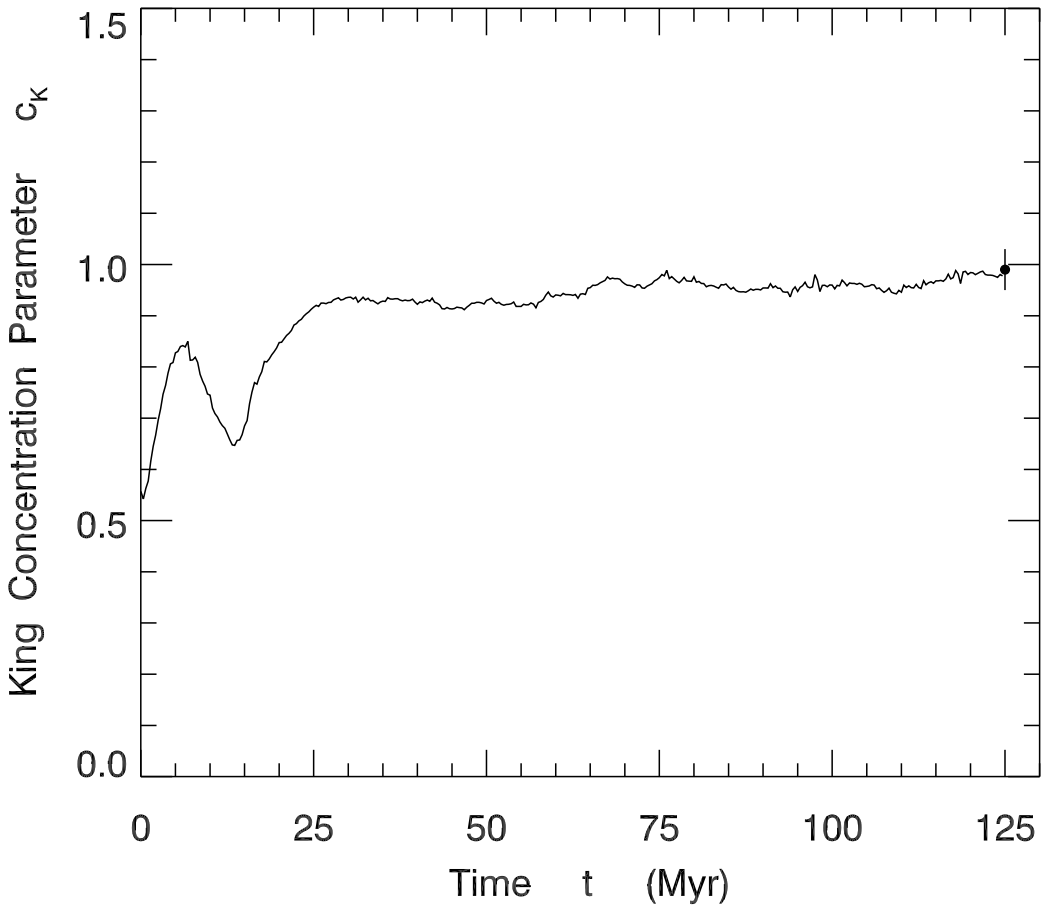

Figure 3.17: Evolution of the King concentration parameter. The curve is an average over simulation runs. The data point is the observed Pleiades value.

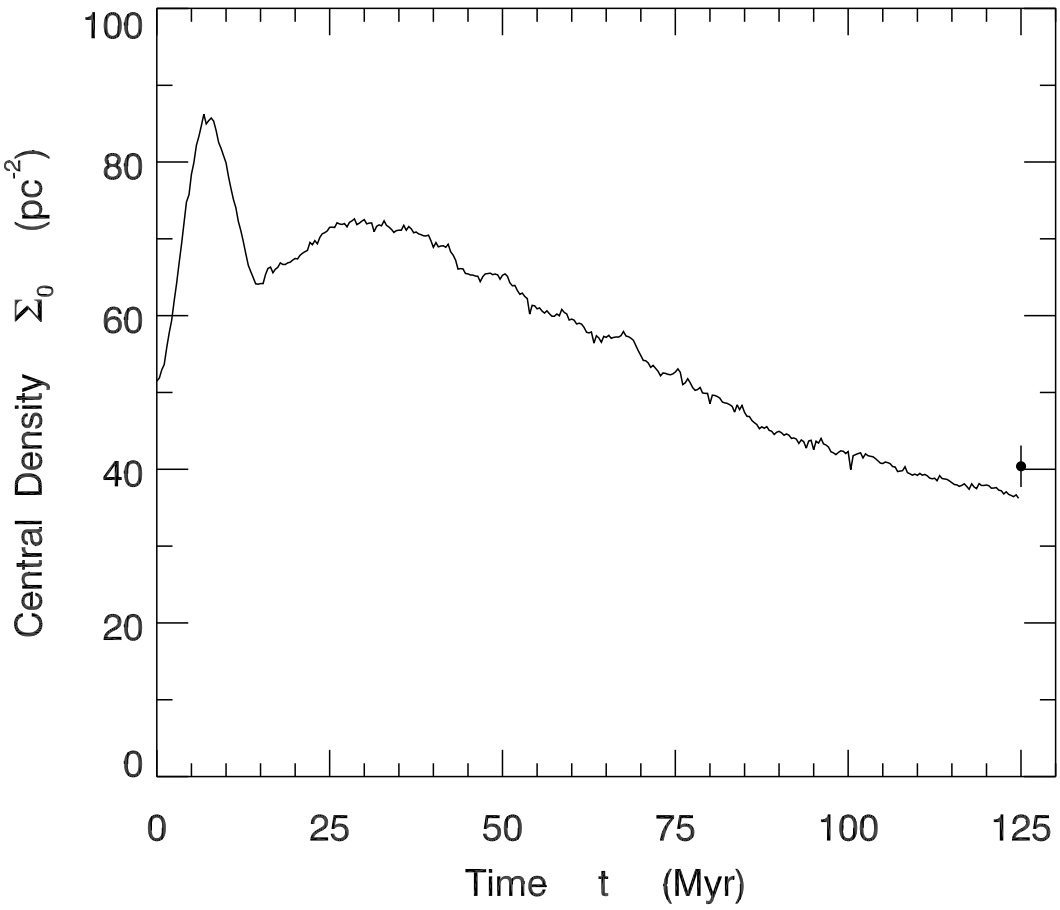

Figure 3.18: Evolution of the central surface number density. Shown is the average over simulation results. The observed Pleiades value is represented by the data point.

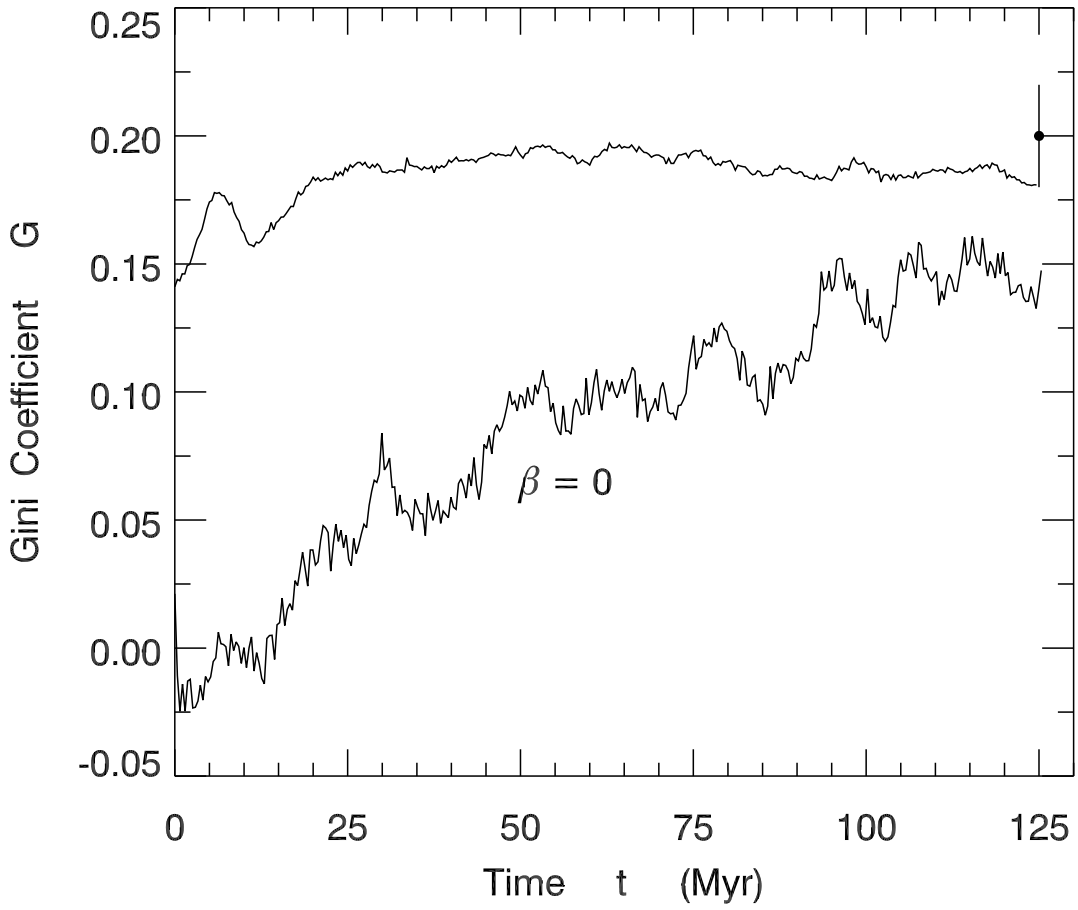

Figure 3.19: Evolution of the Gini coefficient. The upper curve is an average over simulation results. To the right of this curve is the observed Pleiades value. The lower curve shows the result from a single simulation run in which the mass segregation parameter β was artificially set to zero.

ondaries within binaries. Even the few that were primaries were faint relative to their main-sequence companions, and thus would be difficult to detect. Our findings are thus consistent with the observation of Fellhauer et al. (2003) that white dwarfs are generally rarer in open clusters than might be expected statistically from the initial mass function.

Finally, we relaxed the upper mass limit in the single-star mass function and allowed the maximum mass to be arbitrarily large, according to the power law in equation (2.108). Choosing stars stochastically from this distribution yielded a few members with masses as high as 40 $M_\odot$. If we again allowed for stellar evolution and used our standard initial cluster parameters, the evolution *did* take a different turn. The very massive stars represented a significant fraction of the total cluster mass, and their death had a quantitative impact. As before, the cluster went through an initial adjustment, partially from the heavier stellar mass loss. The system then smoothly expanded, but at a faster pace. At 125 Myr, the projected core radius R_c was 3.1 pc, or 1.5 times larger than that of the present-day Pleiades. Similarly, the central surface density Σ_0 was a factor 0.58 lower. Had we begun with very massive stars in an initial state a factor of 1.5 *smaller* than our standard one, a closer match would have resulted.

These results were instructive, if somewhat academic. In reality, stars more massive than about 10 $M_\odot$ would have inflated HII regions so quickly as to ionize and disperse the parent molecular cloud forming the Pleiades. In order to retain even a remnant, gravitationally bound cluster, the initial membership must have been very large, about 10,000 stars in the simulations of Kroupa et al. (2001). We stress that even this figure is a lower bound, as Kroupa et al. (2001) assumed a star formation efficiency in the parent cloud of 33% by mass. Such an efficiency is plausible within individual dense cores (Alves et al. 2007), but significantly higher than observational and theoretical estimates in cluster-forming clouds (e.g. Duerr et al. 1982; Huff & Stahler 2007).

Suppose we nevertheless adopt this scenario as a limiting case, and assume provisionally that the Pleiades progenitor contained at least 10,000 individual stars. Such groups are rare. Equation (39) of McKee & Williams (1997) gives the birthrate of OB associations based on their population of supernova progenitor ($m > 8$). If we use our adopted initial mass function to estimate this population, then the birthrate of relevant OB associations is 0.09 Myr^{-1} kpc^{-2}. This is a factor between 5 and 8 smaller than the total formation rate of open clusters (Adams & Myers 2001; Miller & Scalo 1978). It is unlikely, therefore, that formation through dispersing OB associations dominates, and we continue to use an upper mass limit of about 10 $M_\odot$ for the Pleiades.

3.3.3 Future Evolution

The same calculations that reconstruct the past history of the Pleiades may also be used to predict its development far into the future. It is still believed, following the original proposal by Spitzer (1958), that most open clusters are eventually destroyed by the tidal gravitational field of passing interstellar clouds, now identified as giant molecular complexes. In this project, we do not attempt to model encounters with such external bodies. However,

Starlab can follow the effects of the *Galactic* tidal field, both through imposition of the appropriate external potential and by adding a Coriolis force to individual systems. We switched on the Galactic field, in addition to stellar evolution, and followed the cluster from its initial state for a total of 1 Gyr. While most open clusters do not survive this long, some do last up to several Gyr (Friel 1995). Our simulation thus models at least a portion of the Pleiades' future evolution.[6]

Fate of the Pleiades

Up to the present cluster age of 125 Myr, adding the Galactic tidal field and stellar mass loss made very little difference in the evolution. Beyond this point, the cluster will continue the overall expansion that characterized it in the past. As seen in Figure 3.20, the central density Σ_0 keeps declining. The falloff is roughly exponential, with an e-folding time of 400 Myr. This figure, along with Figures 3.21 and 3.22, show average results from the 4 runs we conducted. Even after averaging, the calculated Σ_0 displays increasing scatter for $t > 700$ Myr. By this time, the *total* population has also fallen to the point that numerical determination of Σ_0 (through a fitted King model) becomes problematic.

The decline in the cluster population, which was modest until the present, accelerates as stars are tidally stripped by the Galactic gravitational field. It is the lighter stars that populate the cluster's outer halo and that preferentially escape. Consequently, the average mass of the remaining cluster members rises. Figure 3.21 shows both these trends. Displayed here is N_s, the number of systems contained within the initial Jacobi radius of 14.3 pc.[7] By 1 Gyr, the total membership has fallen to a few dozen systems. Meanwhile, the average system mass $\langle m \rangle$ rises, almost doubling by the end. Careful inspection of Figure 3.21 shows that $\langle m \rangle$ initially fell slightly to its present-day value. This falloff reflects the loss, through stellar evolution, of the most massive members, an effect which is eventually overwhelmed by the escape of the lightest systems. Notice again the jitter in the $\langle m \rangle$ curve at later times.

Despite this qualitative change in the cluster's internal constitution, the degree of mass segregation remains essentially constant until very late times. Figure 3.22 displays the Gini coefficient. In detail, $G(t)$ exhibits oscillations qualitatively similar to what we saw in lower portion of Figure 3.19. Nevertheless, its average magnitude does not appreciable change until $t \sim 700$ Myr, when it begins a steep descent. The very large scatter during this late epoch again reflects the diminishing population.

What accounts for these trends? During most of the evolution, some process is able to enforce mass segregation, despite the continual depletion of the lightest members. This process evidently loses its efficacy at late times, when the total population falls too low. Earlier, we showed that dynamical relaxation did *not* establish the present-day level of mass segregation. Although we are now spanning a period well in excess of the initial relaxation

[6]The very oldest clusters have large Galactocentric radii, and thus experience both a weaker tidal field and less frequent encounters with giant molecular clouds. Clearly, the Pleiades does not fall into this category.

[7]The Jacobi radius is the spherical average of the zero-velocity surface in the presence of the Galactic tidal field (Binney & Tremaine 2008, equation 8.91).

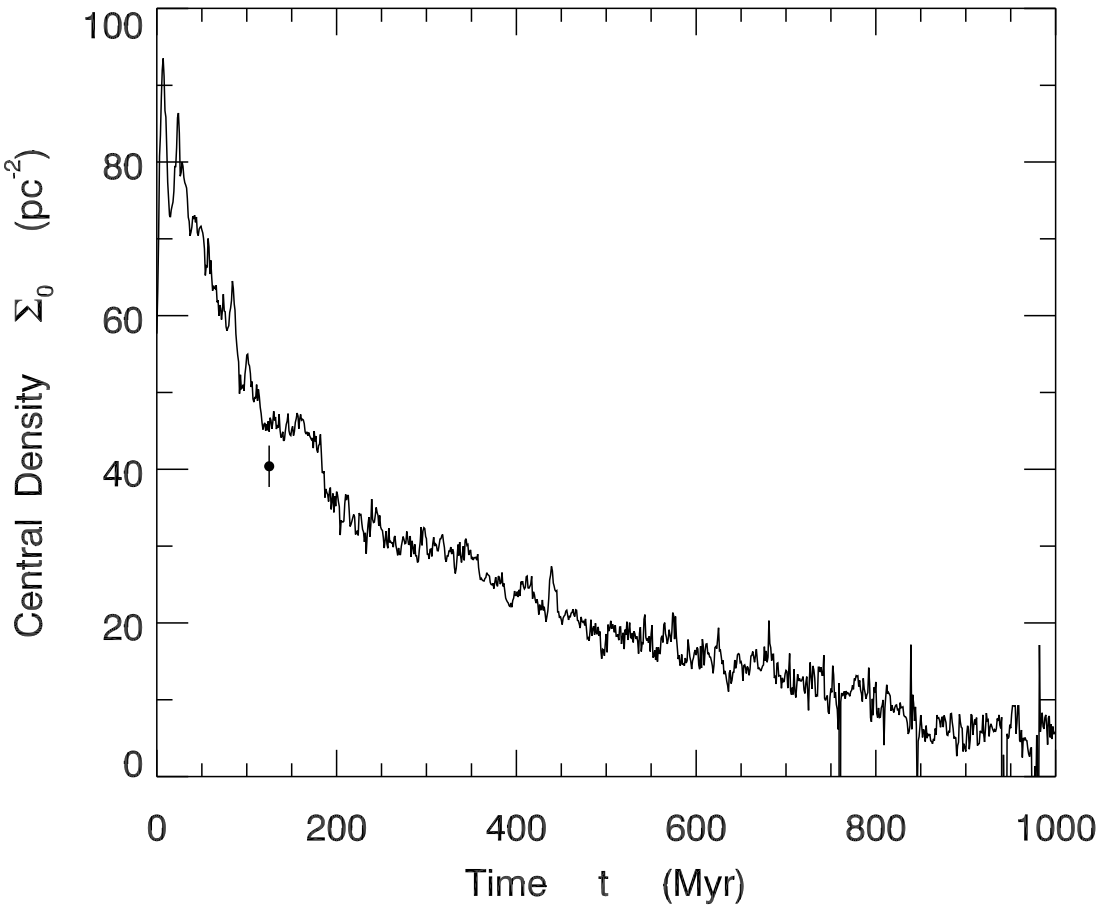

Figure 3.20: Evolution of the central surface number density over a total time of 1 Gyr. The data point is the present-day Pleiades value, with errors indicated.

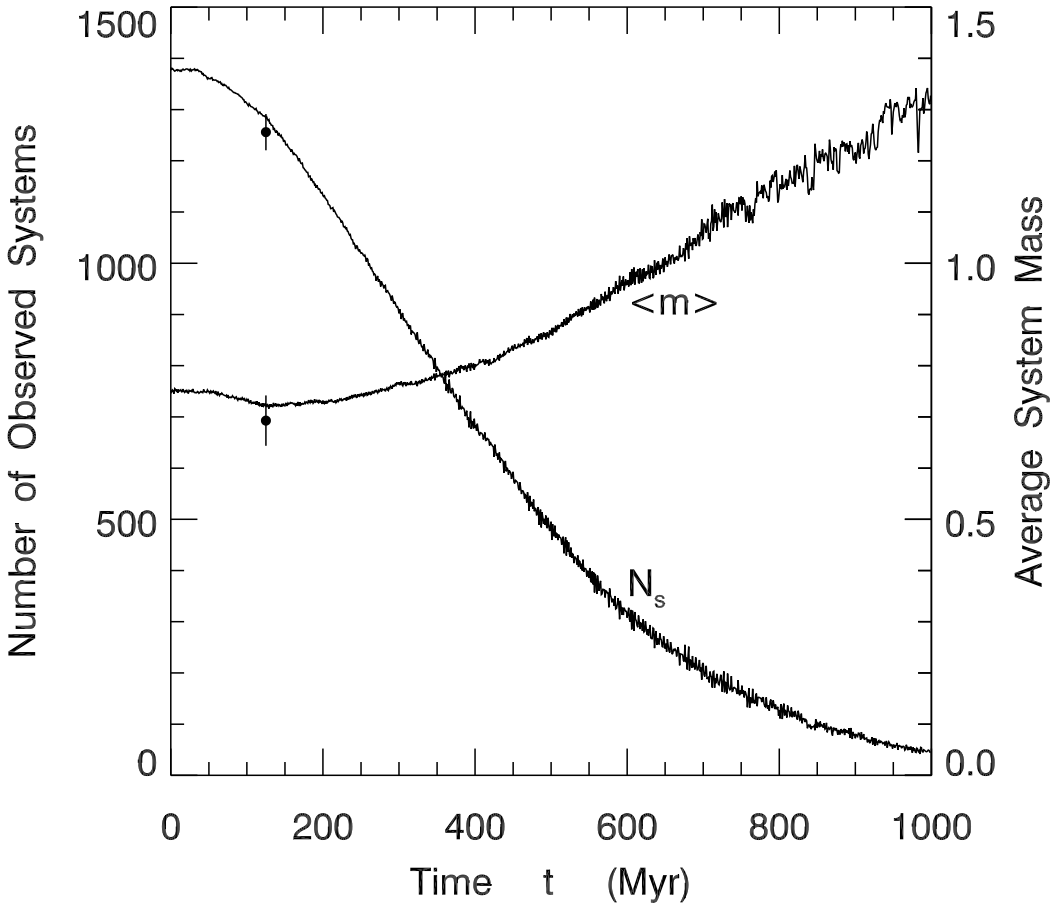

Figure 3.21: Evolution of the total number of stellar systems, N_s, and the average system mass $\langle m \rangle$, over 1 Gyr. Both quantities refer to systems within the initial Jacobi radius of 14.3 pc. The data points show the current Pleiades values, with error bars.

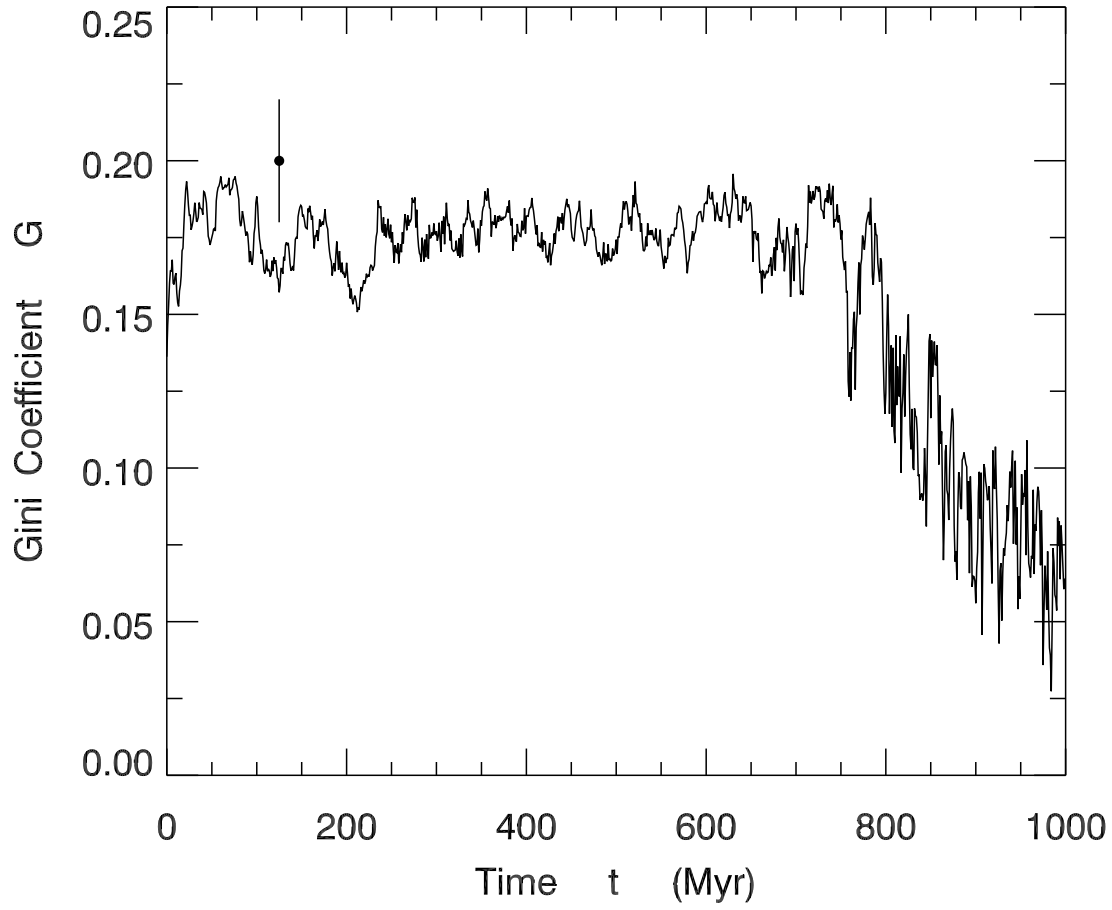

Figure 3.22: Evolution of the Gini coefficient over 1 Gyr. Note the large scatter at late times, reflecting the falloff in total cluster population. The data point to the left is the current Pleiades value, along with error bars.

time (250 Myr), we still do not see the classic behavior - monotonic shrinking of the core that feeds halo expansion. Up to $t \sim 200$ Myr, the projected core radius R_c continues the increase noted earlier. Between 200 and 600 Myr, when 75% of cluster members escape, R_c does decline slightly, from 2.2 to 1.2 pc. Thereafter, the core swells once more.

We believe that the system's overall expansion is due principally to the release of energy in three-body encounters, specifically, close passages of binaries and single stars. Over the Gyr time span, mass loss through stellar evolution and tidal stripping weakens the cluster's gravitational binding, rendering it increasingly responsive to such internal heating. We ascribe the maintenance of mass segregation, i.e., the inward drift of more massive stars, to dynamical friction with the background population. We shall revisit these key processes, binary heating and dynamical friction, momentarily.

Figure 3.23 shows graphically how the cluster will appear far in the future. Here we show positions of the member systems projected into the Galactic plane, both at the present time and at $t = 700$ Myr. One sees at present a slight elongation along the direction toward the Galactic Center. This tidal stretching is well documented observationally (Raboud & Mermilliod 1998). Stars that leave tend to do so along that direction. But any appreciable excursion leads, because of the Galaxy's differential rotation, to a change in angular speed. As a result, two tidal streams develop that are orthogonal to the Galactocentric radius. These streams are present in both panels of Figure 3.23, but are especially noticeable in the diminished cluster shown at the right.

Primordial or Dynamical Binaries

Since we suspected that binaries were important in the gross dynamics of the cluster, we recalculated the entire 1 Gyr evolution after effectively removing all primordial binaries from the system. We began with the same, best-fit initial state as before, which had the usual distribution of single-star masses and initial binary fraction $b = 0.95$. However, we replaced every binary by a single star, located at the system's center of mass and comprising the total of the component masses. In addition, we turned off both stellar evolution and the Galactic tidal field, in order to explore the evolution under the simplest conditions possible. Note that our procedure for fusing binaries into single stars preserved the total cluster mass, number of stellar systems, and mass distribution of those systems. In other words, all two-body interactions between cluster members were the same as before. The important difference is that we eliminated the source or sink of energy associated with the internal motion of binaries.

The results were both surprising and illuminating. The cluster still undergoes overall expansion. Figure 3.24 shows that the central density again falls steadily. The nominal e-folding time is again 400 Myr, but the actual decline is not well fit by an exponential. The root cause of the cluster expansion is that *new* binaries continually form and interact with other stars. This process occurs principally near the relatively dense cluster center, where the most massive stars reside, along with other, more representative members. The component masses in the new binaries are high, typically $8\langle m \rangle$. Prompt formation of binaries is a

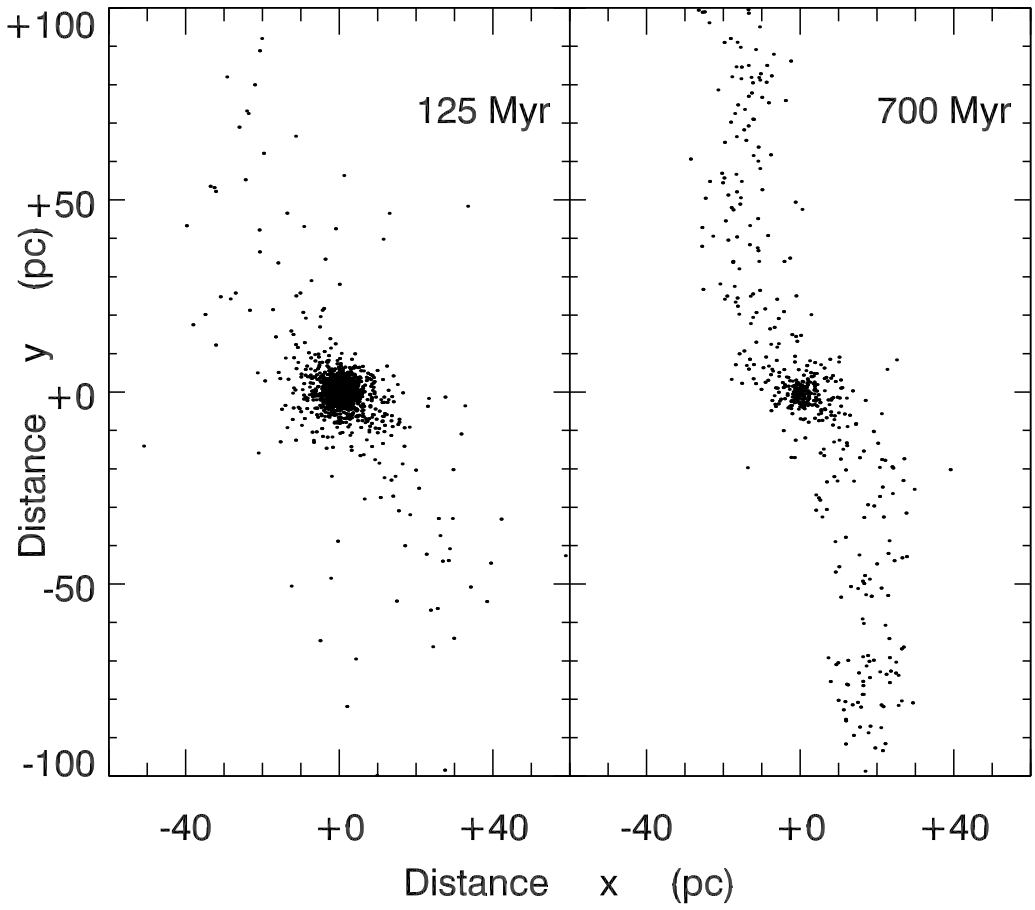

Figure 3.23: Positions of Pleiades members projected onto the Galactic plane. The data are from a single, representative simulation, for the two epochs indicated. A terrestrial observer is located 133 pc in the negative x-direction. The Galactic Center is in the same direction, but 8 kpc distant. Galactic rotation is in the positive y-direction.

well-documented occurrence in systems initially containing only single stars (Aarseth 1971), and the formation rate is greatly enhanced at higher stellar mass (Heggie 1975). In our simulations, only 3 or 4 of these systems exist at any time. Nevertheless, they are significant dynamically, because of the cluster's relatively low gravitational binding.

Any such massive binary with a separation less than 8×10^4 AU = 0.4 pc is hard, i.e., has a gravitational potential energy exceeding the initial mean kinetic energy of all cluster members. Thus, even the relatively wide binaries formed in these simulations, with initial separations of order 10^3 AU, are capable of heating the cluster dynamically. As has long been appreciated (Heggie 1975; Hut 1983), the encounter of a hard binary with a third star usually results in a harder (tightened) binary. Both this pair and the isolated star have more translational kinetic energy than before. The extra energy, which comes at the expense of the binary's tightening, is quickly transferred to other cluster members.

The same dynamical heating operates, of course, in all stellar groups containing binaries. However, very populous systems, such as globular clusters, have such high gravitational binding that almost all newly formed binaries are soft. In this case, energy exchange via three-body encounters has a minor effect, and the classical picture of dynamical relaxation via two-body encounters applies. In relatively sparse systems like open clusters, both primordial and dynamically formed binaries inject so much energy that they impulsively change the velocity distribution function and qualitatively influence the course of evolution. This stochastic resetting of the velocities, which was emphasized in the classic study of Terlevich (1987), is a conspicuous feature of the Pleiades evolution, both past and future.

3.3.4 Conclusions from Simulations

While undertaken primarily to reconstruct the history of the Pleiades, our study has shed light on a well-documented, but still poorly understood, feature of open clusters generally - mass segregation. We demonstrated that the current, rather high degree of segregation in the Pleiades could not have been the result of dynamical relaxation from a pristine state with homogeneous mass distribution. First, the cluster has only been evolving for about half its initial relaxation time. Second, a hypothetical cluster starting with no mass segregation cannot reach the present level. Quantitatively, the Gini coefficient rises, but not enough (recall Figure 3.19).

Two conclusions may be drawn. The ancient Pleiades must have already had substantial mass segregation before it drove off the gas. Some other process, unrelated to dynamical relaxation, must drive this effect, and continues to do so long into the future (Figure 3.22). The most obvious candidate is dynamical friction. A relatively massive star moving through a lower-mass population, experiences a drag force, causing it sink toward the cluster center. The associated time scale for braking, $t_{\rm DF}$, can be substantially smaller than the dynamical relaxation time $t_{\rm relax}$ (Spitzer 1969). According to Portegies Zwart & McMillan (2002), the quantitative relation is

$$t_{\rm DF} = 3.3 \frac{\langle m \rangle}{m} t_{\rm relax} \tag{3.8}$$

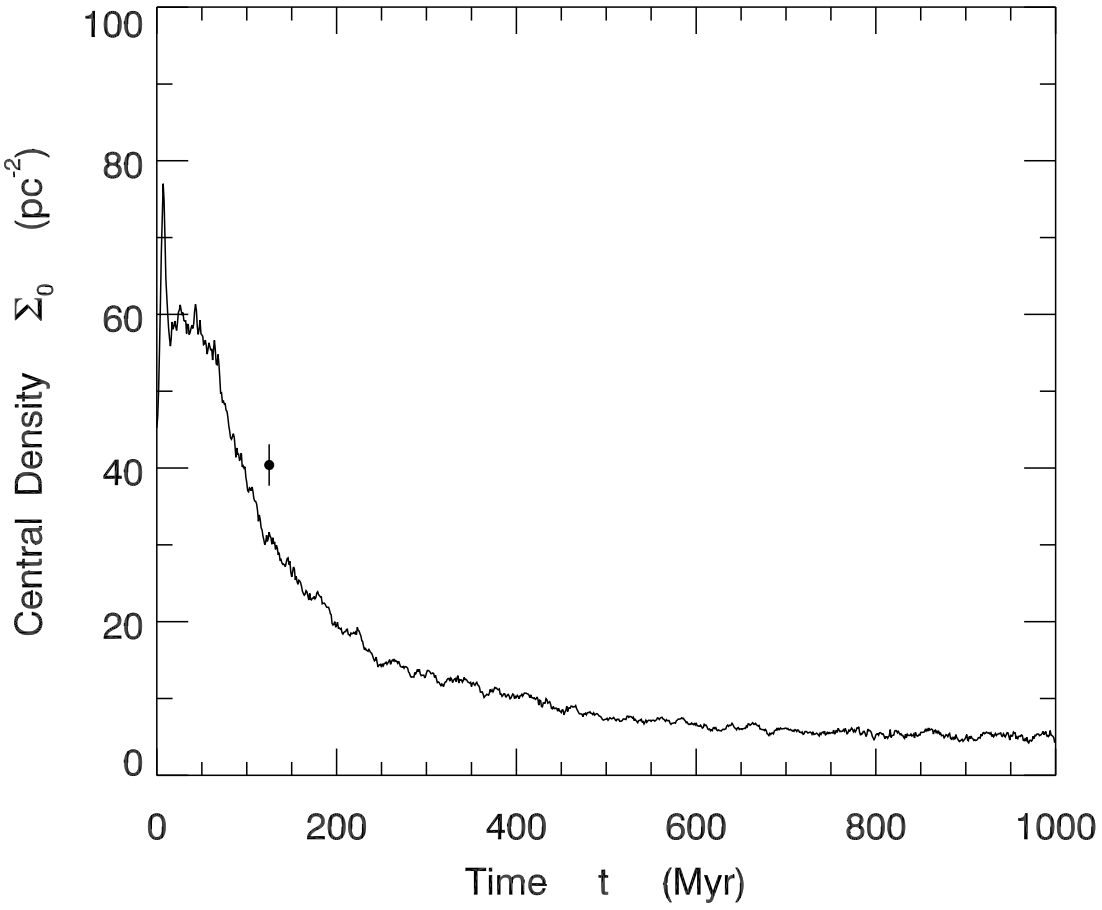

Figure 3.24: Long-term evolution of the central number surface density for a cluster with no primordial binaries. The curve was obtained by averaging 9 simulation runs. The data point shows the current Pleiades central density, with errors.

for a heavy star of mass m in a background of average mass $\langle m \rangle$.

Portegies Zwart & McMillan (2002) and other researchers have invoked dynamical friction to explain mass segregation, focusing on very populous clusters in which massive star infall leads to the runaway growth of a central black hole (see also Gürkan et al. 2004). Our work reveals a further, curious aspect of the phenomenon. Figures 3.19 and 3.22 suggest, and further calculations confirm, that $G(t)$ saturates, regardless of its initial value. Why does the degree of mass segregation level off? A possible explanation is that, as the most massive stars sink to the center, the population there becomes increasingly homogeneous. Since $\langle m \rangle / m$ rises, so does $t_{\rm DF}$. In other words, mass segregation through dynamical friction may be a self-limiting process.

Returning to the prehistory of the Pleiades, another significant finding is the relatively large size of the initial state. The virial radius r_v began at 4 pc, while the projected half-mass radius of the initial cluster was about 2 pc. For comparison, the observed half-light radii of embedded clusters, as seen in the near infrared, range from about 0.5 to 1.0 pc, with some outliers on either side (Lada & Lada 2003). Thus, the initial, gas-free Pleiades had a radius 2 to 4 times larger than typical embedded systems. It may plausibly be argued that the Pleiades is an especially populous open cluster, and therefore began as a larger configuration, far outside the typical range. With this caveat in mind, our result suggests that the system expanded during its earliest, embedded phase. This swelling, which was accompanied, or even preceded, by mass segregation, could have been due to the loss of ambient gas during the formation process. Interestingly, observations of extra-Galactic clusters appear to show a similar, early expansion phase (see Bastian et al. 2008, and references therein).

We have stressed the importance of binary heating to explain the global evolution of the Pleiades, both past and future. This is a three-body effect, not considered in classical studies of dynamical relaxation. As we indicated, binary heating is more effective in less populous systems, including open clusters. In the near future, we hope to explore further this general issue of stellar dynamics, i.e., the demarcation between systems that do and do not undergo classical, dynamical relaxation. This study will necessarily delve further into the role of binaries. We also intend to repeat our Pleiades analysis with another, relatively nearby system of comparable age, to ensure that the Pleiades results are representative for the entire class of open clusters.

Chapter 4

Alpha Persei

4.1 Constructing the Catalog

4.1.1 Membership

Heckmann et al. (1956), first addressed the membership of Alpha Persei by observing proper motions for stars in the area. Their original catalog and later refinements (Heckmann & Lübeck 1958; Fresneau 1980; Trullols et al. 1989) identified most of the relatively bright members, i.e. those with apparent V-magnitudes less than 12. Numerous studies have since extended the list to lower luminosities, reaching below the stellar limit in some parts of the cluster (Stauffer et al. 1985; Prosser 1992; Stauffer et al. 1999; Barrado y Navascués et al. 2002; Deacon & Hambly 2004).

One difficulty faced by these investigations is the fact that the cluster's stars have small motions relative to nearby objects in the field (Prosser 1992). The group's low internal density and small Galactic lattitude ($b = -7°$), also make it harder to separate from the rich background population (Deacon & Hambly 2004). Researchers have therefore sought additional means to select true members.

Stauffer et al. (1999) used measurements of lithium depletion to set the cluster age at 90 Myr. Since this age is far less than that of nearby field stars, other indications of relative youth have been used to cooroborate and extend the proper motion studies. Observers have searched for high rotation velocities, $H\alpha$ emission and lithium absorption lines, and x-ray activity. Photometric fluxes and colors consistent with the cluster locus in the color-magnitude diagram, and radial velocities close to the mean cluster value are additional signposts.

Currently there is no comprehensive photometric catalog of the cluster. Both for our present project and as a service to the astronomy community, we have constructed one that includes a number of visual and infrared wavebands. We first compiled our membership list from the work of Heckmann et al. (1956); Heckmann & Lübeck (1958); Fresneau (1980); Stauffer et al. (1985); Stauffer et al. (1989); Trullols et al. (1989); Prosser (1992); Prosser (1994); Prosser et al. (1996); Prosser & Randich (1998); Prosser et al. (1998); Stauffer

et al. (1999); Barrado y Navascués et al. (2002); Deacon & Hambly (2004); Makarov (2006); and Mermilliod et al. (2008). When these studies disagreed on the membership status of individual stars, we favored the judgment of more recent work and those authors who considered a wider range of criteria. In this manner, we amassed a total of 902 candidate sources, of which we ultimately judged 753 to be bone fide members. These extend to a distance of 30 pc from the cluster center; we take this figure to represent the system's outer radius.

4.1.2 Photometry

We then took, B-, V-, R-, and I-band photometry from the literature, where available. Where multiple measurements exist for the same source, we used the most recent observations. Much of the older literature used the Kron photometric system. Cousins $(R-I)$ and $(V-I)$ colors were computed for these using the transformations of Bessell & Weis (1987):

$$(R-I)_C = 0.102 + 0.9166(R-I)_K + 0.4230(R-I)_K^2 - 0.16647(R-I)_K^3 \quad (4.1)$$

$$(V-I)_C = 0.227 + 0.9567(V-I)_K + 0.0128(V-I)_K^2 - 0.00530(V-I)_K^3. \quad (4.2)$$

Additionally, we used J-, H-, and K_s-band fluxes from the 2MASS database (Skrutskie et al. 2006) for all member systems.

Table 4.3 presents our catalog of the 902 candidate sources and their photometric measurements, noting the origin in the literature for the B-, V-, R-, and I-band data in each case. We have also shown for each source whether or not we judge it to be a member based on the criteria indicated previously. Finally, we list alternate names for sources when such exist.

For the specific goal of analyzing the present-day structure of Alpha Persei, we require fluxes only in two filters. Following Section 3.1, we use the I- and K_s-bands. Figure 4.1 is the color-magnitude diagram for all the sources we take to be members. We have converted apparent magnitudes to absolute ones using a distance to Alpha Persei of 176 pc and an extinction of $A_V = 0.3$ mag (Pinsonneault et al. 1998). The solid curve is a combination of the theoretical zero-age main sequence for stellar masses, in solar units, $m_* > 1$ (Siess et al. 2000) and, for lower-mass stars, a pre-main-sequence isochrone (Baraffe et al. 1998).[1]

Our catalog draws from many different observational surveys, each with its own areal coverage and sensitivity. The compilation in Table 1 is thus by no means complete. Searches have been made even for very faint substellar objects (Basri & Martín 1999; Stauffer et al. 1999; Barrado y Navascués et al. 2002; Lodieu et al. 2005), but each is limited in spatial extent. Studies more fully covering the cluster's large area have a brighter limiting magnitude. In particular, the large majority of data for fainter sources comes from the survey of Deacon & Hambly (2004). Crowding limited their study to sources with $R < 18$ mag. Although we

[1]Both theoretical results are presented in magnitudes. We have applied corrections to the theoretical K-band magnitudes to make them consistent with the 2MASS K_s-band used in our catalog. See Cohen et al. (2003) for this transformation.

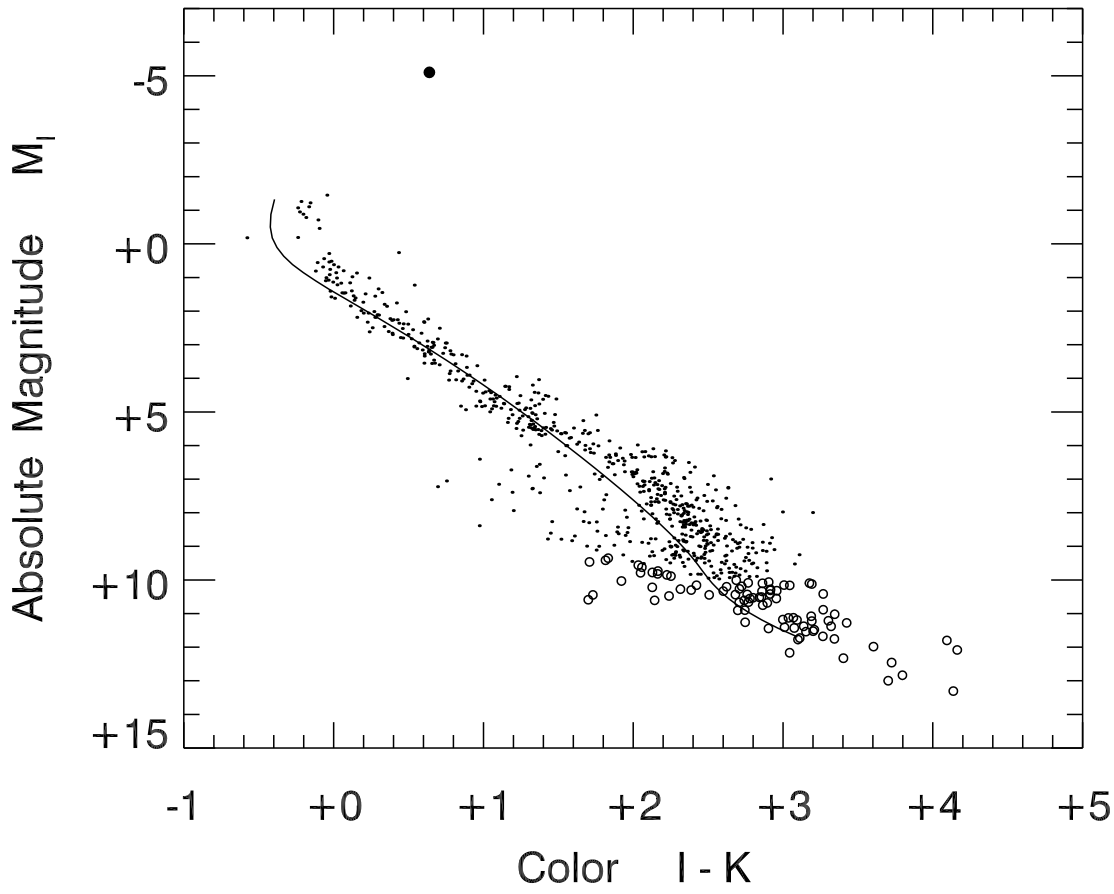

Figure 4.1: Near-infrared color-magnitude diagram for Alpha Persei. Small dots represent the 653 stars in our sample. Open circles are the 99 objects below our completeness limit which have been removed from the sample. The filled circle is the star α Per, which is the only post-main-sequence object. The 90 Myr isochrone for stars with masses between 0.08 and 5.0 $M_\odot$ is shown as the smooth, solid curve.

do have data from some sources fainter than this, our catalog suffers from significant spatial incompleteness below this limit.

For our isochrone, a single star with mass of 0.15 $M_\odot$ would be observed at the $R = 18$ mag limit. This same star would have $M_I = 10.0$ mag and $M_K = 7.5$ mag. In order to avoid biases due to incompleteness, we thus ignore all sources fainter than these limits. Such systems are displayed as open circles in Figure 4.1. The filled circle in the figure represents the star α Per itself, the only post-main-sequence object in the cluster. After making these cuts, our catalog contains 653 sources for our analysis.

4.2 Alpha Persei Today: Computational Method

4.2.1 Finding the Mass Function

As in Section 2.1.1, we search for a theoretical stellar mass function that best reproduces the cluster's observed distribution of photometric fluxes. We define a two-dimensional mass function, $\Phi(m_p, m_s)$ such that $\Phi(m_p, m_s)\Delta m_p \Delta m_s$ is the probability that a binary system exists with primary mass in the interval m_p to $m_p + \Delta m_p$ and secondary mass from m_s to $m_s + \Delta m_s$. Single stars are viewed as binaries with $m_s = 0$.

We further constrain the mass function to have the form

$$\Phi(m_p, m_s) = 2b(1-c)\phi(m_p)\phi(m_s) + bc\phi(m_p)\delta(m_p - m_s) + (1-b)\phi(m_p)\delta(m_s). \qquad (4.3)$$

Here, the function $\phi(m)$ is the probability density of single stars having mass m (in solar units). The parameter b is the fraction of all sources in our catalog that are unresolved binaries. Finally, the parameter c quantifies the degree of correlation between the masses of binary components. Thus, the first term on the righthand side of equation (4.3) represents cluster systems that are uncorrelated binaries. The second term represents binaries in which the component masses are perfectly correlated, while the last term accounts for single stars.

For given $\phi(m)$, b, and c, one may predict the distribution of fluxes using a theoretical mass-luminosity relation. For this purpose, we employ the 90 Myr isochrone shown in Figure 4.1. The predicted flux distribution is then compared to the observed one. We use a maximum likelihood technique to find the single-star mass function and binary parameters that produce the best match (see Section 2.1.2). Since our theoretical isochrone does not include post-main sequence objects, we ignored the star α Per, the only such object, for this fitting. We assigned an approximate mass for this star from the observed spectral type and luminosity class listed in the Bright Star Catalogue (Hoffleit & Jaschek 1991).

We establish the cluster's radial density profile following the method used in Section 2.1.2. That is, we divide the projected cluster into annuli, count the number of sources in a given magnitude range within each annulus, and then convert this number to the relative fraction of sources aAlthough we do have data from some sources fainter than this, our catalog suffers from significant spatial incompleteness below this limit.t each mass. In

contrast to Section 2.1.2, we now use elliptical annuli instead of circular ones in accordance with the cluster's elongated shape (see below).

Recall from Section 2.1.2 that the response matrix, $\mathcal{R}$, converts a given mass distribution into a photometric one. Incorporated into $\mathcal{R}$ are the observational uncertainties of the photometric measurements. Figure 4.2 shows the K-band uncertainty, σ_K, as a function of magnitude. The σ_K-values are generally low for brighter objects and begin to increase towards fainter magnitudes as the sensitivity limit is approached. The smooth curve shows the fit adopted for our analysis. For the I-band we take a single value for the uncertainty, $\sigma_I = 0.15$ mag. The plurality of our I-band fluxes come from POSS II plates, for which the sensitivity limit is 18.5 mag (Hambly et al. 1993). Our lower incompleteness cutoff of $M_I = 10.0$ mag corresponds to an apparent I-magnitude of 16.3, well above this limit. Thus any rise in σ_I should be modest, and a constant value is adequate.

4.2.2 Cluster Shape

Figure 4.3 shows the spatial distribution of sources in our catalog. Immediately apparent is the cluster's non-circular appearance. This high degree of flattening is well-known. Eddington (1910) noted, "The stars are arranged in a kind of chain and not in the form of a globular cluster." This flattening is likely due to stretching by the Galactic tidal field.

We wish to quantify more precisely the degree of flattening observed. To do this, we must first determine the location of the cluster center. Qualitatively, the density of stars should peak at this position. Let $\boldsymbol{x}_k$ be the position vector of point source k on the sky, and $x_{i,k}$ be the ith component of this vector. (In practice we use right ascension and declination as the axes.) The density-weighted center is then given by

$$\boldsymbol{x}_{\rm center} = \frac{\sum_k \rho_k \boldsymbol{x}_k}{\sum_k \rho_k}, \tag{4.4}$$

where ρ_k is the local surface number density. To obtain this surface density, we follow the convention in N-body studies and use the 6th-nearest neighbor

$$\rho_k = d_{6,k}^{-2}, \tag{4.5}$$

where $d_{6,k}$ is the distance to the 6th-nearest source from source k (Casertano & Hut 1985). We then define the radius vector for each source as measured from the cluster center by $\boldsymbol{r_k} \equiv \boldsymbol{x_k} - \boldsymbol{x}_{\rm center}$.

We next define the second moment of the source distribution as the matrix

$$\mathcal{Q}_{ij} = \frac{\sum_k \rho_k r_{i,k} r_{j,k}}{\sum_k \rho_k}. \tag{4.6}$$

This matrix is related to, though different from, the quadrupole moment of the system; the latter is conventionally taken to be the traceless second moment. The matrix $\mathcal{Q}_{ij}$ describes both the elliptical shape and orientation of the cluster. If our original two orthogonal axes are

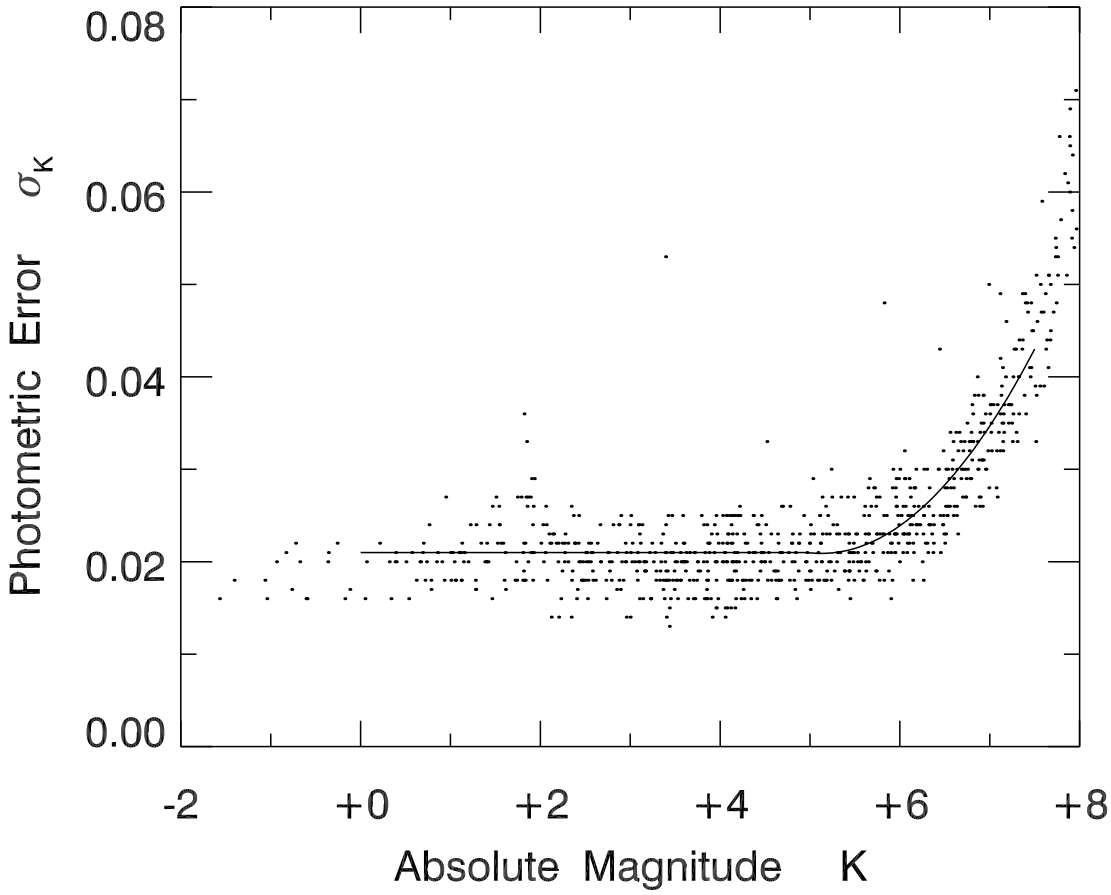

Figure 4.2: Observational error in the K-band measurements as a function of absolute magnitude for the stars in the our catalog. The smooth curve is the approximate fit used in our maximum likelihood analysis. Sources with $K > 7.5$ mag were not used.

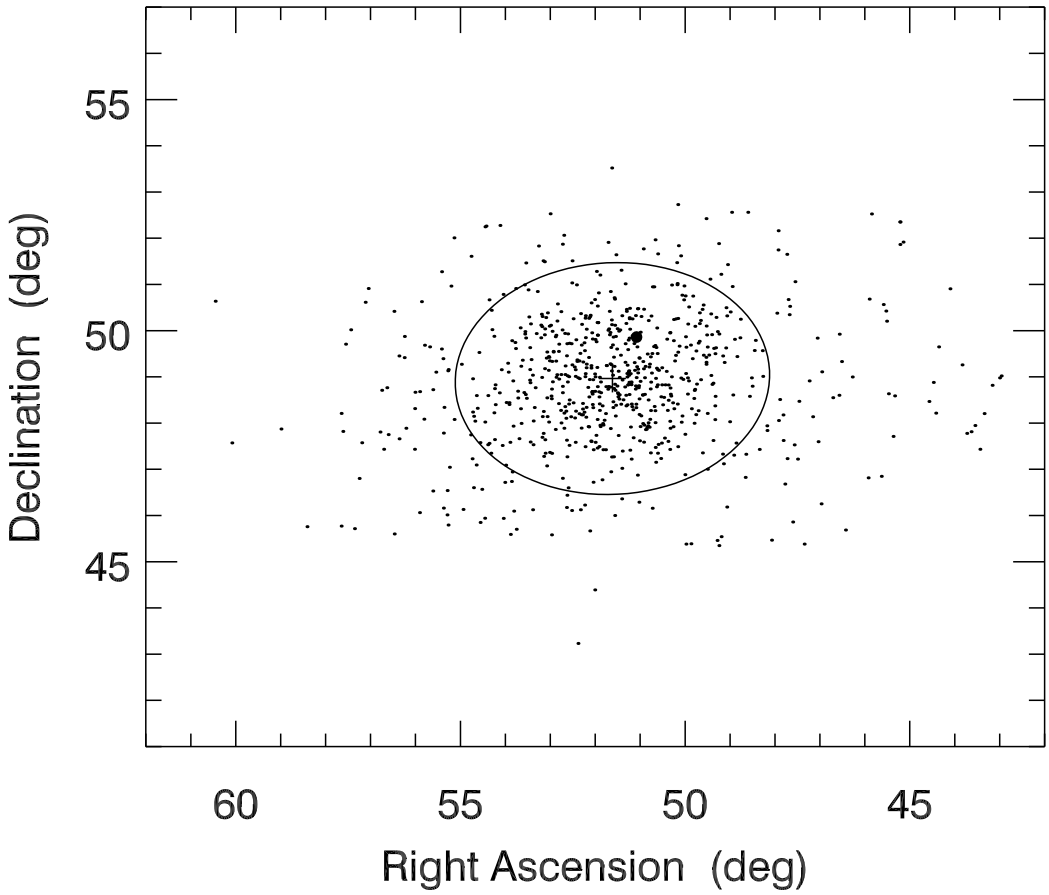

Figure 4.3: Spatial distribution of catalog sources. The filled circle is the star α Per. The cross denotes the density-weighted center of the cluster. The solid curve is the best-fit ellipse to the distribution, scaled to a major axis of 7°.

rotated by some angle ψ, one will align with a principle axis of the ellipse. The transformed matrix, $\mathcal{Q}'_{ij}$ will then be diagonal. Mathematically, the transformation is effected by

$$\mathcal{Q}' = \mathcal{R}\mathcal{Q}\mathcal{R}^{\mathrm{T}}. \tag{4.7}$$

Here, $\mathcal{R}$ is the rotation matrix that transforms the coordinates of any vector:

$$\mathcal{R} = \begin{bmatrix} \cos\psi & \sin\psi \\ -\sin\psi & \cos\psi \end{bmatrix}. \tag{4.8}$$

Expanding out the matrix multiplication gives the elements of the new matrix in terms of the known elements of $\mathcal{Q}$ and the angle ψ:

$$\mathcal{Q}'_{11} = \mathcal{Q}_{11}\cos^2\psi + 2\mathcal{Q}_{12}\sin\psi\cos\psi + \mathcal{Q}_{22}\sin^2\psi \tag{4.9}$$

$$\mathcal{Q}'_{22} = \mathcal{Q}_{11}\sin^2\psi - 2\mathcal{Q}_{12}\sin\psi\cos\psi + \mathcal{Q}_{22}\cos^2\psi \tag{4.10}$$

$$\mathcal{Q}'_{12} = \mathcal{Q}'_{21} = \mathcal{Q}_{12}\left(\cos^2\psi - \sin^2\psi\right) - (\mathcal{Q}_{11} - \mathcal{Q}_{22})\sin\psi\cos\psi, \tag{4.11}$$

where we have used the fact that $\mathcal{Q}_{12} = \mathcal{Q}_{21}$. The requirement that $\mathcal{Q}'$ be diagonal gives us the constraint $\mathcal{Q}'_{12} = \mathcal{Q}'_{21} = 0$. We solve the resulting equation for ψ to find

$$\psi = \frac{1}{2}\tan^{-1}\left(\frac{2\mathcal{Q}_{12}}{\mathcal{Q}_{11} - \mathcal{Q}_{22}}\right). \tag{4.12}$$

Given ψ, $\mathcal{Q}'_{11}$ and $\mathcal{Q}'_{22}$ are readily computed from equations (4.9) and (4.10). If $\mathcal{Q}_{11} = \mathcal{Q}_{22}$ then the distribution is circular and ψ has no meaning. In this case the matrix will already be diagonal and $\mathcal{Q}' = \mathcal{Q}$.

Equation (4.12) yields values of ψ in the range of $-\pi/4$ to $\pi/4$. This is the angle needed to make the original x-axis line up with one of the principle axes, but not necessarily the major axis. If the x-axis has been rotated into the minor axis of the ellipse, then $\mathcal{Q}'_{22} > \mathcal{Q}'_{11}$. In general, we can find the angle ψ' between the x-axis and the major axis, where ψ' is in the range of $-\pi/2$ to $\pi/2$, by the following rules:

$$\psi' = \begin{cases} \psi & \mathcal{Q}'_{11} > \mathcal{Q}'_{22} \\ \psi - \pi/2 & \mathcal{Q}'_{11} < \mathcal{Q}'_{22} \text{ and } \psi > 0 \\ \psi + \pi/2 & \mathcal{Q}'_{11} < \mathcal{Q}'_{22} \text{ and } \psi \leq 0. \end{cases} \tag{4.13}$$

Recomputing $\mathcal{Q}'_{11}$ and $\mathcal{Q}'_{22}$ using ψ' instead of ψ will give the same numerical values for the diagonal elements, but with $\mathcal{Q}'_{11} > \mathcal{Q}'_{22}$. Assuming this condition to hold, $\mathcal{Q}'_{22}/\mathcal{Q}'_{11}$ is then equal to the square of the axis ratio for the ellipse we seek. The eccentricity is found from this ratio by

$$e = \sqrt{1 - \frac{\mathcal{Q}'_{22}}{\mathcal{Q}'_{11}}}. \tag{4.14}$$

Applying this procedure to our source catalog, we find Alpha Persei to have an eccentricity of $e = 0.70 \pm 0.03$ and position angle $\psi' = -2.8°$, as measured from the declination line through the cluster center. Such an ellipse is shown in Figure 4.3. Prosser (1992) found the cluster to have a major axis of at least 7° and a minor axis of 5°. This axis ratio would give an eccentricity of 0.7. Our results are thus in good agreement with this earlier, less precise estimate.

Throughout the remainder of this paper, we will use elliptical bins when analyzing spatial structure of the cluster. The radial values discussed and seen in plots are the semimajor axes of these ellipses. When assigning stars to a bin, we use the semi-major axis of the ellipse it sits on. This quantity is

$$a = r\sqrt{\frac{1 - e^2\cos^2(\theta - \psi')}{1 - e^2}}, \tag{4.15}$$

where r and θ are the standard polar coordinates of the star from the cluster center.

4.3 Alpha Persei Today: Results

4.3.1 Empirical Mass Distribution

Figure 4.4 displays the single-star mass function resulting from our analysis. Points in the figure represent the best-fit values of $\phi(m)$ for each mass bin. The severe drop off, as well as the high uncertainty, in the mass function for the lowest two m-values are not real, but reflect our imposed completeness cutoff for the photometric data. The function $\phi(m)$ is found by matching systems having $M_I < 10$ mag and $M_K < 7.5$ mag, for which the equivalent mass is $m = 0.15$. The fitting routine allows the existence of a few lower-mass objects, which only count when they are secondaries within the binary population. Since these relatively faint secondaries have little effect on the photometric fluxes, their population is poorly constrained.

We wish to compare our actual single-star mass function to a standard, lognormal distribution:

$$\phi(m) = \frac{C}{m}\exp\left[-\frac{(\log m - \log m_0)^2}{2\sigma_m^2}\right]. \tag{4.16}$$

Here m_0 is the mass at which the distribution peaks, σ_m is the characteristic width, and C is a normalization constant. We fit this form to the data in Figure 4.4, excluding the lowest two bins. We find $m_0 = 0.26 \pm 0.13$ and $\sigma_m = 0.44 \pm 0.05$. The rather large uncertainty in the peak mass is primarily due to the lack of data for faint stars. Since we are not sampling below the peak, the fitting cannot tightly constrain its value.

These numbers are also systematically biased because of our method for treating mass correlation within binaries. We model the binary population as being a combination of systems which have both members randomly drawn from $\phi(m)$ and ones in which both have exactly equal mass. In Section 2.1.4, we ran tests analyzing synthetic clusters with more realistic populations in which the binaries have a continuous degree of mass correlation.

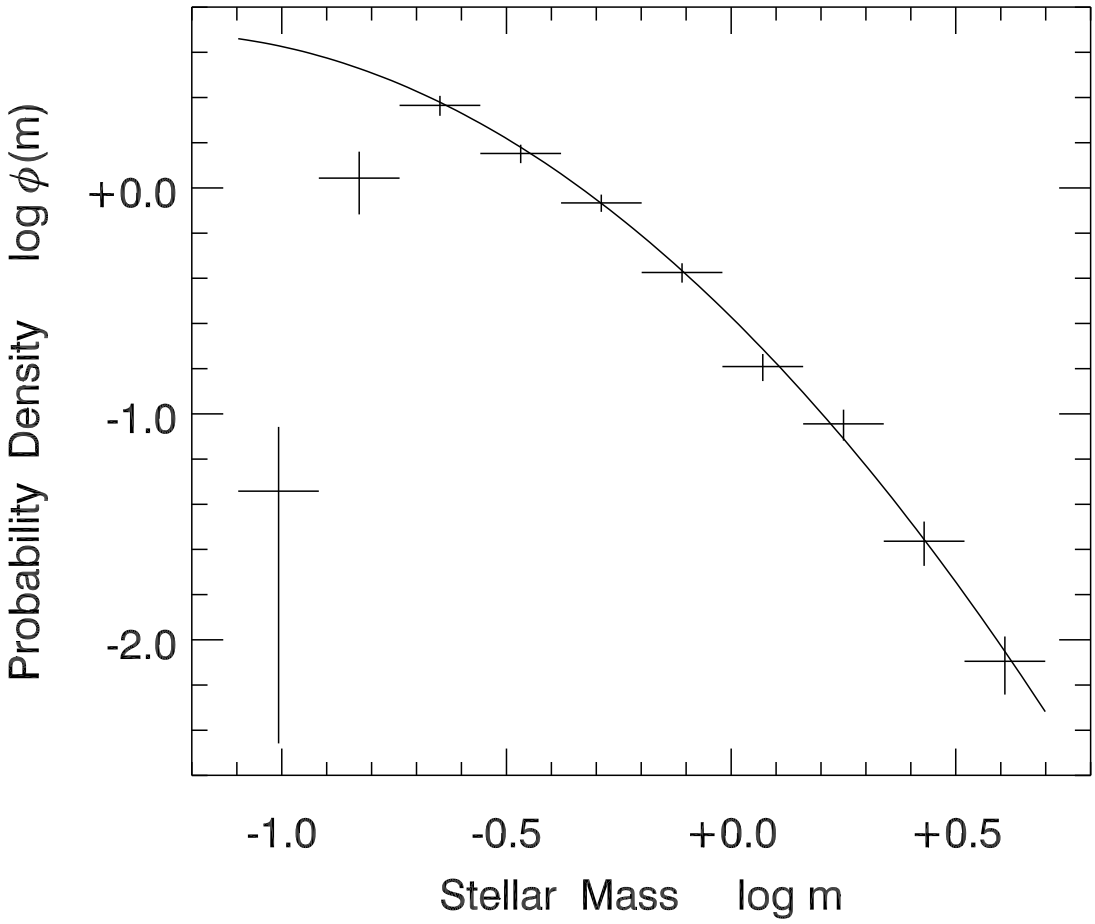

Figure 4.4: Best-fit single star probability density $\phi(m)$ for Alpha Persei. The smooth curve is a lognormal approximation to the results. The two lowest-mass points suffer from incompleteness and were not used in the lognormal fit.

From our value of $c = 0.38$ (see Section 4.3.2 below), Figures 2.4 and 2.5 from Section 2.1.4 show that the present peak mass is systematically overestimated by about 0.07, while the width is underestimated by about 0.08. Applying these corrections gives $m_0 = 0.19 \pm 0.13$ and $\sigma_m = 0.52 \pm 0.05$.

How similar is Alpha Persei to the Pleiades? Both are fairly young open clusters with ages of 90 Myr (Stauffer et al. 1999) and 125 Myr (Stauffer et al. 1998), respectively. For the Pleiades, we found in Section 3.2.1 the best-fit lognormal mass function to have $m_0 = 0.14 \pm 0.05$ and $\sigma_m = 0.46 \pm 0.04$. Figure 4.5 shows the best-fit lognormal for both Alpha Persei (solid curve) and the Pleiades (dashed curve). Although the parameters seem similar for the two clusters, we see that Alpha Persei distinctly favors higher-mass stars.

Do the two clusters actually have significantly different mass distributions? Our Pleiades catalog had 1256 stars, nearly a factor of 2 more than the 653 used here. Thus we would expect to find a comparably lower total mass in Alpha Persei. Integrating our mass distribution gives a total mass of 758 ± 40 $M_\odot$. After adding in the mass for α Per itself (about 10 $M_\odot$) and accounting for the systematic underestimate (by about 33 $M_\odot$) due to our parameterization of correlated binaries (see Section 3.2.1), we readjust the total to 801 ± 40 $M_\odot$. This is surprisingly close to the Pleiades value of 870 $M_\odot$. The average system mass in Alpha Persei is 1.2 $M_\odot$, nearly twice the value of 0.7 $M_\odot$ for the Pleiades.

However, the Pleiades data were complete down to the stellar limit of 0.08 $M_\odot$, whereas the corresponding limit of Alpha Persei is 0.15 $M_\odot$. Thus there are undoubtedly more stars in Alpha Persei than we see here, and these are preferentially lower in mass. Extrapolating our lognormal mass function, we predict that 24% of the cluster's members are below the incompleteness cutoff, and that they constitute less than 6% of the total mass. Including these gives us 863 stars totaling 849 $M_\odot$ and an average mass of just under 1 $M_\odot$. Although lower, this figure is still 40% above the corresponding Pleiades average mass.

This extrapolation suffers from the uncertainty of trying to estimate an unobserved population. As an alternative test, we examine the mass function in the restricted range of $0.3 < m < 3.0$, for which all systems are actually observed. We then fit a power law to this section of the mass function. For Alpha Persei, we find a slope of -1.8 in this region, compared to -2.3 for the Pleiades. Thus we see Alpha Persei's mass function is definitely shallower in this region, over which we are not sensitive to completeness.

Other authors have also remarked on the peculiarity of the mass function of Alpha Persei. Deacon & Hambly (2004) noted a significant amount of flattening in the mass function at the low-mass end, finding it to be shallower than the Pleiades. Makarov (2006) also suggested that low-mass stars are underpopulated in the cluster. Assuming, then, that the difference is real, the obvious question is what accounts for it. We shall return to this important issue presently.

4.3.2 Binarity

A key result from our earlier analysis of the present-day Pleiades was its high proportion of binaries compared to the field population. Moreover, since the binary fraction only de-

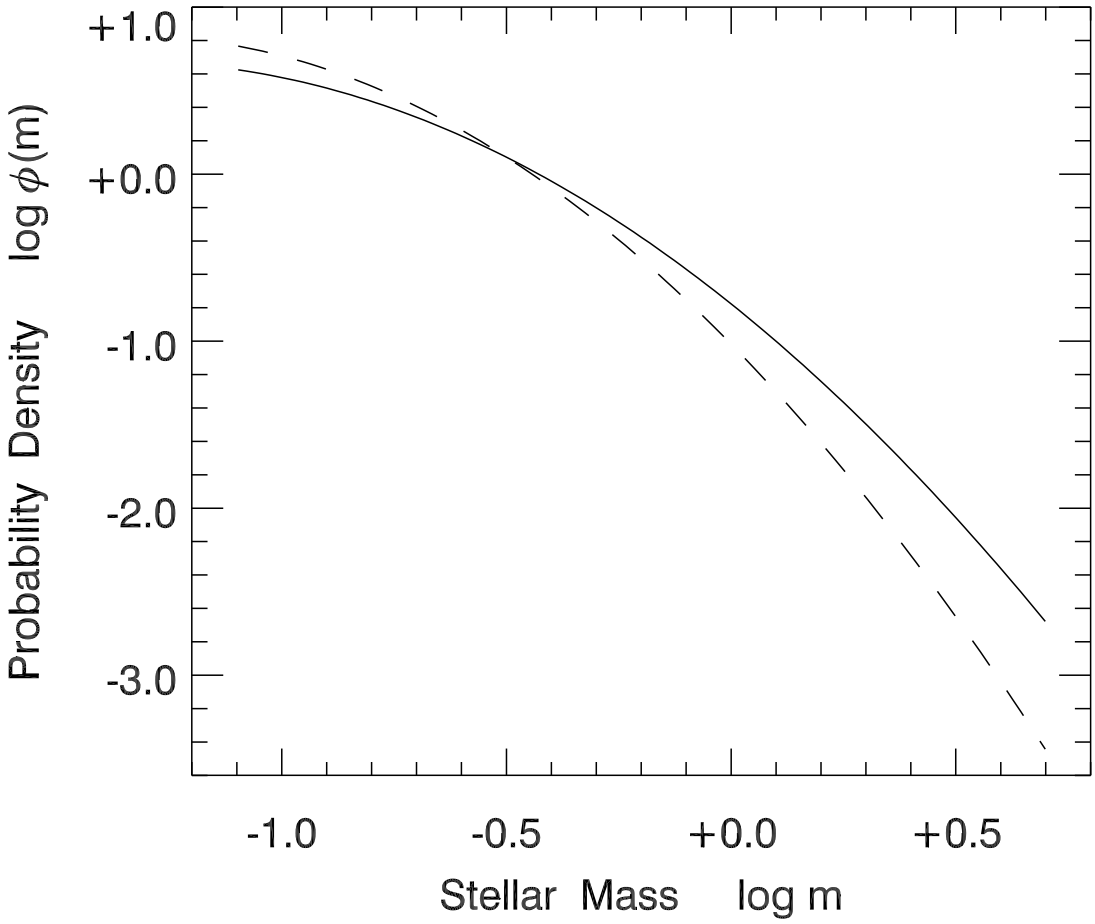

Figure 4.5: Comparison of lognormal fits to the mass functions of Alpha Persei (solid curve) and the Pleiades (dashed curve). Alpha Persei is found to peak at a higher mass and to have a larger width.

creases with time, it was even higher in the cluster's initial configuration. We find a closely analogous result for Alpha Persei.

Binaries in the present-day cluster consist both of those which cannot be resolved in our photometric catalog and those appearing as separate objects. Most of our fainter sources are from the study of Deacon & Hambly (2004), which in turn used the POSS-II plates. The resolution of the latter was $10''$. Adopting this cutoff, we find the unresolved binary fraction in Alpha Persei to be $b = 0.63 \pm 0.03$. This figure is slightly less than that for the Pleiades (0.68).

Given our resolution limit, we may extrapolate to find the total number of binaries, both unresolved and resolved. At the Alpha Persei distance of 176 pc, $10''$ corresponds to a separation of 1800 AU. An edge-on circular binary of exactly this orbital diameter will still be unresolved, since the components spend most of their time closer together. The true minimum separation in this case is 2800 AU. Here, we have divided 1800 AU by $2/\pi$, which is the average of $|\sin\theta|$, for θ randomly distributed between 0 and 2π.

Of course, only a relatively small fraction of binaries are wider than 2800 AU. The average total mass of our unresolved systems is 1.2 $M_\odot$. A binary of that total mass and a 2800 AU separation has a period of 1.3×10^5 yr. What fraction of binaries have even longer periods? If we assume that systems in Alpha Persei follow the period distribution of Duquennoy & Mayor (1991), then 10% of all binary systems would have periods greater than this. Thus the total binary fraction, both resolved and unresolved, would be $0.63/(1-0.10) = 0.70$. The analogous figure was 76% for the Pleiades.

The salient point is that *both* fractions exceed the commonly accepted value of 57% for the total binary fraction in field stars for binaries with G-type primaries (Duquennoy & Mayor 1991). Note, however, that other authors have recently been finding higher binarity even for the field population (see Dawson & Schröder 2010, and references therein). The degree of the discrepancy is therefore still open to question.

We note parenthetically that several authors have obtained much lower binary fractions for Alpha Persei. Patience et al. (2002), using speckle imaging in the near infrared, found that only 9% of the systems they examined contained a binary with separation between 26-581 AU. Extrapolating using the Duquennoy & Mayor (1991) period distribution yields a 30% total binarity. This figure not only falls below our value, but is significantly lower than that for field stars. Makarov (2006) gave an even lower estimate of 20% based on previous studies of the brightest stars in the cluster.

We find that the binary components of Alpha Persei are significantly correlated in mass. In terms of the parameter c from equation (4.3), our best fit value is $c = 0.38 \pm 0.07$, almost identical to the Pleiades value of 0.36. Again, our result means literally that the photometric data is well-reproduced if 38% of the binaries have identical component masses, while the remainder are uncorrelated. Such a sharp division never occurs in reality. Nevertheless, the high degree of mass correlation, however measured, is a significant fact that must be considered in any models of open cluster origin and evolution.

4.3.3 Surface Density

We compute the number and mass surface density profiles following the method of Section 2.1.2. As discussed above, we adopt as our radial coordinate the semimajor axis of the ellipse passing through each observed source. We obtain density profiles by dividing the cluster into nested elliptical bins. The common orientation and eccentricity of the ellipses are obtained by using the density-weighted second moment of the source distribution (recall Section 4.2.2).

Figure 4.6 displays the number (filled circles) and mass (open circles) surface densities for Alpha Persei. It is apparent that the two profiles are nearly identical, in sharp contrast to the Pleiades (see Figure 3.6 in Section 3.2.3). The similarity in profiles seen here means that small patches within the cluster have nearly the same distribution of stellar mass. In other words, there is very little degree of mass segregation, a point to which we shall return presently.

A second important feature of Alpha Persei is its relatively distended state. To quantify matters, we fit a King (1962) model to each empirical profile. A King model is characterized by the central density, Σ_0, projected core radius, R_c, and the concentration parameter $c_K \equiv \log(R_t/R_c)$, where R_t is the projected tidal radius (recall Section 2.3.1). The solid curve in Figure 4.6 is the fit for the number density. Here the core radius is $R_c = 4.6 \pm 0.4$ pc. In contrast, the Pleiades has 2.0 pc, despite its significantly higher total population. The central surface number density in Alpha Persei is $\Sigma_0 = 4.3 \pm 0.4$ pc^{-2}, a full order of magnitude below the Pleiades figure. The concentration parameter, $c_K = 0.90 \pm 0.04$, is also lower than for the Pleiades (0.99).

The dashed curve in Figure 4.6 is a King fit to the surface mass density. Here the core radius is 4.3$\pm$0.9 pc, the central density is 5.2$\pm$1.2 M$_\odot$ pc^{-2}, and the concentration parameter is $c_K = 0.97 \pm 0.14$. These figures are again quite similar to those characterizing the number density profile. In contrast, the central mass density in the Pleiades is 50 M$_\odot$ pc^{-2}.

The simplest way to quantify the degree of mass segregation in Alpha Persei is to consider the average stellar mass in each elliptical bin. This figure follows by taking the ratio of the calculated mass density to number density at every radius. Figure 4.7 plots the result. The average mass is about the same throughout the cluster, with any deviation being consistent with random scatter. In other words, there is no correlation between a star's mass and its location within the cluster. The most massive star by far, α Per itself, is offset more than a degree from the center (Figure 4.3).

A second, and more complete, means of characterizing mass segregation is through G, the Gini coefficient, introduced in Section 2.1.3. To calculate G, recall that we first determine the cumulative number fraction $f_N(R)$, defined as the total fraction of cluster members within the elliptical bin of semimajor axis R. Similarly, we consider the analogous cumulative mass function $f_M(R)$. Figure 4.8 plots these two quantities against each other. A hypothetical cluster with no mass segregation appears as the straight dotted line in this plot. It is evident that Alpha Persei is very nearly such a cluster. Again, the contrast with the Pleiades, represented in the figure by the dashed curve, is striking.

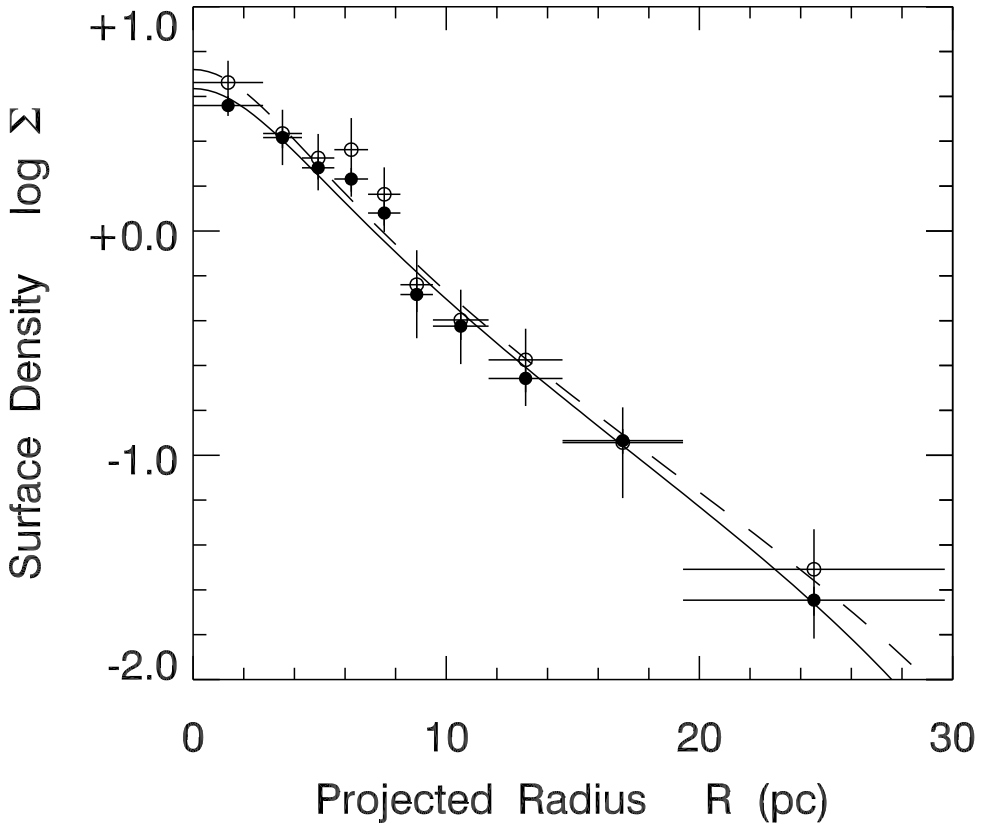

Figure 4.6: Surface density distribution in Alpha Persei. The filled circles represent the surface number density (pc^{-2}), displayed on a logarithmic scale. Open circles are the mass density, in $M_\odot$ pc^{-2}. The solid and dashed smooth curves are King model fits to each, respectively.

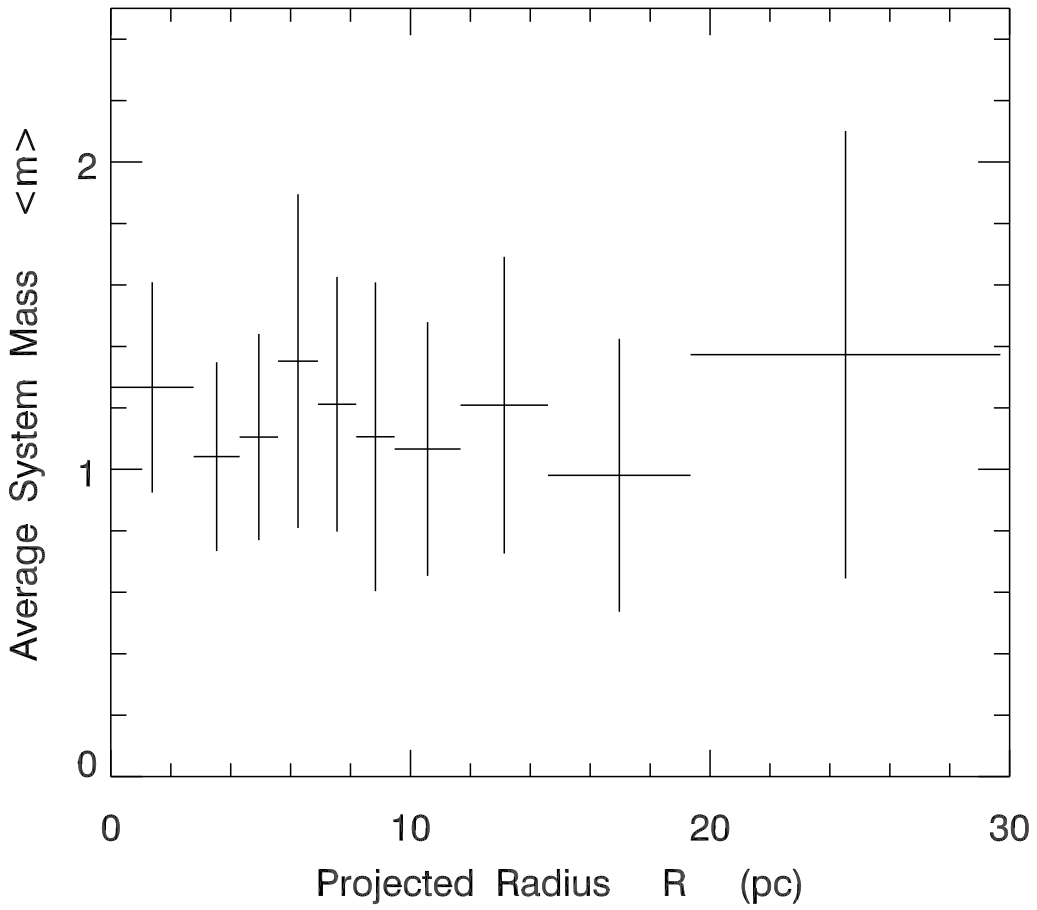

Figure 4.7: Average system mass (primaries plus secondaries) as a function of projected cluster radius.

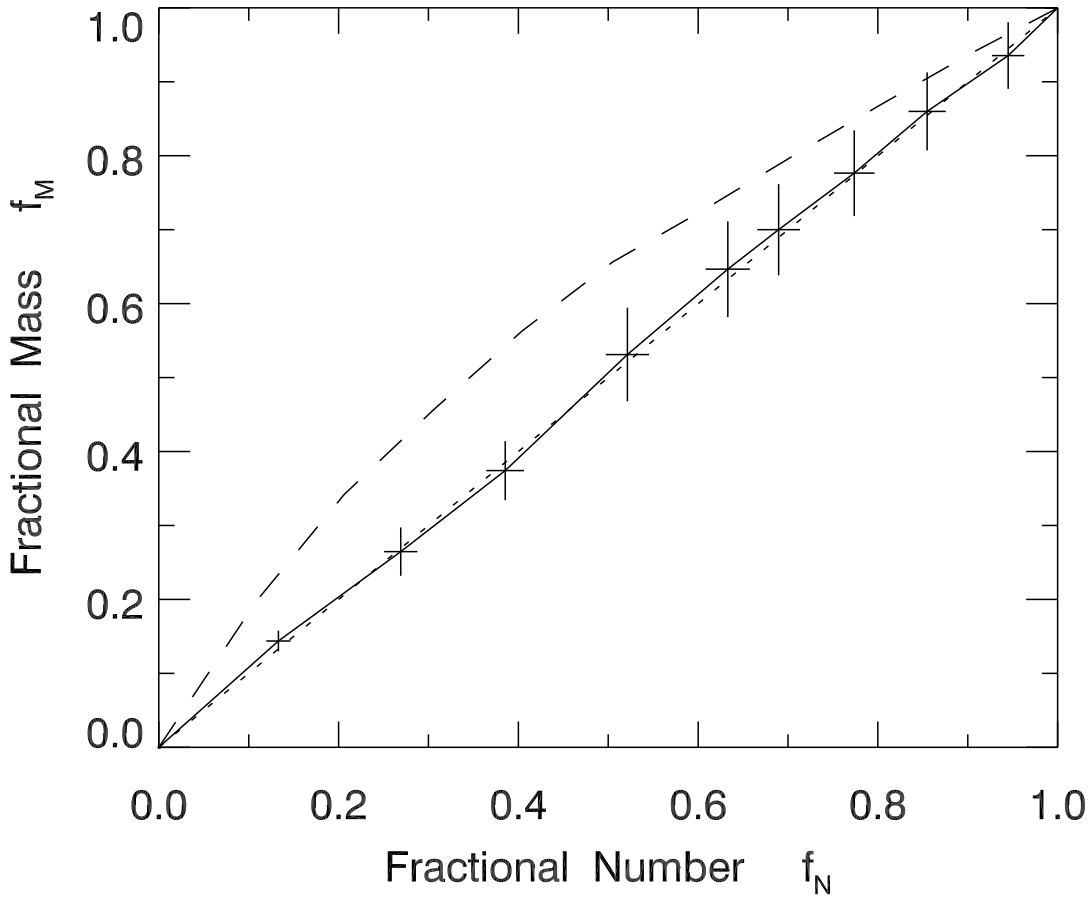

Figure 4.8: Fractional mass versus fractional number. The data points and error bars, along with the solid curve are for Alpha Persei. The dashed curve shows the same plot for the Pleiades for comparison. In both cases, the radial bins contain roughly equal numbers of stars. Finally, the dotted diagonal is the hypothetical result for no mass segregation.

Table 4.1: Initial Alpha Persei Parameters

Symbol	Definition	Optimal Value
n	Polytropic index	2.7 ± 0.3
$N_{\rm tot}$	Number of stellar systems	700 ± 50
r_v	Virial radius	4.7 ± 1.0 pc
m_0	Centroid of mass function	0.21 ± 0.06 $M_\odot$
σ_m	Width of mass function	0.51 ± 0.05
α	Exponent in mass function	-2.23 ± 0.10
b	Fraction of binaries	0.83 ± 0.05
γ	Mass correlation in binaries	0.72 ± 0.09
β	Degree of mass segregation	0.0 ± 0.3

More quantitatively, we compute G as twice the area between the f_M-f_N curve and the diagonal line. We find, for Alpha Persei, that $G = 0.005 \pm 0.04$, a result consistent with no mass segregation. The Pleiades figure of $G = 0.20$ presents a very different picture.

4.4 Evolutionary Simulations

4.4.1 Numerical Procedure

Having established the present-day properties of Alpha Persei, we next seek to understand its origins and evolution, both in the past and future. We again use the N-body code Starlab (Portegies Zwart et al. 2001, Appendix B) to evolve the cluster. We include both mass loss through stellar evolution and the effect of the Galactic tidal field. Our strategy is to vary the properties of the initial state, i.e. that immediately following gas dissipation, until the system evolves over 90 Myr to one most resembling the present day cluster.

We take as our starting point a spherically symmetric polytrope with a single-star mass function that is a lognormal tied to a power law tail at high masses. A fraction of the systems are binaries with correlated masses. Table 4.1 lists the full set of 9 input parameters. Also given are the definitions of each parameter, which are the same as in Section 2.2. We remind the reader that m_0 and σ_m are the centroid and width, respectively, of the lognormal portion of the mass function, while α is the exponent of the power law tail (see equation (2.108) of Section 2.2.2). The index γ measures the degree of mass correlation within binaries, according to the prescription of equation 2.122 in Section 2.2.2. Finally, β characterizes mass segregation (Section 2.2.2). The value $\beta = 0$ describes a cluster in which the mass of a system (binary or single) is uncorrelated to its energy within the cluster, while $\beta = 1$ establishes a one-to-one ordered pairing of mass and energy, i.e. perfect mass segregation.

Since we used elliptical bins to analyze the spatial structure of the present-day clsuter, we used similar bins to characterize the simulations. At each timestep, we find the second moment, $\mathcal{Q}'_{ij}$. Again, the semimajor axis of the now-evolving ellipse serves are the radial

coordinate in establishing profiles. The eccentricity itself becomes another parameter used to judge the goodness of fit between the simulated and the actual clusters. Throughout the evolution, we view the cluster in projection using the same line of sight relative to the Galactocentric radius as the real system.

Because Alpha Persei is found to be on the verge of tidal disruption (see Section 4.4.4 below), the outcome of any simulation is sensitive to stochastic sampling effects and small changes in the input parameters. As a result, the systematic optimization procedure outlined in Section 2.3.3 did not work. The derivative matrix, $\mathcal{D}$, characterizing the relative changes of output to input values, poorly sampled the actual shape of the χ^2 surface, leading to erroneous initial states. While we still computed χ^2 for each input parameter set, we took new steps in a trial and error manner. In the end, we settled on an initial state when no changes in the input parameters noticably improved the fit. As described below, we were able to obtain a fairly good match to the present-day cluster, even without utilizing a more rigourous minimization scheme.

Section 2.3.3 described how we obtained uncertainty estimates for our input parameters using the derivative matrix $\mathcal{D}$. Since the latter was now unreliable, we also had to determine these uncertainties in a less formal manner. In practice, we performed several runs that varyied a single parameter at a time around the best fit value. We then estimated the range of that parameter resulting in an acceptable match, as gauged by uncertainties in the observed quantities. The right-hand column of Table 4.1 lists the resulting errors.

Table 4.2 gives the set of 12 output parameters used to compare the simulated and real clusters. The definitions should be self-explanatory, and again follow those of Section 2.3.1, with the addition of the global eccentricity e. As in Section 2.3.1, we characterized the final single-star mass function by a simple lognormal, whose parameters m_0 and σ_m are listed here. Uncertainties in the observed Alpha Persei values are those previously given in Section 4.3. To calculate uncertanties in the output simulation parameters we did 25 runs using identical input values. The uncertainties listed in Table 4.2 are then the standard deviations of the variations due to stochastic sampling of the various distribution functions.

4.4.2 Initial State

Table 4.1 gives the values of the parameters characterizing our best fit initial state. This configuration is a spherical, $n = 2.7$ polytrope. Such a system has a center-to-average volumetric density contrast of 32. Since our initial state has no mass segregation ($\beta = 0$) this contrast applies to both number and mass density. We noted in Section 2.2.1 that the family of analytic King (1966) models approaches an $n = 2.5$ polytrope as the dimensionless central potential W_0, which also measures central concentration, goes to 0. Our $n = 2.7$ polytrope is very similar to a $W_0 = 0.6$ King model. In contrast, the initial Pleiades was a mass-segregated $n = 3.0$ polytrope with a mass density contrast of 100.

As already mentioned, Alpha Persei is currently in the process of dissolving within the Galactic tidal field. Thus an even slightly less concentrated initial state would expand to a much more distended configuration than the present-day system. Conversely, a more

Table 4.2: Evolved Alpha Persei Properties

Symbol	Definition	Calculated Value	Alpha Persei Value
$N_{\rm s}$	Number of point sources	671 ± 24	653 ± 26
N_4	Number of systems with $m > 4$	4 ± 2	1 ± 1
$M_{\rm tot}$	Cluster mass	807 ± 40 $M_\odot$	820 ± 40 $M_\odot$
$b_{\rm unres}$	Unresolved binary fraction	0.63 ± 0.02	0.63 ± 0.03
m_0	Centroid of mass function	0.22 ± 0.03 $M_\odot$	0.19 ± 0.13 $M_\odot$
σ_m	Width of mass function	0.54 ± 0.04	0.52 ± 0.05
γ	Binary correlation index	0.67 ± 0.01	0.67 ± 0.06
R_c	Core radius	5.4 ± 1.3 pc	4.6 ± 0.4 pc
c_K	King concentration parameter	0.69 ± 0.13	0.90 ± 0.04
Σ_0	Central surface density	5.7 ± 2.3 pc^{-2}	4.3 ± 0.4 pc^{-2}
e	Cluster Eccentricity	0.74 ± 0.08	0.70 ± 0.03
G	Gini coefficient	0.06 ± 0.03	0.005 ± 0.04

concentrated state would fall well short of the correct size. The value of the polytropic index n is therefore rather tightly constrained, as seen by the small uncertainty given in Table 4.1.

The initial virial radius, $r_v = 4.7$ pc, is quite large compared to observed, embedded clusters. To make the comparison more precise, note that the projected half-mass radius is 3.1 pc. In contrast, the observed half-light radii of near-infrared embedded clusters range from 0.5 to 1.0 pc (Lada & Lada 2003). Previously, Makarov (2006) also conjectured that the cluster formed as an extended, low-density group.

The dashed curve in Figure 4.9 shows the surface number density profile of the initial state. Again, slight modifications to this initial profile results in an evolved cluster quite dissimilar from the observed one. The solid curve in the figure, an average over 25 simulation runs, is the evolved profile, which is in good agreement with the observational data, shown here as the points with error bars. The decline of the central density with time is in sharp contrast to the standard theoretical picture of dynamical relaxation (e.g. Binney & Tremaine 2008, Chapter 7).

The initial number of stellar systems, $N_{\rm tot} = 700$ is primarily constrained by the need to match N_s, the observed number of point sources today, as well as $M_{\rm tot}$, the present-day total mass. If one were to observe the initial cluster, it would be very binary rich ($b = 0.83$). Some of these binaries would be wide enough to be resolved. We estimate that the initial number of point sources would have been about 760. Thus the decline to the present-day N_s of 671 (see Table 4.2) is substantial, and reflects tidal stripping, as we discuss presently.

We mentioned in Section 4.3.3 that Alpha Persei today exhibits no sign of mass segregation, as revealed quantitatively through the low value of G and the shape of the f_N-f_M curve (recall Figure 4.8). Table 4.1 gives $\beta = 0$, showing, from a different perspective, the lack of mass segregation in the *initial* state. Again, this value of β is necessary to produce an accurate, evolved configuration. By running simulation with varying values for β, we

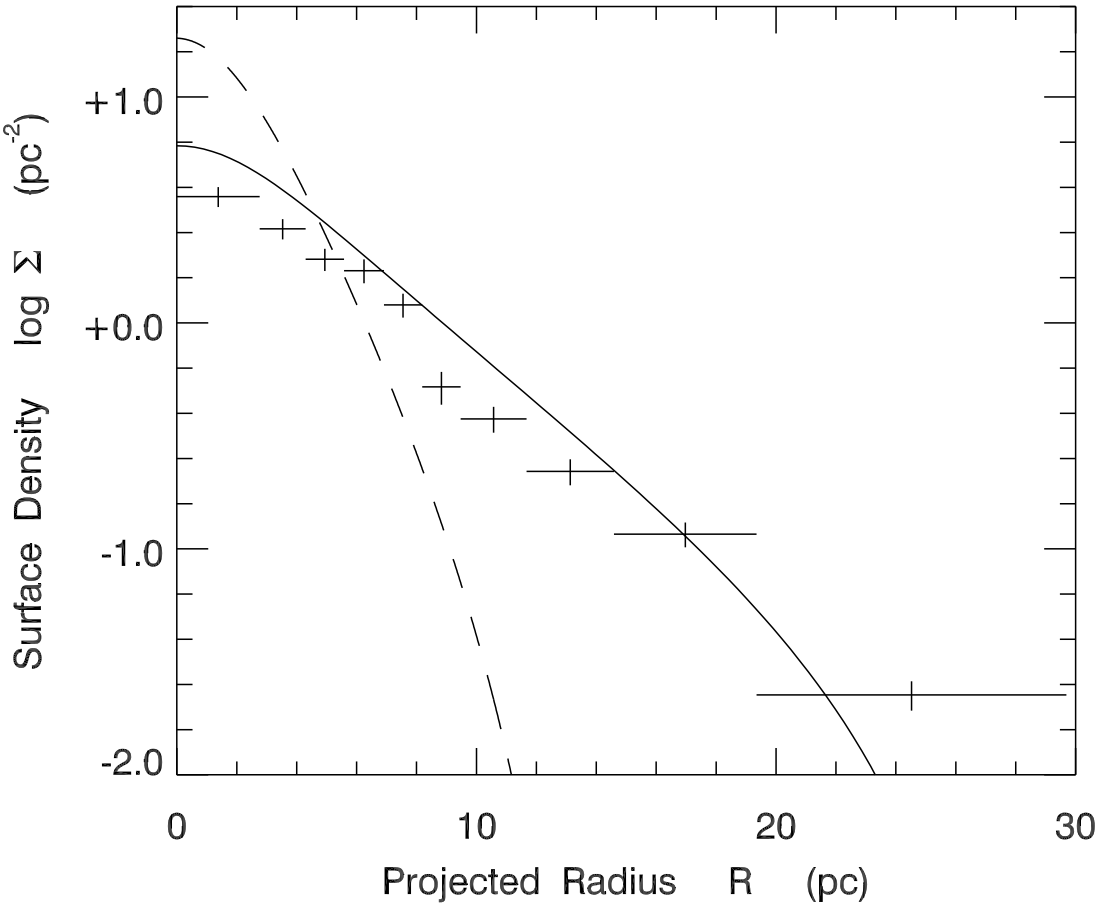

Figure 4.9: Surface number density as a function of projected radius. The dashed curve represents our initial configuration, an $n = 2.7$ polytrope. The solid curve is a King (1962) model fit to our simulation results for the evolved cluster. Table 4.2 lists the parameters for this optimal model. The numerical results displayed are an average of 25 simulation runs. Also shown are the data for Alpha Persei with error bars, taken from Figure 4.6.

found that $\beta = 0.3$ is a rough upper limit, i.e. it produces an evolved state which has an appreciably higher G value. The solid curve in Figure 4.10 shows the present-day f_N-f_M relation for the simulations, again averaged over 25 runs. The result agrees well with the observations, displayed as points with error bars.

Four quantities in Table 4.1, m_0, σ_m, α, and γ, concern the mass function. The mean mass of a single star was initially 0.78 $M_\odot$. This figure may be compared to the analogous one of 0.36 $M_\odot$ for the Pleiades (Section 3.3.1). We see that Alpha Persei had originally, as is true today, an overabundance of relatively massive stars. The slope of the mass function is again set by the need to reproduce the present-day result. Figure 4.11 compares our *evolved* single-star mass function with data points resulting from the maximum likelihood analysis. Here the solid curve is a lognormal fit to the average simulation output.

4.4.3 Past Evolution

We can now describe, based on our suite of simulations, the evolution of the cluster from its initial state to the present epoch. The main trend is an overall expansion of the system. This tendency is already clear in the comparative surface density profiles of Figure 4.9. In addition, Figure 4.12 shows the full variation in time of the virial radius r_v. Note that we obtain r_v by calculating it for a King (1966) model with the same parameters found from the fitting to the surface density profile.

The radius r_v increases in general, but displays a superposed, damped oscillation. Such variation occurs over the crossing time, which is initially about 10 Myr, and gradually increases to about twice that value. Both stellar evolution and the tidally induced loss of members perturb the cluster, which needs to readjust to virial equilibrium as it swells.

Our initial state is spherically symmetric. However, as seen in Figure 4.3, and quantified in Section 4.2.2, Alpha Persei today is highly non-spherical, with an eccentricity of $e = 0.70$. During the course of its simulated evolution, we track the variation of eccentricity; Figure 4.13 displays the result. Because of stochastic sampling of the initial density profile, the calculated e is nonzero even at the start. the initial value, $e = 0.4$ shown in Figure 4.13 corresponds to a major axis only 8% larger than the minor axis. The position angle of the major axis also fluctuates widely at early times.

Beyond this first epoch, the eccentricity grows as expected, but again with large-amplitude oscillations. These are in phase with the oscillations of r_v. Stars escape the cluster primarily through the Lagrange points located directly toward and away from the Galactic center. Differential rotation of the Galaxy carries these stars ahead and behind the cluster, causing the entire system to appear stretched out along the Galactic plane. When the cluster is relatively large, more stars can escape, thus increasing the observed stretching and eccentricity. Analogously, contraction of the cluster reduces the value of e.

The projected surface number density, $\Sigma(R)$, peaks strongly at $R = 0$ (Figure 4.6). As seen in Figure 4.9, however, the central value declined from an even higher level in the past. Figure 4.14 shows the full evolution of the central density. Again, there is the expected overall decline, along with oscillatory behavior. The core radius, R_c, increases from 4.0 to

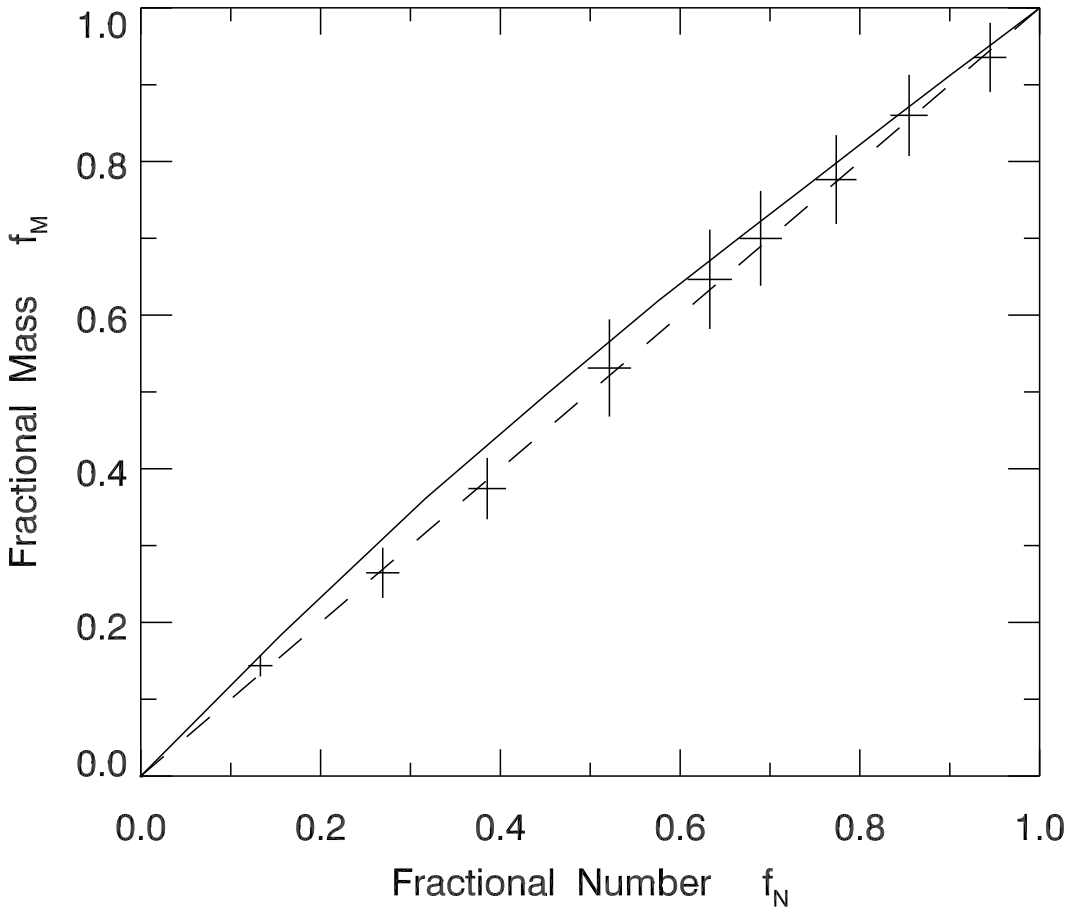

Figure 4.10: Fractional mass versus fractional number. The solid curve shows the average results of our simulations. The crosses represent the actual cluster data with error bars, taken from Figure 4.8. The dashed diagonal line is the hypothetical result for zero mass segregation.

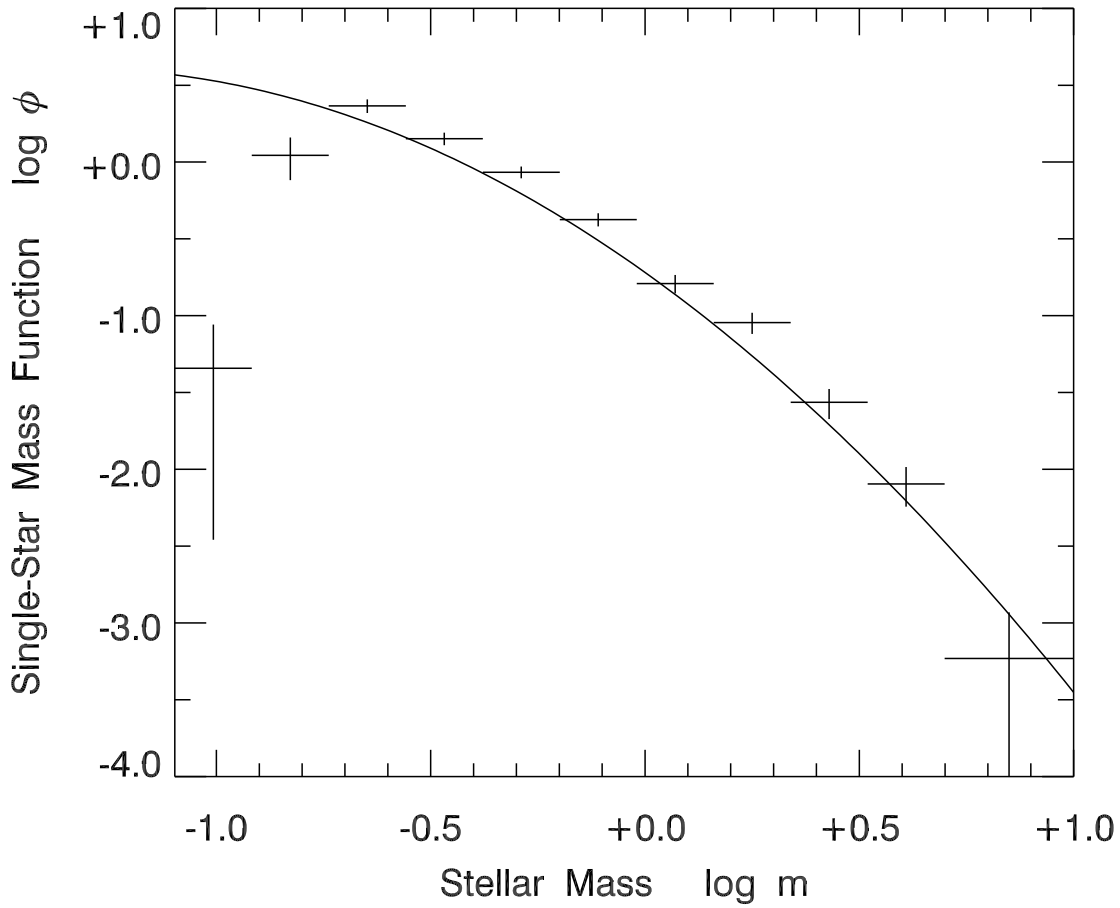

Figure 4.11: Single-star mass function for the evolved cluster. The solid curve is a lognormal fit to simulation data. Also shown are Alpha Persei data, with error bars, from Figure 4.4.

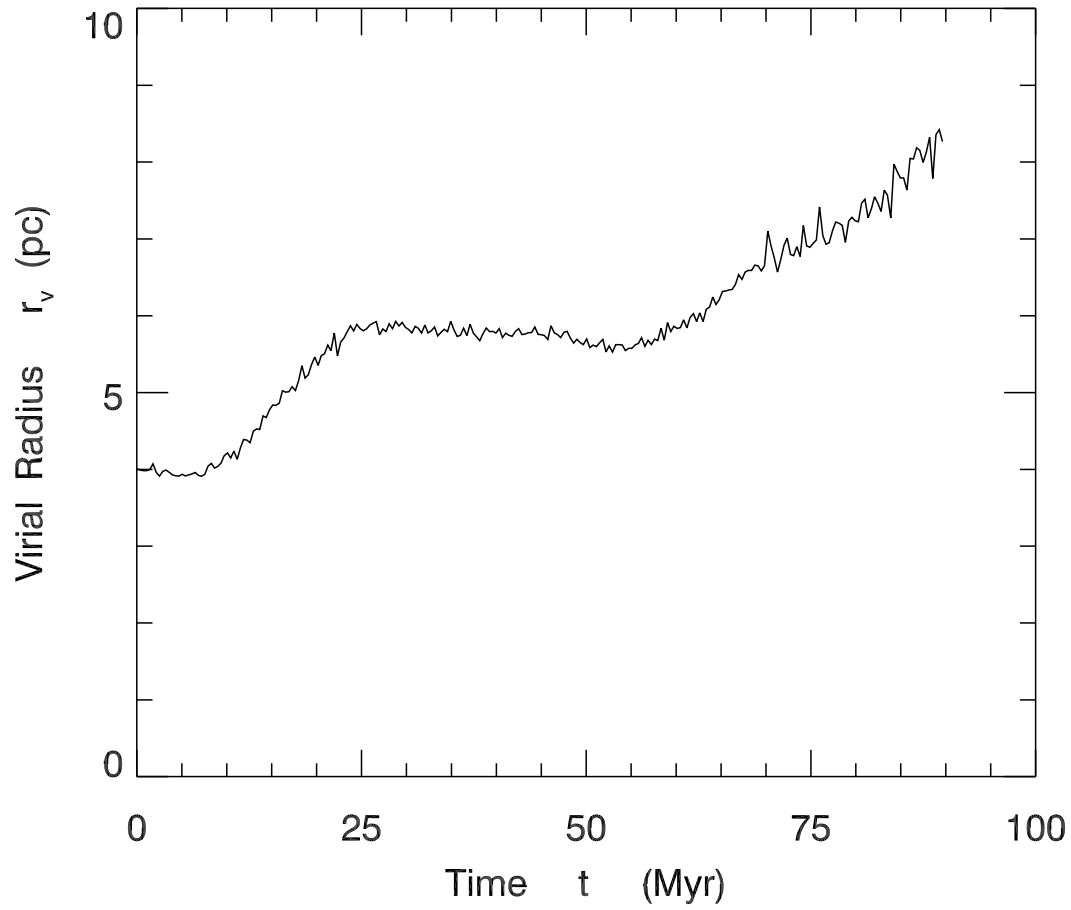

Figure 4.12: Evolution of the three-dimensional virial radius, r_v averaged over 25 simulation runs.

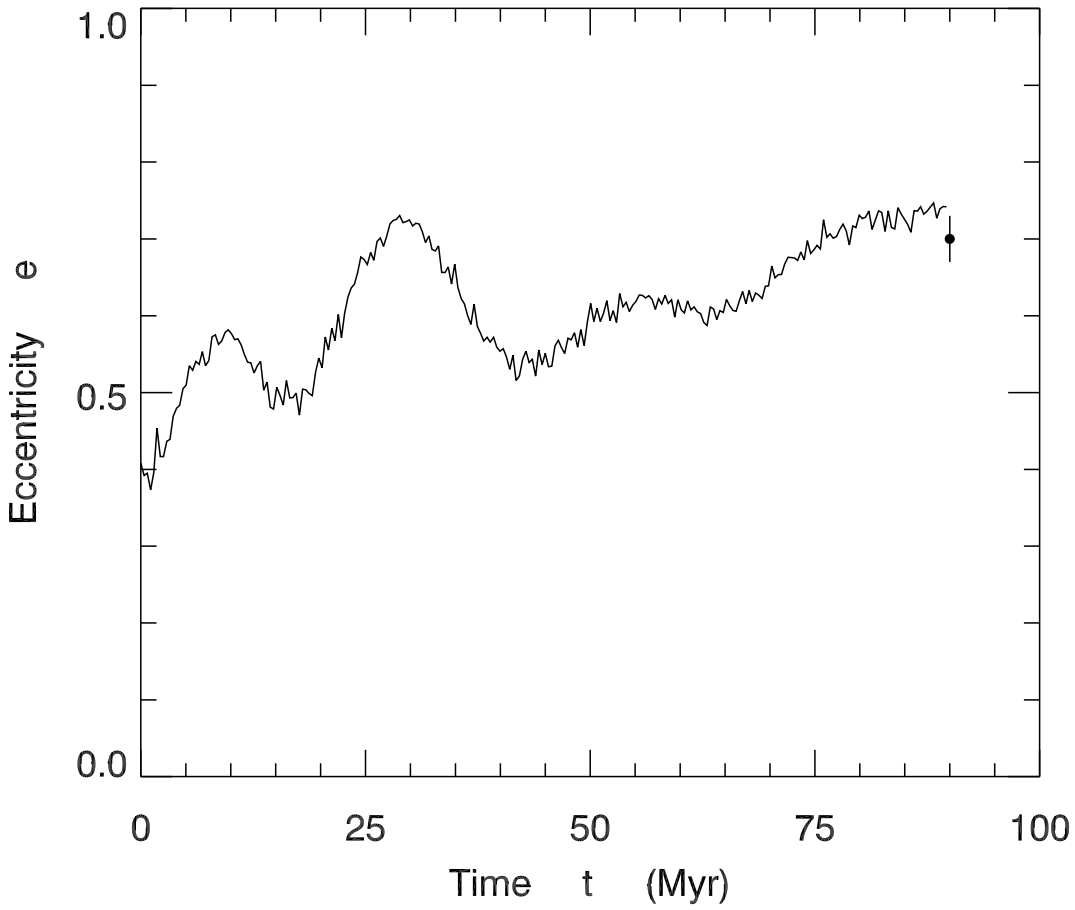

Figure 4.13: Evolution of the cluster eccentricity. Shown is the average over 25 simulation results. The observed Alpha Persei value is represented by the data point.

5.4 pc over this portion of the cluster's history. During the same interval, the central surface number density, Σ_0, falls by a factor of 0.4, which is less than $(4.0/5.4)^2 = 0.55$. The number of systems in the core must therefore also be shrinking.

Initially, Alpha Persei had a total mass of 960 $M_\odot$. By the present time, this figure has fallen to 807 $M_\odot$ in the simulations, in close agreement with the 820 $M_\odot$ obtained through statistical analysis of the cluster. The mass loss over 90 Myr thus amounts to some 16%. This depletion, in the presence of the Galactic tidal field, is primarily driving the expansion. The trend will only accelerate into the future, as we now describe.

4.4.4 Future Evolution

Just as we have simulated the past history of Alpha Persei, we may also predict its evolution far into the future. Following Spitzer (1958), it is still believed that open clusters are usually destroyed by the tidal gravitational field of a giant molecular complex. We do not attempt to model such interactions here. However, Starlab does include the effects of the *Galactic* tidal field by applying both an external potential to the cluster and adding a Coriolis force to individual stellar systems. Beginning with the same initial state as before, we follow the cluster's evolution for a total of 300 Myr. As we shall see, this amount of time is sufficient to fully describe the future of Alpha Persei.

The stretching and evaporative effects of the Galactic tidal field have already been significant for Alpha Persei up to its present age of 90 Myr. Beyond this point, the cluster will continue to expand and dissolve at an accelerating rate. As seen in Figure 4.15, the central density Σ_0 keeps declining. The falloff is roughly exponential, with a characteristic timescale of 90 Myr. Even now, the system is well on its way to dissolution.

The decline in the population accelerates as stars are tidally stripped, leaving less mass to bind the remaining cluster. It is the lighter stars within the cluster's outer halo that preferentially escape. Consequently, while the total number of stars *decreases*, the average mass of the remaining cluster members *increases*. Figure 4.16 shows both these trends. Displayed here is N_s, the number of systems contained within the cluster's present-day radius of 30 pc. By 300 Myr, the total membership has fallen to a few dozen systems. The loss of the most massive members, through stellar evolution, caused the average system mass, $\langle m \rangle$, to fall initially to its present-day value. In the future, however, $\langle m \rangle$ will rise because of the escape of the lightest systems. The increased jitter in the $\langle m \rangle$ curve at late times reflects statistical noise associated with the decreased number of systems.

The mass loss driving the system's overall expansion stems initially from stellar evolution, and later from evaporation of stars in the Galactic tidal field. Indeed, the cluster will not remain intact much longer. Figure 4.17 shows graphically how the cluster will appear far in the future. Here we display positions of the member systems projected into the Galactic plane, both at the present time and at $t = 250$ Myr. One already sees at present a significant elongation along the direction toward the Galactic Center. Stars that leave tend to do so along that direction. But any appreciable excursion leads, because of the Galaxy's differential rotation, to a change in angular speed. As a result, two tidal streams develop

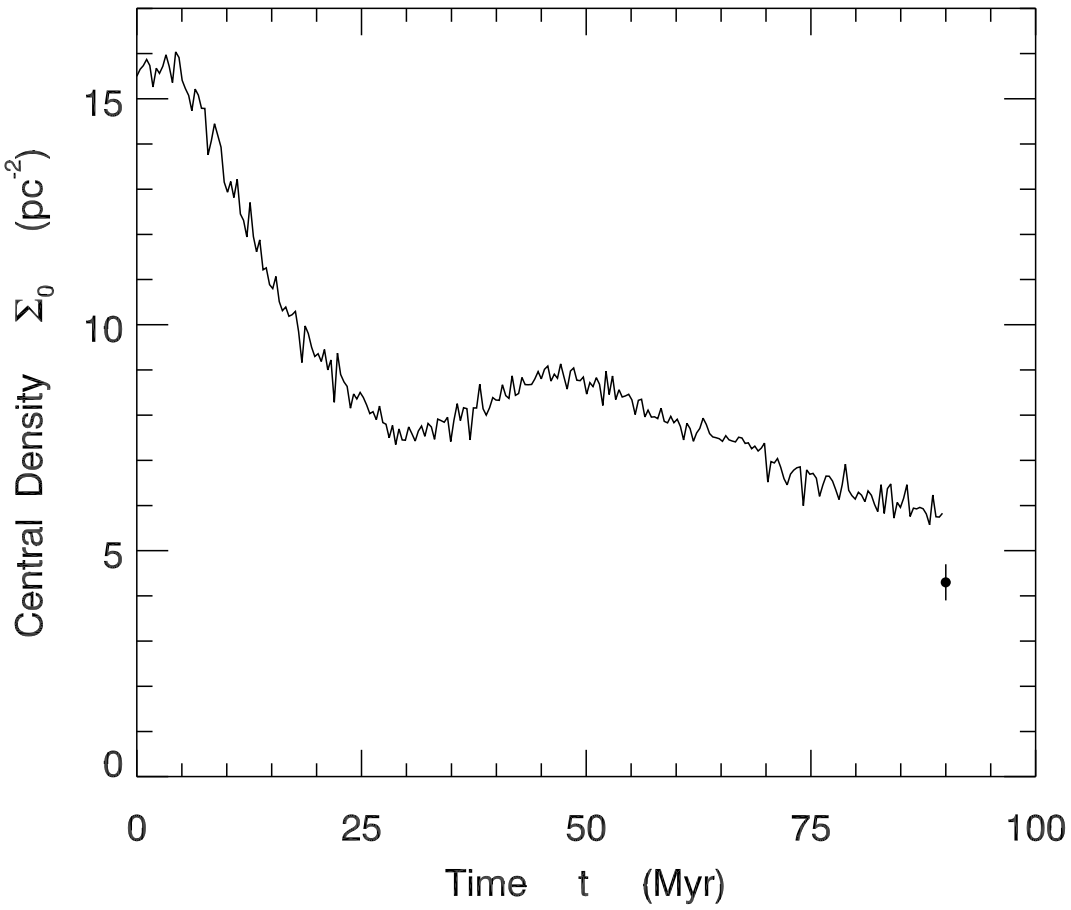

Figure 4.14: Evolution of the central surface number density. Shown is the average over 25 simulation results. The observed Alpha Persei value is represented by the data point.

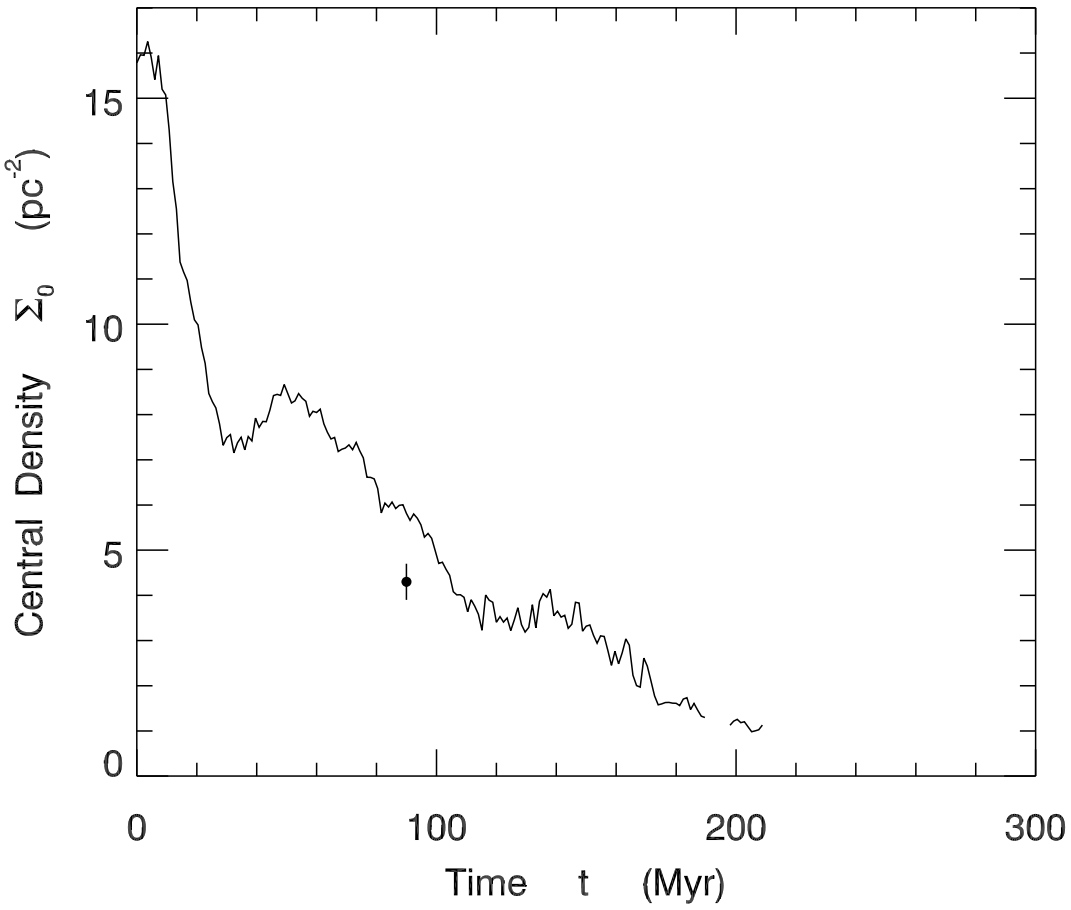

Figure 4.15: Evolution of the central surface number density over a total time of 300 Myr, averaged over 6 simulation runs. The data point is the present-day Alpha Persei value, with errors indicated. Beyond 200 Myr, the cluster was usually too sparse to fit to a King (1962) model.

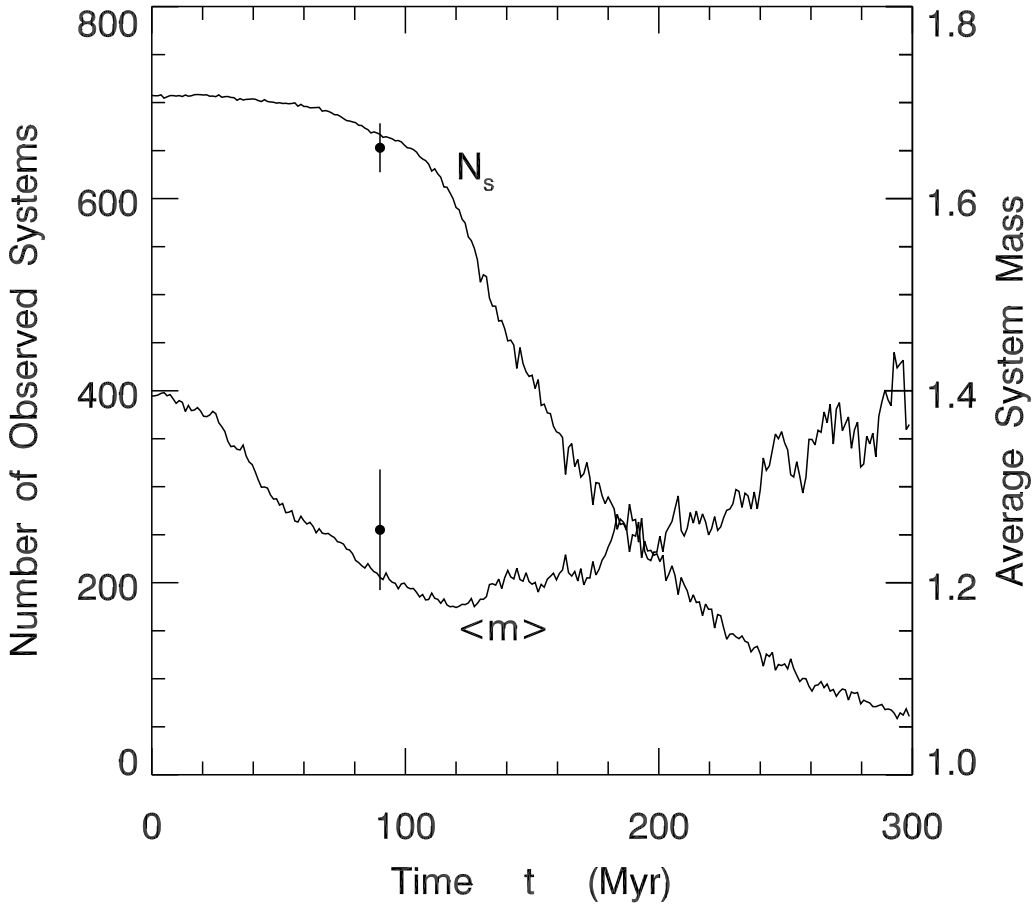

Figure 4.16: Evolution of the total number of stellar systems, N_s, and the average system mass $\langle m \rangle$, over 300 Myr. Shown is the average of 6 simulation runs. Only systems with primary mass over 0.15 $M_\odot$ are included. Both quantities refer to systems within the current observed cluster radius of 30 pc. The data points show the current Alpha Persei values, with error bars.

that are orthogonal to the Galactocentric radius. These streams are present in both panels of Figure 4.17 but are especially noticeable in the diminished cluster shown at the right.

4.5 Summary and Discussion of Alpha Persei

By combining membership and photometric data from more than a dozen previous studies, we have compiled the most complete catalog of Alpha Persei members yet published. This catalog includes the brightest members, which have long been documented, and should be reasonably complete down to $I \approx 16$ mag, while containing many fainter sources as well. It also spans the cluster's rather large areal extent. In addition to providing a starting point for our own analysis, the catalog itself should prove useful to future researchers.

4.5.1 Alpha Persei and the Pleiades

We have applied the maximum likelihood technique developed in Section 2.1.2 to assess the distribution of stellar mass and the incidence of binaries in the present-day Alpha Persei. We also quantified its density profile and lack of mass segregation. We then employed N-body simulations to determine the properties of the cluster in its earliest gas-free state, and to examine its past and future evolution. It is instructive to compare these results to those for the Pleiades (Chatper 3).

The most immediate difference is the shape of the clusters today. Although the Pleiades exhibits a modest elongation (Raboud & Mermilliod 1998), the effect is much more pronounced in Alpha Persei. Our simulations demonstrate that both clusters could have begun as nearly spherical configurations. The growing elongation of Alpha Persei is due to the Galactic tidal field stretching a system that was initially less centrally condensed. At present, the projected core radius of Alpha Persei (4.6 pc) far exceeds that of the Pleaides (2.0 pc), yet another manifestation of this external field.

Initially the clusters had similar sizes. The virial radius of Alpha Persei was 4.7 pc, only slightly greater than the corresponding figure of 4.0 pc for the Pleiades. Yet the internal mass densities were very different. Pronounced mass segregation in the Pleiades, even at this earliest epoch, gave it a projected half-mass radius of 2.0 pc. In Alpha Persei, mass segregation was completely absent, as it is today. The projected half-mass radius was far larger, about 4.0 pc. In both cases, these half-mass radii exceed the analogous half-light radii observed in present-day embedded clusters. The most likely explanation is that clusters generically expand in the process of dispersing the natal gas. There is evidence for such an early expansion phase in extragalactic clusters (see Bastian et al. 2008, and references therein). Why Alpha Persei expanded more than the Pleiades and whether this difference somehow relates to the lack of mass segregation are topics for future investigation.

Another significant difference between the two clusters is the overall distribution of stellar mass. The single star mass distribution of Alpha Persei is more biased toward higher-mass objects. When comparing systems at the present time, it is important to recognize

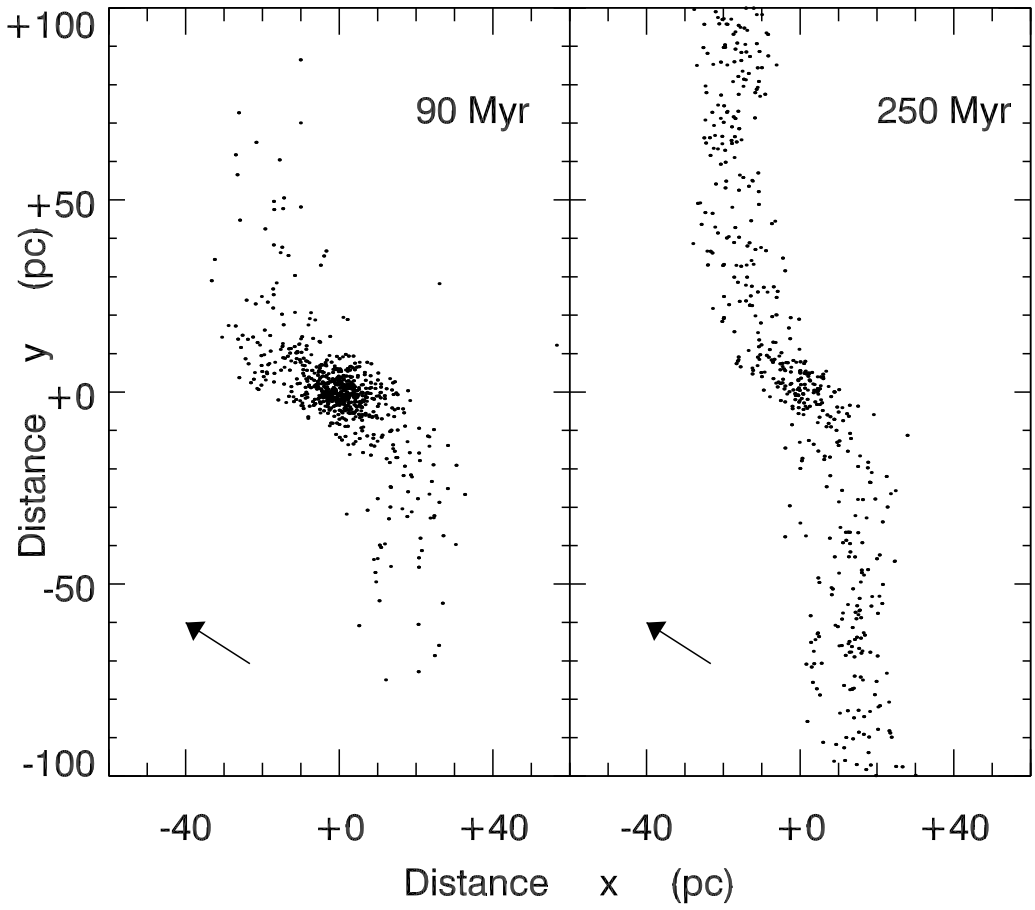

Figure 4.17: Positions of Alpha Persei members projected onto the Galactic plane. The data are from a single, representative simulation, for the two epochs indicated. A terrestrial observer is located 176 pc in the direction of the arrow. The Galactic Center is 8 kpc in the negative x-direction. Galactic rotation is in the positive y-direction.

the fact that our Alpha Persei catalog is more incomplete for the faintest members. Even accounting for the greater degree of incompleteness, the difference in the mass functions today remains, and was also present at the earliest epoch (Section 4.3.1).

Both Alpha Persei and the Pleiades currently have a high binary fraction compared to the field population. This high binarity was also present initially. It is tempting to identify this feature as a key property of developing open clusters. Before doing so, we should remind ourselves that our estimate of the binary fraction is based entirely on photometry. That is, it reflects the overabundance of point sources brighter than the single-star isochrone. We therefore conclude, by examining more critically the potential sources of photometric error.

4.5.2 Sources of Uncertainty

All photometric measurements have some intrinsic error. In our maximum likelihood analysis, we incorporate this error into the response matrix (see Section 2.1.2). The effect, in any case, is a symmetric scatter about the true answer. Thus measurement error displaces as many sources above the fiducial isochrone as below it, and cannot effect the inferred binarity.

We have neglected the finite thickness of the cluster, thereby introducing another uncertainty. For a King model with $R_c = 4.6$ pc and $c_K = 0.90$, as we find for Alpha Persei today, the mean distance from the plane of the sky is 4.5 pc. Such a distance produces a scatter of only 0.06 magnitudes in any measured photometric flux. We reran the analysis, adding this term in quadrature to the intrinsic photometric error. The binary fraction was unchanged. This result is not suprising, since the error associated with finite cluster thickness is again, a symmetric one.

One source of *systematic* error is the cluster distance. In this study, we have used the figure of 176 pc found by Pinsonneault et al. (1998) through main sequence fitting. Other recent distance determinations include 183 pc (van Leeuwen 1999) and 190 pc (Robichon et al. 1999). These are based on Hipparcos data, whose accuracy on cluster parallax measurements has been called into question (see discussions in Pinsonneault et al. 1998; Soderblom et al. 2005). Even so, a larger distance would imply a brighter absolute magnitude for the stars, thus moving them even higher above the isochrone. The result would be an even higher b-value. In order to reproduce the field star estimate of 57% (Duquennoy & Mayor 1991), our distance to Alpha Persei would need to be reduced by 10 pc. Thus far, no observational studies have indicated such a change.

Our method assesses binarity solely based on photometry, and thus we cannot distinguish between physically linked pairs and chance alignments. Could it be that our high binary fraction is in fact due to such superpositions of unrelated stars? The resolution limit of our data is $10''$, or $\Delta R_0 = 1800$ AU at the distance of Alpha Persei (see Section 4.3.2). Consider a star at a projected radius R from the cluster center. The average number of neighboring stars within ΔR_0 is $\pi \Delta R_0^2 n_s(R)$, where $n_s(R)$ is the projected surface number density at R. Now each cluster-centered annulus of width dR contains $2\pi n_s R dR$ stars.

Integrating over all radii yields the total number of chance alignments in the cluster:

$$N_{\rm chance} = 2\pi^2 \Delta R_0^2 \int_0^{R_t} n_s^2(R) R dR, \tag{4.17}$$

where R_t is the cluster's outer radius. Using $n_s(R)$ from Figure 4.6 and $R_t = 30$ pc, we find $N_{\rm chance} = 0.2$. Chance alignments of cluster members therefore have no quantitative impact.

The most significant potential source of systematic error is the cluster age. We adopted here the figure of 90 Myr from Stauffer et al. (1999), based on observations of the lithium depletion boundary. Other studies have estimated it to be as young as 50 Myr (Meynet et al. 1993), though most find the age to be between these two extremes (Ventura et al. 1998; Basri & Martín 1999), with the more recent studies favoring higher values. The isochrone for a younger cluster would be brighter, decreasing the number of stars above it, and thus decreasing the inferred binary fraction. For an age of about 70 Myr, our analysis would give a b-value close to the canonical 0.57. From Figure 3 of Stauffer et al. (1998), this age corresponds to a lithium edge at $M_I \approx 11.0$ mag, or $I \approx 17.3$ mag at the distance to Alpha Persei. This result may be compared with the value of $I = 17.7$ mag estimated by Stauffer et al. (1999). The authors give their uncertainty as 0.15 mag, so the younger age is in disagreement, though not by a large amount.

With this caveat in mind, we conclude that Alpha Persei began its life as a relatively extended system with a high binarity and no mass segregation. Effects such as mass loss due to stellar evolution and heating from this binary population helped to expand the cluster, but the dominant influence throughout its history has been the Galactic tidal field. This field has severely stretched the cluster and will increasingly strip away lower mass members. It appears that Alpha Persei is already beginning to dissolve, and is unlikely to survive beyond an age of 300 Myr.

4.A Alpha Persei Membership Catalog

Here we present the full catalog of stars in our study. The position of the associated 2MASS point source is given, along with its B-, V-, R_C-, I_C-, J-, H-, and K_s-band photometry. B-, V-, R_C, and I_C-band photometry is from the source indicated. The 17th column gives our membership determination based on the determinations of previous studies. See Section 4.1 for details. The final column lists the names used for the each source in the literature.

Table 4.3: Positions and photometry of candidate Alpha Persei members.

RA[a] (h m s)	Dec[a] (d m s)	B	Ref[b]	V	Ref[b]	R_C	Ref[b]	I_C	Ref[b]	J	σ_J	H	σ_H	K_s	σ_K	Mem[c]	Names[d]
02 51 51.83	+49 01 10.4	···		···		17.551	9	15.661	9	14.357	0.032	13.597	0.037	13.442	0.046	Y	DH 1
02 52 00.92	+48 58 40.4	···		···		16.753	9	15.255	9	13.981	0.028	13.327	0.028	13.088	0.038	Y	DH 2
02 52 39.93	+48 48 59.6	7.050	10	7.040	10	···		7.060	11	6.973	0.027	7.027	0.038	7.023	0.024	Y	MA 1, HD 17744
02 53 23.05	+48 12 22.1	···		···		11.545	9	11.308	9	10.688	0.020	10.373	0.018	10.317	0.015	Y	DH 3
02 53 45.28	+47 26 03.1	···		···		14.487	9	13.762	9	13.111	0.024	12.560	0.031	12.460	0.024	Y	DH 4
02 54 12.07	+47 56 54.5	···		···		15.738	9	14.646	9	13.725	0.030	13.062	0.036	12.782	0.028	Y	DH 5
02 54 32.81	+47 48 41.9	···		···		17.150	9	15.044	9	13.769	0.029	13.218	0.033	12.987	0.027	Y	DH 6
02 54 55.70	+47 46 34.5	···		···		18.051	9	15.835	9	14.814	0.039	14.142	0.054	14.016	0.051	Y	DH 7
02 55 20.95	+49 15 37.1	···		···		17.213	9	15.517	9	13.935	0.028	13.288	0.033	13.045	0.033	Y	DH 8
02 56 25.68	+50 54 17.2	···		···		17.956	9	16.197	9	14.598	0.036	13.978	0.041	13.656	0.048	Y	DH 9
02 57 26.33	+49 38 51.1	···		···		18.557	9	16.803	9	14.952	0.041	14.290	0.047	13.931	0.044	Y	DH 10
02 57 41.80	+48 12 57.5	···		···		16.611	9	14.960	9	13.795	0.028	13.124	0.027	12.891	0.026	Y	DH 11
02 57 54.09	+48 52 43.3	8.960	10	8.710	10	···		8.430	11	8.204	0.027	8.158	0.029	8.121	0.027	Y	MA 2, HD 18280
02 58 17.63	+48 28 00.6	···		···		18.902	9	16.673	9	15.229	0.045	14.573	0.057	14.175	0.058	Y	DH 12
03 00 35.59	+51 54 53.6	···		···		17.291	9	15.588	9	13.629	0.025	12.980	0.026	12.711	0.021	Y	DH 13
03 00 52.21	+52 21 06.2	4.957	3	5.000	3	···		5.300	11	5.323	0.037	5.398	0.021	5.429	0.021	Y	HD 18537
03 00 53.13	+51 51 51.2	···		···		14.167	9	13.692	9	11.883	0.022	11.198	0.022	11.032	0.018	Y	DH 14
03 00 53.52	+52 21 07.2	6.740	3	6.740	3	···		6.190	11	6.652	0.023	6.672	0.040	6.658	0.020	Y	HD 18538
03 01 21.36	+48 35 23.6	···		···		15.864	9	14.717	9	13.195	0.023	12.457	0.023	12.257	0.020	Y	DH 15
03 01 29.07	+47 42 41.6	···		···		16.731	9	15.339	9	14.206	0.031	13.601	0.031	13.357	0.034	Y	DH 16
03 01 54.55	+48 37 59.1	···		···		17.678	9	16.148	9	14.826	0.034	14.175	0.040	13.909	0.041	Y	DH 17
03 02 04.04	+50 12 13.4	···		···		18.188	9	16.266	9	14.302	0.031	13.621	0.027	13.332	0.028	Y	DH 18
03 02 07.67	+50 25 24.4	···		···		16.696	9	15.399	9	13.572	0.025	12.876	0.026	12.583	0.024	Y	DH 19
03 02 21.42	+50 33 50.9	···		···		17.743	9	16.100	9	14.110	0.029	13.398	0.033	13.099	0.026	Y	DH 20
03 02 32.46	+46 50 52.1	···		···		18.184	9	15.881	9	14.723	0.038	14.037	0.042	13.703	0.041	Y	DH 21
03 03 24.36	+52 31 26.9	···		···		15.614	9	14.417	9	12.915	0.045	12.133	0.039	12.086	0.048	Y	DH 22
03 03 37.06	+50 40 58.8	···		···		17.470	9	15.423	9	13.420	0.025	12.782	0.026	12.518	0.023	Y	DH 23
03 03 42.36	+46 48 55.1	···		···		17.110	9	15.230	9	14.112	0.026	13.461	0.027	13.143	0.027	Y	DH 24
03 05 07.18	+48 59 50.6	···		···		18.863	9	16.260	9	14.381	0.031	13.767	0.036	13.477	0.037	Y	DH 25
03 05 43.83	+45 41 13.0	···		···		14.112	9	13.427	9	13.129	0.023	12.664	0.022	12.563	0.022	Y	DH 26
03 06 04.67	+49 19 50.6	···		···		15.429	9	14.346	9	12.789	0.025	12.075	0.021	11.879	0.020	Y	DH 27
03 06 16.82	+49 55 21.3	···		···		17.798	9	16.249	9	14.514	0.030	13.797	0.032	13.583	0.036	Y	DH 28
03 06 18.57	+48 36 08.7	···		···		17.881	9	16.202	9	14.529	0.030	13.916	0.031	13.643	0.038	Y	DH 29
03 06 51.39	+48 32 59.5	···		···		14.189	9	13.732	9	12.171	0.022	11.491	0.022	11.327	0.020	Y	DH 30
03 07 04.10	+51 17 40.4	10.557	3	10.000	3	···		9.360	11	8.950	0.034	8.764	0.021	8.672	0.017	N	HE 7
03 07 50.44	+49 06 29.8	10.603	3	10.090	10	···		9.630	11	9.055	0.032	8.869	0.029	8.791	0.018	Y	HE 12, MA 3
03 07 53.64	+46 15 11.6	···		···		16.536	9	15.205	9	14.351	0.029	13.757	0.030	13.505	0.035	Y	DH 31
03 08 01.15	+50 33 33.0	11.217	3	10.620	3	···		9.990	11	9.485	0.023	9.247	0.021	9.152	0.017	N	HE 29
03 08 09.66	+47 35 54.8	···		···		16.585	9	14.600	9	12.922	0.024	12.305	0.033	12.000	0.023	Y	DH 32
03 08 10.85	+48 55 07.5	11.910	3	11.310	3	···		10.641	3	10.061	0.025	9.834	0.021	9.758	0.020	N	HE 17
03 08 14.54	+49 50 21.8	12.260	10	10.580	10	···		10.790	11	9.824	0.023	9.478	0.022	9.340	0.018	Y	MA 4
03 08 38.58	+48 08 10.8	···		···		18.667	9	16.815	9	15.167	0.050	14.460	0.047	14.197	0.054	Y	DH 33
03 08 56.60	+47 20 46.9	11.389	3	10.640	3	···		9.840	11	9.371	0.021	9.002	0.017	9.010	0.021	N	HE 28
03 08 57.24	+48 54 47.5	···		···		17.047	9	15.509	9	13.629	0.025	13.023	0.028	12.742	0.025	Y	DH 34
03 09 04.55	+47 53 04.1	11.733	3	11.150	3	···		10.550	11	9.979	0.017	9.709	0.019	9.646	0.020	N	HE 33
03 09 24.21	+45 22 58.9	8.170	10	8.060	10	···		7.950	11	7.856	0.034	7.872	0.029	7.857	0.018	Y	MA 5, HD 19458
03 09 52.08	+48 28 15.5	11.650	3	10.840	3	···		10.320	11	9.437	0.023	9.115	0.022	8.990	0.018	Y	HE 56, MA 6
03 09 59.22	+47 13 10.5	···		···		13.648	9	13.283	9	12.348	0.021	11.949	0.019	11.873	0.023	Y	DH 35
03 10 13.21	+51 03 29.0	···		···		16.844	9	15.247	9	13.176	0.025	12.543	0.022	12.274	0.025	Y	DH 36
03 10 17.43	+47 31 41.2	8.800	3	8.490	3	···		8.129	3	7.764	0.027	7.650	0.016	7.599	0.022	Y	HE 61, HD 19539

Table 4.3 – Continued

RA[a] (h m s)	Dec[a] (d m s)	B	Ref[b]	V	Ref[b]	R_C	Ref[b]	I_C	Ref[b]	J	σ_J	H	σ_H	K_s	σ_K	Mem[c]	Names[d]
03 10 25.34	+45 51 28.1	···		···		14.649	9	13.604	9	12.732	0.022	12.065	0.019	11.850	0.018	Y	DH 37
03 10 41.77	+50 31 32.1	11.790	3	11.090	3	···		10.280	11	9.707	0.023	9.415	0.022	9.280	0.020	Y	HE 93
03 10 44.29	+50 20 46.8	11.708	3	11.060	3	···		10.380	11	10.082	0.023	9.857	0.022	9.777	0.020	Y	HE 92
03 10 49.40	+50 40 26.2	···		···		17.199	9	15.520	9	13.437	0.023	12.892	0.024	12.522	0.018	Y	DH 38
03 10 55.25	+47 13 54.0	···		···		15.995	9	14.323	9	13.036	0.023	12.389	0.019	12.159	0.016	Y	DH 39
03 10 57.15	+51 39 09.2	···		···		15.265	9	14.368	9	11.981	0.023	11.264	0.021	11.060	0.020	Y	DH 40
03 11 07.73	+46 40 46.2	···		···		15.093	9	14.260	9	13.324	0.025	12.678	0.025	12.527	0.025	Y	DH 41
03 11 15.96	+47 37 29.2	···		···		13.414	9	13.098	9	12.301	0.019	11.908	0.021	11.804	0.019	Y	DH 42
03 11 16.84	+48 10 36.8	11.065	3	10.420	3	···		9.710	11	9.129	0.032	8.841	0.022	8.715	0.018	Y	HE 94, MA 7
03 11 18.06	+49 47 04.7	11.310	3	10.710	3	···		10.002	3	9.493	0.023	9.286	0.023	9.182	0.018	N	HE 106
03 11 35.06	+48 30 35.5	···		···		15.624	9	14.224	9	12.475	0.023	11.772	0.021	11.557	0.020	Y	DH 43
03 11 41.14	+48 03 14.8	8.940	3	8.600	3	···		8.230	11	7.914	0.025	7.790	0.015	7.766	0.027	Y	HE 104, MA 8, HD 19655
03 11 42.90	+52 09 48.6	6.905	3	6.880	3	···		6.910	11	6.806	0.035	6.829	0.021	6.831	0.021	Y	HE 145, MA 9, HD 19624
03 11 43.58	+51 44 50.6	···		···		17.875	9	15.896	9	13.602	0.026	12.990	0.024	12.709	0.025	Y	DH 44
03 11 49.99	+50 22 46.8	10.170	10	9.690	10	···		9.310	11	8.790	0.048	8.560	0.022	8.536	0.023	Y	HE 135, MA 10
03 12 03.04	+50 23 31.2	11.177	3	10.470	3	···		9.770	11	9.099	0.020	8.835	0.024	8.726	0.018	N	HE 143
03 12 18.51	+45 27 59.0	···		···		17.276	9	15.371	9	14.424	0.032	13.777	0.032	13.490	0.037	Y	DH 45
03 12 42.65	+47 50 19.1	9.286	3	8.970	3	···		8.650	11	8.325	0.020	8.244	0.022	8.151	0.027	Y	HE 151, MA 11, HD 19767
03 12 43.23	+47 56 27.9	···		···		14.163	9	13.716	9	12.623	0.023	12.126	0.019	12.031	0.018	Y	DH 46
03 13 05.24	+49 00 33.9	8.070	10	7.960	10	···		7.840	11	7.687	0.023	7.700	0.020	7.663	0.020	Y	HE 167, MA 12, HD 19805
03 13 07.46	+49 34 03.6	12.280	10	10.530	10	···		10.574	3	9.739	0.022	9.287	0.021	9.137	0.018	Y	HE 174, MA 13
03 13 23.87	+48 10 37.1	6.871	3	5.900	3	···		4.850	11	4.468	0.202	3.893	0.228	3.855	0.276	N	HE 175
03 13 24.25	+47 25 48.6	···		···		13.974	9	13.291	9	12.244	0.020	11.548	0.022	11.390	0.020	Y	DH 47
03 13 33.32	+48 46 32.9	11.417	3	10.760	3	···		10.100	11	9.419	0.022	9.207	0.021	9.110	0.017	N	HE 192
03 13 45.08	+49 47 27.9	···		···		18.584	9	16.472	9	14.415	0.031	13.815	0.033	13.498	0.037	Y	DH 48
03 13 50.32	+49 34 07.9	7.190	3	7.160	10	···		7.130	11	7.010	0.029	7.069	0.027	7.045	0.017	Y	HE 212, MA 14, HD 19893
03 13 55.40	+47 30 50.2	11.850	3	11.290	3	···		10.630	3	10.137	0.018	9.920	0.020	9.861	0.020	N	HE 200
03 13 58.00	+47 19 28.9	10.455	3	9.850	3	···		9.250	11	8.749	0.020	8.493	0.018	8.437	0.022	N	HE 201
03 14 01.73	+48 47 47.7	···		···		17.134	9	15.262	9	13.289	0.025	12.637	0.026	12.358	0.023	Y	DH 49
03 14 03.94	+50 22 47.5	9.507	3	8.930	3	···		8.410	11	7.764	0.019	7.602	0.024	7.538	0.018	N	HE 225, HD 19908
03 14 05.98	+48 58 46.1	···		···		16.593	9	15.163	9	13.270	0.023	12.616	0.024	12.321	0.026	Y	DH 50
03 14 16.62	+48 34 40.5	9.473	3	9.140	3	···		8.890	11	8.460	0.018	8.396	0.027	8.321	0.026	Y	HE 220, HD 19954
03 14 24.91	+52 33 38.6	···		···		17.041	9	15.089	9	13.348	0.024	12.713	0.024	12.439	0.024	Y	DH 51
03 14 28.41	+48 21 10.7	10.418	3	9.950	3	···		9.430	11	9.016	0.021	8.871	0.026	8.818	0.020	N	HE 228
03 14 35.89	+47 19 29.1	···		···		18.063	9	15.533	9	14.097	0.028	13.486	0.028	13.140	0.031	Y	DH 52
03 14 39.12	+46 49 28.5	···		···		18.296	9	16.404	9	15.307	0.057	14.696	0.061	14.372	0.072	Y	DH 53
03 14 57.17	+47 08 23.4	11.321	3	10.810	3	···		10.040	11	9.826	0.021	9.598	0.020	9.547	0.019	N	HE 239
03 15 04.58	+50 14 49.4	···		···		17.890	9	15.894	9	13.865	0.026	13.220	0.029	12.994	0.027	Y	DH 54
03 15 07.30	+49 50 45.2	···		···		17.184	9	15.430	9	13.536	0.024	12.915	0.023	12.629	0.021	Y	DH 55
03 15 23.56	+49 26 25.1	10.560	10	10.040	10	···		9.590	11	9.111	0.021	8.924	0.017	8.846	0.018	Y	HE 270, MA 15
03 15 28.07	+47 34 04.9	···		···		16.445	9	14.798	9	13.243	0.024	12.607	0.028	12.360	0.023	Y	DH 56
03 15 31.48	+50 55 32.6	9.960	3	8.430	3	···		6.863	3	5.592	0.025	4.891	0.184	4.692	0.016	N	HE 283, HD 20061
03 15 36.31	+49 48 46.3	···		···		17.028	9	15.233	9	13.368	0.024	12.756	0.026	12.443	0.024	Y	DH 57
03 15 40.04	+47 18 25.3	···		···		18.890	9	16.978	9	15.625	0.053	15.004	0.066	14.724	0.066	Y	DH 58
03 15 42.23	+47 41 01.3	11.012	3	10.410	3	···		10.360	11	9.668	0.024	9.438	0.028	9.373	0.022	N	HE 271
03 15 45.33	+48 36 24.3	···		···		17.692	9	15.861	9	13.738	0.023	13.174	0.027	12.863	0.026	Y	DH 59
03 15 46.65	+47 55 04.8	10.566	3	9.930	3	···		9.300	11	8.710	0.020	8.476	0.045	8.379	0.022	N	HE 276
03 15 48.71	+50 57 21.2	6.800	10	6.710	10	···		6.630	11	6.136	0.018	6.142	0.021	6.086	0.016	Y	HE 295, MA 16, HD 20096
03 15 51.63	+52 33 35.6	···		···		12.860	9	12.820	9	11.126	0.020	10.572	0.017	10.434	0.016	Y	DH 60
03 15 57.93	+48 48 22.1	11.370	3	10.220	3	···		8.942	3	7.970	0.024	7.379	0.018	7.265	0.018	N	HE 289
03 15 58.89	+50 24 18.8	11.764	3	11.120	3	10.812	2	10.424	2	9.901	0.021	9.653	0.022	9.546	0.018	Y	HE 299, MA 17
03 16 01.90	+48 01 40.6	8.304	3	8.090	3	···		7.820	11	7.511	0.021	7.443	0.022	7.387	0.022	Y	HE 285, HD 20135
03 16 04.07	+48 10 34.4	11.355	3	10.710	3	···		10.510	11	9.532	0.020	9.282	0.018	9.217	0.014	N	HE 290
03 16 13.63	+51 25 43.9	9.680	3	9.250	3	···		8.760	11	8.324	0.021	8.207	0.022	8.154	0.021	Y	HE 314, HD 20122
03 16 17.29	+46 11 04.6	···		···		13.607	9	13.338	9	12.435	0.022	11.997	0.031	11.826	0.020	Y	DH 61

Table 4.3 – Continued

RA[a] (h m s)	Dec[a] (d m s)	B	Ref[b]	V	Ref[b]	R_C	Ref[b]	I_C	Ref[b]	J	σ_J	H	σ_H	K_s	σ_K	Mem[c]	Names[d]
03 16 17.66	+50 19 08.4	···		···		16.885	9	15.075	9	13.261	0.025	12.653	0.022	12.348	0.025	Y	DH 62
03 16 21.26	+50 29 47.4	···		···		18.086	9	15.909	9	14.048	0.030	13.491	0.026	13.127	0.030	Y	DH 63
03 16 23.17	+49 37 33.4	10.452	3	9.960	3	···		9.530	11	9.035	0.018	8.843	0.017	8.784	0.016	Y	HE 309, MA 18
03 16 31.30	+49 18 39.3	···		···		12.528	9	12.552	9	11.046	0.023	10.485	0.021	10.363	0.018	Y	DH 64
03 16 35.21	+47 07 11.4	···		···		15.281	9	13.959	9	12.539	0.029	11.915	0.032	11.694	0.022	Y	DH 65
03 16 38.98	+49 27 08.9	···		···		11.779	9	11.395	9	10.452	0.022	10.081	0.021	9.962	0.018	Y	DH 66
03 16 39.81	+47 19 41.5	···		···		16.067	9	14.433	9	12.955	0.029	12.319	0.030	12.082	0.018	Y	DH 67
03 16 44.29	+49 52 39.5	12.700	3	12.110	3	···		11.432	1	10.894	0.020	10.728	0.019	10.669	0.016	N	HE 326
03 16 47.40	+45 32 32.6	···		···		17.100	9	15.482	9	14.433	0.035	13.946	0.057	13.619	0.043	Y	DH 68
03 16 49.09	+51 13 05.5	7.224	3	7.190	3	···		7.170	11	6.983	0.024	7.026	0.022	6.995	0.020	Y	HE 333, MA 19, HD 20191
03 16 59.45	+49 55 35.8	10.888	3	10.330	3	10.054	1	9.710	1	9.281	0.020	9.068	0.019	8.994	0.016	Y	HE 334, MA 20
03 16 59.74	+45 20 51.3	···		···		18.987	9	16.221	9	14.777	0.032	14.177	0.040	13.885	0.043	Y	DH 69
03 17 01.18	+51 53 06.4	···		···		15.238	9	14.348	9	12.205	0.021	11.473	0.019	11.241	0.018	Y	DH 70
03 17 05.58	+47 37 43.7	11.162	3	9.860	3	9.195	1	8.525	1	7.438	0.025	6.832	0.045	6.652	0.021	N	HE 330
03 17 07.55	+49 58 40.1	···		···		13.006	9	12.709	9	11.232	0.020	10.692	0.019	10.528	0.016	Y	DH 71
03 17 09.52	+45 27 33.0	···		···		15.988	9	14.265	9	13.218	0.032	12.604	0.036	12.360	0.025	Y	DH 72
03 17 14.91	+50 17 14.1	···		···		17.864	9	16.143	9	14.282	0.029	13.663	0.033	13.374	0.032	Y	DH 73
03 17 16.92	+49 37 42.7	···		···		15.565	9	13.941	9	12.100	0.022	11.475	0.021	11.212	0.018	Y	DH 74
03 17 19.67	+48 34 47.0	···		···		12.270	9	11.992	9	10.743	0.020	10.270	0.018	10.173	0.014	Y	DH 75
03 17 20.34	+49 30 07.5	10.488	3	9.920	10	···		9.460	11	8.907	0.021	8.665	0.024	8.608	0.018	Y	HE 338, MA 21
03 17 21.50	+48 22 17.9	···		···		13.975	9	13.636	9	11.790	0.020	11.090	0.019	10.893	0.016	Y	DH 76
03 17 21.57	+48 04 32.7	···		···		16.909	9	15.003	9	13.251	0.021	12.596	0.023	12.338	0.023	Y	DH 77
03 17 24.03	+49 21 14.3	12.136	3	11.450	3	···		11.520	11	10.210	0.022	9.897	0.023	9.826	0.020	N	HE 340
03 17 27.54	+49 36 52.9	···		···		20.030	7	17.850	7	15.603	0.060	14.875	0.070	14.530	0.082	Y	AP 300
03 17 31.15	+47 37 29.1	···		···		16.397	9	14.770	9	13.312	0.029	12.653	0.034	12.403	0.018	Y	DH 78
03 17 31.39	+48 51 51.2	13.460	3	12.570	3	12.235	9	11.456	3	10.745	0.020	10.287	0.019	10.154	0.016	Y	AP 119, DH 79
03 17 34.56	+51 42 53.9	9.600	3	9.320	3	···		8.997	3	8.612	0.019	8.514	0.022	8.488	0.016	N	HE 358, HD 20256
03 17 36.93	+48 50 08.5	11.693	3	11.010	3	10.699	1	10.277	1	9.678	0.020	9.366	0.018	9.261	0.014	Y	HE 350, MA 22
03 17 37.43	+48 06 29.0	11.188	3	10.510	3	···		9.840	11	9.234	0.020	8.936	0.024	8.874	0.018	N	HE 347
03 17 37.98	+49 54 48.2	···		15.180	3	14.285	9	12.890	3	11.451	0.020	10.779	0.021	10.517	0.017	Y	AP 120, DH 80
03 17 42.09	+49 01 46.6	12.680	3	11.890	3	···		10.989	3	10.313	0.021	9.940	0.023	9.835	0.020	Y	AP 121
03 17 43.26	+50 21 39.7	7.630	10	7.510	10	···		7.390	11	7.152	0.029	7.109	0.029	7.044	0.018	Y	HE 357, MA 23, HD 20282
03 17 47.14	+51 06 47.7	···		···		17.857	9	15.807	9	13.912	0.026	13.258	0.029	12.957	0.027	Y	DH 81
03 17 54.00	+49 28 24.8	···		17.990	4	16.772	9	15.001	4	13.308	0.024	12.679	0.026	12.393	0.025	Y	AP 267, DH 82
03 18 01.20	+47 00 07.2	···		···		14.404	9	13.091	9	11.851	0.021	11.270	0.035	10.956	0.026	Y	DH 83
03 18 01.51	+48 12 34.3	···		···		14.978	9	14.296	9	12.984	0.023	12.382	0.024	12.242	0.022	Y	DH 84
03 18 01.74	+49 38 39.0	10.110	10	9.680	3	···		9.160	11	8.841	0.021	8.661	0.018	8.604	0.014	Y	HE 361, MA 24
03 18 05.26	+49 54 21.8	10.430	10	9.980	10	···		9.450	11	8.937	0.021	8.753	0.020	8.689	0.020	Y	HE 365, MA 25
03 18 07.07	+50 05 55.6	···		···		17.409	9	15.291	9	13.412	0.022	12.777	0.024	12.485	0.024	Y	DH 85
03 18 08.04	+52 25 28.2	···		···		14.641	9	13.620	9	11.727	0.021	11.109	0.017	10.877	0.018	Y	DH 86
03 18 08.36	+49 16 21.4	···		···		18.291	9	15.992	9	14.086	0.030	13.493	0.033	13.197	0.034	Y	DH 87
03 18 08.56	+49 18 55.1	···		15.180	3	···		13.211	3	11.994	0.022	11.281	0.022	11.093	0.017	Y	AP 122
03 18 09.06	+49 25 19.0	···		···		19.788	8	17.594	8	15.251	0.058	14.507	0.072	14.291	0.078	Y	AP 301
03 18 23.10	+49 28 02.7	···		16.390	4	15.542	9	13.922	4	12.564	0.023	11.908	0.023	11.695	0.019	Y	AP 123, DH 88
03 18 23.89	+50 33 20.8	8.240	3	8.060	3	···		7.862	3	7.584	0.024	7.576	0.022	7.541	0.017	Y	HE 379, MA 26, HD 20344
03 18 27.39	+47 21 15.4	12.345	3	11.550	3	11.030	2	10.609	2	9.833	0.019	9.454	0.028	9.352	0.024	Y	HE 373, MA 27
03 18 29.24	+50 27 31.5	13.160	2	12.310	2	11.826	2	11.370	2	10.647	0.018	10.308	0.017	10.217	0.018	Y	AP 89
03 18 37.49	+48 56 14.6	···		···		18.306	9	15.893	9	14.035	0.030	13.440	0.031	13.173	0.031	Y	DH 89
03 18 37.75	+50 13 20.0	5.089	3	5.160	10	···		5.270	11	5.238	0.018	5.316	0.024	5.326	0.020	Y	HE 383, MA 28, HD 20365
03 18 43.70	+50 23 10.5	10.872	3	10.280	3	···		9.440	11	9.109	0.020	8.834	0.027	8.793	0.020	Y	HE 387
03 18 44.09	+50 09 14.1	···		···		17.214	9	15.219	9	13.683	0.025	13.067	0.026	12.768	0.026	Y	DH 90
03 18 44.78	+49 46 11.9	8.060	10	7.950	10	···		7.830	11	7.675	0.021	7.692	0.024	7.664	0.022	Y	HE 386, MA 29, HD 20391
03 18 50.31	+49 43 52.2	11.840	2	11.170	2	10.780	2	10.414	2	9.867	0.021	9.562	0.021	9.488	0.016	Y	HE 389, AP 90, MA 30
03 18 50.46	+48 16 03.2	13.520	2	12.590	2	12.006	2	11.457	2	10.650	0.018	10.125	0.019	10.000	0.018	Y	AP 91
03 18 58.70	+48 50 42.3	···		13.440	3	···		12.007	3	11.056	0.020	10.407	0.019	10.235	0.016	Y	AP 124

Table 4.3 – Continued

RA[a] (h m s)	Dec[a] (d m s)	B	Ref[b]	V	Ref[b]	R_C	Ref[b]	I_C	Ref[b]	J	σ_J	H	σ_H	K_s	σ_K	Mem[c]	Names[d]
03 19 02.41	+49 33 37.5	17.160	3	15.660	3	14.604	2	13.445	3	12.127	0.022	11.428	0.019	11.227	0.021	Y	AP 92, DH 91
03 19 02.76	+48 10 59.6	12.920	2	11.990	2	11.423	2	10.886	2	9.996	0.018	9.499	0.019	9.363	0.016	Y	AP 93
03 19 07.64	+50 05 42.1	4.970	10	5.040	3	···		5.150	11	5.092	0.019	5.153	0.034	5.196	0.018	Y	HE 401, MA 31, HD 20418
03 19 08.48	+48 43 46.2	···		···		19.710	7	17.630	7	15.597	0.067	15.127	0.090	14.772	0.101	Y	AP 302
03 19 10.92	+48 42 18.4	···		···		18.860	7	16.980	7	14.985	0.047	14.304	0.049	14.128	0.061	Y	AP 303
03 19 11.76	+47 59 50.2	14.970	2	13.850	2	13.149	2	12.553	2	11.663	0.018	11.076	0.017	10.946	0.021	Y	AP 94
03 19 12.97	+47 20 47.0	11.018	3	10.550	3	···		9.810	11	9.621	0.023	9.450	0.015	9.401	0.016	N	HE 394
03 19 13.22	+48 31 53.6	···		···		21.230	7	18.830	7	16.106	0.106	15.441	0.135	14.994	0.123	Y	AP 304
03 19 19.57	+50 44 48.9	11.782	3	11.110	3	10.808	1	10.453	1	9.806	0.021	9.604	0.023	9.488	0.016	Y	HE 407
03 19 21.59	+49 23 31.0	···		···		20.594	8	18.355	8	15.812	0.076	14.960	0.089	14.640	0.090	Y	AP 305
03 19 26.30	+48 18 37.1	···		···		17.244	9	15.726	9	14.243	0.026	13.539	0.026	13.345	0.027	Y	DH 92
03 19 28.03	+50 25 16.8	11.530	3	10.850	3	···		···		···	···	···	···	···	···	N	HE 416
03 19 29.22	+45 23 20.3	···		···		17.847	9	15.764	9	14.424	0.035	13.811	0.033	13.436	0.040	Y	DH 93
03 19 31.17	+49 41 17.2	···		···		17.110	9	15.089	9	13.520	0.022	12.884	0.027	12.586	0.024	Y	DH 94
03 19 41.33	+50 30 45.2	···		···		20.556	8	18.171	8	15.257	0.048	14.526	0.063	13.966	0.047	Y	AP 306
03 19 41.75	+48 54 49.0	9.683	3	9.230	3	···		8.690	11	8.244	0.019	8.068	0.017	7.978	0.018	Y	HE 421, MA 32, HD 20475
03 19 45.60	+50 08 35.7	···		12.160	3	···		11.191	3	10.473	0.021	10.186	0.023	10.073	0.020	Y	AP 125
03 19 47.26	+48 37 40.7	7.713	3	7.640	3	···		7.590	11	7.459	0.020	7.454	0.021	7.457	0.020	Y	HE 423, MA 33, HD 20487
03 19 47.43	+48 58 44.4	···		20.500	4	···		16.902	4	14.834	0.042	14.372	0.062	13.991	0.055	Y	AP 268
03 19 55.41	+49 38 35.1	···		···		17.288	9	15.822	9	14.563	0.035	13.879	0.035	13.720	0.041	Y	DH 95
03 19 55.50	+45 22 55.1	···		···		16.204	9	15.062	9	14.246	0.032	13.541	0.031	13.344	0.037	Y	DH 96
03 19 57.30	+49 04 21.6	···		16.640	4	15.532	9	14.070	4	12.644	0.022	11.999	0.022	11.713	0.021	Y	AP 126, DH 97
03 19 57.68	+49 52 06.9	13.160	2	12.280	2	11.769	2	11.302	2	10.483	0.022	10.056	0.022	9.917	0.018	Y	AP 95
03 19 59.64	+50 45 10.4	···		···		17.602	9	15.701	9	13.729	0.023	13.124	0.026	12.841	0.030	Y	DH 98
03 20 00.96	+47 45 30.3	···		···		15.925	9	14.372	9	12.880	0.022	12.202	0.019	11.992	0.019	Y	DH 99
03 20 01.27	+46 53 01.2	13.490	3	12.570	3	···		11.417	3	10.598	0.020	10.036	0.017	9.900	0.016	Y	AP 127
03 20 03.09	+49 23 14.8	10.468	3	9.860	3	···		9.200	11	8.643	0.019	8.355	0.017	8.327	0.024	N	HE 435
03 20 06.27	+50 58 07.5	7.110	10	7.060	10	···		7.060	11	6.910	0.027	6.936	0.040	6.920	0.020	Y	HE 441, MA 34, HD 20510
03 20 07.44	+50 39 53.4	···		···		20.332	8	18.145	8	15.908	0.077	15.132	0.084	14.934	0.102	Y	AP 385
03 20 12.13	+48 56 41.2	···		16.960	3	···		14.234	4	12.736	0.022	12.082	0.032	11.790	0.021	Y	AP 128
03 20 16.24	+48 09 17.6	···		15.910	3	···		13.322	3	11.851	0.021	11.102	0.031	10.875	0.019	Y	AP 129
03 20 17.70	+50 46 03.0	···		···		24.094	8	21.406	8	···	···	···	···	···	···	Y	AP 409
03 20 20.90	+48 01 05.0	···		···		19.090	7	17.080	7	···	···	···	···	···	···	Y	AP 307
03 20 23.42	+48 58 33.9	15.470	6	14.180	6	···		12.651	6	11.522	0.022	10.872	0.030	10.704	0.019	Y	APX 74
03 20 23.66	+51 37 06.1	7.300	10	7.290	10	···		7.290	11	7.182	0.018	7.230	0.026	7.208	0.027	Y	HE 450, MA 35, HD 20537
03 20 24.96	+47 56 28.3	11.950	3	11.120	3	10.690	1	10.211	1	9.535	0.021	9.186	0.027	9.115	0.021	N	HE 444
03 20 31.73	+49 39 59.8	···		···		17.270	9	15.380	9	13.857	0.028	13.230	0.032	12.977	0.033	Y	DH 100
03 20 36.16	+51 50 15.2	···		···		18.698	9	16.109	9	14.184	0.029	13.576	0.040	13.251	0.028	Y	DH 101
03 20 39.14	+49 32 06.2	···		···		18.900	8	16.924	8	15.004	0.051	14.414	0.067	14.034	0.066	Y	AP 364
03 20 39.28	+47 29 21.8	11.014	3	10.390	3	10.039	1	9.673	1	9.149	0.027	8.793	0.040	8.765	0.021	Y	HE 453, MA 36
03 20 39.39	+50 15 49.5	16.070	3	14.550	3	13.543	2	12.467	3	11.166	0.024	10.393	0.028	10.225	0.023	Y	AP 96
03 20 39.59	+52 43 35.5	11.550	10	10.780	10	···		9.920	11	9.646	0.022	9.308	0.028	9.206	0.020	Y	MA 37
03 20 41.86	+48 24 37.6	12.950	2	12.080	2	11.575	2	11.131	2	10.411	0.022	9.969	0.031	9.884	0.021	Y	AP 97, APX 75
03 20 42.71	+51 01 09.6	···		17.930	4	···		14.888	4	13.269	0.022	12.669	0.036	12.392	0.024	Y	AP 269
03 20 43.47	+50 59 39.6	···		21.870	4	···		17.895	4	15.604	0.055	14.896	0.064	14.583	0.071	Y	AP 270
03 20 44.57	+51 28 19.4	···		···		17.737	9	16.108	9	14.616	0.039	13.922	0.040	13.832	0.047	Y	DH 102
03 20 49.29	+49 19 25.8	12.436	3	11.700	3	11.271	1	10.838	1	10.239	0.022	9.986	0.031	9.850	0.022	N	HE 457
03 20 50.86	+50 15 15.7	···		···		17.697	9	15.636	9	13.877	0.024	13.234	0.032	12.905	0.023	Y	DH 103
03 20 51.58	+49 27 57.5	13.490	5	12.570	5	···		11.562	5	10.873	0.022	10.423	0.030	10.286	0.022	Y	APX 1
03 20 56.53	+49 20 42.9	···		16.120	3	···		13.661	3	12.281	0.022	11.619	0.027	11.386	0.020	Y	AP 131
03 20 59.84	+48 18 36.1	···		···		18.600	7	16.710	7	14.694	0.031	14.055	0.045	13.739	0.045	Y	AP 308
03 21 02.04	+49 44 18.2	12.283	3	11.400	3	10.998	1	10.531	1	9.898	0.022	9.487	0.026	9.434	0.020	N	HE 462
03 21 02.06	+50 14 30.7	···		···		17.553	9	15.263	9	13.448	0.022	12.750	0.032	12.444	0.023	Y	DH 104
03 21 02.33	+49 47 03.6	···		17.130	4	···		14.204	4	12.590	0.024	11.961	0.031	11.694	0.019	Y	AP 132
03 21 04.09	+47 55 19.7	···		17.640	5	···		14.589	5	12.906	0.030	12.275	0.030	11.994	0.026	Y	APX 2

Table 4.3 – Continued

RA[a] (h m s)	Dec[a] (d m s)	B	Ref[b]	V	Ref[b]	R_C	Ref[b]	I_C	Ref[b]	J	σ_J	H	σ_H	K_s	σ_K	Mem[c]	Names[d]
03 21 06.51	+48 26 12.7	13.800	2	12.800	2	12.223	2	11.744	2	10.957	0.022	10.464	0.027	10.327	0.020	Y	AP 98
03 21 12.19	+50 59 08.2	···		17.640	4	16.743	9	14.732	4	13.099	0.024	12.457	0.031	12.222	0.023	Y	AP 133, DH 105
03 21 12.99	+48 59 58.0	17.240	3	15.680	3	14.632	2	13.512	3	12.284	0.026	11.561	0.031	11.376	0.022	Y	AP 99
03 21 16.05	+48 35 07.2	13.930	2	12.800	2	12.109	2	11.464	2	10.362	0.022	9.732	0.031	9.603	0.022	Y	AP 100
03 21 18.41	+48 37 25.5	···		···		18.183	9	16.021	9	14.229	0.030	13.641	0.036	13.273	0.034	Y	DH 106
03 21 20.21	+48 45 27.1	12.760	2	11.960	2	11.490	2	11.069	2	10.340	0.023	9.972	0.028	9.887	0.020	Y	AP 102
03 21 20.48	+47 53 15.2	···		16.090	3	15.215	9	13.678	3	12.312	0.022	11.569	0.031	11.396	0.027	Y	AP 134, DH 107
03 21 21.52	+49 57 37.4	17.200	5	15.610	5	···		12.875	5	11.292	0.026	10.664	0.032	10.396	0.023	Y	APX 3D
03 21 21.80	+48 02 23.0	···		···		22.485	8	19.862	8	···	···	···	···	···	···	Y	AP 397
03 21 22.18	+49 57 03.3	15.140	3	13.890	3	13.124	2	12.467	3	11.430	0.022	10.904	0.033	10.648	0.021	Y	AP 101, APX 3
03 21 22.40	+47 25 53.0	···		17.820	4	16.465	9	14.885	4	13.257	0.025	12.575	0.035	12.318	0.029	Y	AP 135, DH 108
03 21 22.42	+47 42 05.4	12.020	3	10.570	3	9.833	1	9.139	1	8.015	0.020	7.378	0.033	7.165	0.020	N	HE 477
03 21 27.12	+49 48 03.8	···		20.060	4	···		16.623	4	14.724	0.040	14.029	0.049	13.777	0.051	N	AP 271
03 21 30.05	+48 49 23.1	···		···		18.126	8	16.321	8	14.668	0.036	14.029	0.052	13.711	0.040	Y	AP 346
03 21 30.23	+48 29 38.0	9.554	3	9.160	3	8.960	1	8.732	1	8.365	0.019	8.275	0.045	8.186	0.021	Y	HE 481, MA 38
03 21 31.64	+47 36 13.9	···		···		16.633	9	15.378	9	13.999	0.028	13.287	0.037	13.015	0.030	Y	DH 109
03 21 34.83	+48 16 28.9	···		···		18.073	8	16.164	8	14.437	0.034	13.944	0.039	13.520	0.040	Y	AP 340
03 21 38.33	+49 48 55.9	···		17.190	4	15.883	9	14.391	4	12.866	0.024	12.207	0.030	11.945	0.022	Y	AP 136, DH 110
03 21 40.21	+49 07 12.8	10.006	3	9.560	3	9.335	1	9.065	1	8.663	0.025	8.482	0.029	8.457	0.020	Y	HE 490, MA 39
03 21 42.87	+49 48 36.5	···		20.420	4	···		16.688	4	14.605	0.035	14.067	0.049	13.554	0.034	N	AP 272
03 21 46.42	+47 42 55.6	11.608	3	11.070	3	10.707	1	10.352	1	9.885	0.021	9.652	0.027	9.601	0.020	N	HE 493
03 21 46.67	+48 49 33.3	···		···		17.626	9	15.552	9	13.871	0.027	13.256	0.033	12.962	0.032	Y	DH 111
03 21 50.61	+47 40 32.8	17.400	3	15.760	3	14.735	2	13.535	3	12.204	0.021	11.522	0.028	11.266	0.023	Y	AP 103
03 21 54.44	+48 33 15.1	···		···		20.737	8	18.538	8	16.264	0.101	15.854	0.204	15.383	0.167	Y	AP 390
03 21 58.61	+49 12 53.5	9.491	3	9.140	3	8.998	1	8.790	1	8.483	0.021	8.411	0.047	8.356	0.023	N	HE 501, MA 40
03 22 00.09	+48 23 49.1	···		14.560	3	···		12.820	3	11.714	0.021	11.021	0.030	10.813	0.020	Y	AP 138
03 22 03.55	+47 56 04.8	8.465	3	8.350	3	···		8.240	11	8.086	0.021	8.118	0.029	8.102	0.027	N	HE 507, MA 41, HD 20701
03 22 04.77	+49 11 54.5	···		···		16.898	9	15.224	9	13.621	0.028	12.988	0.031	12.761	0.028	Y	DH 112
03 22 05.17	+48 49 37.1	12.840	2	12.060	2	11.608	2	11.198	2	10.546	0.022	10.236	0.030	10.138	0.022	Y	AP 104
03 22 06.82	+47 34 06.8	···		12.000	3	···		10.905	3	10.009	0.019	9.529	0.028	9.364	0.023	Y	AP 139
03 22 07.00	+49 23 09.4	15.030	2	13.820	2	13.050	2	12.416	2	11.459	0.026	10.861	0.030	10.685	0.024	N	AP 105
03 22 09.76	+48 34 02.5	···		15.960	3	···		13.501	3	12.010	0.024	11.351	0.032	11.143	0.023	Y	AP 140
03 22 10.26	+47 13 57.2	···		···		13.226	9	12.994	9	12.006	0.022	11.631	0.031	11.530	0.019	Y	DH 113
03 22 21.92	+49 08 27.7	12.456	3	11.670	3	11.232	1	10.799	1	10.169	0.020	9.759	0.019	9.640	0.016	Y	HE 520, MA 42
03 22 23.89	+51 39 55.9	12.560	3	11.780	3	···		10.792	3	10.458	0.039	10.084	0.040	9.751	0.017	N	HE 521
03 22 24.21	+47 32 12.1	···		18.220	4	16.887	9	15.027	4	13.293	0.024	12.635	0.037	12.364	0.029	Y	AP 141, DH 114
03 22 26.29	+51 39 39.5	9.400	10	9.130	3	···		8.830	11	8.525	0.025	8.451	0.016	8.383	0.014	Y	HE 522, MA 43, HD 20714
03 22 27.32	+47 20 48.3	···		···		18.115	9	15.724	9	14.125	0.029	13.478	0.036	13.164	0.035	Y	DH 115
03 22 27.61	+49 09 22.0	16.810	6	15.100	6	···		13.169	6	11.670	0.021	10.880	0.021	10.680	0.018	Y	APX 81A
03 22 28.07	+48 49 39.4	···		15.740	3	14.841	9	13.544	3	12.276	0.021	11.580	0.023	11.361	0.018	Y	AP 142, DH 116
03 22 28.76	+49 30 18.6	···		···		18.667	9	16.817	9	15.394	0.054	15.044	0.102	14.975	0.123	Y	DH 117
03 22 31.55	+50 03 33.5	15.880	6	14.330	6	···		12.715	6	11.330	0.021	10.589	0.018	10.390	0.018	Y	APX 109A
03 22 32.74	+49 11 16.6	···		18.000	3	···		15.002	3	13.141	0.029	12.563	0.034	12.248	0.029	Y	AP 143
03 22 33.16	+48 47 00.4	···		···		18.572	8	16.703	8	14.831	0.038	14.254	0.062	13.991	0.053	Y	AP 355
03 22 35.77	+49 38 04.4	17.040	5	15.560	5	···		13.223	5	11.794	0.022	11.130	0.019	10.884	0.016	Y	APX 5
03 22 36.81	+47 09 10.8	···		14.370	3	···		12.620	3	11.486	0.021	10.792	0.029	10.628	0.025	Y	AP 144
03 22 38.00	+48 58 03.0	···		···		22.476	8	19.964	8	···	···	···	···	···	···	Y	AP 398
03 22 39.35	+47 28 20.8	···		21.710	4	···		17.815	4	15.748	0.084	14.788	0.091	14.801	0.126	Y	AP 273
03 22 40.48	+51 57 57.8	···		···		18.611	9	16.433	9	14.308	0.031	13.694	0.038	13.417	0.034	Y	DH 118
03 22 40.66	+48 00 33.7	···		···		18.226	8	16.378	8	14.492	0.033	13.881	0.043	13.579	0.040	Y	AP 309, DH 119
03 22 40.90	+49 40 41.5	13.950	3	12.940	3	12.376	2	11.845	3	11.072	0.025	10.574	0.030	10.419	0.021	Y	AP 106, AP 107
03 22 41.54	+48 16 07.5	14.440	5	13.150	5	···		11.631	5	10.650	0.025	9.999	0.023	9.856	0.020	Y	APX 6
03 22 43.23	+48 36 17.2	12.750	3	12.200	3	···		11.569	3	11.024	0.022	10.892	0.023	10.786	0.018	N	HE 531
03 22 45.48	+48 21 33.2	···		···		17.815	8	15.965	8	14.249	0.029	13.658	0.038	13.336	0.032	Y	AP 334
03 22 46.72	+50 56 48.8	12.920	6	12.080	6	···		10.995	6	10.113	0.022	9.632	0.023	9.489	0.016	Y	APX 111A

Table 4.3 – Continued

RA[a] (h m s)	Dec[a] (d m s)	B	Ref[b]	V	Ref[b]	R_C	Ref[b]	I_C	Ref[b]	J	σ_J	H	σ_H	K_s	σ_K	Mem[c]	Names[d]
03 22 48.38	+49 39 23.2	···		16.700	3	···		14.112	3	12.535	0.023	11.847	0.023	11.646	0.019	Y	AP 145
03 22 50.59	+48 21 23.1	11.265	3	10.130	3	9.544	1	8.959	1	8.039	0.024	7.484	0.021	7.355	0.021	N	HE 537
03 22 51.93	+50 16 16.8	12.141	3	11.570	3	11.190	1	10.757	1	10.132	0.020	9.893	0.018	9.780	0.018	N	HE 538
03 22 54.19	+48 49 44.7	···		18.120	6	···		15.122	6	13.393	0.022	12.837	0.024	12.544	0.022	N	AP 274, APX 85
03 22 54.75	+50 56 52.4	16.690	6	15.010	6	···		13.012	6	11.483	0.022	10.742	0.023	10.492	0.016	Y	APX 111C
03 22 55.59	+46 09 30.8	···		···		13.832	9	13.524	9	12.804	0.024	12.346	0.032	12.312	0.029	Y	DH 120
03 22 57.03	+49 30 19.7	···		···		17.757	9	15.563	9	14.058	0.023	13.420	0.030	13.172	0.031	Y	DH 121
03 22 59.48	+49 04 55.6	17.040	6	15.270	6	···		13.272	6	11.728	0.025	10.871	0.020	10.626	0.020	Y	APX 87G
03 23 01.91	+49 24 36.5	12.510	3	11.920	3	···		11.222	3	10.684	0.020	10.474	0.021	10.384	0.018	N	HE 545
03 23 02.38	+50 19 03.4	···		···		18.251	9	15.849	9	14.120	0.028	13.480	0.030	13.151	0.034	Y	DH 122
03 23 03.38	+48 53 05.8	···		21.210	6	19.218	8	17.123	8	15.043	0.042	14.479	0.056	14.147	0.066	Y	AP 275, AP 368, APX 86
03 23 04.83	+48 16 11.2	···		···		20.130	7	17.800	7	15.550	0.062	15.151	0.104	14.614	0.083	Y	AP 310
03 23 05.42	+48 32 55.6	···		15.600	1	···		14.570	11	13.480	0.022	12.903	0.029	12.750	0.023	N	AP 2
03 23 05.47	+49 25 56.8	12.750	5	11.940	5	···		11.068	5	10.434	0.020	10.065	0.019	9.981	0.016	Y	APX 7
03 23 05.70	+47 21 12.1	···		···		12.302	9	12.079	9	11.175	0.023	10.791	0.028	10.717	0.022	Y	DH 123
03 23 06.51	+50 44 07.4	11.825	3	11.170	3	10.811	1	10.434	1	9.883	0.022	9.643	0.023	9.518	0.020	N	HE 551
03 23 06.56	+48 44 16.8	···		···		16.872	9	15.177	9	13.622	0.023	12.973	0.027	12.736	0.024	Y	DH 124
03 23 08.68	+48 04 50.6	···		···		19.564	8	17.497	8	15.442	0.056	14.715	0.070	14.317	0.072	Y	AP 311
03 23 08.70	+49 23 53.4	8.819	3	8.680	3	···		8.540	11	8.416	0.035	8.341	0.017	8.316	0.021	N	HE 554, HD 20808
03 23 09.90	+49 16 30.0	···		···		23.599	8	20.785	8	···	···	···	···	···	···	Y	AP 406
03 23 11.93	+47 54 34.6	···		16.400	3	15.226	9	13.876	4	12.454	0.021	11.735	0.021	11.495	0.018	Y	AP 146, DH 125
03 23 13.23	+49 12 47.7	5.184	3	5.260	3	···		5.420	11	5.403	0.021	5.507	0.020	5.537	0.022	Y	HE 557, MA 44, HD 20809
03 23 16.83	+48 21 38.0	···		16.100	1	···		14.980	11	13.875	0.025	13.229	0.027	13.052	0.029	N	AP 5
03 23 16.92	+50 13 09.2	18.080	6	16.410	6	···		13.859	6	12.457	0.022	11.802	0.021	11.565	0.021	Y	APX 115A
03 23 17.50	+48 29 59.9	···		17.880	6	···		14.882	6	13.244	0.024	12.637	0.026	12.308	0.023	Y	APX 89A
03 23 17.78	+48 00 24.0	···		···		13.143	9	12.913	9	11.525	0.021	11.082	0.018	10.937	0.018	Y	DH 126
03 23 18.96	+48 55 10.4	···		21.600	4	···		17.762	4	15.869	0.083	15.176	0.101	15.089	0.138	N	AP 276
03 23 19.40	+47 56 28.4	···		18.520	4	···		15.513	4	13.824	0.028	13.149	0.029	12.891	0.025	Y	AP 277
03 23 22.72	+49 29 39.6	···		16.720	5	···		14.178	5	12.613	0.022	11.950	0.023	11.705	0.016	Y	APX 11
03 23 25.06	+47 54 37.9	···		17.110	4	···		14.311	4	12.698	0.024	12.025	0.031	11.734	0.021	Y	AP 147
03 23 26.92	+47 52 12.0	···		19.030	4	···		15.802	4	14.059	0.029	13.400	0.036	13.072	0.036	Y	AP 278
03 23 28.32	+48 48 25.1	···		21.100	6	···		17.294	4	15.314	0.047	14.685	0.080	14.492	0.080	N	AP 279, APX 92
03 23 31.39	+46 52 10.2	9.960	3	9.470	3	···		8.859	3	8.380	0.023	8.163	0.033	8.108	0.033	N	HE 573
03 23 31.69	+47 51 29.4	···		19.860	4	···		16.458	4	14.551	0.033	13.786	0.043	13.580	0.040	Y	AP 280
03 23 33.98	+49 13 33.3	13.950	5	12.970	5	···		11.866	5	11.125	0.022	10.666	0.024	10.538	0.020	Y	APX 14
03 23 35.11	+50 39 52.4	10.193	3	8.940	3	8.305	1	7.720	1	6.695	0.020	6.154	0.022	6.000	0.022	N	HE 574, HD 232784
03 23 36.63	+48 58 53.4	13.950	2	12.920	2	12.361	2	11.835	2	10.900	0.023	10.442	0.024	10.309	0.021	Y	AP 108, DH 127
03 23 37.14	+48 37 15.4	···		···		18.723	8	16.809	8	14.989	0.038	14.340	0.054	14.016	0.053	Y	AP 359
03 23 40.31	+47 57 29.7	10.466	3	9.790	3	···		9.300	11	8.814	0.020	8.610	0.029	8.531	0.021	Y	HE 577, MA 45
03 23 41.83	+47 35 18.6	···		···		17.293	9	15.364	9	13.844	0.031	13.239	0.038	13.008	0.035	Y	DH 128
03 23 41.92	+50 27 46.4	···		16.570	6	15.384	9	14.102	6	12.561	0.023	11.905	0.021	11.642	0.019	Y	APX 118, DH 129
03 23 42.58	+49 10 31.5	17.090	3	15.530	3	14.417	1	13.438	3	12.166	0.024	11.420	0.021	11.255	0.022	Y	AP 6
03 23 43.15	+51 46 13.3	7.954	3	7.880	10	···		7.770	11	7.599	0.027	7.589	0.022	7.541	0.017	Y	HE 575, MA 46, HD 20842
03 23 45.70	+49 19 52.7	···		···		15.929	9	14.432	9	12.883	0.021	12.266	0.023	11.998	0.019	Y	DH 130
03 23 46.54	+47 59 20.6	···		···		16.428	9	14.600	9	12.848	0.021	12.172	0.024	11.872	0.021	Y	DH 131
03 23 47.34	+48 36 16.1	7.005	3	6.990	3	···		6.990	11	6.918	0.023	6.912	0.020	6.880	0.018	Y	HE 581, MA 47, HD 20863
03 23 48.48	+48 36 43.0	···		···		18.014	8	16.208	8	14.621	0.029	14.071	0.043	13.718	0.048	Y	AP 343
03 23 55.08	+50 18 24.1	10.506	3	9.990	3	9.676	1	9.321	1	8.831	0.027	8.554	0.022	8.465	0.014	Y	HE 588, MA 48
03 23 56.35	+48 09 21.0	···		···		17.164	8	15.479	8	13.882	0.023	13.306	0.027	13.038	0.029	Y	AP 329, DH 132
03 23 59.88	+49 58 01.7	15.240	6	13.940	6	···		12.382	6	11.293	0.021	10.688	0.019	10.506	0.018	Y	APX 120A
03 23 59.92	+48 54 10.8	···		···		19.300	8	17.274	8	15.408	0.062	14.730	0.077	14.465	0.083	Y	AP 371
03 24 00.35	+47 55 29.7	···		···		18.847	8	16.880	8	14.985	0.044	14.303	0.046	13.913	0.051	Y	AP 363
03 24 03.37	+47 37 05.2	···		17.650	5	···		14.842	5	13.211	0.025	12.559	0.031	12.274	0.025	Y	APX 17A
03 24 05.09	+49 24 16.2	···		···		18.289	9	15.932	9	14.609	0.035	13.940	0.043	13.787	0.046	Y	DH 133
03 24 05.66	+48 11 10.7	···		16.740	3	15.657	9	14.133	3	12.635	0.021	11.945	0.021	11.697	0.019	Y	AP 8, DH 134

Table 4.3 – Continued

RA[a] (h m s)	Dec[a] (d m s)	B	Ref[b]	V	Ref[b]	R_C	Ref[b]	I_C	Ref[b]	J	σ_J	H	σ_H	K_s	σ_K	Mem[c]	Names[d]
03 24 05.98	+48 31 27.9	···		17.480	5	···		14.717	5	13.091	0.021	12.477	0.024	12.205	0.021	Y	APX 18
03 24 06.47	+51 02 40.3	12.320	3	11.620	3	···		10.796	3	10.150	0.020	9.905	0.017	9.821	0.018	N	HE 592
03 24 06.54	+46 17 18.7	9.010	10	8.720	10	···		8.390	11	7.958	0.021	7.870	0.047	7.798	0.026	Y	MA 49, HD 20903
03 24 06.70	+49 24 51.9	17.370	3	15.840	3	14.781	2	13.587	3	12.319	0.021	11.630	0.019	11.415	0.018	Y	AP 109, APX 100, DH 135
03 24 08.11	+48 48 29.7	···		···		19.680	7	17.550	7	15.500	0.065	15.028	0.100	14.440	0.079	Y	AP 313
03 24 09.85	+48 45 55.9	···		17.660	5	16.423	9	14.797	5	13.205	0.021	12.590	0.022	12.343	0.022	Y	APX 19, DH 136
03 24 12.07	+50 28 35.7	12.750	6	11.860	6	···		10.814	6	10.169	0.022	9.827	0.023	9.709	0.016	Y	APX 124B
03 24 13.36	+49 05 12.0	16.020	1	14.960	1	14.351	1	13.778	1	12.914	0.021	12.399	0.021	12.292	0.023	Y	AP 12
03 24 13.36	+49 10 08.1	14.400	1	13.660	1	13.223	1	12.778	1	12.113	0.021	11.771	0.022	11.694	0.021	Y	AP 11
03 24 13.51	+51 42 48.2	10.850	3	10.350	3	10.080	1	9.769	1	9.288	0.020	9.130	0.017	9.031	0.019	N	HE 595
03 24 14.95	+46 52 31.4	···		···		17.192	9	15.233	9	13.782	0.029	13.175	0.036	12.884	0.034	Y	DH 137
03 24 14.99	+50 28 25.7	13.900	6	12.840	6	···		11.658	6	10.925	0.020	10.448	0.024	10.317	0.014	Y	APX 124A
03 24 15.12	+49 12 30.0	12.493	3	11.860	3	11.485	1	11.086	1	10.486	0.021	10.201	0.019	10.086	0.016	N	HE 600
03 24 15.63	+51 15 25.4	12.250	3	11.510	3	···		10.677	3	10.029	0.018	9.745	0.015	9.657	0.019	N	HE 597
03 24 17.06	+49 39 00.3	12.137	3	11.400	3	11.012	1	10.635	1	10.102	0.021	9.739	0.023	9.622	0.018	Y	HE 601
03 24 17.64	+48 23 54.5	···		21.410	4	···		17.563	4	15.324	0.056	14.647	0.068	14.589	0.089	N	AP 281
03 24 18.67	+47 28 01.9	11.744	3	11.130	3	10.821	1	10.443	1	9.943	0.026	9.640	0.032	9.622	0.023	N	HE 608
03 24 19.17	+49 13 16.5	9.320	5	8.980	3	···		8.600	5	8.293	0.018	8.180	0.042	8.113	0.026	Y	HE 606, AP 13, APX 21, MA 51
03 24 19.36	+49 51 40.1	2.290	10	1.820	10	···		1.270	11	0.830	0.184	0.413	0.162	0.520	0.164	Y	HE 605, MA 50, HD 20902, α Per
03 24 19.92	+48 47 19.8	12.760	3	11.930	3	11.482	1	11.048	3	10.463	0.018	10.063	0.017	9.963	0.016	Y	AP 14
03 24 21.27	+48 58 59.6	···		···		19.286	8	17.271	8	15.388	0.058	14.754	0.077	14.415	0.079	Y	AP 370
03 24 22.55	+48 24 26.1	···		18.480	4	16.929	8	15.217	8	13.698	0.025	13.082	0.031	12.773	0.030	Y	AP 282
03 24 22.74	+48 20 01.1	···		17.890	4	16.734	9	14.874	4	13.141	0.019	12.489	0.021	12.247	0.024	Y	AP 148, DH 138
03 24 25.04	+50 19 34.6	9.628	3	9.220	3	8.975	1	8.705	1	8.266	0.021	8.067	0.016	7.991	0.020	Y	HE 609, MA 52
03 24 25.10	+48 48 21.3	15.410	1	14.120	1	13.325	1	12.582	1	11.551	0.018	10.912	0.017	10.758	0.020	Y	AP 15
03 24 26.09	+48 44 07.3	···		16.030	3	15.083	9	13.683	3	12.377	0.019	11.673	0.019	11.469	0.020	Y	AP 16, DH 139
03 24 30.04	+49 08 23.8	7.958	3	7.870	3	···		7.780	11	7.705	0.023	7.693	0.020	7.693	0.024	Y	HE 612, MA 53, HD 20931
03 24 32.16	+49 18 28.0	16.830	3	15.280	3	14.301	1	13.150	3	11.839	0.020	11.121	0.019	10.909	0.018	Y	AP 17
03 24 33.49	+49 43 13.9	12.890	5	12.070	5	···		11.121	5	10.386	0.018	9.945	0.017	9.788	0.016	Y	APX 24A
03 24 37.15	+47 40 52.2	···		···		17.242	9	15.495	9	13.748	0.025	13.095	0.035	12.859	0.029	Y	DH 140
03 24 38.79	+48 17 17.2	···		19.030	4	17.448	8	15.696	8	14.129	0.026	13.523	0.032	13.274	0.037	Y	AP 283
03 24 41.61	+49 15 54.4	···		16.200	1	···		15.390	11	14.329	0.030	13.679	0.034	13.467	0.037	N	AP 18
03 24 43.21	+50 15 16.5	19.570	6	17.840	6	16.523	9	14.878	6	13.228	0.022	12.564	0.022	12.302	0.023	Y	APX 128A, DH 141
03 24 43.49	+49 53 13.0	13.500	5	12.580	5	···		11.514	5	10.740	0.018	10.243	0.017	10.106	0.016	Y	APX 27A
03 24 44.36	+48 21 27.1	···		···		22.084	8	19.678	8	16.912	0.217	16.018	0.238	15.430	0.187	Y	AP 395
03 24 47.08	+48 24 42.1	10.349	3	9.860	3	···		9.550	11	8.881	0.021	8.700	0.027	8.663	0.016	Y	HE 621, MA 54
03 24 48.06	+47 13 08.9	···		16.930	3	···		14.277	3	12.776	0.022	12.145	0.031	11.871	0.026	Y	AP 150
03 24 48.38	+48 53 19.9	···		11.710	3	···		10.702	3	10.080	0.019	9.548	0.017	9.422	0.019	Y	AP 149
03 24 48.66	+48 49 47.1	···		···		18.777	8	16.680	8	14.613	0.038	14.000	···	13.653	···	Y	AP 353
03 24 49.14	+47 20 40.4	9.280	3	8.220	3	···		7.116	3	6.172	0.018	5.625	0.029	5.495	0.017	N	HE 623
03 24 49.71	+48 52 18.4	12.480	10	11.660	10	11.152	1	10.739	3	10.108	0.018	9.719	0.017	9.592	0.019	Y	HE 622, AP 19, MA 55
03 24 52.09	+47 54 54.5	7.744	3	7.630	3	···		7.530	11	7.320	0.017	7.334	0.020	7.312	0.018	Y	HE 625, MA 56, HD 20961
03 24 52.48	+49 04 14.7	17.210	1	15.660	1	14.546	1	13.192	3	11.747	0.019	11.116	0.019	10.857	0.019	Y	AP 20
03 24 55.11	+47 24 54.1	10.186	3	9.710	3	9.456	1	9.176	1	8.829	0.019	8.658	0.028	8.604	0.026	Y	HE 632, MA 57
03 24 55.86	+50 01 51.6	13.190	2	12.270	2	11.742	2	11.262	2	10.564	0.020	10.144	0.015	10.034	0.019	Y	AP 110
03 24 56.99	+50 28 54.4	13.080	6	12.190	6	···		11.192	6	10.538	0.018	10.135	0.017	10.015	0.019	Y	APX 131A
03 24 58.69	+50 16 46.6	19.810	6	18.240	6	16.787	9	15.171	6	13.316	0.023	12.675	0.024	12.398	0.025	Y	APX 133A, DH 142
03 24 58.77	+50 15 24.1	11.840	3	11.190	3	···		10.395	3	9.766	0.019	9.517	0.016	9.420	0.019	Y	HE 628
03 24 58.92	+49 50 15.3	16.040	6	14.690	6	···		12.730	6	11.471	0.019	10.804	0.017	10.606	0.018	Y	APX 132A
03 24 59.23	+48 37 10.4	···		14.720	5	···		12.913	5	11.822	0.022	11.117	0.027	10.944	0.026	Y	APX 30A
03 24 59.36	+49 03 28.5	···		···		17.208	9	15.533	9	14.218	0.028	13.600	0.034	13.298	0.037	Y	DH 143
03 24 59.80	+48 53 01.1	12.770	5	11.910	5	···		10.806	5	9.954	0.018	9.477	0.017	9.331	0.019	Y	APX 28
03 25 00.65	+49 07 53.2	···		···		17.554	9	15.490	9	14.071	0.026	13.485	0.035	13.187	0.035	Y	DH 144
03 25 01.35	+49 02 05.7	17.170	3	15.570	3	14.547	1	13.336	3	11.964	0.019	11.306	0.019	11.087	0.020	Y	AP 21
03 25 02.77	+50 12 01.7	10.810	3	10.250	3	···		9.532	3	9.061	0.021	8.808	0.017	8.732	0.020	N	HE 633

Table 4.3 – Continued

RA[a] (h m s)	Dec[a] (d m s)	B	Ref[b]	V	Ref[b]	R_C	Ref[b]	I_C	Ref[b]	J	σ_J	H	σ_H	K_s	σ_K	Mem[c]	Names[d]
03 25 03.26	+49 06 42.4	···		17.300	3	16.102	9	14.465	3	12.933	0.021	12.292	0.022	12.034	0.023	Y	AP 151, DH 145
03 25 03.79	+48 49 58.6	···		···		20.108	8	17.910	8	15.696	0.070	15.113	0.100	14.646	0.102	Y	AP 380
03 25 04.38	+49 47 43.5	9.388	3	9.050	3	···		8.750	11	8.337	0.024	8.236	0.029	8.175	0.018	Y	HE 635, MA 58, HD 20969
03 25 06.83	+49 35 23.8	···		···		13.304	9	12.931	9	12.132	0.022	11.586	0.019	11.447	0.019	Y	DH 146
03 25 07.22	+48 49 26.0	···		16.950	4	···		14.557	4	13.116	0.022	12.440	0.026	12.203	0.021	Y	AP 22
03 25 09.93	+48 23 39.3	···		···		16.495	9	14.762	9	13.072	0.023	12.441	0.023	12.140	0.023	Y	DH 147
03 25 10.03	+49 15 05.7	8.269	3	8.150	3	···		7.990	11	7.887	0.019	7.901	0.022	7.873	0.017	Y	HE 639, MA 59, HD 20986
03 25 10.41	+48 59 45.4	···		···		15.682	9	14.139	9	12.588	0.021	12.011	0.023	11.750	0.018	Y	DH 148
03 25 11.00	+49 04 16.5	18.380	5	16.830	5	···		14.251	5	12.769	0.022	12.118	0.023	11.882	0.019	Y	APX 31
03 25 11.42	+48 30 45.0	···		16.200	1	···		14.850	11	13.690	0.025	12.951	0.030	12.761	0.022	N	AP 23
03 25 13.46	+48 38 49.1	···		16.300	1	···		15.040	11	13.898	0.025	13.348	0.030	13.156	0.027	N	AP 24
03 25 13.55	+50 27 32.9	···		···		17.743	8	15.865	8	14.274	0.030	13.590	0.030	13.280	0.032	Y	AP 333
03 25 13.78	+50 25 06.6	···		18.820	6	···		15.496	6	13.550	0.024	12.882	0.022	12.523	0.025	Y	APX 139E
03 25 15.91	+50 09 24.1	13.040	6	12.190	6	···		11.212	6	10.561	0.021	10.229	0.018	10.114	0.016	Y	APX 141
03 25 16.23	+48 22 24.0	13.130	1	12.250	1	11.757	1	11.301	1	10.538	0.025	10.126	0.021	10.010	0.020	Y	AP 25, DH 149
03 25 16.90	+48 36 09.1	···		···		17.626	8	15.805	8	14.062	0.032	13.425	0.035	13.190	0.031	Y	AP 332
03 25 20.44	+49 43 03.3	18.390	6	16.880	6	···		14.035	6	12.338	0.026	11.731	0.027	11.434	0.026	Y	APX 142A
03 25 20.55	+51 00 47.6	···		···		18.779	9	16.650	9	14.511	0.035	13.858	0.041	13.623	0.049	Y	DH 150
03 25 20.71	+49 18 58.1	8.609	3	8.420	3	···		8.220	11	8.037	0.020	8.035	0.024	7.998	0.018	Y	HE 651, MA 60, HD 21005
03 25 22.65	+50 47 39.4	10.743	3	10.310	3	10.104	1	9.835	1	9.425	0.021	9.296	0.017	9.212	0.020	N	HE 647
03 25 22.96	+48 46 56.2	···		18.340	4	···		15.242	3	13.639	0.024	13.039	0.030	12.782	0.025	Y	AP 152
03 25 23.54	+51 02 00.4	12.800	3	12.240	3	···		11.648	3	11.145	0.019	11.046	0.019	10.962	0.020	N	HE 648
03 25 24.31	+47 43 20.6	12.890	2	12.200	2	11.738	2	11.328	2	10.615	0.023	10.345	0.026	10.220	0.020	N	AP 111
03 25 29.49	+47 58 02.3	9.663	3	9.250	3	···		8.750	11	8.369	0.021	8.263	0.020	8.194	0.029	N	HE 658
03 25 31.91	+48 30 11.1	14.830	3	13.680	3	12.971	2	12.334	3	11.383	0.020	10.734	0.021	10.601	0.016	Y	AP 112
03 25 35.72	+47 23 43.8	···		···		16.818	9	14.938	9	13.264	0.024	12.639	0.028	12.371	0.028	Y	DH 151
03 25 36.12	+48 55 57.4	···		···		17.036	9	15.007	9	13.522	0.024	12.933	0.029	12.572	0.021	Y	DH 152
03 25 37.63	+50 19 18.0	10.660	10	10.060	3	9.758	1	9.392	1	8.900	0.021	8.703	0.015	8.614	0.019	Y	HE 660, MA 61
03 25 37.66	+47 01 14.3	8.926	3	8.640	3	···		8.560	11	8.377	0.025	8.329	0.042	8.295	0.020	Y	HE 665, MA 62, HD 21046
03 25 38.68	+46 21 42.1	···		···		15.082	9	14.344	9	13.423	0.025	12.746	0.033	12.561	0.030	Y	DH 153
03 25 39.18	+51 03 36.8	12.237	3	11.670	3	11.543	1	11.210	1	10.639	0.018	10.544	0.017	10.433	0.020	N	HE 656
03 25 41.89	+51 18 22.6	···		17.960	3	17.195	9	14.998	3	13.331	0.024	12.683	0.026	12.464	0.026	Y	AP 153, DH 154
03 25 42.74	+51 47 58.2	11.830	3	11.220	3	···		10.522	3	9.939	0.020	9.710	0.017	9.626	0.017	N	HE 659
03 25 43.59	+48 24 26.0	···		···		17.105	9	15.361	9	13.672	0.024	13.069	0.026	12.770	0.023	Y	DH 155
03 25 45.04	+49 28 07.0	···		···		17.249	9	15.151	9	13.792	0.025	13.206	0.027	12.894	0.030	Y	DH 156
03 25 48.50	+50 00 59.0	···		···		22.715	8	20.151	8	···	···	···	···	···	···	Y	AP 399
03 25 51.38	+48 59 14.6	15.510	5	14.000	5	···		12.356	5	11.077	0.021	10.378	0.015	10.218	0.015	Y	APX 35B
03 25 51.63	+48 36 46.6	17.600	1	16.460	1	15.859	1	15.153	1	14.251	0.035	13.786	0.042	13.615	···	Y	AP 27
03 25 52.99	+48 31 09.0	14.140	1	13.090	1	12.489	1	11.928	1	11.087	0.019	10.536	0.017	10.433	0.019	Y	AP 28
03 25 54.80	+47 27 50.6	11.144	3	9.690	1	8.946	1	8.277	1	7.115	0.020	6.463	0.029	6.327	0.020	N	HE 680
03 25 55.27	+49 59 19.8	14.850	6	13.600	6	···		12.023	6	11.012	0.021	10.392	0.017	10.215	0.015	Y	APX 147B
03 25 57.37	+49 07 14.8	5.981	3	6.060	3	···		6.180	11	6.198	0.021	6.274	0.016	6.309	0.016	Y	HE 675, MA 63, HD 21071
03 25 57.40	+47 43 52.5	···		17.770	3	···		14.550	3	12.734	0.027	12.123	0.029	11.855	0.018	Y	AP 154
03 25 58.83	+48 37 52.2	17.200	1	15.930	1	15.266	1	14.633	1	13.496	0.023	12.954	0.026	12.856	0.028	Y	AP 29
03 25 59.29	+48 34 12.2	···		···		17.329	9	15.650	9	14.352	0.031	13.724	0.036	13.403	0.041	Y	DH 157
03 26 01.31	+48 39 09.7	···		16.800	3	···		14.175	3	12.601	0.021	11.919	0.023	11.692	0.023	Y	AP 155
03 26 02.70	+50 02 25.5	16.330	6	14.590	6	···		12.707	6	11.417	0.022	10.574	0.017	10.378	0.015	Y	APX 148A
03 26 03.04	+49 47 54.5	9.281	3	8.950	3	···		8.670	11	8.192	0.021	8.116	0.029	8.075	0.022	N	HE 679
03 26 03.84	+50 40 49.0	12.081	3	11.430	1	11.051	1	10.674	1	10.139	0.018	9.887	0.017	9.815	0.018	N	HE 676
03 26 04.21	+48 48 07.1	11.160	1	10.590	3	10.253	1	9.930	1	9.494	0.018	9.215	0.019	9.165	0.020	Y	HE 684, AP 32, MA 64
03 26 05.78	+49 36 12.2	···		···		18.427	9	16.591	9	15.490	0.066	14.767	0.071	14.353	0.070	Y	DH 158
03 26 09.32	+51 38 29.8	···		···		14.813	9	13.366	9	11.246	0.021	10.598	0.019	10.338	0.015	Y	DH 159
03 26 10.61	+48 13 18.3	8.680	3	8.480	3	···		8.330	11	8.090	0.018	8.067	0.022	8.073	0.019	N	HE 694, HD 21092
03 26 10.85	+48 23 02.7	7.524	3	7.490	3	···		7.470	11	7.358	0.018	7.429	0.018	7.415	0.021	Y	HE 692, MA 65, HD 21091
03 26 12.08	+49 52 28.6	···		···		16.936	9	14.942	9	13.841	0.027	13.203	0.032	12.941	0.029	Y	DH 160

Table 4.3 – Continued

RA[a] (h m s)	Dec[a] (d m s)	B	Ref[b]	V	Ref[b]	R_C	Ref[b]	I_C	Ref[b]	J	σ_J	H	σ_H	K_s	σ_K	Mem[c]	Names[d]
03 26 12.65	+48 09 08.8	13.940	3	12.920	3	12.346	1	11.845	3	10.991	0.021	10.514	0.015	10.395	0.020	Y	AP 33
03 26 14.19	+48 42 38.3	···		16.200	3	···		13.825	3	12.479	0.021	11.797	0.023	11.555	0.023	Y	AP 34
03 26 15.83	+50 06 56.6	16.900	6	15.420	6	···		13.441	6	12.162	0.021	11.476	0.015	11.264	0.017	Y	APX 150A
03 26 15.96	+49 12 46.2	···		15.900	1	···		14.790	11	13.689	0.026	13.053	0.024	12.855	0.025	N	AP 35
03 26 15.99	+45 59 54.5	···		···		16.167	9	14.799	9	13.681	0.027	13.056	0.033	12.793	0.026	Y	DH 161
03 26 16.40	+48 50 28.4	13.570	1	12.610	1	12.066	1	11.564	1	10.810	0.017	10.322	0.019	10.214	0.020	Y	AP 37
03 26 16.56	+50 41 00.1	14.140	6	13.080	6	···		11.889	6	11.094	0.019	10.581	0.017	10.449	0.018	Y	APX 151A
03 26 19.36	+49 13 32.6	12.370	1	11.610	1	11.179	1	10.757	1	10.183	0.020	9.790	0.015	9.697	0.013	Y	HE 696, AP 38
03 26 19.55	+50 42 46.2	15.810	6	14.310	6	···		12.637	6	11.381	0.018	10.735	0.017	10.544	0.018	Y	APX 151B
03 26 21.60	+48 44 50.0	···		···		24.331	8	21.565	8	···	···	···	···	···	···	Y	AP 410
03 26 22.22	+49 25 37.5	12.011	3	11.310	3	10.855	1	10.456	1	9.900	0.018	9.503	0.017	9.414	0.020	Y	HE 699, MA 66
03 26 22.46	+48 27 01.5	···		16.400	1	···		15.510	11	14.692	0.034	14.218	0.045	14.152	0.065	N	AP 39
03 26 22.63	+47 16 09.4	···		11.890	3	···		10.960	3	10.281	0.029	9.917	0.030	9.764	0.022	Y	AP 156
03 26 24.56	+49 51 36.9	···		···		18.578	9	15.992	9	14.720	0.037	14.089	0.043	13.823	0.050	Y	DH 162
03 26 25.33	+48 20 06.9	12.880	1	12.030	1	11.564	1	11.119	1	10.374	0.021	10.001	0.017	9.875	0.019	Y	AP 41
03 26 25.74	+49 07 16.3	···		15.800	1	···		15.040	11	13.934	0.030	13.347	0.029	13.211	0.036	N	AP 40
03 26 26.03	+48 27 33.5	···		···		17.624	9	15.509	9	13.968	0.025	13.414	0.030	13.062	0.031	Y	DH 163
03 26 27.64	+49 02 12.4	13.810	1	12.840	1	12.260	1	11.687	1	10.775	0.021	10.262	0.015	10.110	0.017	Y	AP 43
03 26 28.42	+49 41 29.3	···		17.220	4	15.787	9	14.240	4	12.565	0.022	11.950	0.019	11.692	0.020	Y	AP 157, DH 164
03 26 28.80	+48 25 43.9	···		16.600	1	···		15.990	11	14.987	0.040	14.532	0.060	14.330	0.067	N	AP 44
03 26 32.05	+53 31 10.4	···		···		18.676	9	16.492	9	14.102	0.032	13.506	0.038	13.189	0.038	Y	DH 165
03 26 32.64	+47 15 59.2	8.360	10	8.180	10	···		7.980	11	7.797	0.025	7.799	0.069	7.726	0.026	Y	HE 710, MA 67, HD 21122
03 26 33.24	+50 07 41.7	···		···		17.967	8	16.148	8	14.350	0.031	13.764	0.031	13.397	0.035	Y	AP 339
03 26 33.70	+50 13 54.5	12.780	3	11.930	3	···		10.913	3	10.200	0.020	9.817	0.017	9.697	0.015	Y	AP 158
03 26 34.10	+49 07 46.1	···		···		20.247	8	18.049	8	15.876	0.090	15.275	0.106	14.672	0.100	Y	AP 315
03 26 35.48	+49 15 43.8	···		···		19.045	8	17.040	8	15.123	0.048	14.538	0.061	14.222	0.056	Y	AP 366
03 26 36.66	+49 38 13.0	···		17.960	4	···		14.918	4	13.240	0.024	12.618	0.032	12.373	0.024	Y	AP 159
03 26 36.84	+46 56 50.4	···		···		16.105	9	14.404	9	13.039	0.024	12.430	0.036	12.168	0.022	Y	DH 166
03 26 39.17	+47 52 56.4	10.170	1	9.660	1	9.362	1	9.029	1	8.600	0.030	8.482	0.051	8.335	0.018	Y	HE 721, MA 70
03 26 39.45	+50 50 47.5	7.720	10	7.640	10	···		7.540	11	7.347	0.025	7.434	0.036	7.382	0.018	Y	HE 703, MA 68, HD 21117
03 26 40.75	+48 46 36.8	10.192	3	9.720	3	9.476	1	9.196	1	8.764	0.025	8.583	0.047	8.567	0.022	Y	HE 715, AP 49, MA 69
03 26 40.87	+49 57 34.8	18.730	6	17.290	6	16.112	9	14.564	6	13.035	0.026	12.363	0.029	12.081	0.025	Y	APX 153A, DH 167
03 26 40.96	+49 17 00.6	15.870	1	14.830	1	14.186	1	13.648	1	12.784	0.026	12.336	0.032	12.211	0.028	Y	AP 48
03 26 42.05	+49 47 20.7	10.792	3	10.020	3	9.629	1	9.207	1	8.579	0.017	8.282	0.029	8.183	0.026	N	HE 707
03 26 42.36	+49 00 34.4	11.615	3	10.420	3	9.807	1	9.210	1	8.206	0.024	7.640	0.045	7.481	0.024	N	HE 716, AP 50
03 26 43.91	+49 54 34.4	11.602	3	10.920	3	10.555	1	10.155	1	9.632	0.025	9.299	0.026	9.216	0.021	Y	HE 709, MA 71
03 26 45.10	+50 25 06.7	···		···		19.461	8	17.258	8	14.884	0.041	14.258	0.043	13.879	0.049	Y	AP 369
03 26 47.99	+50 02 15.5	···		···		18.445	8	16.562	8	14.618	0.034	14.042	0.051	13.727	0.045	Y	AP 349, DH 168
03 26 50.11	+48 47 32.1	10.880	3	10.300	10	9.995	1	9.651	1	9.200	0.023	9.010	0.029	8.894	0.022	Y	HE 727, AP 51, MA 72
03 26 50.24	+47 54 57.9	7.833	3	7.720	3	···		7.620	11	7.439	0.025	7.410	0.031	7.411	0.021	N	HE 729, HD 21152
03 26 51.62	+51 54 40.3	···		···		18.702	9	16.523	9	14.312	0.034	13.658	0.038	13.405	0.033	Y	DH 169
03 26 52.08	+50 00 32.6	···		···		18.238	8	16.270	8	14.329	0.030	13.688	0.044	13.386	0.038	Y	AP 344
03 26 52.98	+48 43 51.5	16.590	1	15.480	1	14.881	1	14.308	1	13.548	0.024	13.114	0.033	12.998	0.029	Y	AP 53
03 27 00.30	+49 14 38.0	···		···		19.713	8	17.670	8	···	···	···	···	···	···	Y	AP 378
03 27 00.98	+49 14 40.8	···		···		19.930	7	17.750	7	15.608	0.059	14.936	0.076	14.501	0.078	Y	AP 316
03 27 03.24	+48 47 13.4	10.439	3	9.940	3	···		9.450	11	8.966	0.037	8.743	0.028	8.682	0.022	Y	HE 733, MA 73
03 27 05.16	+48 12 19.8	6.814	3	6.830	3	···		6.890	11	6.752	0.018	6.849	0.034	6.796	0.016	Y	HE 735, MA 74, HD 21181
03 27 05.59	+47 25 30.0	···		19.440	4	17.810	9	16.038	4	14.158	0.030	13.501	0.035	13.213	0.030	Y	AP 284, DH 170
03 27 12.17	+48 03 42.9	···		17.800	4	···		14.910	4	13.286	0.032	12.598	0.036	12.311	0.032	Y	AP 285
03 27 13.31	+46 49 23.6	10.100	3	8.990	3	···		7.808	3	6.855	0.043	6.269	0.031	6.141	0.017	N	HE 741
03 27 14.12	+50 52 44.0	10.716	3	10.170	3	9.892	1	9.570	1	9.079	0.025	8.822	0.027	8.778	0.021	N	HE 732, MA 75, HD 232793
03 27 18.24	+47 57 28.6	···		18.700	4	···		15.281	4	13.204	0.035	12.551	0.033	12.261	0.030	Y	AP 286
03 27 18.87	+47 25 24.2	···		14.860	4	···		12.701	4	11.363	0.026	10.669	0.031	10.448	0.021	Y	AP 161
03 27 20.37	+47 59 25.1	14.470	3	13.400	3	12.660	2	12.151	3	11.214	0.024	10.587	0.029	10.468	0.020	Y	AP 114
03 27 23.30	+48 22 24.6	14.000	1	13.000	1	12.409	1	11.847	1	11.021	0.021	10.465	0.023	10.339	0.022	Y	AP 56

Table 4.3 – Continued

RA[a] (h m s)	Dec[a] (d m s)	B	Ref[b]	V	Ref[b]	R_C	Ref[b]	I_C	Ref[b]	J	σ_J	H	σ_H	K_s	σ_K	Mem[c]	Names[d]
03 27 23.94	+46 46 17.3	···		···		17.801	9	15.615	9	14.155	0.029	13.513	0.030	13.240	0.032	Y	DH 171
03 27 30.09	+48 52 10.4	···		15.700	1	···		14.380	11	13.275	0.027	12.591	0.030	12.420	0.028	N	AP 57
03 27 31.31	+48 39 23.1	···		···		19.745	8	17.586	8	15.140	0.054	14.546	0.054	14.172	0.055	Y	AP 377
03 27 31.64	+48 53 23.2	···		···		18.669	8	16.693	8	14.543	0.036	14.011	0.040	13.624	0.044	Y	AP 354
03 27 33.82	+47 55 22.1	···		15.250	5	···		12.680	5	11.281	0.021	10.667	0.021	10.468	0.025	Y	APX 40
03 27 34.94	+47 57 16.6	···		19.600	4	18.187	9	16.010	4	13.987	0.031	13.398	0.034	13.073	0.033	Y	AP 287, DH 172
03 27 35.20	+51 12 11.8	···		···		15.565	9	14.159	9	12.273	0.022	11.589	0.031	11.369	0.025	Y	DH 173
03 27 37.57	+48 16 22.6	8.054	3	7.950	3	···		7.830	11	7.691	0.023	7.688	0.020	7.643	0.020	Y	HE 756, MA 77, HD 21239
03 27 37.79	+48 59 28.8	11.126	3	10.540	3	10.254	1	9.921	1	9.433	0.020	9.194	0.023	9.137	0.024	Y	HE 750, AP 58, MA 76
03 27 38.59	+48 24 59.2	17.440	3	15.740	3	14.669	1	13.207	3	11.792	0.022	11.102	0.021	10.900	0.023	Y	AP 60
03 27 38.77	+48 29 42.9	15.770	2	14.130	2	13.256	2	12.438	2	11.085	0.021	10.320	0.021	10.123	0.022	N	AP 115
03 27 38.96	+49 35 59.7	6.960	3	6.990	3	···		6.992	3	6.892	0.023	6.986	0.024	6.959	0.022	N	HE 747, MA 78, HD 21238
03 27 39.87	+47 29 27.5	···		17.170	4	···		14.426	4	12.858	0.029	12.190	0.030	11.953	0.022	Y	AP 288
03 27 40.01	+48 33 55.8	···		···		20.235	8	18.125	8	15.749	0.078	15.235	0.113	14.671	0.100	Y	AP 384
03 27 41.21	+48 40 33.7	···		···		20.819	8	18.455	8	15.338	0.063	14.719	0.081	14.181	0.064	Y	AP 389
03 27 43.42	+50 48 57.7	18.840	3	17.090	3	16.110	9	14.309	3	12.770	0.023	12.107	0.030	11.858	0.025	Y	AP 162, DH 174
03 27 46.74	+50 10 21.6	15.740	6	14.270	6	···		12.559	6	11.206	0.022	10.603	0.030	10.391	0.025	Y	APX 156B
03 27 46.78	+50 10 35.5	13.920	6	12.920	6	···		11.729	6	10.911	0.023	10.443	0.030	10.288	0.025	Y	APX 156A
03 27 47.75	+49 00 18.5	13.860	1	12.770	1	12.147	1	11.598	1	10.702	0.020	10.225	0.021	10.076	0.024	N	AP 61
03 27 48.15	+48 55 25.9	18.270	1	16.840	1	16.157	1	15.475	1	14.673	0.041	14.173	0.046	14.094	0.062	N	AP 62
03 27 48.45	+49 54 02.0	15.360	6	13.930	6	···		12.324	6	11.272	0.023	10.657	0.030	10.483	0.025	Y	APX 155B
03 27 48.52	+49 54 18.4	···		17.680	6	···		14.745	6	13.132	0.026	12.474	0.031	12.217	0.026	Y	APX 155D
03 27 48.59	+48 47 18.6	···		···		16.342	9	14.557	9	13.224	0.025	12.600	0.027	12.379	0.027	Y	DH 175
03 27 49.06	+50 31 52.1	···		···		16.477	9	14.856	9	13.052	0.024	12.422	0.027	12.183	0.030	Y	DH 176
03 27 49.31	+47 27 33.6	···		17.300	4	15.895	9	14.186	4	12.419	0.027	11.799	0.032	11.515	0.024	Y	AP 164, DH 177
03 27 49.88	+48 04 45.1	···		18.810	3	17.373	9	15.434	3	13.721	0.029	13.035	0.031	12.847	0.031	Y	AP 163, DH 178
03 27 50.32	+50 10 28.7	15.990	6	14.420	6	···		12.651	6	11.254	0.022	10.545	0.029	10.336	0.025	Y	APX 156C
03 27 51.03	+49 12 10.0	13.210	1	12.290	1	11.767	1	11.253	1	10.513	0.021	9.993	0.030	9.860	0.022	Y	AP 63
03 27 53.91	+51 16 54.7	···		···		16.127	9	14.864	9	12.855	0.023	12.194	0.032	11.969	0.028	Y	DH 179
03 27 55.02	+49 45 37.2	11.265	3	10.660	3	10.338	1	9.972	1	9.482	0.022	9.214	0.028	9.156	0.025	Y	HE 767, MA 79
03 27 55.76	+47 44 09.4	7.307	3	7.260	3	···		7.230	11	7.078	0.023	7.136	0.059	7.105	0.020	Y	HE 775, MA 80, HD 21279
03 28 00.49	+47 34 56.4	···		···		15.887	9	14.360	9	12.826	0.027	12.168	0.029	11.884	0.022	Y	DH 180
03 28 00.81	+49 00 00.9	14.050	1	13.000	1	12.410	1	11.896	1	11.037	0.021	10.510	0.021	10.422	0.025	Y	AP 65
03 28 00.92	+49 48 27.7	14.420	6	13.170	6	···		11.795	6	10.894	0.023	10.317	0.028	10.214	0.025	Y	APX 157D
03 28 02.21	+48 41 06.9	···		···		19.727	8	17.391	8	14.847	0.044	14.296	0.051	13.935	0.050	Y	AP 372
03 28 02.94	+44 23 24.5	8.560	10	8.120	10	···		7.600	11	7.217	0.030	7.015	0.069	6.951	0.021	Y	MA 81, HD 21312
03 28 03.08	+50 40 19.1	···		17.160	4	16.135	9	14.461	4	12.900	0.023	12.237	0.031	12.032	0.027	Y	AP 165, DH 181
03 28 03.09	+49 03 46.6	4.878	3	4.970	3	···		5.110	11	5.117	0.041	5.223	0.038	5.217	0.016	Y	HE 774, MA 82, HD 21278
03 28 06.40	+49 03 06.3	···		12.100	1	···		···		9.692	0.019	8.972	0.023	8.797	0.022	N	AP 66
03 28 07.07	+50 32 09.1	11.783	3	11.100	3	10.722	1	10.278	1	9.636	0.022	9.325	0.028	9.259	0.024	N	HE 771
03 28 10.37	+49 25 01.4	···		16.500	1	···		14.760	11	13.628	0.027	13.006	0.038	12.805	0.029	N	AP 67
03 28 10.51	+47 25 26.4	···		13.520	3	···		12.136	3	11.194	0.027	10.576	0.030	10.443	0.020	Y	AP 167
03 28 11.21	+46 43 07.6	···		···		18.260	9	16.160	9	14.905	0.036	14.200	0.041	14.000	0.048	Y	DH 182
03 28 12.89	+48 19 57.2	···		···		15.923	9	14.405	9	12.883	0.026	12.196	0.026	11.999	0.027	Y	DH 183
03 28 13.36	+48 56 15.5	···		18.060	5	···		15.026	5	13.345	0.026	12.714	0.031	12.428	0.028	Y	APX 42B
03 28 13.62	+49 13 13.5	14.480	1	13.380	1	12.738	1	12.189	1	11.362	0.019	10.840	0.028	10.720	0.025	N	AP 68
03 28 15.12	+49 49 06.2	15.010	6	13.510	6	···		11.923	6	10.836	0.019	10.197	0.028	10.051	0.025	Y	APX 157B
03 28 15.51	+48 24 11.8	17.280	1	16.150	1	15.516	1	14.978	1	14.035	0.033	13.554	0.037	13.420	0.037	Y	AP 69
03 28 16.00	+48 37 40.0	···		···		22.179	8	19.781	8	···	···	···	···	···	···	Y	AP 396
03 28 16.59	+48 40 54.3	···		16.760	5	···		13.988	5	12.341	0.025	11.685	0.027	11.458	0.025	Y	APX 43B
03 28 17.24	+48 40 57.8	14.320	5	13.260	5	···		12.020	5	11.079	0.021	10.526	0.024	10.395	0.022	Y	APX 43A
03 28 18.59	+49 57 10.5	8.256	3	8.090	3	···		7.930	11	7.649	0.021	7.609	0.036	7.544	0.024	Y	HE 780, MA 83, HD 21302
03 28 18.68	+48 39 48.2	13.830	1	12.830	1	12.269	1	11.755	1	10.999	0.021	10.484	0.029	10.331	0.025	Y	AP 70
03 28 21.80	+50 36 06.0	13.270	6	12.380	6	···		11.266	6	10.403	0.021	9.984	0.030	9.845	0.025	Y	APX 158
03 28 21.89	+47 36 06.6	···		···		15.175	9	13.761	9	12.200	0.030	11.519	0.034	11.266	0.024	Y	DH 184

Table 4.3 – Continued

RA[a] (h m s)	Dec[a] (d m s)	B	Ref[b]	V	Ref[b]	R_C	Ref[b]	I_C	Ref[b]	J	σ_J	H	σ_H	K_s	σ_K	Mem[c]	Names[d]
03 28 22.54	+49 14 29.3	13.770	1	12.780	1	12.217	1	11.714	1	10.942	0.021	10.477	0.028	10.383	0.024	Y	AP 72
03 28 22.94	+49 11 24.0	···		···		19.057	8	17.030	8	15.016	0.052	14.330	0.062	14.150	0.060	Y	AP 365
03 28 23.74	+47 36 49.9	···		13.280	3	12.710	9	12.021	3	11.044	0.025	10.560	0.030	10.392	0.020	Y	AP 169, DH 185
03 28 26.87	+50 20 01.1	···		···		21.511	8	19.207	8	16.472	0.135	15.713	0.155	15.299	0.160	Y	AP 392
03 28 28.74	+50 14 54.7	···		19.900	4	···		16.524	4	14.558	0.037	13.971	0.043	13.682	0.047	N	AP 289
03 28 28.99	+50 18 10.1	···		19.200	4	17.756	9	15.789	4	13.810	0.032	13.162	0.040	12.907	0.032	Y	AP 290, DH 186
03 28 29.09	+45 40 03.7	···		···		17.734	9	15.723	9	14.739	0.036	14.079	0.047	13.779	0.038	Y	DH 187
03 28 31.49	+48 56 27.4	10.106	3	9.660	3	···		8.990	11	8.838	0.019	8.686	0.021	8.642	0.022	Y	HE 799, MA 84
03 28 34.04	+48 33 55.8	17.280	1	16.080	1	15.324	1	14.667	1	13.652	0.026	13.018	0.032	12.853	0.033	Y	AP 74
03 28 34.67	+50 16 00.8	10.606	3	10.060	3	9.765	1	9.421	1	8.975	0.021	8.746	0.028	8.687	0.025	Y	HE 794, MA 85
03 28 35.06	+47 55 04.2	···		17.870	5	16.639	9	14.962	5	13.309	0.027	12.668	0.035	12.403	0.025	Y	APX 45B, DH 188
03 28 36.00	+49 25 09.6	···		17.480	5	15.894	9	14.672	5	13.051	0.023	12.426	0.031	12.176	0.028	Y	APX 44C, DH 189
03 28 37.98	+49 23 15.5	8.583	3	8.410	3	···		8.180	11	8.070	0.019	8.048	0.026	8.047	0.027	N	HE 802, MA 86, HD 21345
03 28 38.12	+47 55 25.3	···		17.990	5	···		15.091	5	13.394	0.029	12.769	0.033	12.510	0.020	Y	APX 45A
03 28 39.95	+48 46 17.7	···		17.370	5	···		14.635	5	13.049	0.027	12.429	0.027	12.213	0.027	Y	APX 46
03 28 47.43	+49 16 28.0	15.090	1	13.820	1	13.030	1	12.233	3	11.144	0.029	10.509	0.033	10.284	0.020	Y	AP 75
03 28 47.71	+50 01 58.4	···		···		18.536	8	16.638	8	14.710	0.042	14.089	0.046	13.818	0.039	Y	AP 351, DH 190
03 28 48.48	+49 11 54.2	14.000	2	13.050	2	12.462	2	11.936	2	11.038	0.027	10.432	0.031	10.336	0.020	Y	AP 117
03 28 48.74	+48 20 24.8	···		16.920	5	15.966	9	14.286	5	12.760	0.027	12.124	0.032	11.910	0.020	Y	AP 76, APX 48, DH 191
03 28 50.08	+48 07 37.4	···		18.420	3	···		15.262	3	13.530	0.032	12.854	0.034	12.635	0.022	Y	AP 170
03 28 51.65	+49 18 30.8	17.310	1	16.100	3	15.657	1	15.224	1	14.362	0.033	13.955	0.043	13.774	0.033	N	AP 77
03 28 52.33	+49 50 54.1	5.536	3	5.580	3	···		5.660	11	5.596	0.024	5.680	0.040	5.654	0.016	Y	HE 810, MA 87, HD 21362
03 28 52.96	+50 19 25.8	···		19.800	4	17.802	8	15.970	8	14.417	0.040	13.761	0.036	13.520	0.036	Y	AP 291, AP 335
03 28 53.66	+49 04 13.1	7.573	3	7.460	3	···		7.350	11	7.186	0.025	7.153	0.040	7.117	0.021	Y	HE 817, MA 88, HD 21375
03 28 54.34	+50 16 18.4	···		16.210	4	···		13.807	4	12.412	0.027	11.744	0.034	11.488	0.020	Y	AP 292
03 28 54.36	+47 29 20.3	13.740	5	12.750	5	···		11.578	5	10.707	0.027	10.200	0.030	10.111	0.018	Y	APX 49A
03 28 55.08	+49 00 12.3	···		···		16.346	9	15.049	9	14.055	0.029	13.300	0.032	13.124	0.033	Y	DH 192
03 28 56.65	+46 13 35.3	···		···		16.553	9	15.367	9	14.436	0.032	13.731	0.033	13.567	0.033	Y	DH 193
03 28 57.21	+49 34 01.9	···		15.750	3	···		13.582	3	12.362	0.025	11.655	0.033	11.433	0.018	Y	AP 171
03 28 59.63	+48 14 08.3	12.300	2	11.620	4	11.164	2	10.777	4	10.144	0.033	9.829	0.038	9.654	0.053	Y	HE 828
03 29 00.12	+49 44 12.0	14.370	5	13.280	5	···		12.002	5	11.008	0.027	10.465	0.030	10.342	0.023	Y	APX 50
03 29 02.09	+50 20 45.9	12.603	3	11.180	3	10.461	1	9.767	1	8.660	0.043	8.043	0.069	7.845	0.022	N	HE 815
03 29 06.33	+49 19 12.9	···		17.540	5	···		14.686	5	13.071	0.027	12.448	0.030	12.173	0.018	Y	APX 52
03 29 07.63	+48 18 10.5	7.367	3	7.360	3	···		7.380	11	7.306	0.043	7.357	0.055	7.320	0.018	Y	HE 831, MA 89, HD 21398
03 29 08.20	+48 25 35.0	···		···		21.585	8	19.250	8	···	···	···	···	···	···	Y	AP 393
03 29 08.26	+48 10 50.8	10.522	3	10.050	4	···		9.419	4	8.995	0.018	8.832	0.030	8.772	0.020	Y	HE 833
03 29 08.74	+47 47 07.2	9.700	3	9.200	3	···		8.521	3	8.046	0.023	7.837	0.038	7.782	0.022	N	HE 836
03 29 12.96	+50 08 05.2	···		16.500	3	15.508	9	14.041	3	12.607	0.025	11.981	0.030	11.685	0.018	Y	AP 172, DH 194
03 29 14.15	+49 41 16.9	···		12.260	3	···		11.185	3	10.393	0.025	9.865	0.030	9.732	0.018	Y	AP 173
03 29 14.68	+48 10 51.4	···		15.310	3	···		12.731	3	11.251	0.025	10.593	0.030	10.362	0.018	Y	AP 174
03 29 15.49	+47 53 32.2	···		17.450	3	···		14.615	3	13.047	0.026	12.472	0.033	12.159	0.021	Y	AP 175
03 29 18.74	+50 22 10.8	···		···		19.898	8	17.779	8	15.684	0.066	15.106	0.086	14.658	0.084	Y	AP 379
03 29 18.99	+46 07 27.4	···		16.410	3	15.118	9	13.611	3	12.078	0.027	11.437	0.032	11.210	0.020	Y	AP 176, DH 195
03 29 22.06	+49 30 32.2	4.562	3	4.660	3	···		4.920	11	5.311	0.262	4.898	0.034	4.854	0.018	Y	HE 835, MA 90, HD 21428
03 29 24.96	+48 57 45.1	10.831	3	10.280	3	9.973	1	9.640	1	9.199	0.024	9.006	0.072	8.924	0.024	Y	HE 841, MA 91
03 29 26.24	+48 12 11.7	10.580	10	9.990	4	9.664	1	9.263	4	8.816	0.023	8.533	0.047	8.528	0.020	Y	HE 848, AP 79, MA 92
03 29 26.28	+46 56 16.3	6.366	3	6.240	3	···		6.140	11	5.875	0.030	5.902	0.059	5.903	0.021	N	HE 861, HD 21455
03 29 26.69	+49 20 35.4	14.080	1	13.060	1	12.469	1	11.907	1	11.124	0.027	10.590	0.030	10.450	0.025	Y	AP 78
03 29 32.15	+43 13 50.6	9.240	10	8.900	10	···		8.490	11	8.273	0.041	8.144	0.067	8.079	0.018	Y	MA 93, HD 21490
03 29 33.97	+48 58 54.8	···		···		17.533	9	15.447	9	14.016	0.030	13.437	0.036	13.130	0.038	Y	DH 196
03 29 35.90	+49 04 31.0	12.130	3	11.290	3	···		10.321	3	9.559	0.021	9.148	0.023	9.069	0.024	N	HE 850
03 29 37.85	+49 21 57.8	15.870	1	15.000	1	14.485	1	13.983	1	13.322	0.025	13.012	0.038	12.819	0.034	Y	AP 80
03 29 38.17	+49 20 01.1	···		···		16.639	9	14.554	9	13.227	0.026	12.661	0.033	12.295	0.026	Y	DH 197
03 29 40.49	+50 59 23.7	···		···		15.607	9	14.558	9	12.647	0.022	11.980	0.027	11.747	0.021	Y	DH 198
03 29 42.17	+49 19 16.7	13.330	1	12.430	1	11.956	1	11.500	1	10.815	0.020	10.468	0.028	10.379	0.022	N	AP 81

Table 4.3 – Continued

RA[a] (h m s)	Dec[a] (d m s)	B	Ref[b]	V	Ref[b]	R_C	Ref[b]	I_C	Ref[b]	J	σ_J	H	σ_H	K_s	σ_K	Mem[c]	Names[d]
03 29 43.76	+49 48 05.5	14.960	6	13.800	6	···		12.377	6	11.444	0.020	10.882	0.025	10.716	0.021	Y	APX 159
03 29 44.81	+48 15 25.3	···		···		12.223	9	12.040	9	11.035	0.020	10.639	0.023	10.560	0.022	Y	DH 199
03 29 46.86	+49 00 34.3	9.727	3	9.210	1	8.909	1	8.608	1	8.153	0.023	7.931	0.036	7.869	0.021	Y	HE 863, AP 83, MA 95
03 29 46.90	+47 34 58.0	10.070	3	9.550	3	···		8.881	3	8.404	0.032	8.141	0.038	8.064	0.018	Y	HE 876, MA 96
03 29 47.02	+49 09 13.6	8.832	3	8.520	3	···		8.110	11	7.945	0.025	7.867	0.020	7.804	0.024	Y	HE 862, MA 94, HD 21480
03 29 49.98	+47 58 36.7	7.763	3	7.660	3	···		7.540	11	7.347	0.023	7.314	0.031	7.284	0.021	N	HE 875, MA 98, HD 21481
03 29 50.37	+48 06 34.2	···		17.320	5	16.079	9	14.658	5	13.080	0.025	12.463	0.027	12.218	0.029	Y	APX 55, DH 200
03 29 51.85	+49 12 48.7	7.372	3	7.280	3	···		7.240	11	7.005	0.024	7.007	0.031	6.977	0.018	Y	HE 868, MA 97, HD 21479
03 29 53.28	+48 06 52.4	10.863	3	10.380	3	10.120	1	9.808	1	9.372	0.019	9.209	0.021	9.133	0.024	N	HE 879
03 29 57.88	+48 26 14.1	···		···		17.433	9	15.391	9	13.896	0.030	13.350	0.035	13.031	0.033	Y	DH 201
03 29 58.42	+50 15 25.2	···		···		15.102	9	14.112	9	12.784	0.023	12.137	0.028	11.914	0.025	Y	DH 202
03 30 00.84	+49 17 44.5	···		16.200	1	···		15.370	11	14.282	0.035	13.612	0.041	13.391	0.039	N	AP 84
03 30 03.72	+51 30 43.6	11.042	3	10.480	3	10.186	1	9.831	1	9.337	0.019	9.119	0.026	9.053	0.020	Y	HE 859
03 30 04.80	+49 15 35.5	···		16.890	3	15.673	9	14.265	3	12.813	0.022	12.195	0.032	11.937	0.026	Y	AP 178, DH 203
03 30 05.51	+51 02 04.0	11.415	3	10.730	3	···		10.410	11	9.253	0.019	9.026	0.022	8.931	0.020	Y	HE 865
03 30 05.78	+46 06 23.8	···		···		17.723	9	15.786	9	14.826	0.035	14.092	0.043	13.860	0.039	Y	DH 204
03 30 08.54	+49 42 57.1	12.890	6	12.060	6	···		11.198	6	10.635	0.019	10.324	0.026	10.240	0.022	Y	APX 160A
03 30 11.12	+48 08 13.0	···		16.770	3	···		13.935	3	12.266	0.022	11.640	0.026	11.398	0.023	Y	AP 179
03 30 18.93	+49 43 34.9	···		18.670	6	17.364	9	15.363	6	13.532	0.027	12.933	0.028	12.629	0.025	Y	APX 160G, DH 205
03 30 19.33	+48 29 57.3	9.066	3	8.790	3	···		8.630	11	8.240	0.025	8.177	0.031	8.121	0.020	Y	HE 885, MA 99, HD 21527
03 30 20.21	+47 31 10.0	···		···		15.126	9	14.141	9	12.830	0.022	12.066	0.029	11.913	0.023	Y	DH 206
03 30 21.84	+49 00 16.5	···		···		15.657	9	13.978	9	12.461	0.022	11.847	0.031	11.582	0.023	Y	DH 207
03 30 22.48	+48 24 41.4	15.630	1	14.310	1	13.492	1	12.723	1	11.589	0.023	10.941	0.030	10.769	0.024	Y	AP 86
03 30 24.36	+46 35 56.1	···		16.320	4	···		13.796	4	12.407	0.023	11.739	0.029	11.476	0.023	Y	AP 180
03 30 27.25	+49 55 45.9	15.760	6	14.330	6	···		12.724	6	11.456	0.023	10.801	0.027	10.623	0.021	Y	APX 161I
03 30 29.12	+48 53 19.3	···		···		18.295	9	16.258	9	14.828	0.038	14.160	0.043	13.895	0.044	Y	DH 208
03 30 29.67	+49 01 29.2	···		17.600	3	16.347	9	14.620	3	12.956	0.022	12.324	0.029	12.063	0.023	Y	AP 181, DH 209
03 30 31.18	+47 16 10.3	···		···		12.092	9	11.922	9	10.719	0.019	10.259	0.028	10.137	0.021	Y	DH 210
03 30 31.21	+46 26 15.0	···		···		18.875	9	16.960	9	15.906	0.065	15.245	0.074	15.149	0.105	Y	DH 211
03 30 31.96	+49 43 03.9	···		···		17.719	9	15.335	9	13.602	0.027	13.026	0.033	12.690	0.030	Y	DH 212
03 30 33.24	+46 10 27.2	···		···		15.317	9	13.836	9	12.766	0.025	12.145	0.032	11.908	0.023	Y	DH 213
03 30 33.24	+49 27 21.4	13.660	5	12.700	5	···		11.625	5	10.824	0.022	10.294	0.027	10.197	0.024	Y	APX 59
03 30 33.97	+47 37 41.4	9.056	3	8.780	3	···		8.480	11	8.194	0.032	8.091	0.045	8.079	0.036	Y	HE 906, MA 101, HD 21553
03 30 36.49	+48 15 29.3	···		17.340	4	16.025	9	14.495	4	12.886	0.023	12.260	0.032	11.979	0.028	Y	AP 182, DH 214
03 30 36.94	+48 06 13.0	5.780	3	5.820	3	···		5.910	11	5.823	0.020	5.924	0.042	5.896	0.020	Y	HE 904, MA 100, HD 21551
03 30 41.21	+49 14 10.0	16.930	1	15.910	1	15.378	1	14.757	1	14.166	0.032	13.819	0.049	13.674	0.048	Y	AP 87
03 30 41.88	+49 03 02.2	12.700	5	11.890	5	···		10.989	5	10.317	0.019	9.907	0.028	9.817	0.021	Y	APX 61
03 30 42.36	+48 21 25.4	···		···		19.610	7	17.450	7	15.147	0.050	14.710	0.074	14.151	0.069	Y	AP 318
03 30 43.01	+49 56 23.6	···		···		17.969	9	15.639	9	14.155	0.043	13.472	0.097	13.250	0.050	Y	DH 215
03 30 47.60	+47 53 21.6	11.801	3	11.100	3	10.543	1	10.155	1	9.655	0.019	9.346	0.028	9.267	0.025	Y	HE 917
03 30 47.63	+48 13 01.5	···		19.020	4	···		15.792	4	14.080	0.032	13.499	0.041	13.265	0.037	Y	AP 293
03 30 48.40	+52 03 48.1	···		···		18.782	9	16.922	9	14.814	0.038	14.141	0.045	13.856	0.047	Y	DH 216
03 30 55.19	+48 47 40.3	···		···		17.912	9	15.850	9	14.317	0.033	13.714	0.038	13.411	0.036	Y	DH 217
03 30 55.27	+48 39 22.8	···		16.500	3	15.449	9	14.060	3	12.657	0.023	12.009	0.029	11.782	0.023	Y	AP 184, DH 218
03 30 55.73	+51 52 16.7	···		···		17.466	9	15.623	9	13.296	0.025	12.697	0.032	12.405	0.022	Y	DH 219
03 30 55.80	+46 48 21.2	···		16.450	3	···		13.871	3	12.399	0.025	11.705	0.029	11.442	0.023	Y	AP 185
03 30 56.80	+50 00 50.7	···		15.820	3	14.725	9	13.567	3	12.203	0.022	11.475	0.029	11.266	0.019	Y	AP 183, DH 220
03 31 02.40	+48 00 09.3	···		18.360	5	···		15.362	5	13.679	0.025	13.032	0.035	12.814	0.026	Y	APX 62A
03 31 03.14	+49 02 55.8	···		···		18.840	7	16.890	7	14.979	0.044	14.274	0.045	13.937	0.045	Y	AP 319
03 31 03.39	+50 24 41.5	···		···		18.054	8	16.165	8	14.400	0.030	13.735	0.037	13.469	0.035	Y	AP 341
03 31 05.10	+48 16 24.3	···		17.170	4	···		14.684	4	13.285	0.021	12.658	0.032	12.417	0.028	Y	AP 186
03 31 11.32	+47 56 48.6	12.150	3	11.650	3	···		11.096	3	10.599	0.019	10.425	0.027	10.371	0.025	N	HE 932
03 31 14.66	+49 42 22.4	8.789	3	8.590	3	···		8.430	11	8.185	0.021	8.145	0.047	8.089	0.022	Y	HE 921, MA 102, HD 21600
03 31 15.09	+48 57 05.9	···		···		18.012	9	15.867	9	14.381	0.030	13.808	0.040	13.512	0.033	Y	DH 221
03 31 16.12	+48 25 12.1	···		16.100	5	14.906	9	13.356	5	11.805	0.025	11.167	0.031	10.906	0.022	Y	APX 63, DH 222

Table 4.3 – Continued

RA[a] (h m s)	Dec[a] (d m s)	B	Ref[b]	V	Ref[b]	R_C	Ref[b]	I_C	Ref[b]	J	σ_J	H	σ_H	K_s	σ_K	Mem[c]	Names[d]
03 31 16.50	+49 33 03.4	···		16.490	3	15.456	9	14.004	3	12.579	0.022	11.906	0.033	11.682	0.023	Y	AP 187, DH 223
03 31 22.34	+50 34 42.7	···		···		14.448	9	13.531	9	11.851	0.026	11.134	0.032	10.925	0.021	Y	DH 224
03 31 24.31	+50 12 27.5	···		14.350	3	···		12.725	3	11.657	0.022	10.924	0.027	10.799	0.021	Y	AP 188
03 31 25.21	+49 02 51.0	···		···		18.690	7	16.790	7	14.802	0.026	14.189	0.045	13.765	0.039	Y	AP 320
03 31 25.73	+47 41 20.6	11.740	3	11.170	3	···		10.481	3	9.995	0.019	9.716	0.027	9.654	0.024	N	HE 945
03 31 28.99	+48 59 28.4	10.699	3	10.060	3	9.689	1	9.323	1	8.860	0.018	8.593	0.036	8.460	0.022	Y	HE 935, MA 104
03 31 30.16	+49 54 07.4	9.011	3	8.750	3	···		8.560	11	8.223	0.023	8.137	0.045	8.174	0.024	Y	HE 931, MA 103, HD 21619
03 31 30.64	+49 20 32.8	···		···		16.401	9	14.590	9	13.023	0.025	12.366	0.031	12.123	0.021	Y	DH 225
03 31 33.14	+47 51 44.8	6.730	3	6.750	3	···		6.810	11	6.722	0.018	6.754	0.033	6.766	0.020	Y	HE 955, APX 64, MA 105, HD 21641
03 31 33.76	+49 52 02.1	···		···		18.175	8	16.342	8	14.558	0.036	13.883	0.051	13.660	0.036	Y	AP 347
03 31 43.78	+50 06 05.9	11.995	3	11.410	3	11.031	1	10.653	1	10.110	0.024	9.833	0.028	9.749	0.019	N	HE 936, APX 164
03 31 44.56	+49 32 12.6	10.050	3	9.620	3	···		8.870	11	8.735	0.037	8.522	0.029	8.502	0.019	Y	HE 944, MA 106
03 31 44.88	+49 33 03.7	13.990	3	13.050	3	12.449	9	11.868	3	10.999	0.027	10.425	0.029	10.310	0.021	Y	AP 189, DH 226
03 31 48.73	+48 53 30.1	···		15.870	3	···		13.617	3	12.195	0.032	11.680	0.044	11.293	0.029	Y	AP 190
03 31 50.65	+49 59 14.7	···		18.160	6	···		15.198	6	13.559	0.024	12.854	0.028	12.600	0.024	Y	APX 166A
03 31 51.66	+49 20 00.4	···		15.630	3	14.443	9	13.144	3	11.712	0.021	11.034	0.032	10.826	0.023	Y	AP 191, DH 227
03 31 52.87	+47 20 43.6	···		17.650	4	···		14.608	4	13.008	0.025	12.395	0.023	12.135	0.019	Y	AP 294
03 31 53.75	+45 34 52.2	···		···		14.738	9	13.987	9	12.940	0.020	12.264	0.023	12.073	0.021	Y	DH 228
03 31 53.94	+48 44 06.6	6.592	3	6.620	3	···		6.660	11	6.575	0.024	6.623	0.042	6.581	0.020	Y	HE 965, MA 107, HD 21672
03 31 54.21	+48 31 38.4	10.976	3	10.410	3	···		9.940	11	9.351	0.022	9.061	0.028	9.018	0.021	Y	HE 968, MA 108
03 31 55.80	+48 35 01.7	8.377	3	8.190	3	···		8.050	11	7.850	0.030	7.842	0.045	7.803	0.024	Y	HE 970, MA 109
03 31 57.92	+48 10 42.1	12.224	3	11.670	3	11.300	1	10.923	1	10.414	0.022	10.120	0.032	10.090	0.021	N	HE 979
03 31 58.67	+50 06 55.6	15.000	6	13.820	6	···		12.368	6	11.395	0.022	10.776	0.030	10.579	0.021	Y	APX 167
03 31 58.71	+49 52 12.6	9.592	3	9.200	3	···		8.830	11	8.382	0.021	8.224	0.042	8.172	0.021	N	HE 958, MA 110
03 32 00.67	+52 31 42.2	···		···		16.900	9	15.564	9	13.530	0.027	12.848	0.029	12.636	0.024	Y	DH 229
03 32 03.82	+47 21 56.5	···		18.420	4	···		15.648	4	14.062	0.029	13.418	0.033	13.132	0.030	Y	AP 192
03 32 04.60	+49 20 48.0	···		···		23.152	8	20.611	8	···	···	···	···	···	···	Y	AP 403
03 32 06.01	+50 05 53.9	···		···		17.465	8	15.731	8	14.107	0.028	13.432	0.035	13.147	0.026	Y	AP 331, DH 230
03 32 06.89	+49 25 22.5	···		···		18.490	8	16.574	8	14.698	0.067	14.095	0.056	13.840	0.059	Y	AP 350
03 32 08.60	+48 01 24.6	5.356	3	5.460	3	···		5.590	11	5.567	0.023	5.665	0.040	5.665	0.016	Y	HE 985, MA 111, HD 21699
03 32 09.59	+49 26 20.4	12.510	5	11.620	5	···		10.622	5	9.895	0.024	9.453	0.031	9.342	0.021	Y	HE 973, APX 67
03 32 10.22	+49 08 28.8	···		12.280	3	···		11.321	3	10.496	0.022	10.076	0.032	9.972	0.021	Y	AP 193
03 32 10.48	+50 39 31.4	12.270	3	11.160	3	···		9.930	3	8.945	0.029	8.423	0.034	8.267	0.022	N	HE 960
03 32 14.96	+46 39 22.8	12.760	3	12.020	3	···		11.158	3	10.556	0.023	10.220	0.021	10.123	0.018	N	AP 194
03 32 15.72	+50 23 09.4	···		···		12.708	9	12.355	9	11.405	0.022	11.003	0.029	10.933	0.021	Y	DH 231
03 32 16.76	+48 08 27.7	10.362	3	9.800	3	···		9.200	11	8.666	0.023	8.423	0.034	8.396	0.023	Y	HE 988
03 32 18.26	+48 32 48.3	···		···		17.338	9	15.337	9	13.844	0.029	13.268	0.032	12.946	0.030	Y	DH 232
03 32 18.77	+49 32 15.8	···		···		19.950	7	17.750	7	15.463	0.059	14.666	0.057	14.318	0.057	Y	AP 321
03 32 18.80	+49 32 18.0	···		···		19.561	8	17.472	8	···	···	···	···	···	···	Y	AP 374
03 32 19.32	+47 04 27.0	···		12.510	3	···		11.493	3	10.683	0.022	10.215	0.020	10.123	0.019	Y	AP 196
03 32 20.87	+48 41 04.9	12.720	3	11.850	3	···		10.891	3	10.172	0.022	9.731	0.030	9.659	0.021	N	AP 195
03 32 21.69	+49 24 22.3	···		···		17.654	9	15.636	9	14.152	0.027	13.491	0.037	13.219	0.030	Y	DH 233
03 32 24.00	+50 16 58.0	···		···		19.062	8	16.838	8	···	···	···	···	···	···	Y	AP 360
03 32 27.67	+47 20 56.8	···		19.540	4	18.041	9	16.224	4	14.374	0.030	13.666	0.029	13.407	0.032	Y	AP 295, DH 234
03 32 29.09	+47 38 21.3	13.310	3	12.310	3	···		11.138	3	10.312	0.023	9.768	0.024	9.657	0.018	Y	AP 197
03 32 29.84	+50 02 16.5	15.900	6	14.510	6	···		13.020	6	11.890	0.026	11.234	0.032	11.081	0.018	Y	APX 174
03 32 30.69	+49 10 34.7	12.870	3	12.060	3	11.501	2	11.111	3	10.331	0.026	9.859	0.031	9.767	0.018	Y	AP 118
03 32 31.48	+49 54 42.4	15.660	6	14.240	6	···		12.750	6	11.515	0.027	10.919	0.032	10.712	0.020	Y	APX 173A
03 32 31.88	+51 29 22.5	10.810	3	10.240	3	···		9.580	3	9.137	0.043	8.891	0.031	8.837	0.021	Y	HE 972, MA 112, HD 232804
03 32 35.61	+47 16 46.8	···		···		16.958	9	15.193	9	13.530	0.026	12.877	0.024	12.615	0.023	Y	DH 235
03 32 37.36	+48 15 07.1	···		···		17.052	9	15.200	9	13.708	0.027	13.080	0.029	12.789	0.025	Y	DH 236
03 32 38.35	+47 46 33.2	···		16.250	5	···		13.616	5	11.989	0.022	11.360	0.023	11.130	0.019	Y	APX 69A
03 32 38.99	+51 30 43.1	···		···		18.960	9	16.787	9	14.265	0.031	13.651	0.037	13.408	0.035	Y	DH 237
03 32 42.58	+48 08 20.2	10.056	3	9.610	3	···		8.980	11	8.718	0.054	8.555	0.074	8.505	0.022	Y	HE 1005
03 32 43.64	+50 18 22.6	···		···		19.732	8	17.564	8	15.422	0.054	14.756	0.050	14.360	0.057	Y	AP 376

Table 4.3 – Continued

RA[a] (h m s)	Dec[a] (d m s)	B	Ref[b]	V	Ref[b]	R_C	Ref[b]	I_C	Ref[b]	J	σ_J	H	σ_H	K_s	σ_K	Mem[c]	Names[d]
03 32 44.44	+47 41 35.2	13.080	3	12.100	3	···		11.015	3	10.223	0.022	9.734	0.024	9.588	0.018	Y	AP 199
03 32 45.18	+50 05 15.6	···		15.340	3	···		13.428	3	12.160	0.026	11.484	0.030	11.256	0.022	Y	AP 198
03 32 46.15	+48 59 11.5	···		···		18.332	9	16.644	9	15.255	0.035	14.579	0.042	14.218	0.071	Y	DH 238
03 32 47.87	+50 21 18.8	11.564	3	10.840	3	10.469	2	10.047	2	9.408	0.024	9.146	0.030	9.050	0.018	Y	HE 992
03 32 51.08	+49 50 44.0	···		13.080	3	12.526	9	11.850	3	10.787	0.026	10.277	0.033	10.138	0.022	Y	AP 201, DH 239
03 32 51.17	+50 07 06.6	···		12.650	3	···		11.449	3	10.599	0.026	10.014	0.032	9.863	0.020	Y	AP 200
03 33 03.25	+51 49 55.1	···		···		18.565	9	16.529	9	14.904	0.039	14.262	0.050	13.996	0.054	Y	DH 240
03 33 09.43	+50 50 42.9	···		15.200	3	···		13.240	3	12.120	0.022	11.418	0.027	11.255	0.019	Y	AP 202
03 33 11.81	+48 01 02.8	12.120	3	10.320	3	···		7.127	3	5.254	0.218	4.156	0.162	3.832	0.300	N	HE 1034
03 33 15.06	+49 56 12.7	15.160	6	13.860	6	···		12.505	6	11.420	0.022	10.862	0.029	10.718	0.021	Y	APX 182A
03 33 20.71	+48 45 48.9	···		···		19.630	7	17.500	7	15.227	0.041	14.711	0.056	14.353	0.064	Y	AP 323
03 33 22.25	+47 25 19.4	8.350	3	8.250	3	···		8.090	3	7.862	0.020	7.855	0.026	7.820	0.022	N	HE 1056, MA 113, HD 21855
03 33 23.99	+50 07 46.7	···		15.480	6	···		13.435	6	12.245	0.026	11.517	0.028	11.350	0.021	N	APX 184
03 33 25.57	+48 20 12.4	···		18.100	3	16.574	9	15.013	3	13.216	0.029	12.693	0.034	12.338	0.021	Y	AP 203, DH 241
03 33 27.99	+49 11 57.7	12.167	3	11.340	3	10.926	2	10.517	2	9.899	0.024	9.590	0.028	9.475	0.021	N	HE 1036
03 33 31.56	+48 02 39.5	13.910	5	12.960	5	···		11.827	5	11.031	0.022	10.554	0.031	10.416	0.019	Y	APX 72
03 33 32.17	+47 31 51.3	···		···		16.311	9	14.737	9	13.236	0.025	12.569	0.026	12.292	0.021	Y	DH 242
03 33 34.12	+46 07 25.9	···		15.200	3	14.208	9	13.193	3	11.937	0.022	11.250	0.021	11.064	0.023	Y	AP 205, DH 243
03 33 35.35	+49 02 13.4	···		17.300	4	16.188	9	14.565	4	13.078	0.026	12.431	0.030	12.212	0.023	Y	AP 204, DH 244
03 33 42.15	+47 20 48.7	13.590	3	12.680	3	···		11.663	3	10.943	0.022	10.500	0.023	10.407	0.020	N	AP 206
03 33 42.38	+49 22 25.1	···		···		17.058	9	15.121	9	13.628	0.024	13.002	0.035	12.739	0.024	Y	DH 245
03 33 45.75	+50 08 51.3	···		···		18.148	8	16.302	8	14.514	0.032	13.847	0.033	13.550	0.043	Y	AP 345
03 33 47.14	+47 35 31.1	···		15.540	3	14.499	9	13.344	3	11.999	0.021	11.323	0.019	11.112	0.016	Y	AP 208, DH 246
03 33 48.19	+48 52 28.2	···		···		20.460	7	18.100	7	15.821	0.063	15.076	0.067	14.877	0.099	Y	AP 324
03 33 49.95	+49 09 34.3	···		16.270	3	···		13.737	3	12.380	0.026	11.809	0.038	11.559	0.024	Y	AP 207
03 33 50.02	+49 37 59.9	···		15.110	6	···		13.160	6	11.938	0.026	11.223	0.031	11.054	0.022	Y	APX 193A
03 33 50.40	+48 55 39.3	···		16.370	4	···		14.042	4	12.737	0.024	12.047	0.036	11.769	0.023	Y	AP 209
03 33 54.37	+50 17 47.9	9.879	3	9.480	3	···		9.070	11	8.706	0.034	8.601	0.042	8.567	0.020	Y	HE 1050, MA 114
03 33 57.57	+48 09 32.4	9.910	3	9.510	3	···		9.005	3	8.574	0.024	8.445	0.053	8.410	0.023	N	HE 1074
03 33 57.67	+51 40 48.4	11.770	3	11.110	3	···		10.363	3	9.767	0.024	9.513	0.032	9.432	0.019	N	HE 1032
03 33 58.93	+50 52 56.0	10.430	3	9.940	3	···		9.319	3	8.873	0.025	8.673	0.031	8.640	0.022	Y	HE 1045, MA 115
03 33 59.89	+50 41 33.5	12.620	3	11.760	3	···		10.811	3	10.038	0.024	9.766	0.029	9.675	0.019	N	HE 1051
03 34 07.49	+48 32 05.5	···		···		17.990	8	16.067	8	14.317	0.032	13.691	0.033	13.376	0.036	Y	AP 337, DH 247
03 34 11.21	+51 27 51.5	···		15.960	3	···		13.548	3	12.162	0.024	11.554	0.032	11.302	0.023	Y	AP 210
03 34 11.31	+49 50 26.3	···		15.070	3	···		13.158	3	11.931	0.022	11.235	0.029	11.060	0.022	Y	AP 211
03 34 12.96	+48 37 02.9	7.367	3	7.340	3	···		7.390	11	7.206	0.020	7.300	0.049	7.260	0.021	Y	HE 1082, MA 116, HD 21931
03 34 15.62	+49 58 45.3	···		···		17.364	8	15.659	8	13.942	0.029	13.247	0.036	12.937	0.033	Y	AP 330
03 34 16.10	+49 55 42.6	13.130	6	12.210	6	···		11.202	6	10.509	0.021	10.067	0.029	10.009	0.020	Y	APX 198A
03 34 18.40	+50 59 27.9	···		···		15.967	9	14.723	9	12.664	0.027	12.001	0.033	11.745	0.022	Y	DH 248
03 34 21.59	+48 39 36.0	9.050	3	8.830	3	···		8.555	3	8.233	0.023	8.215	0.036	8.163	0.029	Y	HE 1084, MA 117
03 34 28.56	+47 04 24.6	12.005	3	11.200	3	···		10.410	11	9.707	0.022	9.341	0.029	9.264	0.021	N	HE 1100
03 34 29.35	+49 21 43.5	···		13.240	3	···		12.078	3	11.273	0.022	10.754	0.031	10.581	0.018	Y	AP 212
03 34 36.04	+47 59 32.2	···		···		17.473	9	15.282	9	14.056	0.031	13.417	0.035	13.072	0.033	Y	DH 249
03 34 37.80	+49 13 53.0	···		···		18.634	8	16.756	8	···	···	···	···	···	···	Y	AP 358
03 34 39.40	+48 18 43.1	12.380	3	11.550	3	···		10.610	3	9.898	0.019	9.493	0.028	9.357	0.024	Y	AP 213
03 34 40.78	+50 03 40.3	···		···		19.113	8	17.056	8	15.091	0.038	14.573	0.058	14.050	0.057	Y	AP 367
03 34 42.70	+47 41 04.2	10.950	3	10.720	3	···		10.330	3	9.883	0.022	9.786	0.029	9.724	0.025	N	HE 1104
03 34 43.36	+47 53 12.6	11.628	3	11.030	3	···		9.760	11	9.664	0.023	9.319	0.028	9.206	0.022	N	HE 1102, MA 118
03 34 47.00	+47 39 49.2	···		···		18.067	9	15.629	9	14.158	0.032	13.474	0.036	13.262	0.036	Y	DH 250
03 34 47.98	+51 44 19.0	11.710	3	10.480	3	···		9.125	3	8.076	0.027	7.490	0.038	7.363	0.021	N	HE 1073
03 34 53.67	+48 32 29.4	···		···		16.571	9	14.660	9	13.064	0.024	12.433	0.031	12.202	0.023	Y	DH 251
03 34 54.73	+48 41 19.3	16.820	3	15.230	3	···		13.299	3	12.112	0.023	11.404	0.027	11.190	0.025	Y	AP 214
03 35 01.75	+45 42 10.1	···		···		14.609	9	13.219	9	12.293	0.021	11.574	0.028	11.369	0.025	Y	DH 252
03 35 05.02	+50 54 45.1	11.990	3	11.320	3	···		10.535	3	9.900	0.023	9.586	0.028	9.502	0.022	Y	HE 1086, MA 119
03 35 06.12	+49 36 42.6	14.810	6	13.680	6	···		12.373	6	11.396	0.021	10.824	0.027	10.705	0.023	Y	APX 202A

Table 4.3 – Continued

RA[a] (h m s)	Dec[a] (d m s)	B	Ref[b]	V	Ref[b]	R_C	Ref[b]	I_C	Ref[b]	J	σ_J	H	σ_H	K_s	σ_K	Mem[c]	Names[d]
03 35 08.75	+49 44 39.6	11.940	2	11.250	2	10.814	2	10.426	2	9.785	0.019	9.444	0.028	9.311	0.020	Y	HE 1101, MA 120
03 35 15.78	+46 05 40.2	···		15.190	3	···		13.164	3	11.970	0.019	11.234	0.029	11.037	0.026	Y	AP 217
03 35 18.85	+47 56 05.1	···		16.730	3	15.617	9	14.169	3	12.678	0.021	11.991	0.030	11.748	0.027	Y	AP 216, DH 253
03 35 20.02	+48 54 39.0	···		16.610	3	15.740	9	14.114	3	12.638	0.026	11.958	0.030	11.739	0.020	Y	AP 215, DH 254
03 35 23.93	+46 56 30.5	···		···		15.206	9	13.759	9	12.537	0.023	11.827	0.031	11.605	0.027	Y	DH 255
03 35 25.88	+49 46 54.3	···		···		21.842	8	19.370	8	16.634	0.149	16.189	0.208	15.557	0.152	Y	AP 394
03 35 26.67	+49 38 01.1	12.380	3	11.670	3	···		10.750	3	10.138	0.022	9.739	0.028	9.649	0.021	N	HE 1110
03 35 27.87	+46 44 10.1	···		18.350	3	···		15.201	3	13.459	0.025	12.794	0.033	12.527	0.030	Y	AP 218
03 35 33.14	+45 35 32.0	···		···		15.763	9	14.638	9	13.352	0.025	12.600	0.022	12.364	0.022	Y	DH 256
03 35 35.55	+47 34 57.8	···		···		15.282	9	13.763	9	12.373	0.023	11.654	0.020	11.443	0.018	Y	DH 257
03 35 40.26	+48 24 01.8	···		16.550	4	···		14.147	4	12.596	0.022	11.883	0.032	11.649	0.023	Y	AP 219
03 35 40.28	+48 26 28.0	···		18.570	4	···		15.307	4	13.529	0.039	12.997	0.044	12.702	0.043	Y	AP 296
03 35 44.16	+49 06 07.2	···		12.680	3	···		11.624	3	10.878	0.022	10.300	0.031	10.193	0.021	Y	AP 220
03 35 47.36	+49 17 43.1	···		···		19.950	7	17.650	7	15.278	0.046	14.555	0.051	14.114	0.051	Y	AP 325
03 35 55.64	+48 26 41.9	···		17.630	4	16.344	9	14.722	4	13.128	0.024	12.496	0.035	12.199	0.023	Y	AP 297, DH 258
03 35 58.49	+47 05 27.8	6.870	3	6.890	3	···		6.930	11	6.862	0.021	6.912	0.018	6.929	0.020	Y	HE 1153, MA 121, HD 22136
03 36 02.88	+46 42 57.6	···		15.680	3	···		13.474	3	12.188	0.022	11.459	0.024	11.219	0.020	Y	AP 221
03 36 10.84	+45 56 13.3	···		18.430	3	16.860	9	15.132	3	13.335	0.022	12.703	0.027	12.412	0.021	Y	AP 223, DH 259
03 36 12.08	+50 47 03.1	···		···		16.387	9	15.115	9	13.023	0.021	12.313	0.032	12.081	0.023	Y	DH 260
03 36 16.85	+47 30 57.4	···		···		15.426	9	14.048	9	12.777	0.023	12.088	0.023	11.821	0.020	Y	DH 261
03 36 22.04	+49 09 20.8	12.610	3	11.830	3	···		10.890	3	10.048	0.022	9.652	0.031	9.535	0.021	Y	AP 225
03 36 29.01	+52 16 31.8	···		···		18.794	9	16.467	9	14.098	0.034	13.516	0.037	13.180	0.026	Y	DH 262
03 36 29.37	+48 11 33.4	4.120	3	4.200	3	···		4.390	11	4.316	0.256	4.153	0.027	4.107	0.264	N	HE 1164, MA 122, HD 22192
03 36 31.85	+48 39 16.8	10.650	3	10.160	3	···		9.529	3	9.081	0.021	8.887	0.032	8.826	0.021	Y	HE 1160, MA 123
03 36 39.77	+47 47 32.3	11.150	3	10.570	3	···		9.872	3	9.375	0.019	9.078	0.018	9.027	0.020	N	HE 1181
03 36 53.64	+48 23 58.1	···		12.450	3	···		11.413	3	10.573	0.021	10.066	0.027	9.977	0.021	Y	AP 226
03 36 55.07	+48 49 42.8	10.560	3	10.070	3	···		9.488	3	9.047	0.034	8.880	0.028	8.822	0.022	Y	HE 1180, MA 124
03 36 57.72	+48 44 45.6	11.913	3	11.190	3	···		10.230	11	9.836	0.022	9.479	0.030	9.348	0.020	Y	HE 1185, MA 125
03 36 58.41	+47 38 34.5	15.960	5	14.520	5	···		12.943	5	11.729	0.022	11.036	0.019	10.898	0.019	Y	APX 73A
03 37 00.25	+50 56 25.1	12.158	3	11.520	3	···		11.190	11	10.204	0.026	9.955	0.026	9.922	0.021	N	HE 1151
03 37 01.33	+49 52 42.9	···		···		15.998	9	14.997	9	13.900	0.028	13.212	0.032	12.986	0.030	Y	DH 263
03 37 01.60	+48 13 21.7	···		15.430	3	14.209	9	13.234	3	12.020	0.022	11.317	0.025	11.132	0.022	Y	AP 227, DH 264
03 37 09.32	+48 36 10.6	11.940	3	11.310	3	···		10.573	3	10.021	0.021	9.757	0.028	9.708	0.021	N	HE 1196
03 37 11.65	+50 01 22.4	···		···		17.425	9	15.395	9	13.451	0.027	12.881	0.035	12.524	0.026	Y	DH 265
03 37 12.11	+49 41 07.3	10.553	3	10.200	3	···		10.110	11	9.455	0.024	9.344	0.026	9.282	0.022	N	HE 1183
03 37 13.96	+49 33 27.1	10.612	3	10.060	3	···		9.610	11	8.972	0.032	8.729	0.031	8.649	0.022	N	HE 1187
03 37 14.68	+50 26 26.0	···		···		12.476	9	12.270	9	11.145	0.026	10.643	0.032	10.524	0.023	Y	DH 266
03 37 17.57	+47 20 53.9	9.596	3	9.170	3	···		8.630	11	8.337	0.024	8.181	0.018	8.094	0.018	Y	HE 1218
03 37 22.47	+48 19 15.5	11.410	3	10.850	3	···		10.181	3	9.688	0.021	9.474	0.025	9.413	0.020	N	HE 1208
03 37 27.43	+50 39 54.4	···		···		17.113	9	15.467	9	13.312	0.027	12.652	0.030	12.416	0.026	Y	DH 267
03 37 27.49	+47 33 44.1	···		14.630	3	13.673	9	12.861	3	11.798	0.021	11.129	0.021	10.913	0.018	Y	AP 229, DH 268
03 37 33.80	+48 35 37.6	···		···		16.685	9	14.817	9	13.597	0.031	13.072	0.035	12.742	0.032	Y	DH 269
03 37 34.37	+47 31 54.2	···		14.600	3	···		12.831	3	11.652	0.038	10.939	0.039	10.781	0.033	Y	AP 230
03 37 42.97	+52 15 49.7	···		···		16.408	9	14.821	9	12.840	0.023	12.211	0.023	11.959	0.021	Y	DH 270
03 37 43.08	+48 07 02.7	9.372	3	8.880	3	···		8.990	11	7.907	0.018	7.708	0.017	7.660	0.020	N	HE 1225, HD 22326
03 37 48.93	+52 14 46.3	···		···		17.242	9	15.871	9	13.891	0.025	13.189	0.031	12.962	0.030	Y	DH 271
03 37 49.37	+48 01 17.5	···		14.070	3	···		12.599	3	11.539	0.022	10.890	0.021	10.754	0.020	Y	AP 231
03 37 50.70	+45 56 25.3	···		14.840	3	···		12.531	3	11.140	0.020	10.430	0.021	10.205	0.020	Y	AP 232
03 38 05.67	+46 33 57.9	···		18.420	4	···		15.575	4	13.996	0.028	13.381	0.034	13.063	0.037	Y	AP 234
03 38 08.46	+49 35 12.1	10.690	3	9.530	3	···		8.300	3	7.319	0.021	6.806	0.022	6.599	0.016	N	HE 1224
03 38 14.76	+45 51 03.8	14.150	3	13.120	3	···		11.909	3	11.034	0.021	10.468	0.018	10.343	0.018	Y	AP 235
03 38 15.41	+51 35 22.5	10.913	3	10.320	3	···		9.730	11	9.164	0.021	8.941	0.021	8.840	0.019	N	HE 1202
03 38 15.58	+47 34 37.2	7.454	3	7.450	3	···		7.450	11	7.363	0.023	7.393	0.022	7.375	0.021	Y	HE 1259, MA 126, HD 22401
03 38 15.91	+47 49 05.3	11.570	3	11.220	3	···		10.868	3	10.481	0.022	10.377	0.021	10.295	0.020	N	HE 1256
03 38 20.87	+49 31 36.3	···		···		16.129	9	14.272	9	12.497	0.020	11.852	0.019	11.575	0.017	Y	DH 272

Table 4.3 – Continued

RA[a] (h m s)	Dec[a] (d m s)	B	Ref[b]	V	Ref[b]	R_C	Ref[b]	I_C	Ref[b]	J	σ_J	H	σ_H	K_s	σ_K	Mem[c]	Names[d]
03 38 26.93	+49 12 20.5	6.950	3	6.860	3	···		6.776	3	6.634	0.021	6.624	0.020	6.644	0.020	N	HE 1245, HD 22417
03 38 30.29	+48 19 12.4	···		17.430	4	16.206	9	14.604	4	13.037	0.023	12.376	0.019	12.156	0.022	Y	AP 236, DH 273
03 38 35.09	+48 35 36.6	8.870	3	8.650	3	···		8.385	3	8.104	0.020	8.067	0.020	8.005	0.027	Y	HE 1260, MA 127, HD 22440
03 38 36.04	+47 05 36.9	···		16.840	3	···		13.860	3	12.192	0.021	11.570	0.019	11.278	0.018	Y	AP 237
03 38 43.39	+48 02 25.8	···		14.310	4	···		12.446	4	11.309	0.023	10.598	0.019	10.425	0.015	Y	AP 238
03 38 49.20	+48 08 43.6	···		16.390	3	···		14.043	4	12.719	0.023	12.026	0.021	11.790	0.020	Y	AP 239
03 38 50.51	+46 36 12.6	10.780	10	10.260	10	···		9.650	11	9.158	0.022	8.850	0.016	8.757	0.018	Y	MA 128
03 38 51.73	+49 24 18.4	10.109	3	9.050	3	···		7.990	11	7.094	0.019	6.600	0.022	6.473	0.022	N	HE 1262
03 38 55.09	+48 57 28.4	···		···		21.100	7	18.700	7	16.194	0.109	15.462	0.115	15.186	0.151	Y	AP 326
03 38 55.41	+48 14 16.7	···		17.220	4	···		14.018	4	12.272	0.024	11.667	0.028	11.379	0.022	Y	AP 240
03 38 57.84	+47 13 42.0	···		···		18.286	9	16.191	9	14.786	0.039	14.122	0.041	13.917	0.051	Y	DH 274
03 39 02.91	+51 36 37.1	11.530	3	10.810	3	···		9.996	3	9.360	0.024	9.017	0.025	8.929	0.020	Y	HE 1234, MA 129
03 39 05.95	+51 23 39.2	11.540	3	10.990	3	···		10.379	3	9.913	0.024	9.806	0.029	9.734	0.021	N	HE 1240
03 39 05.95	+47 44 43.5	···		15.990	3	14.952	9	13.662	3	12.265	0.021	11.578	0.019	11.344	0.018	Y	AP 241, DH 275
03 39 45.72	+47 45 04.8	11.790	3	11.170	3	···		10.510	11	10.070	0.022	9.752	0.020	9.691	0.018	N	HE 1316
03 39 46.03	+46 07 47.2	···		18.450	4	···		15.615	4	14.043	0.029	13.399	0.030	13.033	0.032	Y	AP 243
03 39 48.17	+49 19 41.7	11.978	3	11.350	3	···		10.650	11	10.076	0.022	9.758	0.030	9.672	0.018	N	HE 1300
03 39 53.58	+47 23 01.7	11.425	3	10.910	3	···		10.090	11	9.913	0.020	9.731	0.021	9.663	0.014	N	HE 1325
03 39 55.02	+49 16 20.0	···		···		17.069	9	15.036	9	13.472	0.025	12.893	0.035	12.578	0.026	Y	DH 276
03 40 06.11	+46 49 34.6	11.670	3	11.120	3	···		10.441	3	9.955	0.023	9.717	0.021	9.647	0.018	N	HE 1350
03 40 22.78	+50 01 38.2	10.310	3	9.880	3	···		9.403	3	8.939	0.027	8.809	0.029	8.737	0.018	N	HE 1308
03 40 22.94	+47 33 39.6	12.236	3	11.810	3	···		12.040	11	11.011	0.022	10.915	0.021	10.828	0.018	N	HE 1351
03 40 28.66	+48 45 39.2	12.570	3	12.020	3	···		11.409	3	10.904	0.021	10.721	0.028	10.631	0.025	N	HE 1332
03 40 33.93	+48 04 35.7	···		12.890	3	···		11.805	3	10.967	0.022	10.445	0.026	10.352	0.023	Y	AP 244
03 40 34.51	+52 00 30.0	9.460	10	9.110	10	···		8.700	11	8.454	0.021	8.375	0.042	8.365	0.022	Y	MA 130, HD 22603
03 40 35.73	+50 10 12.9	11.750	3	11.320	3	···		10.805	3	10.371	0.023	10.214	0.029	10.162	0.023	N	HE 1315
03 40 50.50	+50 57 55.0	16.800	3	15.240	3	···		12.707	3	11.300	0.022	10.686	0.031	10.478	0.026	Y	AP 246
03 40 56.47	+49 30 22.1	9.932	3	9.770	3	···		9.820	11	9.421	0.023	9.391	0.027	9.363	0.020	N	HE 1344
03 40 58.28	+47 02 37.1	···		13.200	3	···		12.038	3	11.203	0.020	10.646	0.019	10.517	0.018	Y	AP 247
03 41 04.77	+49 09 32.5	···		15.960	3	14.955	9	13.717	3	12.403	0.023	11.723	0.031	11.503	0.027	Y	AP 248, DH 277
03 41 05.74	+45 47 37.8	10.840	10	10.310	10	···		9.670	11	9.076	0.024	8.798	0.031	8.705	0.020	Y	MA 131
03 41 07.50	+49 07 55.2	···		13.370	3	···		11.986	3	11.076	0.020	10.503	0.026	10.334	0.022	Y	AP 249
03 41 10.58	+46 32 26.4	···		14.940	3	···		13.152	3	11.966	0.022	11.240	0.020	11.100	0.021	Y	AP 250
03 41 11.26	+46 00 49.4	···		18.370	4	···		15.381	4	13.708	0.021	13.086	0.031	12.824	0.028	Y	AP 251
03 41 13.52	+45 48 02.4	14.070	3	12.950	3	···		11.710	3	10.786	0.022	10.234	0.022	10.110	0.020	N	AP 252
03 41 27.95	+48 20 18.8	···		···		18.513	9	16.165	9	14.341	0.037	13.698	0.040	13.374	0.049	Y	DH 278
03 41 28.69	+50 07 13.4	11.441	3	10.640	3	···		9.860	11	9.104	0.022	8.750	0.030	8.629	0.025	N	HE 1354
03 41 30.65	+46 09 34.9	···		18.250	4	···		15.288	4	13.598	0.026	12.926	0.035	12.687	0.030	Y	AP 253
03 41 30.99	+47 46 58.8	···		···		15.565	9	14.636	9	14.015	0.027	13.266	0.036	13.069	0.033	Y	DH 279
03 41 33.62	+49 23 37.9	···		···		15.707	9	14.504	9	13.366	0.025	12.669	0.036	12.439	0.030	Y	DH 280
03 41 37.06	+49 54 41.6	11.720	3	10.470	3	···		9.163	3	8.152	0.021	7.539	0.026	7.380	0.018	N	HE 1364
03 41 40.95	+51 16 35.6	9.930	3	9.470	3	···		8.926	3	8.502	0.018	8.323	0.021	8.288	0.024	Y	HE 1349, MA 132, HD 232823
03 41 41.28	+49 36 04.9	···		···		17.837	9	15.722	9	14.097	0.031	13.520	0.039	13.186	0.038	Y	DH 281
03 41 42.33	+49 33 22.1	12.139	3	11.740	3	···		10.720	11	10.907	0.020	10.793	0.026	10.742	0.021	N	HE 1375
03 42 11.25	+49 06 12.6	···		···		16.356	9	15.147	9	13.878	0.027	13.130	0.036	12.921	0.034	Y	DH 282
03 42 27.22	+48 43 19.3	···		···		13.805	9	13.252	9	12.233	0.023	11.737	0.029	11.593	0.021	Y	DH 283
03 42 27.46	+46 31 48.3	···		15.670	3	···		13.417	3	12.068	0.023	11.390	0.029	11.137	0.022	Y	AP 254
03 42 44.65	+49 39 01.1	···		12.180	3	···		11.279	3	10.599	0.023	10.219	0.027	10.114	0.024	Y	AP 255
03 43 12.15	+49 41 02.5	···		···		12.056	9	11.683	9	10.821	0.023	10.495	0.027	10.412	0.025	Y	DH 284
03 43 15.24	+48 05 01.1	···		···		16.277	9	15.159	9	14.497	0.039	13.747	0.033	13.531	0.043	Y	DH 285
03 43 27.77	+50 37 36.8	···		···		13.696	9	13.041	9	11.571	0.021	10.883	0.027	10.721	0.020	Y	DH 286
03 43 37.37	+48 40 45.4	···		···		14.915	9	14.152	9	12.845	0.026	12.138	0.028	12.005	0.023	Y	DH 287
03 43 38.51	+46 03 47.7	12.600	3	11.790	3	···		10.870	3	10.198	0.021	9.792	0.027	9.682	0.025	Y	AP 256
03 44 02.60	+48 39 58.7	···		13.000	3	12.417	9	11.886	3	11.063	0.023	10.570	0.028	10.446	0.023	Y	AP 257, DH 288
03 44 04.65	+48 18 48.7	···		···		15.808	9	14.922	9	13.932	0.025	13.215	0.034	13.053	0.034	Y	DH 289

Table 4.3 – Continued

RA[a] (h m s)	Dec[a] (d m s)	B	Ref[b]	V	Ref[b]	R_C	Ref[b]	I_C	Ref[b]	J	σ_J	H	σ_H	K_s	σ_K	Mem[c]	Names[d]
03 44 05.11	+47 25 59.7	···		···		13.291	9	12.673	9	11.859	0.020	11.192	0.025	11.020	0.021	Y	DH 290
03 44 51.23	+47 53 17.3	···		···		14.148	9	13.597	9	13.244	0.025	12.878	0.032	12.792	0.030	Y	DH 291
03 44 58.94	+49 52 32.8	···		···		17.285	9	15.753	9	14.197	0.032	13.498	0.037	13.277	0.035	Y	DH 292
03 44 59.83	+49 24 57.0	···		···		16.100	9	14.635	9	13.019	0.024	12.350	0.029	12.111	0.025	Y	DH 293
03 45 27.54	+47 39 37.4	7.150	10	7.160	10	···		7.180	11	7.157	0.024	7.194	0.031	7.191	0.018	Y	MA 133, HD 23219
03 45 28.46	+49 27 07.5	···		···		14.441	9	13.381	9	12.384	0.033	11.735	0.038	11.497	0.030	Y	DH 294
03 45 53.25	+45 35 59.6	7.640	10	7.570	10	···		7.510	11	7.400	0.018	7.425	0.034	7.405	0.020	Y	MA 134, HD 23287
03 45 54.74	+50 25 09.3	9.830	10	9.460	10	···		9.030	11	8.693	0.027	8.563	0.021	8.529	0.022	Y	MA 135, HD 23255
03 46 25.53	+47 45 07.5	···		···		17.164	9	15.628	9	14.548	0.030	13.836	0.034	13.587	0.044	Y	DH 295
03 46 32.77	+48 45 51.8	···		17.900	3	···		14.733	3	12.756	0.026	12.265	0.033	11.908	0.028	Y	AP 259
03 46 50.32	+47 25 59.8	···		···		14.307	9	13.658	9	12.948	0.022	12.327	0.031	12.224	0.026	Y	DH 296
03 47 00.62	+48 42 32.2	···		···		17.867	9	16.301	9	14.649	0.034	13.841	0.033	13.652	0.049	Y	DH 297
03 47 09.63	+47 48 23.6	···		14.700	3	···		12.664	3	11.495	0.021	10.874	0.029	10.671	0.024	Y	AP 260
03 48 12.04	+50 54 46.6	···		18.630	4	···		15.686	4	14.085	0.032	13.509	0.040	13.122	0.040	Y	AP 262
03 48 28.19	+50 36 46.6	···		···		18.297	9	16.533	9	14.245	0.035	13.692	0.036	13.377	0.042	Y	DH 298
03 48 47.41	+47 34 27.7	···		···		18.818	9	16.848	9	15.259	0.049	14.615	0.058	14.498	0.078	Y	DH 299
03 49 01.00	+46 48 09.7	8.100	10	7.910	10	···		7.710	11	7.416	0.021	7.300	0.036	7.302	0.020	Y	MA 136, HD 23690
03 49 26.22	+45 43 00.1	14.400	3	13.210	3	···		11.913	3	11.432	0.022	10.721	0.028	10.540	0.022	Y	AP 263
03 49 45.88	+50 01 11.5	···		···		16.303	9	15.078	9	13.462	0.027	12.851	0.033	12.587	0.028	Y	DH 300
03 50 13.25	+49 42 22.8	···		···		14.813	9	14.150	9	12.811	0.026	12.103	0.031	11.923	0.029	Y	DH 301
03 50 27.83	+47 49 05.4	13.130	3	12.120	3	···		10.987	3	10.019	0.019	9.494	0.027	9.392	0.024	Y	AP 264
03 50 36.60	+45 46 09.9	···		16.430	3	···		13.990	3	12.611	0.025	11.929	0.030	11.679	0.027	Y	AP 266
03 50 37.06	+48 12 31.7	···		17.610	4	16.582	9	14.720	4	13.114	0.024	12.504	0.031	12.236	0.025	Y	AP 265, DH 302
03 53 39.50	+45 45 29.3	8.800	10	8.590	10	···		8.360	11	8.153	0.029	8.110	0.029	8.067	0.021	Y	MA 137, HD 24260
03 55 58.17	+47 52 17.1	5.290	3	5.370	3	···		5.490	11	5.484	0.017	5.541	0.021	5.584	0.020	Y	HD 24504
04 00 20.50	+47 34 18.7	8.570	10	8.370	10	···		8.170	11	7.837	0.020	7.789	0.024	7.722	0.016	Y	MA 138, HD 24980
04 01 49.97	+50 38 17.6	8.170	10	8.050	10	···		7.920	11	7.705	0.020	7.716	0.049	7.679	0.020	Y	MA 139, HD 25109

[a] J2000.0 position of the associated 2MASS point source.

[b] References for photometry. (1) Stauffer et al. (1985). (2) Stauffer et al. (1989). (3) Prosser (1992). (4) Prosser (1994). (5) Prosser & Randich (1998). (6) Prosser et al. (1998). (7) Stauffer et al. (1999). (8) Barrado y Navascués et al. (2002). (9) Deacon & Hambly (2004). (10) Makarov (2006). (11) Monet et al. (2003).

[c] See Section 2 of the text for how we compiled the membership determinations of previous studies.

[d] AP 1-88 from Stauffer et al. (1985). AP 89-118 from Stauffer et al. (1989). AP 119-266 from Prosser (1992). AP 267-297 from Prosser (1994). AP 300-326 from Stauffer et al. (1999). AP 327-412 from Barrado y Navascués et al. (2002). APX 1-73 from Prosser & Randich (1998). APX 74-203 from Prosser et al. (1998). DH from Deacon & Hambly (2004). HD from Prosser (1992). HE from Heckmann et al. (1956). MA from Makarov (2006).

Chapter 5

Dynamical Evolution of Clusters

5.1 Cluster Energetics

Having established the current state, histories, and futures of two representative open clusters, we wish to understand that evolution in greater detail. We discard for the moment the need to match with real star clusters, instead looking at more idealized theoretical models. The goal is to understand first the simplest cases, then relax the assumptions behind it and add in the properties of real clusters one at a time. In this way we will better understand which factors are the most important and how they interplay with each other.

We have run a suite of N-body simulations, all employing the publicly available code Starlab (Portegies Zwart et al. 2001, Appendix B). Significantly for our purposes, the code uses no softening in the gravitational potential, so that the formation and dynamical interactions of binaries are followed accurately. As we did not have access to any special-purpose hardware, our simulations were limited by time constraints to $N \lesssim 10^4$.

5.1.1 Single-Mass Models

Let us first adopt the simplified, and assuredly unrealistic, assumption that all stars have identical mass. Many of the classic theoretical papers in stellar dynamics, as well as textbook accounts, have utilized such single-mass models. We assume the cluster starts out in virial equilibrium, with a mass density profile corresponding to an $n = 3$ polytrope (see Section 2.2.1). We recently found that this particular configuration best describes the very early state of the Pleiades, just after gas removal (see Section 3.3.1). We stress, however, that the precise initial state is of little consequence; the system loses memory of this state well within one relaxation time, as in the case of the Pleiades.

In this and our other simulations, we model only isolated systems, with no tidal gravitational field either from the Galaxy or from passing molecular clouds. More complete models should include such an external field, which eventually destroys all clusters. However, the presence of the field does not qualitatively alter our main conclusions regarding cluster evolution up to the point of dissolution.

Figure 5.1 shows the evolution of Lagrangian mass shells in a cluster with the representative population of $N = 4096$. Here we display the temporal change of the shell radii, expressed as fractions of the cluster's initial virial radius, r_v. Each shell has the indicated value of M_r/M_0, where M_r is the interior mass and M_0 the initial mass of the whole cluster. The time itself is normalized to the initial relaxation time $t_{\rm relax}$, for which we utilize equation (1.37) in Binney & Tremaine (2008):

$$t_{\rm relax} \equiv \frac{N}{8 \ln \Lambda} t_{\rm cross}, \tag{5.1}$$

where $\ln \Lambda = \ln(0.4N)$. Following standard practice (e.g., Portegies Zwart et al. 1998, Section 2.4), the crossing time $t_{\rm cross}$ is given by

$$t_{\rm cross} \equiv \left(\frac{8 r_v^3}{G M_0} \right)^{1/2}. \tag{5.2}$$

We need not choose values for r_v or $t_{\rm cross}$ as long as we compare only nondimensional versions of all the relevant quantities (Heggie & Mathieu 1986).

As we see in the figure, interior shells contract, while those closer to the cluster boundary expand. This behavior is the hallmark of dynamical relaxation. In this plot, the steeply accelerating contraction that signifies core collapse is not present, simply because of the limited time range covered. Makino (1996), who investigated single-mass models using a special-purpose (Grape-4) computer, found core collapse to occur after about 6 initial relaxation times. (See his Figure 1 plotting the central density for the 4k run, after noting that $t_{\rm relax}$ corresponds to 62 of his scaled N-body time units.) Our results, over a more restricted interval, are fully consistent with Makino's.

Other researchers, utilizing a variety of techniques, have verified through simulations that dynamical relaxation occurs in single-mass systems (e.g., Takahashi 1995; Baumgardt et al. 2003). Nevertheless, it is worth revisiting the basic energetics of the process. The cluster's total energy is conserved, so its dual contraction and expansion reflects energy *transfer* from the inside out. According to Figure 5.1, the shell with $M_r/M_0 = 0.70$ grows only slowly. Thus, this shell lies just outside the core-halo boundary.

We arrive at the same conclusion by calculating directly the mean rate of energy transfer. Let K_r be the total kinetic energy within mass M_r, and $\dot{K}_r$ the time derivative of this quantity. After finding the best-fit straight line to $K_r(t)$ over the full time span of the simulation ($3t_{\rm relax}$), we then calculate $\dot{K}_r$ as the slope of this line. Figure 5.2 shows $\dot{K}_r$ as a function of the mass fraction M_r/M_0. What we actually display is the nondimensional quantity $\dot{k}_r$, where

$$\dot{k}_r \equiv \frac{\dot{K}_r t_{\rm relax}}{K_i}, \tag{5.3}$$

and where K_i is the cluster's total initial kinetic energy.

The curve in Figure 5.2 has a small, central dip, a numerical artifact of the large scatter in $K_r(t)$ over this region containing relatively few stars. Thereafter, $\dot{K}_r$ rises, attains a

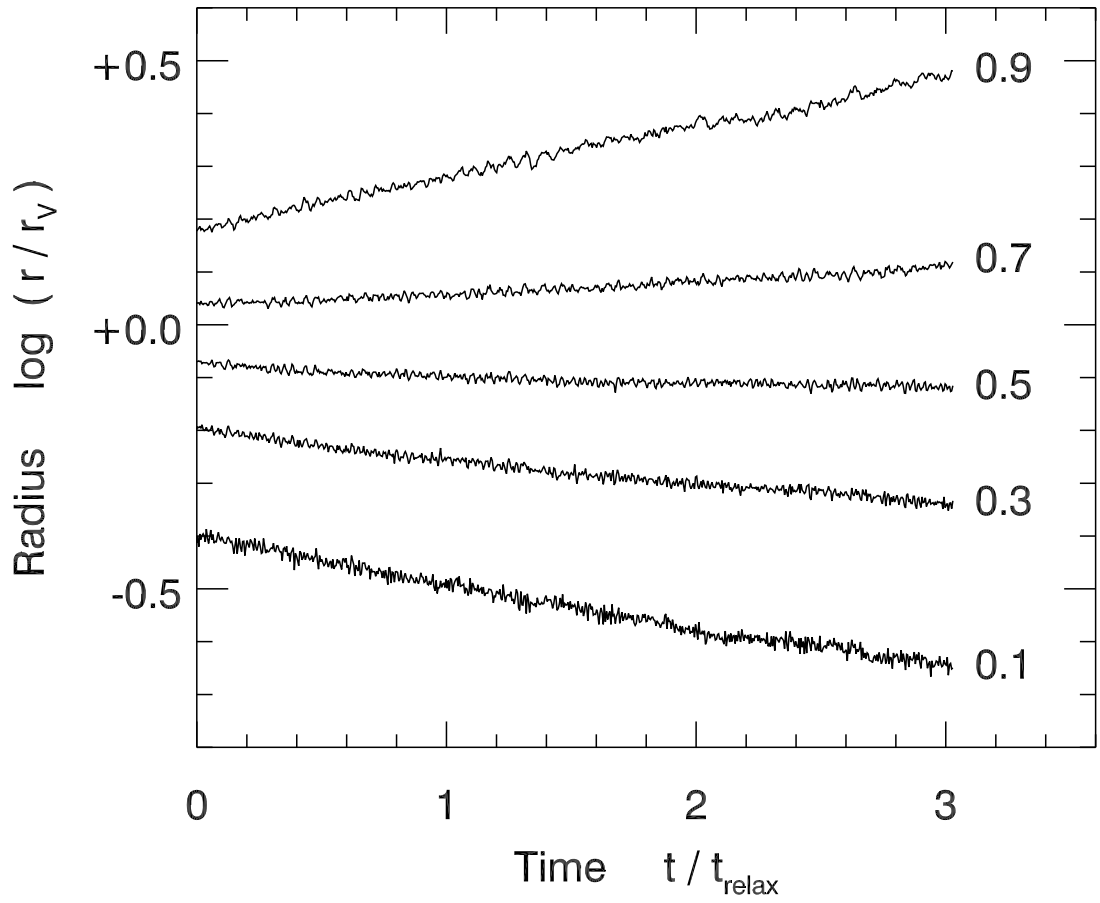

Figure 5.1: Temporal evolution of the radii of Lagrangian mass shells, for a single-mass cluster model ($N = 4096$). Each curve is labeled by the corresponding mass fraction of the cluster. The radii are normalized to the initial virial value, r_v, and the time to the initial relaxation time, $t_{\rm relax}$.

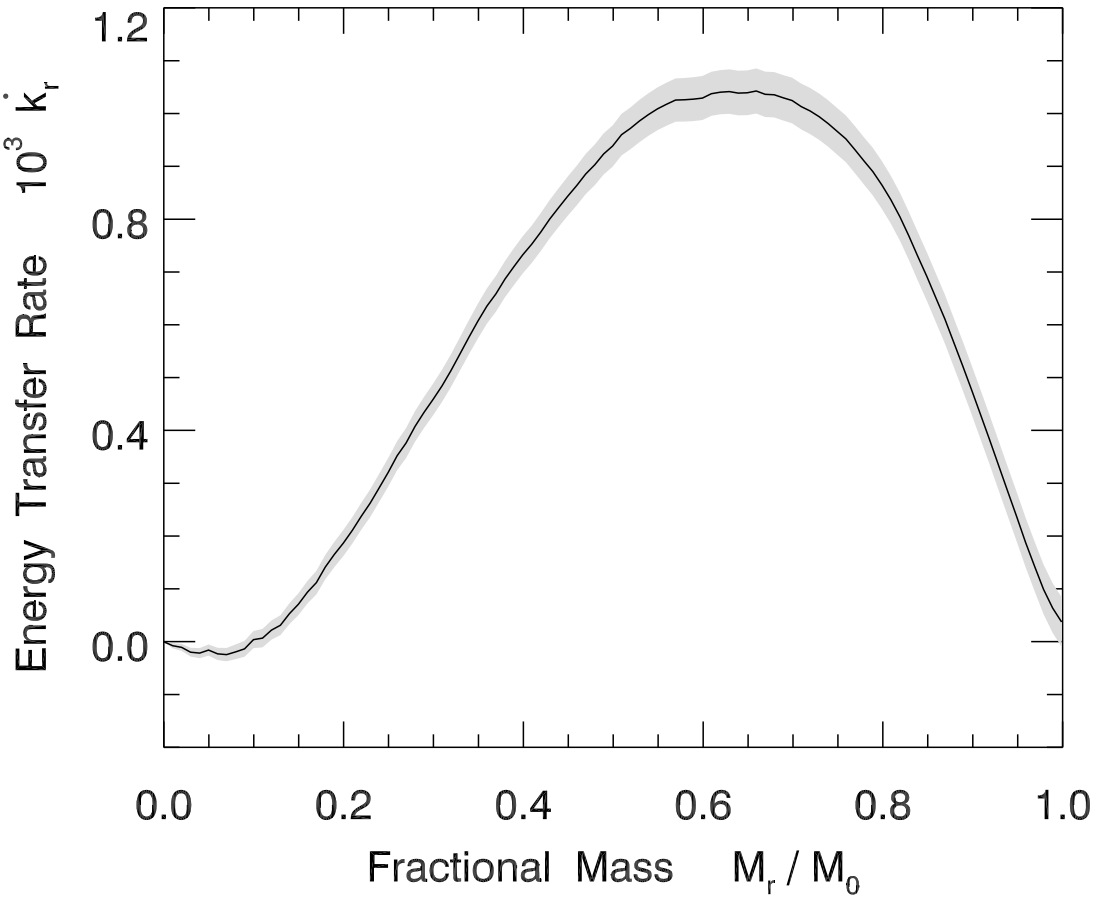

Figure 5.2: Profile of the mean energy transfer rate for a single-mass cluster model ($N = 4096$). The rate, displayed as the nondimensional quantity $\dot{k}_r$ given in the text, is plotted against the mass fraction M_r/M_0. The shading indicates the 1-σ error in the value of $\dot{k}_r$ at each point.

maximum, and then monotonically declines. Within the rising portion of the curve, the kinetic energy ΔK_r in a shell of thickness ΔM_r *increases* with time. That is,

$$\Delta K_r = \frac{\partial}{\partial t}\left(\frac{\partial K_r}{\partial M_r}\Delta M_r\right)\Delta t \tag{5.4}$$

$$= \frac{\partial \dot{K}_r}{\partial M_r}\Delta M_r \Delta t \tag{5.5}$$

$$> 0. \tag{5.6}$$

A certain, interior region of the cluster is thus gaining kinetic energy. Self-gravitating systems have negative heat capacity. Thus, the increasing kinetic energy (and therefore temperature) of the inner core signifies a *decreasing* total energy.[1] Analogous reasoning shows that the region corresponding to the descending portion of the $\dot{K}_r$-M_r curve is *gaining* total energy, and therefore comprises the halo, which receives its energy from the core. It is natural, therefore, to locate the core-halo boundary at the peak of the curve, i.e., where $\dot{K}_r = 0$. According to Figure 5.2, this boundary is at $M_r/M_0 \approx 0.6$, in agreement with the analysis of Figure 5.1.

5.1.2 Models with a Realistic Mass Function

Core Contraction vs. Mass Segregation

We next eliminate the most egregious simplification in the model, the assumption of a uniform stellar mass. As has long been appreciated (e.g., Inagaki & Wiyanto 1984; de La Fuente Marcos 1995), relaxing this assumption has a profound effect on cluster evolution. We turn again to our recent study of the Pleiades (Sections 2.2.2 and 3.3.1), and use, as our stellar mass distribution, the one characterizing the cluster in its infancy, soon after gas dispersal. This distribution was a lognormal, joining smoothly onto a power law at higher masses. The full distribution is given in equation (2.108) in Section 2.2.2, with the parameter values listed in Table 3.1. Following that study, we take the minimum and maximum stellar masses to be $m_{\rm min} = 0.08$ and $m_{\rm max} = 10$ $\mathrm{M}_\odot$, respectively. (See Section 5.2.3 for reconsideration of the maximum mass.) Once again, we assume that the mass density profile of the cluster is that of an $n = 3$ polytrope. Cluster members are all single stars, whose masses are drawn randomly from the assumed stellar distribution. We set $N = 4096$, and ignore both mass loss during stellar evolution and any tidal gravitational field.

The left panel of Figure 5.3 shows the evolution of Lagrangian mass shells, in a manner analogous to Figure 5.1. In this case, we note first that radii tend to exhibit more jitter in their evolution. This characteristic stems from the redistribution of stellar mass over the crossing time. Even after averaging over the jitter, interior mass shells do not monotonically contract, as they did before. These radii initially shrink. However, at some relatively early

[1] This argument is only suggestive, as the gravitational potential energy of any interior region actually depends on the distribution of mass surrounding it.

time $t_b = 0.37 t_{\rm relax}$, they reach a minimum and begin to expand. (We will later identify this time with binary formation; see below.) This expansion continues, with ups and downs, for the remainder of the simulation. Radii corresponding to $M_r/M_0 \gtrsim 0.7$ expand from the start.

For the single-mass model, the shrinking of any interior radius unambiguously signifies that the average distance between stars is also diminishing in that region. In the present case, the interpretation of early contraction is complicated by the phenomenon of mass segregation. The mass of any star is drawn from the same distribution, regardless of that object's initial location in the cluster.[2] Thus, there is no mass segregation initially. However, relatively massive stars quickly drift toward the center, under the influence of dynamical friction. As these stars accumulate, the radius of any region *of fixed mass* may shrink, even if the average interstellar spacing does not.

To illustrate this point graphically, the right panel of Figure 5.3 shows, for the same simulation, the evolution of radii containing a fixed *number fraction*, N_r/N, of the cluster. Here, N_r is the interior number of stars. Since no mass segregation was imposed at the start, the Lagrangian mass shell with $M_r/M_0 = 0.10$ initially has the same radius as the "number shell" with $N_r/N = 0.10$. The radius of the former contracts at early times, but Figure 5.3b shows that the radius of the latter stays constant and later grows. The average interstellar separation within the volume is not shrinking.

Tracking the radii of Lagrangian mass shells is a widely employed technique for visualizing cluster evolution. Other authors who have studied relatively low-N systems under similar assumptions have documented the early contraction of interior shells. This development is said to demonstrate core collapse (e.g., Giersz & Heggie 1997; Hurley et al. 2004). The putative collapse occurs within one initial relaxation time, much earlier than in single-mass models, and ends before the central mass density has risen dramatically. However, contraction of inner mass shells may be due to mass segregation and thus it alone does not definitively show the occurrence core collapse.

In any cluster containing a range of stellar masses, any temporal increase in mass segregation obscures the physically distinct phenomenon of core contraction. The latter may still be occurring, and is in this case to a limited degree. Consider again Figure 5.3b, where we have added a deeply embedded, number shell corresponding to $N_r/N = 0.03$. This shell *does* contract initially, although only by a relatively small amount before the turnaround at t_b. True dynamical relaxation occurs at the start, but the accompanying interior contraction is weak, and is soon aborted.

Energy Transfer: Before and After

As in the single-mass model, calculation of the mean energy transfer rate adds physical insight. Figure 5.4 is an energy transfer profile before turnaround, i.e., over the interval $0 < t < t_b$. The curve is similar to that in Figure 5.2. The rate $\dot{K}_r$ eventually rises smoothly,

[2]More precisely, there is no correlation between a star's mass and its energy; see Section 2.2.2.

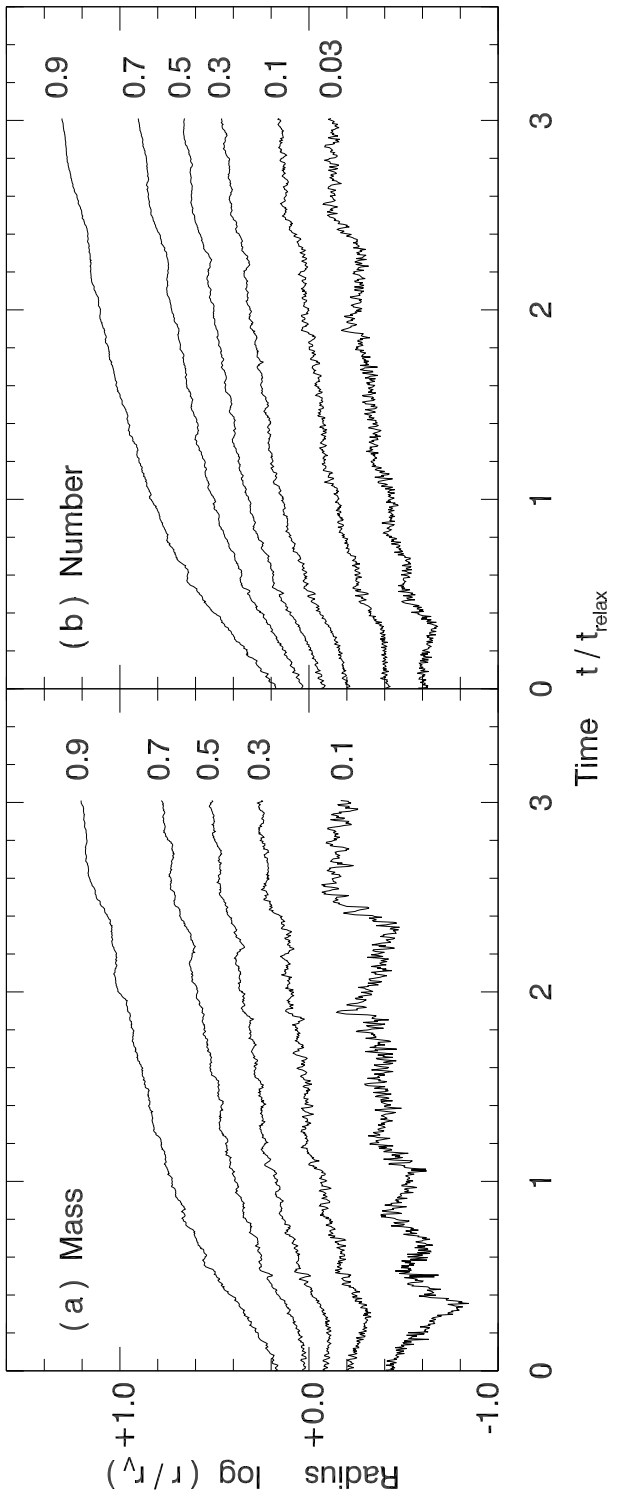

Figure 5.3: Evolution of the radii of (a) mass shells, and (b) number shells, for a cluster with a realistic stellar mass distribution ($N = 4096$). Each curve is labeled by the appropriate mass or number fraction of the entire cluster.

peaks a bit beyond $M_r/M_0 = 0.5$, and thereafter declines. Such a profile is again indicative of dynamical relaxation. Identifying the core-halo boundary with the peak of the $\dot{K}_r$-M_r curve is consistent with the pattern of mass shell curves in Figure 5.3b. Thus, the radius corresponding to $M_r/M_0 = 0.5$ initially contracts slightly, while that with $M_r/M_0 = 0.7$ expands.

Figure 5.5 displays the energy transfer profile after the turnaround. Here, the mean rate $\dot{K}_r$ is determined over the interval $t_b < t < 3t_{\rm relax}$. The profile is now qualitatively different, and illustrates a distinct mode of cluster evolution. The kinetic energy in every mass shell falls with time. So does, therefore, the kinetic energy of the entire cluster. From the virial theorem, the cluster as a whole is gaining in *total* energy. This injection of energy accounts for the system's global expansion, as seen in all the radii of Figure 5.3 for $t > t_b$. The central engine driving the expansion is binary heating, as we verify shortly.

We have run analogous simulations for cluster populations ranging from $N = 512$ to 16,384. The upper limit was a practical one; the last case required three months on a desktop computer. All simulations gave qualitatively the same result. The cluster experiences an early, transient phase of dynamical relaxation. During this epoch, the central number density rises by only a modest amount, typically a factor of 2. The central mass density rises by about a factor of 10, with the larger increase reflecting the onset of mass segregation. In all cases the end of this early period coincides with the formation of the first long-lived binary system, with $t_b \approx 0.3t_{\rm relax}$ for all N, consistent with the findings of Portegies Zwart & McMillan (2002). From this early epoch until the end of the simulation, the cluster undergoes global expansion. As we shall next see, even the brief, transient period of dynamical relaxation was itself an artifact that vanishes under more realistic initial conditions.

5.1.3 The Example of the Pleiades

One feature of our simplified cluster models is that they consist initially of only single stars. It is well known that most field stars of solar-type mass have at least one binary companion (Duquennoy & Mayor 1991). The observational assessment of binarity in even the nearest open clusters is challenging, but the indication so far is that the fraction is comparable to the field-star value (e.g., Bouvier et al. 1997; Dawson & Schröder 2010). Since, as we will see, binary heating plays a key role in dynamical evolution, we should try to gauge the influence of primordial pairs.

For this purpose, we may utilize our simulated history of the Pleiades (Section 3.3.2). Our initial state, another $n = 3$ polytrope, was that which evolved, over the 125 Myr age of the cluster, to a configuration most closely resembling the current one.[3] In Section 3.2.2, we found that 76% of the stellar systems today are binary. The best-fit initial state in Section 3.3.1 consisted essentially of *all* binaries, with the corresponding fraction being 95%. We endowed these binaries with a lognormal period distribution and a thermal distribution

[3]For most of the simulations in Section 3.3, including those reviewed here, we ignored both stellar mass loss and the Galactic tidal field. Adding both effects had a negligible impact on the evolution up to the present age of the cluster (Section 3.3.3).

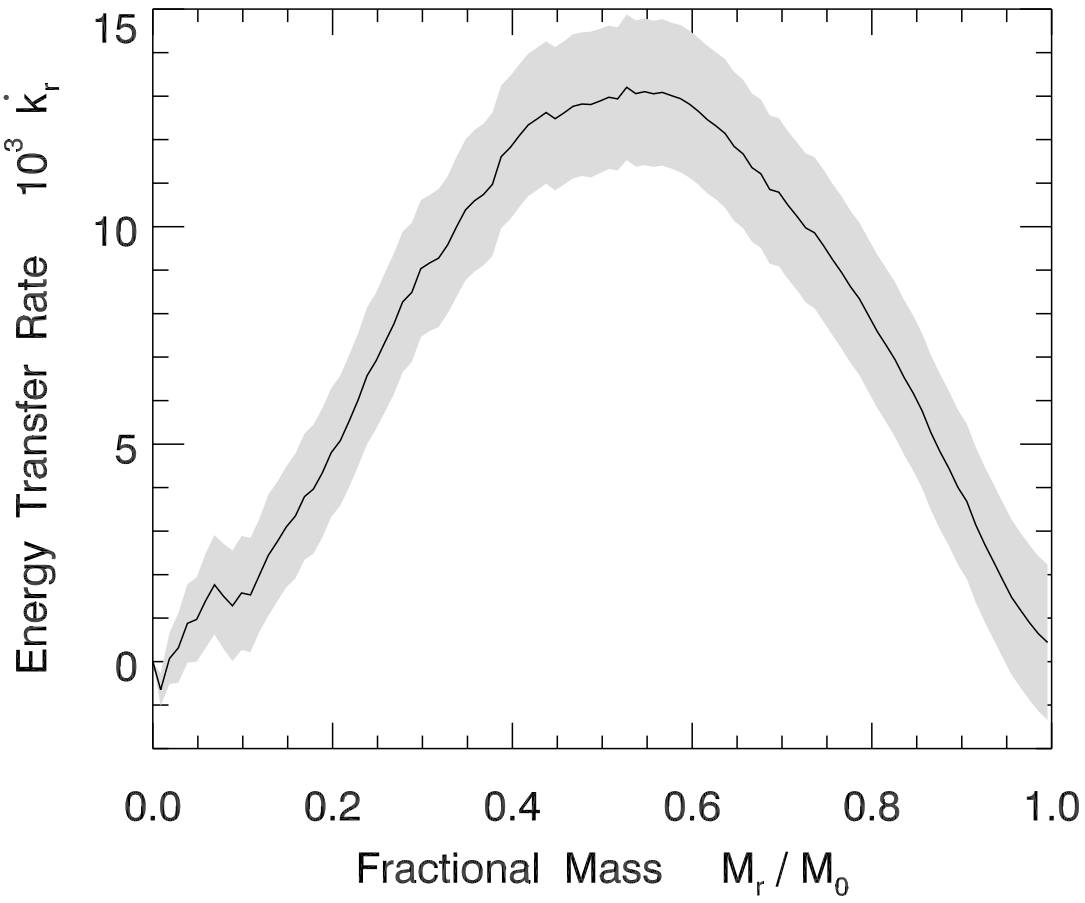

Figure 5.4: Early-time energy transfer profile for an $N = 4096$ cluster with a realistic stellar mass distribution. As in Figure 5.2, the shading indicates the estimated uncertainty at each point.

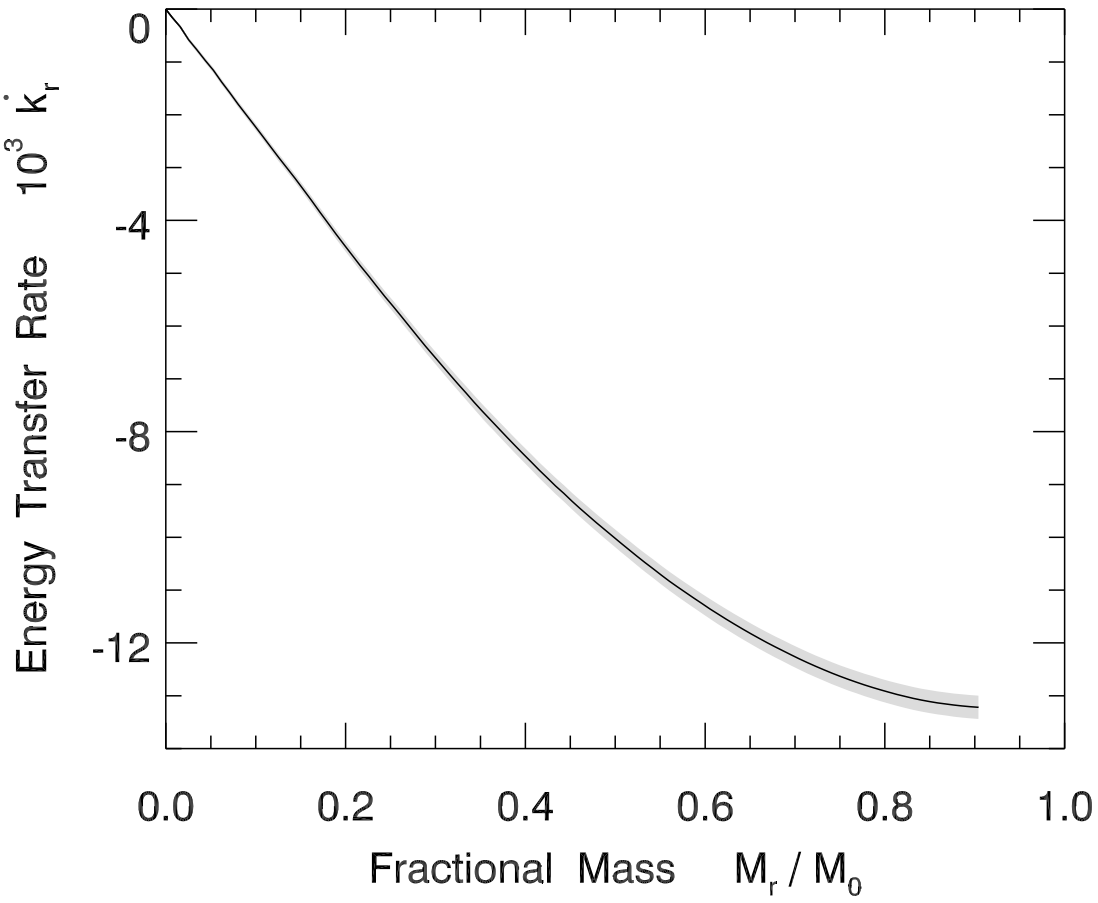

Figure 5.5: Late-time energy transfer profile for an $N = 4096$ cluster with a realistic stellar mass distribution. As in Figure 5.2, the shading indicates the estimated uncertainty at each point.

of eccentricities, reflecting both conditions in the field population and in the Pleiades itself (Duquennoy & Mayor 1991; Bouvier et al. 1997). In addition, the masses of the primary and secondary stars were correlated (see Section 2.2.2).

Finally, the initial state had a finite degree of mass segregation, i.e., the masses and energies of stellar systems were also correlated. The reader is again referred to Section 2.2.2 for the detailed prescription. Mass segregation may be characterized quantitatively through the Gini coefficient (Section 2.1.3). This quantity measures how fast the cumulative mass increases outward relative to the cumulative number of systems. The initial state of the Pleiades had $G \approx 0.14$. The initial number of stellar systems, both binary and single, was $N = 1215$.

Figure 5.6 shows the evolution of mass- and number-shell radii. Note that the current age of the Pleiades corresponds to about 0.5 initial relaxation times. Thus, these plots span a significantly briefer interval than those in Figures 5.1 and 5.3. Bearing this fact in mind, we see that the curves are generally similar to those in Figure 5.3. After a brief initial plunge, the radii of mass shells with $M_r/M_0 \gtrsim 0.3$ expand, while the $M_r/M_0 = 0.1$ shell contracts, at least over this time. Number shells undergo an analogous, early contraction, and then either remain static ($N_r/N = 0.03$) or expand. If binaries are energetically significant, why is the cluster evolution not radically altered? This is an important question, to which we shall return presently (see Section 5.2.2).

The early dips seen in all the curves of Figure 5.6 signify that the cluster as a whole initially contracts. This behavior is an artifact of our specific method for implementing mass segregation. As explained in Section 3.3.2, the configuration starts out in precise virial equilibrium. However, the redistribution of higher stellar masses toward the center alters slightly the gravitational potential from that associated with an $n = 3$ polytrope. Over a period lasting about two crossing times ($0.08t_{\rm relax}$), the cluster "bounces," and then settles into a configuration that evolves smoothly thereafter.

The bounce does not occur if we impose no mass segregation initially. In that case, both the mass density of stars and the gravitational potential correspond exactly to an $n = 3$ polytrope. Figure 5.7 shows results from such a simulation. In this "Pleiades-like" cluster, the initial state is identical to that in Figure 5.6, but without mass segregation. Over the time span covered ($0.5t_{\rm relax}$), number shells either remain static or expand (Figure 5.7b). The early contraction of the innermost shells seen in Figure 5.3 never occurs, due to the heating by primordial binaries. In summary, there is no evidence of classical dynamical relaxation; the cluster evolves purely through expansion. The radii of interior mass shells do contract (Figure 5.7a) as a result of increasing mass segregation; the Gini coefficient grows from 0 to 0.15 over this time (see Figure 3.19 in Section 3.3.2).

Returning to the more realistic Pleiades simulation, it is again instructive to visualize the internal transport of energy. From our description thus far, there should be no core-halo boundary, identified by the peaks of the energy transfer profiles in Figures 5.2 and 5.4. Figure 5.8, which plots $\dot{K}_r$ as a function of M_r, bears out this expectation. Here, we have computed $\dot{K}_r$ by a linear fit over the full time span of the simulation. We see that $\dot{K}_r$ monotonically falls from zero to increasingly negative values. (Compare Figure 5.5 and the

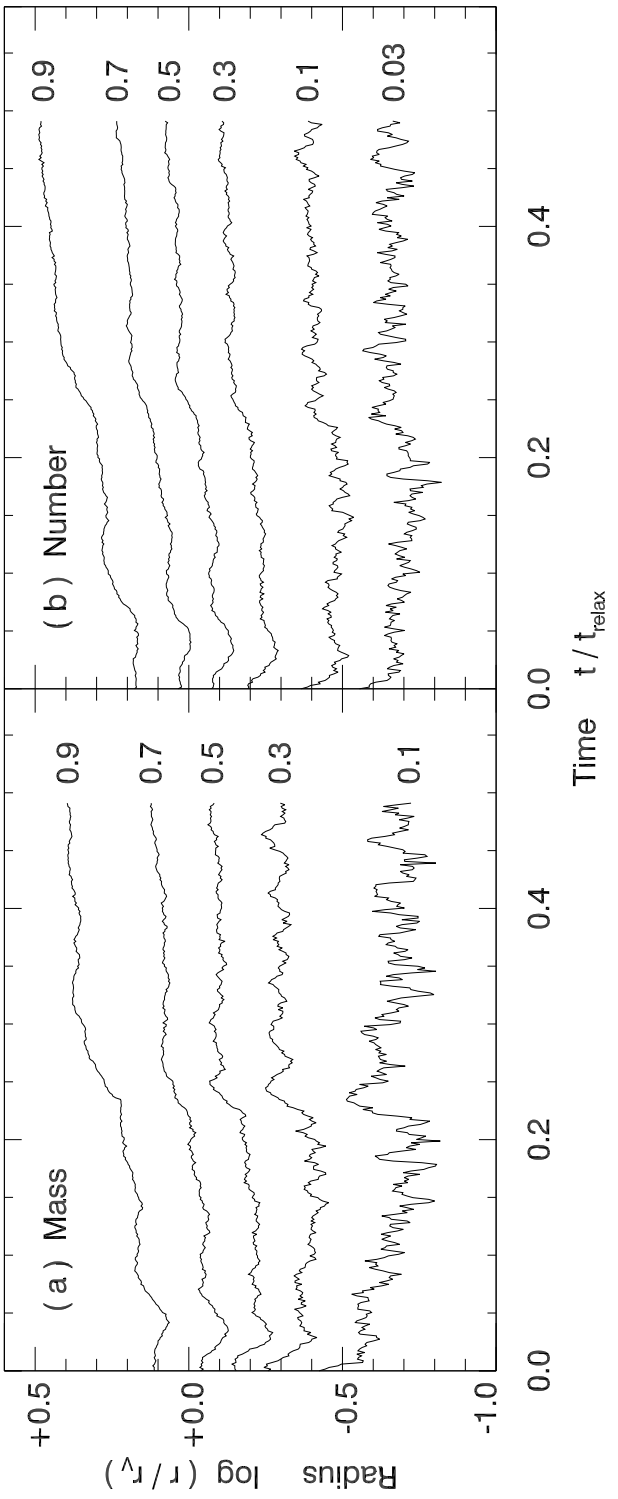

Figure 5.6: Evolution of the radii of (a) mass shells, and (b) number shells, for the Pleiades ($N = 1215$). As in Figure 5.3, which covers a much longer time, each curve is labeled by the appropriate mass or number fraction.

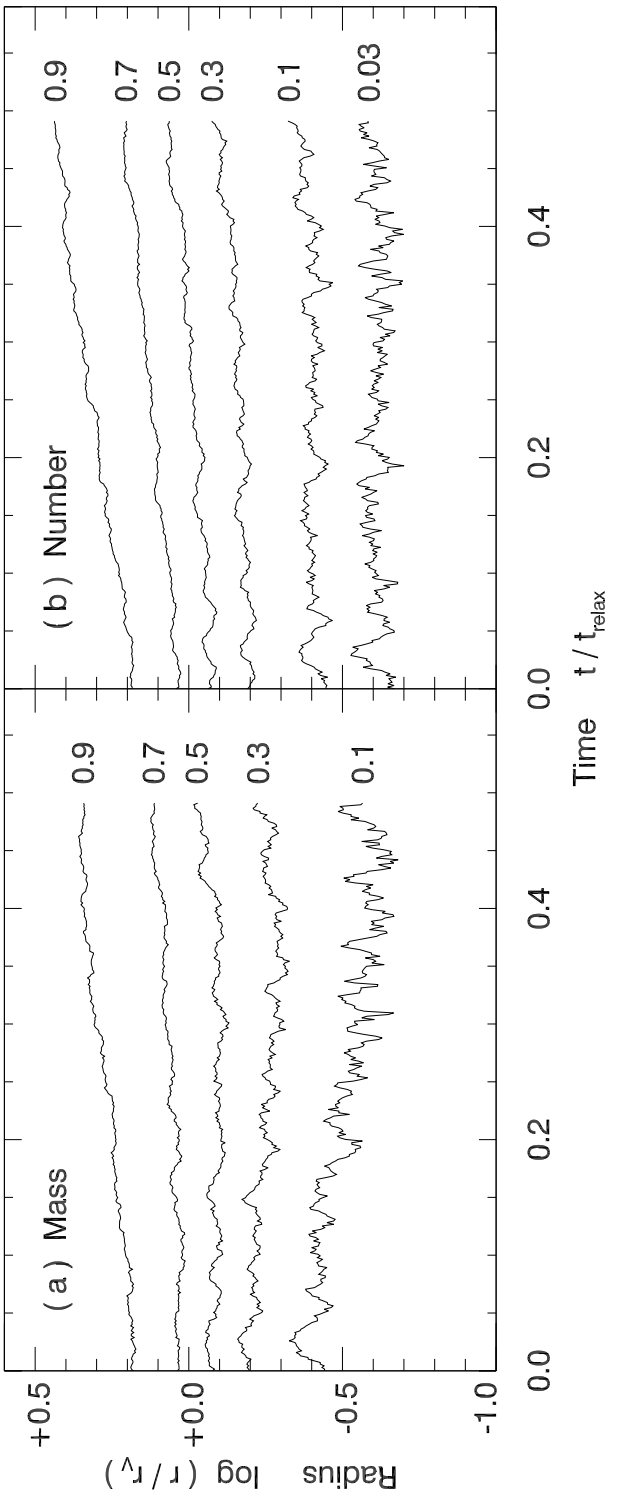

Figure 5.7: Evolution of the radii of (a) mass shells, and (b) number shells, for a Pleiades-like cluster with no initial mass segregation.

accompanying discussion.) The cluster as a whole is cooling down, and is therefore gaining in total energy. The Pleiades evolved to its present state through global expansion, not dynamical relaxation.

5.2 The Role of Binaries

5.2.1 First Appearance

Classical Theory

Let us reconsider the highly idealized clusters with which we began - one with stars of identical mass, and the other with a continuous range of stellar masses. In both cases, the initial systems contained neither binaries nor higher-order multiple systems. The evolving, single-mass cluster spawned no new binaries over the duration of our simulation. However, Makino (1996) found, in his more extensive investigation of the single-mass model, that binaries do eventually form in the contracting interior, and that their heating reverses core collapse at $t \approx 6t_{\rm relax}$. The core subsequently undergoes the gravothermal oscillations predicted by Bettwieser & Sugimoto (1984) and Goodman (1987) using fluid models with an internal energy source.

In our cluster with a realistic stellar mass distribution, the interior contraction ends much sooner, within a single initial relaxation time. Is this prompt reversal also due to binary heating? The answer is yes. We have confirmed that the turnaround at $t = t_b$ coincides with the appearance of the first hard binary. Here, we remind the reader that a "hard" binary is one whose gravitational binding energy exceeds the average, center-of-mass kinetic energy of all other stellar systems. It is only such pairs that donate energy to neighboring stars during a close flyby, and thereby become even harder. This is the essence of binary heating (Heggie 1975).

Why do binaries form so much earlier in this cluster than in the single-mass model? Closer inspection reveals that these new systems are comprised of stars that are appreciably more massive than the average cluster member. This fact is readily understood in a qualitative sense. In clusters with no initial mass segregation, the relatively massive stars promptly sink to the center. Once in close proximity, these objects have a stronger mutual attraction than other cluster members, and are thus more prone to forming binaries.

In more detail, a gravitationally bound pair of such stars can only form by giving energy to a third star. Binary formation is thus a three-body process. In the traditional analysis of cluster evolution based on single-mass models, three-body encounters throughout the bulk of the system are considered too rare to be of significance. Binney & Tremaine (2008, Page 558) show that t_b^*, the time for the first binary to form via this route, is much longer than $t_{\rm relax}$. Specifically, they estimate that

$$\frac{t_b^*}{t_{\rm relax}} \sim 10N \ln N. \tag{5.7}$$

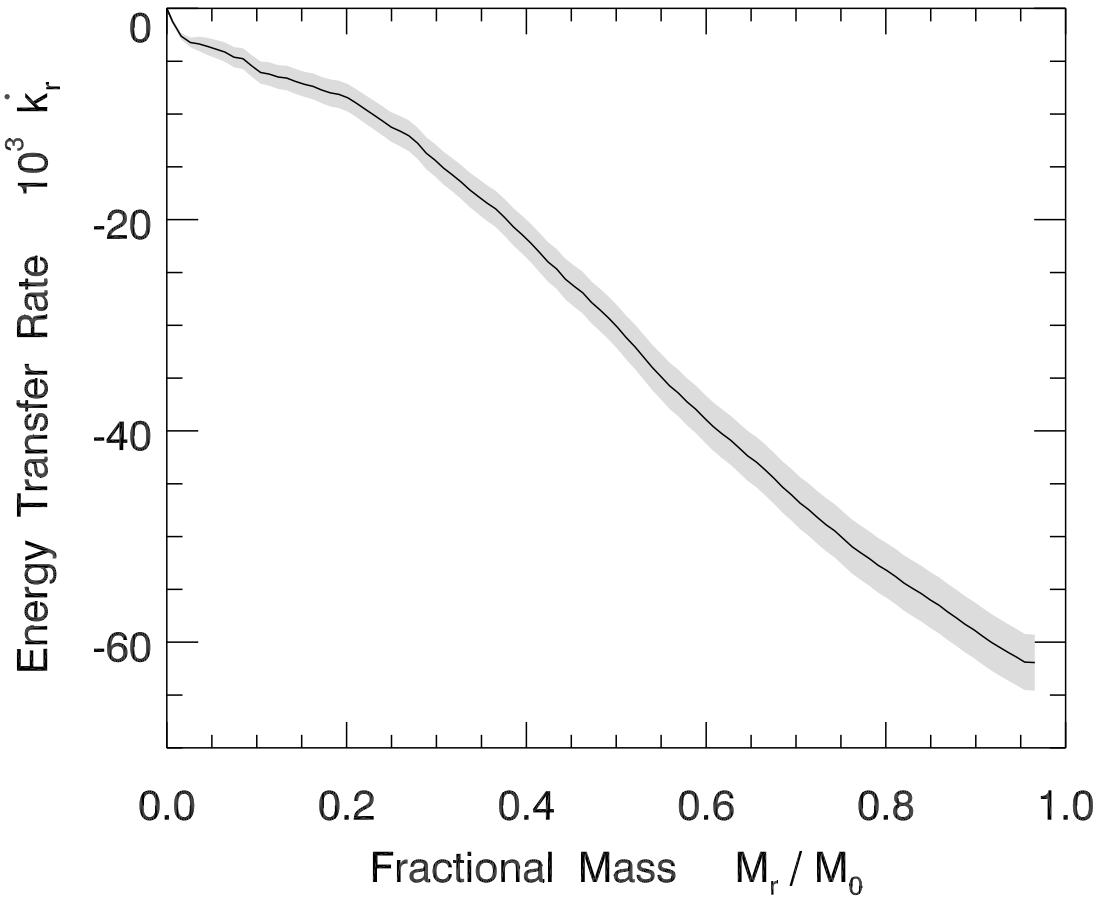

Figure 5.8: Energy transfer profile for the Pleiades. As in Figure 5.2, the shading indicates the estimated uncertainty at each point.

Our superscript on t_b^* emphasizes that this time pertains to the highly specialized case of equal-mass stars. The derivation of equation (5.7) assumes that the binary-forming stars reside in a region of average density. This assumption breaks down if the interactions occur in a deeply collapsing core. Three-body interactions *can* proceed here efficiently (e.g., Heggie 1984). However, the process is too slow in regions where the density is not greatly enhanced.[4]

With a Mass Spectrum

The situation changes dramatically once the cluster is endowed with a distribution of stellar masses. Here, binaries can form even where the density is close to the average. We may demonstrate this fact through a slight alteration of the heuristic derivation for t_b^* given in Binney & Tremaine (2008). Suppose that stars require a minimum mass m to be part of a binary. The time Δt for a given one of these objects to come within distance b of another with comparable mass is

$$\Delta t \sim \left(f_m n b^2 \sigma\right)^{-1}. \tag{5.8}$$

Here f_m is the number fraction of such stars, n is the average cluster number density, and σ the velocity dispersion. During this encounter, there is a probability $p \sim 4\pi n b^3/3$ that a third star will also be within the interaction distance b. This star can have the average mass $\langle m \rangle \equiv M_0/N$. Thus, the time for the original star to suffer a binary-forming triple encounter is about $\Delta t/p = 3/\left(4\pi f_m n^2 b^5 \sigma\right)$. There are $f_m N$ such stars in the cluster. The time for *any* such star to form a binary is

$$t_b \sim \frac{3}{4\pi N f_m^2 n^2 b^5 \sigma}. \tag{5.9}$$

In order for a hard binary to form, the gravitational potential energy of the binary must be equal to or greater than the average kinetic energy in the cluster:

$$\frac{Gm^2}{b} \sim \langle m \rangle \sigma^2. \tag{5.10}$$

Thus,

$$t_b \sim \frac{3\sigma^9 \langle m \rangle^5}{4\pi N f_m^2 n^2 G^5 m^{10}}. \tag{5.11}$$

From the virial theorem, $\sigma^2 \sim GN\langle m \rangle / r_v$, where r_v is the cluster's virial radius. Using this expression along with the approximation that $n \sim 3N/\left(4\pi r_v^3\right)$ we find

$$t_b \sim \frac{4\pi N^{3/2} r_v^{3/2}}{3 f_m^2 G^{1/2} \langle m \rangle^{1/2}} \left(\frac{\langle m \rangle}{m}\right)^{10}. \tag{5.12}$$

[4]Although binaries could, in principle, form via three-body interactions within globular clusters, those that eventually arrest core collapse are actually extremely tight systems created earlier by tidal capture (Fabian et al. 1975).

Now the relaxation time from equation (5.1) may be approximated as

$$t_{\rm relax} = \frac{N}{\sqrt{8}\ln N}\frac{r_v^{3/2}}{G^{1/2}N^{1/2}\langle m\rangle^{1/2}}. \tag{5.13}$$

Dividing equation (5.12) by equation (5.13) yields

$$\frac{t_b}{t_{\rm relax}} \sim \frac{10N\ln N}{f_m^2}\left(\frac{\langle m\rangle}{m}\right)^{10}, \tag{5.14}$$

which is a simple modification of the analogous equation (5.7).

On the righthand side of equation (5.14), the factor f_m^{-2} is necessarily greater than unity. On the other hand, $(\langle m\rangle/m)^{10}$ is, in practice, so small that $t_b < t_b^*$. Consider, for example, the models described in Section 5.1.2, which had a stellar mass distribution appropriate for the infant Pleiades. Here, $\langle m\rangle = 0.36$ M$_\odot$. In our $N = 4096$ cluster, we find empirically that the minimum mass in any newly formed binary is $m \approx 4$ M$_\odot$; the corresponding f_m-value is 8×10^{-3}. Equation (5.14) then predicts that $t_b/t_{\rm relax} \sim 0.2$, in good agreement with our numerical results.

This derivation is, of course, highly simplified, and the quantitative result above should not be given too much weight. The relative velocity of an encounter in the core will typically be larger than in the rest of the cluster, and the core density will be higher than the average. A more complete derivation of t_b would also consider the physical basis for the minimum mass m. Presumably, this limit is set by the rate at which dynamical friction allows stars of various mass to drift inward. We will not embellish the argument along these lines, but simply note that equation (5.14) adds justification for our main points: (1) The rate of binary formation is very sensitive to the stellar mass distribution, and (2) even in hypothetical clusters composed entirely of single stars, binaries form relatively quickly. It is only by adopting the extreme assumption that these single stars have identical mass that binary formation can be delayed to the point of core collapse.[5]

5.2.2 Energy Input

A hard binary that resides within a cluster, no matter how it formed, adds energy to the whole system. The process, like the creation of new pairs, is a three-body interaction. As a result of the encounter, the binary usually tightens and releases energy. This heating accounts for the expansion of both the mass and number shells in Figure 5.3, for $t > t_b$. Expansion driven by binaries is global, and differs qualitatively from the dual contraction and expansion seen in the single-mass model (Figure 5.1).

This difference is also apparent when we view the evolution of the cluster's aggregate energy. First, we need to distinguish *internal* and *top-level* energies. In the first category is the gravitational binding energy of each binary, and the kinetic energy of both component

[5]Binary formation is also delayed by stellar mass loss; see Section 5.3.

stars with respect to their center of mass. In the top-level category are the center-of-mass kinetic energies of all bound stellar systems, whether single or multiple, and the gravitational potential energy of this array. Thus, the kinetic energy K_r considered previously was actually a top-level quantity. The cluster's total energy E_0 is the sum of the two contributions:

$$E_0 = E_{\rm int} + E_{\rm top}. \tag{5.15}$$

Here, we are ignoring the relatively small amount of energy carried off by escaping stars. In the absence of an external tidal field, E_0 remains strictly constant. Binary heating, whether by creation of a new pair or interaction of an existing pair with single stars, lowers $E_{\rm int}$ and transfers the same amount of energy to $E_{\rm top}$.

The solid curve in Figure 5.9 shows the evolution of the top-level energy in the model cluster with a realistic stellar mass distribution ($N = 4096$). Here $E_{\rm top}$ is normalized to E_i, its initial value. Since this cluster begins with all single stars, $E_{\rm top}$ and E_0 are identical at the start. Upon the formation of the first hard binary at $t = 0.37t_{\rm relax}$, $E_{\rm top}$ takes a substantial, upward jump. Subsequent jumps occur whenever new hard binaries form, or when existing ones impulsively heat the cluster. As an instructive comparison, the dashed curve in Figure 5.9 shows $E_{\rm top}$ for the single-mass model described in Section 5.1.1. The curve is very nearly flat. Despite some weak and transient interactions, no stable, hard binaries form over the span of the simulation.

One interesting feature of Figure 5.9 is that the jumps tend to diminish with time. Indeed, $\Delta E_{\rm top}$ scales roughly with E_0, where the latter approaches zero as the cluster inflates. To see the origin of this scaling, consider in more detail the energetics of the three-body interaction. The energy released as the binary tightens is shared by that pair and the passing star. Both recoil from the site of the original encounter.[6] In our simulations, the binary is lifted to a much higher orbit, but usually does not become unbound. The pair then drifts back down, via dynamical friction, and gives its energy to surrounding stars. If ΔE_b denotes this contribution to the total energy change $\Delta E_{\rm top}$, then $\Delta E_b \lesssim m_b\sigma^2$, where m_b is the binary mass.

The recoiling single star, of mass $\langle m\rangle$, rockets away at high speed, much larger than σ, and is lost to the cluster. On its way out, the star does work $\Delta E_s = \langle m\rangle\Phi_g$ on the system. Here, Φ_g is the depth of the top-level gravitational potential well at the interaction site, which is close to the cluster center. Now both σ^2 and Φ_g are proportional to $E_{\rm top}$ itself. Thus, the total energy change, $\Delta E_{\rm top} = \Delta E_b + \Delta E_s$, is also proportional to $E_{\rm top}$.

The time when the first hard binary appears, $t_b = 0.37t_{\rm relax}$, is also when the cluster begins to expand (Figure 5.3). Thus, the binary immediately begins to heat the system through interactions with its neighbors. Eventually, the binary itself is ejected as a result of such an encounter, to be replaced later by another. Over the course of the simulation, a total of 4 hard binaries arise. But a snapshot of the cluster at any time shows it to contain either a single binary or none at all. For example, the flat portion of the energy curve (Figure 5.9)

[6] In some cases, the single star changes places with one of the binary components (Heggie et al. 1996). This detail need not concern us.

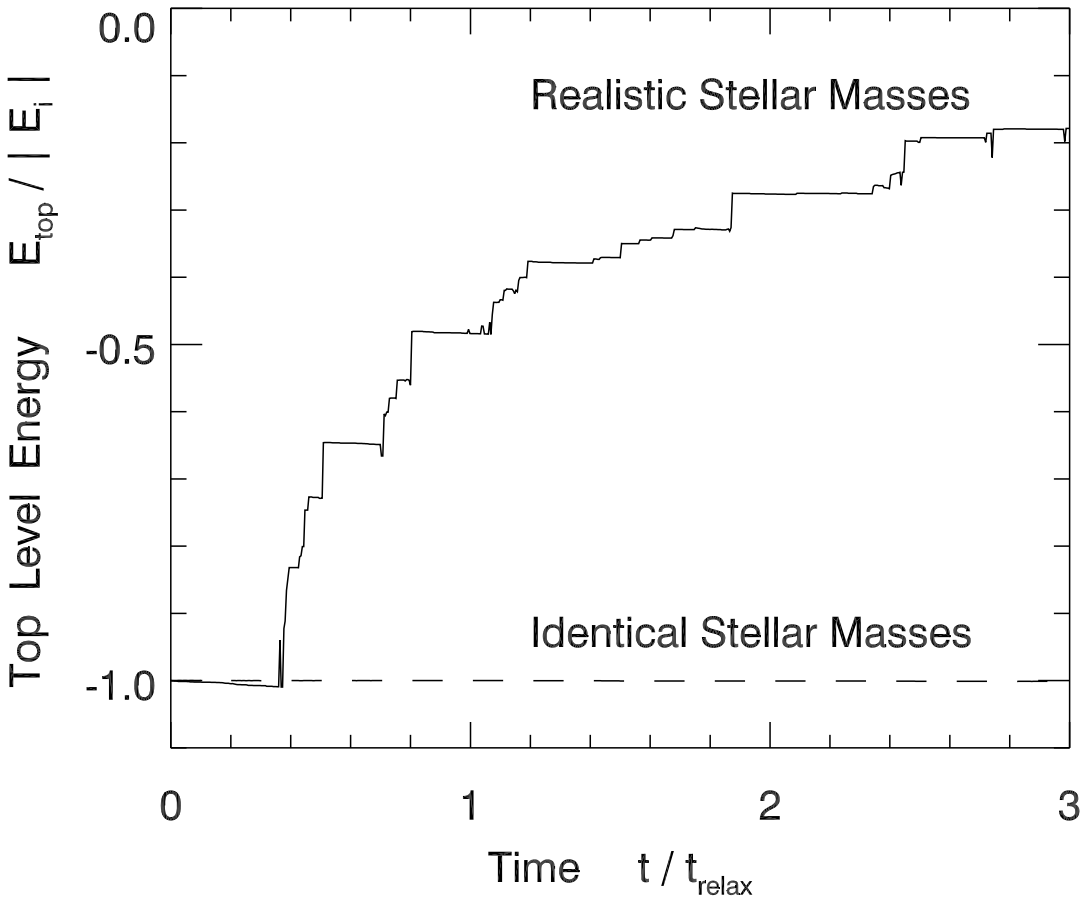

Figure 5.9: Energy evolution for an $N = 4096$ cluster with a realistic mass distribution. The dashed curve shows the evolution in the analogous, single-mass model.

between $t = 0.51t_{\rm relax}$ and $0.70t_{\rm relax}$ represents such a barren period. It is indeed remarkable, as many investigators have noted, how a handful of binaries control the fate of a populous cluster.

In more detail, there is variation of the heating rate with N. Smaller systems experience fewer binary interactions. On the other hand, each interaction creates a larger $\Delta E_{\rm top}$ relative to E_0. Larger systems have more frequent interactions, with each contributing less relative energy. In the end, the rate of energy input actually varies little, when averaged over a sufficiently long period.

What if the cluster is seeded with many binaries initially? Figure 5.10 shows the evolution of the top-level energy for the Pleiades simulation. There are now many binaries even at the start, and thus no initial period of constant $E_{\rm top}$. Remarkably, however, the evolution is quite similar to the case of no primordial binaries. The top-level energy is changed in a few discrete jumps. These few major interactions always involve binary (or triple) systems composed of the few most massive stars (see also de La Fuente Marcos (1996b)).

The important lesson is that only a special subset of binaries strongly influences a cluster's evolution. These are systems which are relatively massive, wide enough to have a significant interaction cross section with other stars, and yet tight enough to be hard. To be sure, the primordial binaries in the Pleiades-like simulation shown in Figure 5.7 do halt the initial contraction. Relatively little energy input is required to do so. Virtually all primordial binaries are either of too low a mass, or are so tight that they effectively interact as a single system. It is the subsequent coupling of relatively few massive stars that inject much greater energy and principally drive the cluster's expansion.

5.2.3 Very Massive Stars

We have seen how binary heating can dominate a cluster's evolution. For a realistic stellar mass spectrum, the effect begins very quickly, in less than a single relaxation time. Under these circumstances, the cluster is still very far from the point of true core collapse.

Following our Pleiades study (Section 2.2.2), we have set the maximum mass at $m_{\rm max} = 10$ M$_\odot$. The reasoning here was that more massive objects would have ionized the parent cloud, allowing the stars to disperse before they could form a bound cluster. In any event, it is instructive when elucidating basic physical principles, to relax this assumption and gauge the effect. We now allow stars in our $N = 4096$ cluster to be drawn from the same mass function as before, but with a nominal upper limit of $m_{\rm max} = 100$ M$_\odot$. In practice, no star ever realizes this mass; the largest generated is about 60 M$_\odot$. Again, there are no primordial binaries.

Based on our earlier arguments, we would expect binary formation to begin even sooner. Indeed this is the case. The first stable, hard binary forms at $t_b = 0.18t_{\rm relax}$, a factor of 2 earlier in time. Figure 5.11 shows the evolution of both Lagrangian mass and number shells. By either measure, the cluster undergoes global expansion at all radii. Not surprisingly, there are detailed differences from the $m_{\rm max} = 10$ M$_\odot$ case. The apparent early contraction of the innermost mass shells is now *entirely* due to mass segregation. Even the number shell

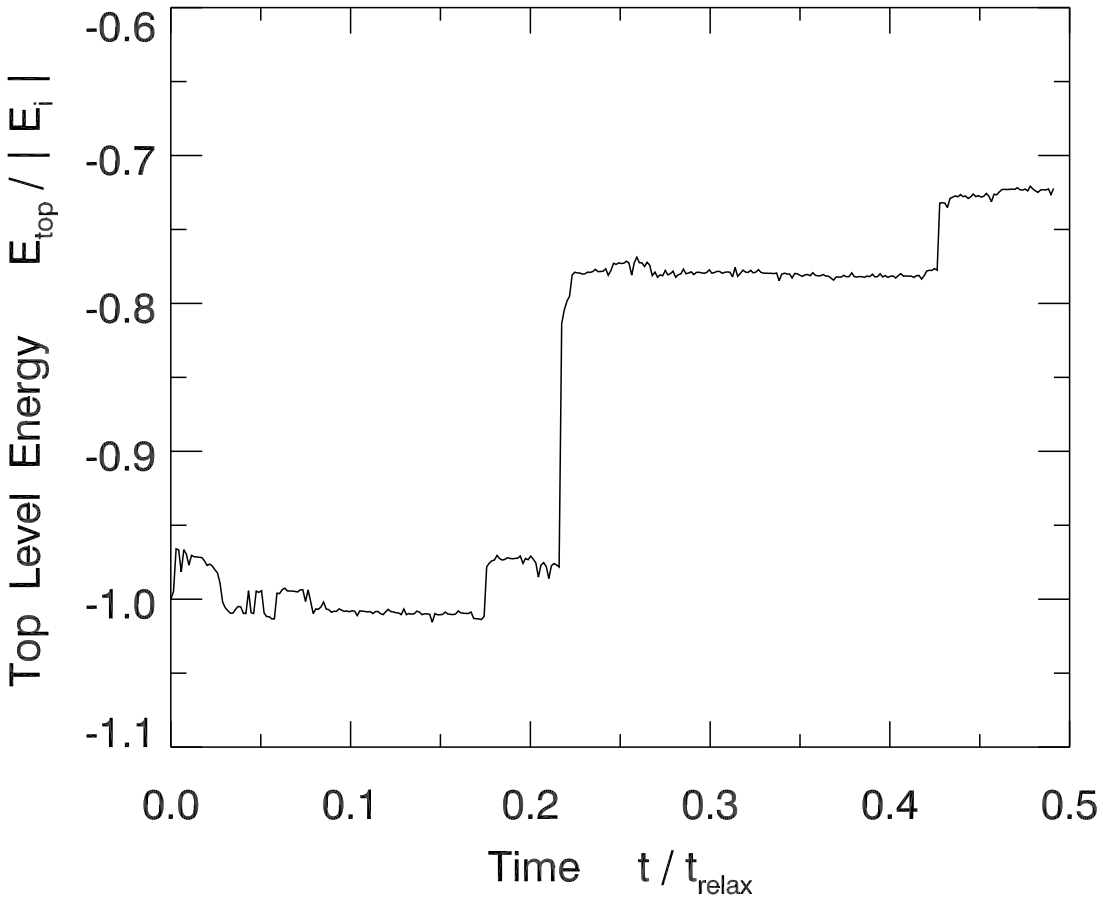

Figure 5.10: Energy evolution for the Pleiades.

with $N_r/N_0 = 0.03$ expands from the start.

A closer analysis shows that there is again never more than a single binary in the cluster at any instant, although the specific pair changes identity in time. Both components of this pair are always among the top 5 stars by mass. These binaries generate especially strong heating.

Figure 5.12 shows the evolution of the top-level energy. For comparison, we also reproduce the analogous plot from Figure 5.9 for the simulation with $m_{\max} = 10$ M$_\odot$. Binary heating now begins much sooner, and the individual three-body encounters inject larger amounts of energy. This result corroborates our earlier conclusion that ΔE_b is proportional to the mass of the binary system.

In the presence of very massive stars, the cluster energy, $|E_0|$, diminishes to only 7% of its initial value over the time considered. In some of our simulations, the heating was so severe as to effectively dissolve the cluster, inflating it to thousands of times its initial size (in the absence of a tidal field). Globular clusters may have been born in parent clouds so massive that even multiple stars producing HII regions do not disrupt them (Kroupa & Boily 2002). Why, then, are young globular clusters not dispersed by binary heating? How do they evolve to the point of core collapse? To answer these questions, we now include the last key ingredient - stellar evolution.

5.3 The Role of Stellar Evolution

It has long been appreciated that the mass loss associated with stellar evolution can have a dramatic effect on the early life of a cluster (Angeletti & Giannone 1977; Applegate 1986; Terlevich 1987; Bastian et al. 2008). As its largest stars die out, the cluster's total mass can decrease significantly. The loss of gravitational binding causes the cluster to expand. This initial phase of expansion, which is ubiquitous in simulations, is quickly stifled because lower mass stars survive much longer.

The loss of the cluster's most massive stars has another effect, more relevant here, that is not as widely appreciated (see however de La Fuente Marcos 1996a). As we have seen, it is these same stars that reverse core contraction and drive global expansion through binary formation and heating. Because of mass loss, however, the objects die out before they can pair with others. Stellar evolution thus tamps down binary heating and postpones the global expansion that this heating drives.

The code Starlab is able to track stellar evolution, including mass loss, by applying analytic fitting formulae. Once we switch on this module, however, we need to give an explicit size scale for our cluster, in order to set the relation between dynamical and stellar evolutionary times. We select a virial radius of $r_v = 4$ pc as a representative value. In our stellar mass function, we continue to set $m_{\max} = 100$ M$_\odot$. As before, we focus on the case $N = 4096$. Our cluster has an initial crossing time of 8 Myr, and an initial relaxation time of $t_{\rm relax} = 570$ Myr. We follow the evolution of the cluster for 8.5 Gyr, which is about 15 relaxation times.

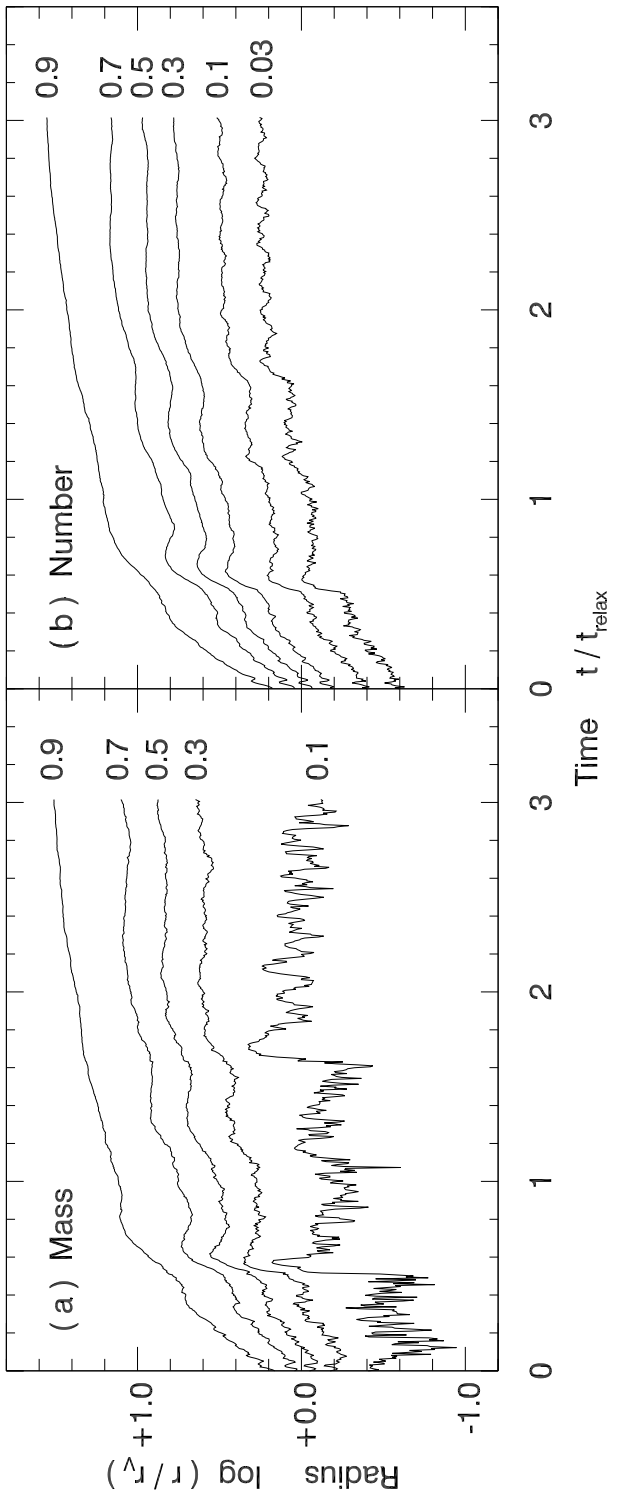

Figure 5.11: Evolution of the radii of (a) mass shells, and (b) number shells, for an $N = 4096$ cluster that includes very massive stars. As in Figure 5.3, each curve is labeled by the appropriate mass or number fraction.

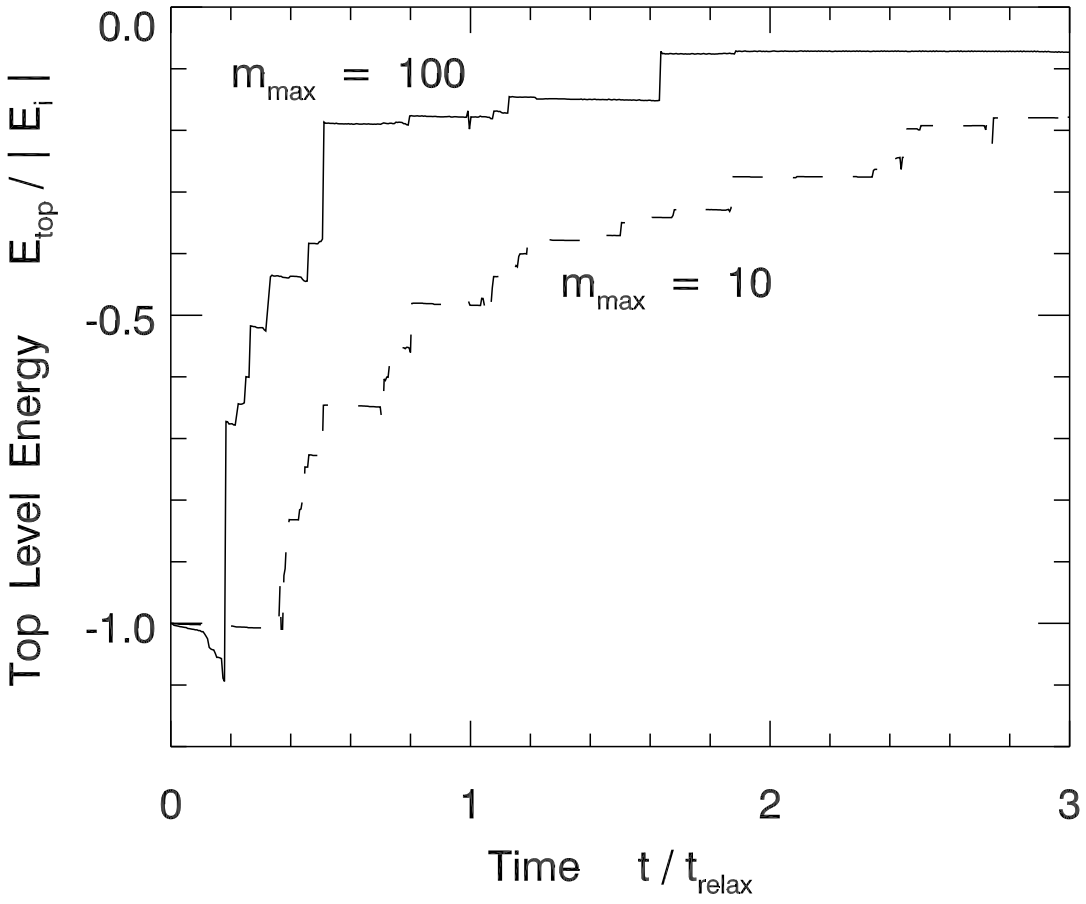

Figure 5.12: Energy evolution for an $N = 4096$ cluster that includes very massive stars. For comparison, the dashed curve reprodcues that from Figure 5.9, where the maximum mass is 10 $M_\odot$.

Figure 5.13 shows the evolution of Lagrangian radii. At first glance, the pattern looks similar to Figure 5.11, which shows the same cluster, but without stellar evolution. Closer inspection reveals important differences. The cluster now undergoes a rapid expansion. During the first 800 Myr, corresponding to 1.5 initial relaxation times, the virial radius increases by a factor of 2. Once the maximum mass of the stars falls below about 2 $M_\odot$, the expansion slows.

The next, slower phase of expansion lasts until about 3 Gyr, or 5.5 $t_{\rm relax}$. Here, heating is provided by an 18 $M_\odot$ black hole left behind by a formerly 67 $M_\odot$ star. Due to its mass, it readily forms a binary system with another star, and this system is the source of the heating. The quantitative details of this phase are as uncertain as our knowledge of the late stages of massive stellar evolution. For example, Hurley et al. (2000) find that the same 67 $M_\odot$ star leaves behind a 4 $M_\odot$ black hole, which would create much less heating and expansion.

Neither of these phases are in the previous Figure 5.11, which omitted stellar evolution. Instead there is an initial brief contraction of the innermost mass shells. As noted earlier, the innermost number shells do not contract, so we are actually witnessing the effects of mass segregation. In the present case, significant contraction of both the mass and number shells occurs. The 18 $M_\odot$ black hole and its companions have been ejected, and no new binaries form. Hence the system is undergoing true dynamical relaxation. Compared to the system with no stellar evolution, this phase is quite protracted, lasting 6 $t_{\rm relax}$.[7] Again, the most massive binaries, that would have halted contraction earlier have died off.

Eventually, however, new binaries do form. As before, it is the highest mass stars present that interact and cause heating. The cluster thereafter enters a prolonged phase of global expansion. This lasts through the end of the simulation. In summary, stellar mass loss has delayed binary formation, and therefore cluster expansion, but not prevented their occurrence.

5.4 Discussion of Real Clusters

5.4.1 Open vs. Globular Clusters

The simulations we performed without stellar evolution all found that t_b, the epoch marking the onset of binary formation, was a fixed fraction of $t_{\rm relax}$. We have just seen, in the specific case of $N = 4096$ that stellar mass loss modifies this result, increasing $t_b/t_{\rm relax}$. Another path to the same conclusion comes from equation (5.14). Stellar evolution lowers the minimum mass m of stars that are around to form a hard binary that can heat the cluster. The ratio $\langle m\rangle/m$ thus increases, and $t_b/t_{\rm relax}$ rises accordingly.

As we consider clusters of higher N, a basic point to note is that $t_{\rm relax}$ itself increases. If the average mass $\langle m\rangle$ is unchanged, then equation (5.13) shows that $t_{\rm relax}$ scales as $N^{1/2}r_v^{3/2}$,

[7] Due to the earlier expansion, the relaxation time at the start of core contraction is 10 times longer than its initial value. The contraction phase lasts for only 0.6 times this readjusted and more appropriate relaxation time.

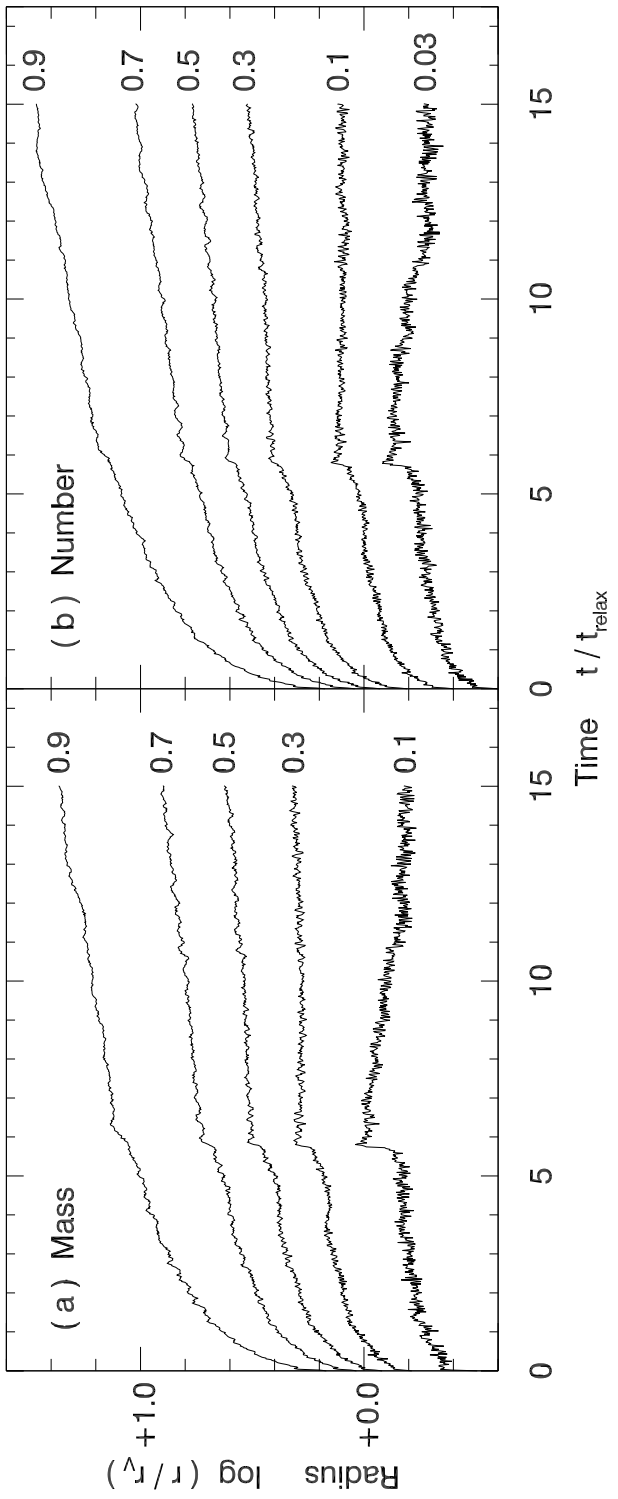

Figure 5.13: Evolution of the radii of (a) mass shells, and (b) number shells, for an $N = 4096$ cluster that includes stellar mass loss. As in Figure 5.3, each curve is labeled by the appropriate mass or number fraction.

ignoring the logarithmic factor. Thus, for similar virial radii r_v, clusters of higher population take longer to relax. The binary formation time t_b in these systems is longer, and, because of stellar evolution, is a higher fraction of $t_{\rm relax}$ itself.

By a given age, therefore, a cluster of higher population has experienced more dynamical relaxation. That is, its core has contracted further. In our view, this trend represents the critical difference between open and globular clusters. The former undergo, at best, a brief, tepid period of core contraction. In our Pleiades simulation, even this mild contraction is stifled by heating from primordial binaries. Globular clusters, on the other hand, undergo much longer periods of dynamical relaxation. In some cases, this prolonged epoch results in true core collapse.

5.4.2 Cluster Death

Throughout this study, we have carried out our simulations to arbitrary times, just long enough to illustrate the main evolutionary phases. The smaller-N groups on which we focus, are eventually destroyed tidally, either by the general Galactic field or by the close passage of giant molecular clouds. Binney & Tremaine (2008, equation (8.57)) give the cloud disruption time scale as

$$t_{\rm dis} = 250 \text{ Myr} \left(\frac{M}{300 \text{ M}_\odot} \right)^{1/2} \left(\frac{r_h}{2 \text{ pc}} \right)^{-3/2} , \tag{5.16}$$

where r_h is the half-mass radius. Consider again our simulation of an $N = 4096$ cluster, with stellar evolution included. Here, $M = 1700$ M$_\odot$ and $r_h = 3.3$ pc. According to equation (5.16) $t_{\rm dis} = 280$ Myr, or $0.5 t_{\rm relax}$. Figure 5.13 shows that the cluster is torn apart very early, during the initial phase of rapid expansion accompanying the death of its most massive stars.

Tidal disruption by passing clouds has long been considered the dominant cluster disruption mechanism (Spitzer 1958). As noted, however, even the Galactic tidal field will eventually do the job. In our Pleiades simulation of Section 3.3.3 the cluster was largely destroyed in this way by 700 Myr. An isolated cluster of this size would be just entering its phase of weak contraction. Because of this external tidal field, however, the simulated Pleaides never even began to contract, but globally expanded until it totally dissolved. Such tidal disruption may account for the mass-independent pattern of cluster death observed in the Antennae Galaxies (Fall et al. 2009) as well as the the Magellanic Clouds (Chandar et al. 2010).

A few open clusters do survive for ages much longer than the ones just mentioned (Friel 1995). These lie in the outer reaches of the Galaxy, where the encounter rate with giant molecular clouds is relatively low, and the general tidal field is also weaker. Our isolated $N = 4096$ cluster eventually begins core contraction at 3 Gyr, corresponding to $6 t_{\rm relax}$. Even the weakened Galactic tidal field will begin to disrupt the system by this age, as seen in the simulation of the even richer system M67 (Hurley et al. 2005). The lesson here is that, while open clusters can in principle enter a phase of tepid core contraction, none reach this point in reality.

5.4.3 Summary of Cluster Evolution

The classical theory of dynamical relaxation is relatively simple, an elegant illustration of how systems with negative heat capacity evolve (Lynden-Bell 1999). However the theory does not describe accurately real clusters, at least those of modest population on which we have focused. The two main factors changing the picture are binary heating and stellar evolution. Both processes are, of course, well understood, but their combined effect has not been appreciated.

All clusters are born with a large fraction of binaries, but these do not provide the largest effect. It is the system's most massive stars coupling together that generate most of the heating through three-body interactions. This heating easily reverses incipient core contraction, so that the central density climbs only slightly before the new phase of global expansion begins. This phase resembles, at least qualitatively, the post-collapse evolution described by Hénon (1972). However, the reversal from contraction occurs at much lower density than in earlier accounts.

Mass loss accompanying stellar evolution modifies the picture, but does not change it qualitatively. Since the most massive stars die out before they can couple with others, the degree of binary heating, and therefore the vigor of global expansion, is less. In addition, the earlier phase of core contraction lasts longer and leads to a higher central density before reversal. Both modifications increase with the cluster population N. We thus see why some globular clusters indeed reach the point of true core collapse, which can be reversed only by the tightest of binaries.

The new picture of cluster evolution presented here is more complex than the classical one, but it is motivated by the basic physical effects that are incorporated in modern numerical simulations. With the benefit of hindsight, it is easy to see why earlier, simplified methods reinforced the impression that dynamical relaxation is ubiquitous. In single mass models, binary formation is so delayed that it becomes irrelevant. Statistical models, based on solving the Fokker-Planck equation, neglect three-body effects entirely. Finally, the contraction of Lagrangian mass shells is not a reliable sign of core contraction, but may reflect a different phenomenon, mass segregation. Our new picture is itself far from complete. Future simulations carried out at higher N will reveal in detail how the transition is made to a more vigorously contracting central core.

Bibliography

Aarseth, S. J. 1971, Ap&SS, 14, 118
Adams, F. C. 2000, ApJ, 542, 964
Adams, F. C., & Myers, P. C. 2001, ApJ, 553, 744
Adams, J. D., Stauffer, J. R., Monet, D. G., Skrutskie, M. F., & Beichman, C. A. 2001, AJ, 121, 2053
Alves, J., Lombardi, M., & Lada, C. J. 2007, A&A, 462, L17
Angeletti, L., & Giannone, P. 1977, A&A, 58, 363
Applegate, J. H. 1986, ApJ, 301, 132
Artyukhina, N. M. 1972, AZh, 49, 389
Bailyn, C. D. 1995, ARA&A, 33, 133
Baraffe, I., Chabrier, G., Allard, F., & Hauschildt, P. H. 1998, A&A, 337, 403
Barrado y Navascués, D., Bouvier, J., Stauffer, J. R., Lodieu, N., & McCaughrean, M. J. 2002, A&A, 395, 813
Basri, G., & Martín, E. L. 1999, ApJ, 510, 266
Bastian, N., Gieles, M., Goodwin, S. P., Trancho, G., Smith, L. J., Konstantopoulos, I., & Efremov, Y. 2008, MNRAS, 389, 223
Bastian, N., & Goodwin, S. P. 2006, MNRAS, 369, L9
Baumgardt, H., De Marchi, G., & Kroupa, P. 2008, ApJ, 685, 247
Baumgardt, H., Heggie, D. C., Hut, P., & Makino, J. 2003, MNRAS, 341, 247
Baumgardt, H., & Kroupa, P. 2007, MNRAS, 380, 1589
Bessell, M. S., & Weis, E. W. 1987, PASP, 99, 642
Bettwieser, E., & Sugimoto, D. 1984, MNRAS, 208, 493
Bihain, G., Rebolo, R., Béjar, V. J. S., Caballero, J. A., Bailer-Jones, C. A. L., Mundt, R., Acosta-Pulido, J. A., & Manchado Torres, A. 2006, A&A, 458, 805
Binney, J., & Merrifield, M. 1998, Galactic astronomy (Princeton, NJ: Princeton University Press)
Binney, J., & Tremaine, S. 2008, Galactic Dynamics: Second Edition (Princeton, NJ: Princeton University Press)
Bonatto, C., & Bica, E. 2003, A&A, 405, 525
Bonnell, I. A., & Davies, M. B. 1998, MNRAS, 295, 691
Bouvier, J., Rigaut, F., & Nadeau, D. 1997, A&A, 323, 139
Brown, A. G. A. 2001, in Revista Mexicana de Astronomia y Astrofisica, vol. 27, Vol. 11,

Revista Mexicana de Astronomia y Astrofisica Conference Series, 89–+
Casertano, S., & Hut, P. 1985, ApJ, 298, 80
Chabrier, G. 2003, PASP, 115, 763
Chabrier, G. 2005, in Astrophysics and Space Science Library, Vol. 327, The Initial Mass Function 50 Years Later, ed. E. Corbelli, F. Palla, & H. Zinnecker (Dordrecht: Springer), 41
Chandar, R., Fall, S. M., & Whitmore, B. C. 2010, ApJ, 711, 1263
Chernoff, D. F., & Djorgovski, S. 1989, ApJ, 339, 904
Clarke, C. J., Bonnell, I. A., & Hillenbrand, L. A. 2000, Protostars and Planets IV, 151
Cohen, M., Wheaton, W. A., & Megeath, S. T. 2003, AJ, 126, 1090
Covey, K. R., et al. 2008, AJ, 136, 1778
Cowan, G. 1998, Statistical Data Analysis (Oxford: Oxford University Press)
Davenport, J. R. A., & Sandquist, E. L. 2010, ApJ, 711, 559
Dawson, S. A., & Schröder, K. 2010, MNRAS, 404, 917
de La Fuente Marcos, R. 1995, A&A, 301, 407
—. 1996a, A&A, 308, 141
—. 1996b, A&A, 314, 453
Deacon, N. R., & Hambly, N. C. 2004, A&A, 416, 125
Dias, W. S., Alessi, B. S., Moitinho, A., & Lépine, J. R. D. 2002, A&A, 389, 871
Djorgovski, S., & King, I. R. 1986, ApJ, 305, L61
Duerr, R., Imhoff, C. L., & Lada, C. J. 1982, ApJ, 261, 135
Duquennoy, A., & Mayor, M. 1991, A&A, 248, 485
Eddington, A. S. 1910, MNRAS, 71, 43
Elmegreen, B. G., Efremov, Y., Pudritz, R. E., & Zinnecker, H. 2000, Protostars and Planets IV, 179
Elson, R. A. W. 1991, ApJS, 76, 185
Fabian, A. C., Pringle, J. E., & Rees, M. J. 1975, MNRAS, 172, 15P
Fall, S. M., Chandar, R., & Whitmore, B. C. 2005, ApJ, 631, L133
—. 2009, ApJ, 704, 453
Fall, S. M., Krumholz, M. R., & Matzner, C. D. 2010, ApJ, 710, L142
Fellhauer, M., Lin, D. N. C., Bolte, M., Aarseth, S. J., & Williams, K. A. 2003, ApJ, 595, L53
Fischer, D. A., & Marcy, G. W. 1992, ApJ, 396, 178
Fresneau, A. 1980, AJ, 85, 66
Friel, E. D. 1995, ARA&A, 33, 381
García, B., & Mermilliod, J. C. 2001, A&A, 368, 122
Giersz, M., & Heggie, D. C. 1997, MNRAS, 286, 709
Goodman, J. 1987, ApJ, 313, 576
Goodwin, S. P. 2009, Ap&SS, 324, 259
Goodwin, S. P., & Bastian, N. 2006, MNRAS, 373, 752
Graybill, F. A. 1983, Matrices with Applications in Statistics (Belmont: Wadsworth)
Gürkan, M. A., Freitag, M., & Rasio, F. A. 2004, ApJ, 604, 632

Haisch, Jr., K. E., Greene, T. P., Barsony, M., & Stahler, S. W. 2004, AJ, 127, 1747
Hambly, N. C., Hawkins, M. R. S., & Jameson, R. F. 1993, A&AS, 100, 607
Heckmann, O., Dieckvoss, W., & Kox, H. 1956, Astronomische Nachrichten, 283, 109
Heckmann, O., & Lübeck, K. 1958, Zeitschrift fur Astrophysik, 45, 243
Heggie, D. C. 1975, MNRAS, 173, 729
—. 1984, MNRAS, 206, 179
Heggie, D. C., Hut, P., & McMillan, S. L. W. 1996, ApJ, 467, 359
Heggie, D. C., & Mathieu, R. D. 1986, in Lecture Notes in Physics, Berlin Springer Verlag, Vol. 267, The Use of Supercomputers in Stellar Dynamics, ed. P. Hut & S. L. W. McMillan (Berlin: Springer-Verlag), 233–+
Hénon, M. 1972, in Astrophysics and Space Science Library, Vol. 31, IAU Colloq. 10: Gravitational N-Body Problem (Dodrecht: Redel), 406–+
Herbig, G. H. 1978, Can Post-T Tauri Stars Be Found?, ed. Mirzoyan, L. V. (Yerevan: Armenian Academy of Sciences), 171
Hillenbrand, L. A. 1997, AJ, 113, 1733
Hills, J. G. 1975, AJ, 80, 1075
Hoffleit, D., & Jaschek, C., eds. 1991, The Bright star catalogue (New Haven, Conn.: Yale University Press)
Huff, E. M., & Stahler, S. W. 2006, ApJ, 644, 355
—. 2007, ApJ, 666, 281
Hurley, J. R., Pols, O. R., Aarseth, S. J., & Tout, C. A. 2005, MNRAS, 363, 293
Hurley, J. R., Pols, O. R., & Tout, C. A. 2000, MNRAS, 315, 543
Hurley, J. R., Tout, C. A., Aarseth, S. J., & Pols, O. R. 2004, MNRAS, 355, 1207
Hut, P. 1983, ApJ, 272, L29
Inagaki, S., & Wiyanto, P. 1984, PASJ, 36, 391
Jones, B. F., & Stauffer, J. R. 1991, AJ, 102, 1080
Kenyon, S. J., & Hartmann, L. 1995, ApJS, 101, 117
King, I. 1962, AJ, 67, 471
King, I. R. 1966, AJ, 71, 64
Klessen, R. S., Heitsch, F., & Mac Low, M. 2000, ApJ, 535, 887
Kroupa, P. 2001, MNRAS, 322, 231
Kroupa, P., Aarseth, S., & Hurley, J. 2001, MNRAS, 321, 699
Kroupa, P., & Boily, C. M. 2002, MNRAS, 336, 1188
Lada, C. J. 2006, ApJ, 640, L63
Lada, C. J., & Lada, E. A. 2003, ARA&A, 41, 57
Lada, C. J., Margulis, M., & Dearborn, D. 1984, ApJ, 285, 141
Landy, S. D., & Szalay, A. S. 1993, ApJ, 412, 64
Li, Y., Klessen, R. S., & Mac Low, M. 2003, ApJ, 592, 975
Lodieu, N., McCaughrean, M. J., Barrado Y Navascués, D., Bouvier, J., & Stauffer, J. R. 2005, A&A, 436, 853
Luhman, K. L. 2007, ApJS, 173, 104
Lynden-Bell, D. 1999, Physica A Statistical Mechanics and its Applications, 263, 293

Lynden-Bell, D., & Wood, R. 1968, MNRAS, 138, 495
Makarov, V. V. 2006, AJ, 131, 2967
Makino, J. 1996, ApJ, 471, 796
Mason, B. D., Henry, T. J., Hartkopf, W. I., ten Brummelaar, T., & Soderblom, D. R. 1998, AJ, 116, 2975
McCaughrean, M. J., & Stauffer, J. R. 1994, AJ, 108, 1382
McKee, C. F., & Ostriker, E. C. 2007, ARA&A, 45, 565
McKee, C. F., & Williams, J. P. 1997, ApJ, 476, 144
Mermilliod, J. 1995, in Astrophysics and Space Science Library, Vol. 203, Information & On-Line Data in Astronomy, ed. D. Egret & M. A. Albrecht (Dordrecht: Kluwer), 127–138
Mermilliod, J., Queloz, D., & Mayor, M. 2008, A&A, 488, 409
Mermilliod, J., Rosvick, J. M., Duquennoy, A., & Mayor, M. 1992, A&A, 265, 513
Meynet, G., Mermilliod, J., & Maeder, A. 1993, A&AS, 98, 477
Michell, J. 1767, Royal Society of London Philosophical Transactions Series I, 57, 234
Miller, G. E., & Scalo, J. M. 1978, PASP, 90, 506
Moitinho, A., Alfaro, E. J., Yun, J. L., & Phelps, R. L. 1997, AJ, 113, 1359
Monet, D. G., et al. 2003, AJ, 125, 984
Moraux, E., Kroupa, P., & Bouvier, J. 2004, A&A, 426, 75
Palla, F., & Stahler, S. W. 2000, ApJ, 540, 255
Patience, J., Ghez, A. M., Reid, I. N., & Matthews, K. 2002, AJ, 123, 1570
Peebles, P. J. E. 1980, The large-scale structure of the universe (Princeton, NJ: Princeton University Press)
Pinfield, D. J., Dobbie, P. D., Jameson, R. F., Steele, I. A., Jones, H. R. A., & Katsiyannis, A. C. 2003, MNRAS, 342, 1241
Pinfield, D. J., Hodgkin, S. T., Jameson, R. F., Cossburn, M. R., Hambly, N. C., & Devereux, N. 2000, MNRAS, 313, 347
Pinfield, D. J., Jameson, R. F., & Hodgkin, S. T. 1998, MNRAS, 299, 955
Pinsonneault, M. H., Stauffer, J., Soderblom, D. R., King, J. R., & Hanson, R. B. 1998, ApJ, 504, 170
Portegies Zwart, S., Gaburov, E., Chen, H., & Gürkan, M. A. 2007, MNRAS, 378, L29
Portegies Zwart, S. F., Hut, P., Makino, J., & McMillan, S. L. W. 1998, A&A, 337, 363
Portegies Zwart, S. F., & McMillan, S. L. W. 2002, ApJ, 576, 899
Portegies Zwart, S. F., McMillan, S. L. W., Hut, P., & Makino, J. 2001, MNRAS, 321, 199
Press, W. H., Teukolsky, S. A., Vetterling, W. T., & Flannery, B. P. 2002, Numerical recipes in C++ : the art of scientific computing (Cambridge: Cambridge University Press)
Prosser, C. F. 1992, AJ, 103, 488
—. 1994, AJ, 107, 1422
Prosser, C. F., Randich, S., Stauffer, J. R., Schmitt, J. H. M. M., & Simon, T. 1996, AJ, 112, 1570
Prosser, C. P., & Randich, S. 1998, Astronomische Nachrichten, 319, 201
Prosser, C. P., Randich, S., & Simon, T. 1998, Astronomische Nachrichten, 319, 215
Raboud, D., & Mermilliod, J. 1998, A&A, 329, 101

Rieke, G. H., & Lebofsky, M. J. 1985, ApJ, 288, 618
Robichon, N., Arenou, F., Mermilliod, J., & Turon, C. 1999, A&A, 345, 471
Romani, R. W., & Weinberg, M. D. 1991, ApJ, 372, 487
Sagar, R., Miakutin, V. I., Piskunov, A. E., & Dluzhnevskaia, O. B. 1988, MNRAS, 234, 831
Salpeter, E. E. 1955, ApJ, 121, 161
Schwartz, M. J., & Becklin, E. E. 2005, AJ, 130, 2352
Sen, A. 1997, Statistical Data Analysis (Oxford: Clarendon Press)
Siess, L., Dufour, E., & Forestini, M. 2000, A&A, 358, 593
Skrutskie, M. F., et al. 2006, AJ, 131, 1163
Soderblom, D. R., Nelan, E., Benedict, G. F., McArthur, B., Ramirez, I., Spiesman, W., & Jones, B. F. 2005, AJ, 129, 1616
Spitzer, Jr., L. 1958, ApJ, 127, 17
—. 1969, ApJ, 158, L139+
Stauffer, J. R., Hartmann, L. W., Burnham, J. N., & Jones, B. F. 1985, ApJ, 289, 247
Stauffer, J. R., Hartmann, L. W., & Jones, B. F. 1989, ApJ, 346, 160
Stauffer, J. R., Schultz, G., & Kirkpatrick, J. D. 1998, ApJ, 499, L199
Stauffer, J. R., et al. 1999, ApJ, 527, 219
—. 2007, ApJS, 172, 663
Steele, I. A., & Jameson, R. F. 1995, MNRAS, 272, 630
Stolte, A., Brandner, W., Brandl, B., & Zinnecker, H. 2006, AJ, 132, 253
Takahashi, K. 1995, PASJ, 47, 561
Tassis, K. 2007, MNRAS, 379, L50
Terlevich, E. 1983, PhD thesis, Ph. D. thesis, University of Cambridge, Cambridge
—. 1987, MNRAS, 224, 193
Trager, S. C., King, I. R., & Djorgovski, S. 1995, AJ, 109, 218
Trullols, E., Rosselo, G., Jordi, C., & Lahulla, F. 1989, A&AS, 81, 47
Trumpler, R. J. 1921, Lick Observatory Bulletin, 10, 110
van den Bergh, S., & Sher, D. 1960, Publications of the David Dunlap Observatory, 2, 203
van Leeuwen, F. 1999, A&A, 341, L71
Vázquez-Semadeni, E., Ballesteros-Paredes, J., & Klessen, R. S. 2003, ApJ, 585, L131
Ventura, P., Zeppieri, A., Mazzitelli, I., & D'Antona, F. 1998, A&A, 334, 953
Wielen, R. 1974, in Stars and the Milky Way System, ed. L. N. Mavridis (Berlin: Springer), 326
Zinnecker, H., & Mathieu, R., eds. 2001, IAU Symposium, Vol. 200, The Formation of Binary Stars (San Francisco: ASP)